Unraveling the surface formation of regular and deuterated water in space : a combined laboratory and computational study

Lamberts, A.L.M.

Unraveling the surface formation of regular and deuterated water in space

A combined laboratory and computational study

Thanja Lamberts

Unraveling the surface formation of regular and deuterated water in space– A combined laboratory and computational study, Thesis, Leiden University
Ontrafelen van de oppervlaktevorming van gewoon en gedeutereerd water in de ruimte – Een gecombineerde laboratorium en computationele studie, Proefschrift, Universiteit Leiden

168 pages; illustrated, with bibliographic references and summary in Dutch

ISBN/EAN: 978-94-6259-678-8

Printed by Ipskamp Drukkers

Cover design by Gaetano Fiorin and Thanja Lamberts

This work has been financially supported by the Nederlandse Organisatie voor Wetenschappelijk Onderzoek (NWO) *and by the* European Research Council (ERC).

Unraveling the surface formation of regular and deuterated water in space

A combined laboratory and computational study

Proefschrift

ter verkrijging van
de graad van doctor aan de Universiteit Leiden
op gezag van de Rector Magnificus prof. mr. C. J. J. .M. Stolker,
volgens besluit van het College voor Promoties
te verdedigen op woensdag 20 mei 2015
klokke 13:45 uur

door

Agneta Luciana Matthanja Lamberts
geboren te 's Gravenhage
in 1987

Promotiecommissie

Promotor	Prof. dr. H. V. J. Linnartz	
Co-promotores	Dr. H. M. Cuppen	Radboud Universiteit Nijmegen
	Dr. S. Ioppolo	The Open University
Overige leden	Prof. dr. H. J. A. Röttgering	
	Prof. dr. A. G. G. M. Tielens	
	Prof. dr. G. C. Groenenboom	Radboud Universiteit Nijmegen
	Prof. dr. N. J. Mason	The Open University
	Dr. D. A. Semenov	Max Planck Institute for Astronomy

Voor Hetty en Timo

CONTENTS

ACRONYMS

AKMC Adaptive Kinetic Monte Carlo

CEM Channel Electron Multiplier

CTRW Continuous-Time Random-Walk

DAN Dutch Astrochemistry Network

ER Eley-Rideal

FTIR Fourier Transform InfraRed

HA Hot-Atom

HABS Hydrogen Atom Beam Source

HIFI Heterodyne Instrument for the Far-Infrared

HSO Herschel Space Telescope

IRF Interstellar Radiation Field

ISM InterStellar Medium

ISO Infrared Space Observatory

JFC Jupiter Family Comet

KMC Kinetic Monte Carlo

LASSIE Laboratory Astrochemical Surface Science In Europe

LH Langmuir-Hinshelwood

MALDI Matrix-Assisted Laser Desorption/Ionization

MWAS MicroWave Atom Source

OCC Oort Cloud Comet

QCM Quartz Crystal Microbalance

QMS Quadrupole Mass Spectrometer

RAIR Reflection Absorption InfraRed

REMPI Resonance Enhanced Multiphoton Ionization

SEM Secondary Electron Multiplier

SMOW Standard Mean Ocean Water

SST Spitzer Space Telescope

SURFRESIDE Surface REaction SImulation DEvice

TOF Time Of Flight

TPD Temperature Programmed Desorption

UHV Ultra High Vacuum

WISH Water In Star-forming regions with Herschel

YSO Young Stellar Object

1

INTRODUCTION

'L'eau peut aussi être bonne pour le coeur...' is what the little prince said in the book written by Antoine de Saint-Exupéry. Indeed, water is at the very least important for the physical life on Earth. Contrary to what might be expected considering its importance, how and if water was delivered to our planet is still under debate. It has been postulated that Earth's water reservoir has been formed already before the formation of the Sun. Moreover, water is abundantly observed throughout the interstellar medium. Not only in the cold quiescent birth places of new stars, but also in highly energetic flows of material surrounding a young star. Many of these astronomical observations have proven the existence of gas-phase water. It seems to be most likely though that these vapors originate from the sublimation of ices covering small dust grains. Oxygen and hydrogen atoms or molecules freeze out on the cold grain surface ($10 - 20$ K) in regions of relatively high densities ($10^4 - 10^5$ cm^{-3}). Given enough time, several hundred thousand years, thick layers of water-dominated ices are formed through consecutive reactions of the frozen-out material. Surface chemistry is thus crucial in understanding the abundances of water found in space. Next to the formation of regular water, the combination of oxygen, hydrogen, and deuterium atoms, results in heavy, or singly-deuterated water. As a result of the low temperatures involved, deuterium is preferentially incorporated into water molecules, enhancing the ratio of deuterated over regular water with respect to its elemental ratio. This ratio is therefore often used as a tracer in relating the water found in the interstellar medium to that of Earth's oceans.

This thesis focuses on the surface formation of water at low temperatures, both experimentally and under interstellar conditions. It describes the use of a large reaction network as well as the studies of particular reaction routes of regular and deuterated water.

1.1 WATER DURING THE VARIOUS STAGES OF STAR FORMATION

Low-mass star formation is relatively well-understood, and therefore this sequence of events is described below in conjunction with the water detections in the various stages of star and planet formation. A number of different regions corresponding to these stages with their representative density, temperature, and A_V is summarized in Table 1.1.

Table 1.1: Types of interstellar and circumstellar clouds and their physical characteristics, adapted from van Dishoeck et al. (2013).

Name	Density (cm^{-3})	Temp. (K)	A_V (mag)	Example
Diffuse cloud	10^2	$30-100$	$\leqslant 1$	ζ Oph
Translucent cloud	10^3	$15-50$	$1-5$	HD 154368
Cold dense cloud	10^4-10^5	$10-20$	>10	Taurus Cloud
Prestellar core	$\geqslant 10^5$	$8-15$	$10-100$	L1544
Protostellar envelope				
cold outer	10^4-10^7	$8-100$	$10-100$	NGC 1333 IRAS4A
warm inner	10^7-10^9	$\geqslant 100$	$100-1000$	W_3 IRS5
Shock	10^4-10^5	$200-2000$	$\leqslant$ few	L1157 B1
Protoplanetary disk				
outer	10^6-10^{10}	$10-500$	$1-100$	TW Hya
inner	10^9-10^{15}	$100-3000$	$1-1000$	AS 205

It is in the cold, dense regions of the interstellar medium (ISM) that star formation commences (Shu et al., 1987). The dense regions, or *dark clouds*, originate from more dilute, or *diffuse*, environments thanks to gravitational attraction or external shockwaves. In the diffuse regions, the interstellar radiation field (IRF) is the cause of efficient destruction of molecules and ices, whereas in dense regions H_2 is largely responsible for shielding from the IRF which keeps the temperature low in the center of the cloud ($\sim 10-20$ K). Therefore, ices are abundantly present in the denser regions (*e.g.*, Whittet et al. (1988) and Chapter 5). The name 'dark' is given, because visible light at cannot penetrate through the clouds and reach a telescope. At this point, the cloud needs a cooling mechanism different from molecular radiation and it is the far-infrared light radiated by dust grains that mediates the further collapse. Since a cloud accumulates mass, the gravitational force increases and, eventually, the cloud collapses to form a *prestellar core* ($\sim 8-15$ K). The first water vapor detection towards a cloud on the verge of star formation, namely the prestellar core L1544, has been reported recently (Caselli et al., 2012). The high sensitivity of the Herschel Space Observatory (HSO) has made this detection possible. Further contraction of the cloud eventually raises the temperature of the inner region until the internal pressure can support the resulting *protostar* against a continuing collapse. The protostar is still surrounded by an envelope of atoms and molecules which continue to accrete onto the center. The outer envelope remains cold and ices can thus be present there as detected by the ISO and the SST, but the inner envelope is heated by the star and molecules evaporate. The rotating envelope eventually forms an *accretion disk* which dissipates its angular momentum via bipolar outflows. Water has been detected in the gas phase in a variety of regions around protostars thanks to the Water In Star forming regions with Herschel (WISH) program. It is seen in an infalling motion in the envelope, in shocked regions along the outflow cavity walls, and in the outflows themselves (Nisini et al., 2010; Kristensen et al., 2012).

The dust in the disks is known to grow up to cm-sized particles (Kessler-Silacci et al., 2006) and grain growth in general is thought to be the start of planet formation. The 13 orders of magnitude separating the sub-micron particles from terrestrial planets, however, are not easily connected (Williams & Cieza, 2011). Also in planet forming disks, water vapor has been detected by the Heterodyne Instrument for the Far-Infrared (HIFI) on the HSO. Cold water vapor around the young star TW Hydrae are observed and this likely originates from icy grains near the disk surface. The correlation between the observed gas to the water ice reservoir from which it originates hints at a reservoir equivalent to several thousand Earth oceans in mass (Hogerheijde et al., 2011). Not all material present in the disk ends up in planets and the remaining material can nowadays be found in comets and asteroids. Comets contain mainly ice, dust, rocky materials, and organic compounds, whereas asteroids are dry and consist of metals and rocky material. A comet can lose material upon approaching the Sun, as a part of the ice melts and evaporates, in the coma – consisting of sublimated cometary material – water has indeed been observed. For example as a part of the recent Rosetta mission towards the comet 67P/Churyumov-Gerasimenko both HDO and H_2O have been detected (see also Section 1.4) (Altwegg et al., 2015). Eventually a protostar will start to burn, or rather fuse, hydrogen and the star enters the main sequence phase in the Hertzsprung-Russell diagram (Rosenberg, 1910).

The star formation process of high-mass stars, those with masses exceeding that of 8 times the solar mass, is not well-understood. This is partially related to the shorter lifetime and the large distances associated with the molecular outflows. Therefore, the outflow of one star-forming core can influence that of the neighboring cores. Recently, however, within the WISH key programme, it was suggested from a study of 51 young stellar objects (YSOs) that physical processes in protostellar envelopes have similar characteristics in high- and low-mass stars (San José-García et al., 2013).

When the fuel, not only hydrogen, but also the heavier elements, has run out, the remnants of a star can take several forms depending on the mass during its lifetime: a white dwarf, neutron star, pulsar, or black hole. Most importantly for the present dicussion is that during stellar death there are various ways for a star to inject mass into the ISM. This can be through winds, planetary nebulae, or supernovea. In this way, the cycle of matter is completed.

1.2 ICES IN THE INTERSTELLAR MEDIUM

The existence of water ice in the ISM had been postulated several decades prior to its detection: *'In view of the high boiling-point of water (...) is it not likely that this would precipitate the most freely?'* (Eddington, 1937). After the realization that interstellar particles, *i.e.*, grains, indeed are present, *'It may now be asked of what kind of molecules they exist'* (van de Hulst, 1949). Water was already thought to be the main component of the ices, but it took until 1973 for solid water to be observed by Gillett & Forrest through its 3 μm feature.

The infrared absorption feature of the solid water OH stretch can be observed superimposed on the continuum spectrum of an embedded YSO or a background star. The Infrared Space Observatory (ISO), in the 1990's, played a large role in the observations of interstellar ices in the spectral range of $2.5 - 30$ μm. It observed 23 relatively bright sources in various regions of the ISM: embedded YSOs and field stars sampling quiescent dark clouds and the diffuse interstellar medium (Gibb et al., 2004). Furthermore, the cores-to-disks (c2d) program combined Spitzer Space Telescope (SST) observations in the spectral range of $3 - 38$ μm of 41 low-luminosity YSOs with ground-based observations (Keck NIRSPEC or VLT ISAAC) (Boogert et al., 2008). It is thanks to these large-scale projects that the average composition of interstellar ice has been determined. Indeed the main component of interstellar ices is water, followed

by carbon monoxide (CO), carbon dioxide (CO_2), and minor contributions from methanol (CH_3OH), formic acid (HCOOH), formaldehyde (H_2CO), and methane (CH_4) (van Dishoeck, 2004). The name 'ices' in astrochemistry is actually not only reserved for water ice, but for all solids that consist of volatiles (molecules that are liquid or gaseous at room temperature).

1.3 SOLID STATE WATER FORMATION: SURFACE CHEMISTRY

Most of the ice species form on the surface of dust grains, even though the dust constitutes only 1% of the total mass in the ISM. Freeze-out of atoms and molecules takes place only when the temperature is low enough. In that case, there is a local high density of species present on the surface, allowing the formation of water from oxygen atoms and hydrogen atoms and molecules. Since frozen molecules are not isolated when they react with each other, gas-phase reaction dynamics cannot be directly extended to the solid phase; although the initially proposed surface reaction networks were largely constructed based on analogies with gas-phase data (Tielens & Hagen, 1982). The four main processes that occur on the surface – accretion, desorption, diffusion, and reaction – are always in competition with each other. For an accurate understanding of the microscopic interplay between them, both detailed experiments and models are needed.

Accretion is governed by the gas-phase abundance, n, of a species. The rate of deposition, $R_{deposition}$, also depends on the gas-phase mean velocity of the species, v, and the surface site density, ρ, scaled by a factor 4 taking to account for the fact that accretion takes place only from one direction:

$$R_{deposition} = \frac{n\, v}{4\rho} \,. \tag{1}$$

Desorption depends on the binding energy of a particle to the grain surface or neighboring ice molecules. There are several ways to define the binding energy. One way is to derive an overall average value experimentally (see Chapter 2), but if a microscopic model is used, the interaction with a variety of adjacent sites can be taken into account explicitly.

Diffusion is also associated with the binding energy, albeit in a less stringent way. In this case it is not only the binding energy of a species in its initial state, but also the gain or loss in energy upon moving that determines its trajectory in astrochemical models. Both the desorption and diffusion rates are often assumed to be thermally activated and follow Arrhenius type expressions (see Chapter 3).

Surface reactions are generally devided into three types – schematically depicted in Figure 1.1: the Langmuir-Hinshelwood (LH) mechanism is a diffusive mechanism in which the species move over the surface and attempt to react upon meeting, the Eley-Rideal (ER) mechanism, where one (stationary) reactant is hit by another species from the gas phase, and the hot-atom (HA) mechanism, which is a combination of both mechanisms where non-thermalized species travel some distance over the surface finding reactants on their way. In all cases, the excess heat which becomes available through the reaction can be used for desorption of the products. Since in dense clouds the temperature of the gas phase is similar to the grain temperature, the hot-atom mechanism is generally not considered. It can be important in experimental conditions or, for instance, in shock regions where the gas phase is often much warmer than the grain. It is worth mentioning that the reaction rate is different for Eley-Rideal and Langmuir-Hinshelwood: for the former the two reactants have one attempt to cross the reaction barrier, whereas for the latter the two reactants will remain adsorbed in close vicinity until they react or one of them diffuses away or desorbs. Furthermore, energetic processing of an ice can result in the breaking of a bond, which is typically also considered to be a 'reaction' with a photon or an energetic particle (see Chapter 2).

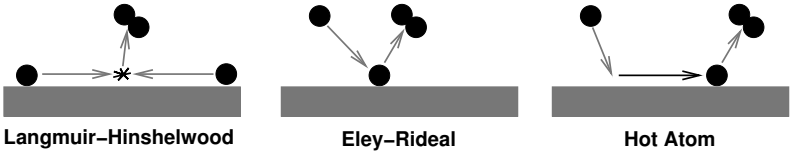

Figure 1.1: Schematic representation of the three mechanisms for surface reaction: the Langmuir-Hinshelwood mechanism, a diffusive mechanism in which the species move over the surface and try to react upon meeting, the Eley-Rideal mechanism where one (stationary) reactant is hit by another species from the gas phase, and the hot-atom mechanism which is a combination of both mechanisms where non-thermalized species travel some distance over the surface finding reactants on their way.

Although many of the above applies only to surface processes, it has been found both experimentally and theoretically that bulk processes, *i.e.*, in thick ices, play a large role in the chemistry. For instance, UV photons can penetrate up to several layers of ice and pores inside an amorphous ice can provide pathways to diffusion inside such a cavity.

1.4 ORIGIN OF WATER ON EARTH: HDO

Water is not only abundant in the ISM, in its liquid phase it also plays an ultimate role for the origin of life on Earth. The origin of the ocean's water is nonetheless unclear, because Earth was formed within the so-called snow line. This is the line around a protostar that separates the inner area where bare grains exist from the outer area where grains are covered with ice. Planets formed within the snow line are therefore rather dry compared to those formed outside this line (Min et al., 2011).

Several hypotheses exist on how water arrived in the inner Solar System. One of these was put forward by Drake (2005) and Stimpfl et al. (2006) who showed that chemisorption sites exist on forsterite grains where water can absorb. Grains can retain a submonolayer of water well beyond the snow line in this way. Muralidharan et al. (2008) build on this work by applying a lattice-gas Kinetic Monte Carlo (KMC) simulation. Due to the many and conservative assumptions used in the model, the authors argue that the results only give a conservative lower limit to the amount of water that can be absorbed onto grains prior to accretion into planets. Their results show that this amount can indeed be substantial. Furthermore, the bombardment of carbonaceous asteroids or comets that originate from the ice-rich outer region of the early solar system is another plausible mechanism, accounting at least partially for water on Earth (Owen et al., 1992; Morbidelli et al., 2000; Cleeves et al., 2014). Such a scenario is supported by recent models where water delivery takes place during the formation phase of terrestrial planets (O'Brien et al., 2014). Finally, a large part of the carbonaceous chondrites contains hydrated silicates and hydrous carbon (Robert, 2003). Dynamic solar system models for planetary water delivery seem to indicate that carbonaceous chondritic planetesimals could have delivered water during primary accretion of Earth (Sarafian et al., 2014).

A common tracer in the origin of water on Earth is the HDO/H_2O ratio, of which the Earth ocean value is found to be higher than the primordial ratio of $\sim 1.5 \times 10^{-5}$ (Piskunov et al., 1997; Oliveira et al., 2003). Linking the HDO/H_2O ratio found in cometary, interstellar, and laboratory ices as well as those found through gas-phase observations to the ratio in our oceans is therefore one of the challenges currently faced by the community (Rodgers & Charnley, 2002; Hartogh et al., 2011). Figure 1.2 summarizes the HDO/H_2O ratio in various astrochemically in-

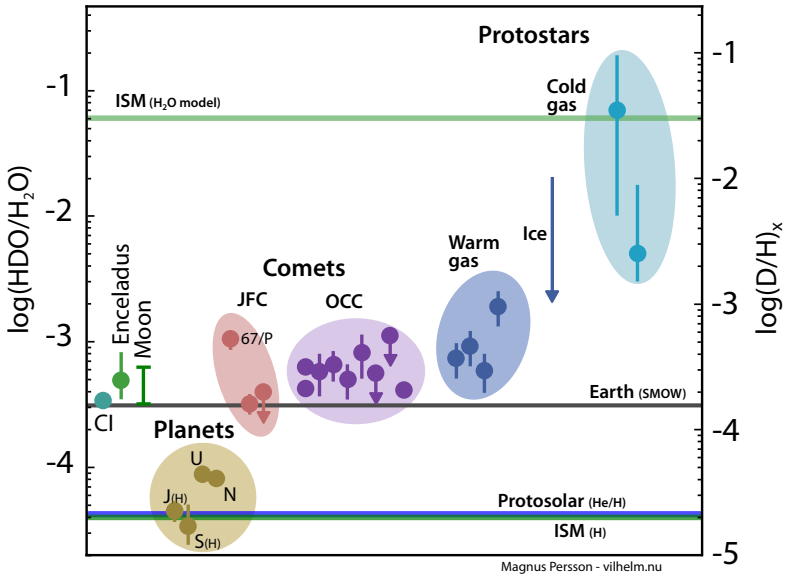

Figure 1.2: D/H ratio for water in various regions in space. Retrieved from Persson (2015), references can be found in Persson et al. (2014), Albertsson et al. (2014), and Altwegg et al. (2015).

teresting regions and compares it to the primordial interstellar D/H ratio, the protosolar D/H ratio, the Standard Mean Ocean Water (SMOW) HDO/H_2O value, and a recently modeled HDO/H_2O value in the early solar nebula. From the figure it can be deduced that there is a considerable spread in the ratios found in both Jupiter Family Comets (JFC) and Oort Cloud Comets (OCC). The hypothesis that JFCs can be entirely responsible for the delivery of water to Earth therefore seems unlikely (Altwegg et al., 2015). It is very likely, though, that a considerable fraction of the solar system's water originates from primitive sources (Cleeves et al., 2014; O'Brien et al., 2014).

The main causes of preferential incorporation of deuterium over hydrogen in molecules, or fractionation, find their origin in the lower zero-point energy of an X-D bond with respect to an X-H bond as a result of the larger mass of deuterium. Firstly, the molecule H_2D^+ is more stable than the ubiquitous H_3^+, and the reaction $H_3^+ + HD \longrightarrow H_2D^+ + H_2$ enhances the H_2D^+/H_3^+ ratio in the gas-phase. Following the freeze-out of the main destruction partners of H_2D^+, namely CO and O, dissociative recombination with an electron takes place $H_2D^+ + e^- \longrightarrow D + H_2$ liberating D atoms. This process can increase the gas-phase D/H ratio to values larger than 0.1 (Roberts et al., 2003). The number of deuterium atoms landing on the grain surface is larger, thus increasing its probability to be incorporated into (water) molecules (Tielens, 1983; Caselli et al., 2012). Secondly, the binding energy of D atoms to a grain or water surface is larger, increasing the time that it spends on the surface, *e.g.*, Lipshtat et al. (2004). Finally, specific surface reaction rates are influenced by the enthalpy of the bonds that are destroyed and formed, which in itself is subject to zero-point energy. One example is substitution of H for D in solid methanol, which has been found to be efficient, whereas the reverse reaction (substituting D for H) is not (Nagaoka et al., 2005).

1.5 THIS THESIS

This thesis is devoted to the study of regular and deuterated water in ices and on surfaces against an interstellar background. A large network for the formation of regular water has been studied with the use of a Kinetic Monte Carlo model. A specific reaction has been investigated as well: $H_2 + O \longrightarrow OH + H$. Furthermore, in the light of deuterium fractionation, a thermal study on deuteron scrambling in the ice has been performed: $H_2O + D_2O \longrightarrow 2HDO$. Finally, two low-temperature routes relevant to HDO formation have been investigated: $H_2O + OD \longrightarrow OH + HDO$ and $D_2O + OH \longrightarrow OD + HDO$.

First of all, **Chapter 2** describes the use of an Ultra-High Vacuum (UHV) experimental setup equipped with a Reflection Absorption Infrared (RAIR) spectrometer and a Quadrupole Mass Spectrometer (QMS) in the context of various other possible techniques used in the field of astrochemistry. Furthermore, the specific experimental setup used in the Sakcler Laboratory for Astrophysics is introduced and its calibration is outlined.

In **Chapter 3** the Continuous-Time Random-Walk (CTRW), or KMC, model is compared to other commonly used astrochemical models. The technical aspects, such as neccessary input parameters, are introduced along with the algorithm implemented in the code used for this thesis. Finally, a number of published astrochemical studies making use of KMC are summarized.

Chapters 4 and 5 build on the laboratory studies of molecular oxygen hydrogenation: $O_2 + H$. This route was chosen because it consists of reaction pathways that are relatively well-separated from the $O + H$ and $O_3 + H$ reaction routes: it starts out with two barrierless reactions $H + O_2 \longrightarrow HO_2$ and $H + HO_2 \longrightarrow H_2O_2$. The experiments have been performed and analyzed previously by Ioppolo et al. (2010) and Cuppen et al. (2010). Being able to use KMC simulations to reproduce the main experimental conclusions provides a benchmarked model that can then be used to run simulations under interstellar conditions. Four different experiments are chosen to be modeled to probe a large region of the parameter space spanned by the large number of reaction, diffusion and desorption rates. First, experiments in which a layer of pre-deposited O_2 was hydrogenated are modeled at 15 and 25 K. Then, again at both temperatures, so-called co-deposition experiments are used, in which hydrogen and oxygen were frozen out simultaneously. The full water surface formation chemical network is included in the model, but to understand the influence of separate parameters, a single process rate is varied at the time, either diffusion or reaction rates. Although initially a number of key reactions ($H + O_2$, $H + HO_2$, $OH + OH$, $H + H_2O_2$, $H + OH$) and the neccessity for including a high hydrogen diffusion rate was established, the diffusion of radicals other than H turned out to play an important role. Therefore, a follow-up study focuses on the breakdown of the so-called Markov chain assumption for the formation of two OH radicals by the reaction $H + HO_2$. A combined effect of directionality of the OH radical movement together with energy dissipation can explain the experimental observation of OH radicals. This optimized model is then used to run simulations under diffuse, translucent, and dense cloud conditions. From these model runs information is obtained about the main reaction routes producing water in the different interstellar regions.

In astrochemical environments it is possible that one reaction within a network dominates water formation as a result of the relative abundances of the species involved. Such a behavior has been previously postulated for the role of the endothermic reaction $H_2 + O \longrightarrow OH + H$

in dark clouds. In **Chapter 6** precisely executed temperature-programmed desorption (TPD) experiments are described that determine an absolute conservative upper limit to the production of water on the surface after co-deposition of H_2 and O. Furthermore, a set of KMC simulations – using the optimized parameters from Chapter 5 – is used to establish an upper limit to the reaction rate itself. Incorporating this rate into the same model, but run with astrochemically relevant parameters, allows to find the upper limit to the contribution of the reaction $H_2 + O$ for the formation of OH, and hence water formation. This value is 11% in dense interstellar clouds and therefore we conclude that the reaction $H_2 + O$ does not dominate water formation in these regions.

Chapter 7 shifts focus towards the processes that influence the HDO/H_2O ratio in the ice. Here, the thermally induced proton/deuteron exchange in mixed amorphous H_2O:D_2O ices is monitored. The characteristic vibrational bending modes of the three isotopes involved – H_2O, HDO, and D_2O – are evaluated over time and as a function of temperature (90 – 140 K). The amorphous nature of the interstellar ice analogues investigated implies a high concentration of structural defects compared to crystalline samples. These deviations from perfect crystallinity aid the H and D atoms in exchanging from one oxygen centre to another. Therefore, the activation energy of the reaction $H_2O + D_2O \longrightarrow 2HDO$ obtained from an Arrhenius plot is lower than that of crystalline ices: 3840 versus 5000 K. The characteristic timescales that can be derived for the reaction ($\tau < 10^4$ years at $T > 70$ K) indicate that the process can be important in interstellar environments. Therefore, astronomical detections of D_2O remain challenging because of its potential to react with H_2O to form HDO. Furthermore, it has been demonstrated experimentally previously as well as in this chapter that proton/deuteron exchange also takes place in ice mixtures incorporating other hydrogen bonded molecules, *i.e.*, those with OH and NH moieties. In general, H/D exchange should thus be included in models that are applied to protoplanetary disks or to simulate the warming up of cometary ices in their passage of the perihelion, to examine the extent of its influence on the final deuteron over hydrogen ratio.

Lastly, **Chapter 8** investigates two reactions that provide a cross link between the oxygen hydrogenation and deuteration networks. Hydrogen abstraction by hydroxyl radicals is reported to be important in the framework of complex hydrocarbon molecules. The OH radical is furthermore known to play a key role as intermediate species in the solid state formation of water on icy grains in space. Therefore, the reactions $H_2O + OD \longrightarrow OH + HDO$ and $D_2O + OH \longrightarrow OD + HDO$ are studied experimentally at 15 K. It is established that the reaction rate or efficiency of the second reaction is maximum 20% of that of the first. In other words, hydrogen transfer is more efficient than deuterium transfer, which is supported theoretically both by arguments of Gibbs free energy as well as through assuming tunneling plays a role. Including abstraction reactions in the H_2O, HDO, and D_2O surface formation reaction network can play an important a role in the ISM. KMC simulations including all six possible abstraction reactions between water and hydroxyl radicals show that the HDO/H_2O ice ratio indeed changes with respect to simulations excluding these reactions. This conclusion holds provided that enough hydroxyl radicals are generated via photodissociation, *i.e.*, in a translucent cloud.

BIBLIOGRAPHY

Albertsson, T., Semenov, D., & Henning, T. 2014, Astrophys. J., 784, 39
Altwegg, K., Balsiger, H., Bar-Nun, A., et al. 2015, Science, 347
Boogert, A. C. A., Pontoppidan, K. M., Knez, C., et al. 2008, Astrophys. J., 678, 985
Caselli, P., Keto, E., Bergin, E. A., et al. 2012, Astrophys. J. Lett., 759, L37
Cleeves, L. I., Bergin, E. A., Alexander, C. M. O., et al. 2014, Science, 345, 1590
Cuppen, H. M., Ioppolo, S., Romanzin, C., & Linnartz, H. 2010, Phys. Chem. Chem. Phys., 12, 12077
Drake, M. J. 2005, Meteor. Planet. Sci., 40, 519
Eddington, A. S. 1937, Observ., 60, 99
Gibb, E. L., Whittet, D. C. B., Boogert, A. C. A., & Tielens, A. G. G. M. 2004, Astrophys. J. Suppl. Ser., 151, 35
Gillett, F. C. & Forrest, W. J. 1973, Astrophys. J., 179, 483
Hartogh, P., Lis, D. C., Bockelée-Morvan, D., et al. 2011, Nature, 478, 218
Hogerheijde, M. R., Bergin, E. A., Brinch, C., et al. 2011, Science, 334, 338
Ioppolo, S., Cuppen, H. M., Romanzin, C., van Dishoeck, E. F., & Linnartz, H. 2010, Phys. Chem. Chem. Phys., 12, 12065
Kessler-Silacci, J., Augereau, J.-C., Dullemond, C. P., et al. 2006, Astrophys. J., 639, 275
Kristensen, L. E., van Dishoeck, E. F., Bergin, E. A., et al. 2012, Astron. Astrophys., 542, A8
Lipshtat, A., Biham, O., & Herbst, E. 2004, Mon. Not. R. Astron. Soc., 348, 1055
Min, M., Dullemond, C. P., Kama, M., & Dominik, C. 2011, Icarus, 212, 416
Morbidelli, A., Chambers, J., Lunine, J. I., et al. 2000, Meteoritics and Planetary Science, 35, 1309
Muralidharan, K., Deymier, P., Stimpfl, M., de Leeuw, N. H., & Drake, M. J. 2008, Icarus, 198, 400
Nagaoka, A., Watanabe, N., & Kouchi, A. 2005, Astrophys. J. Lett., 624, L29
Nisini, B., Benedettini, M., Codella, C., et al. 2010, Astron. Astrophys., 518, L120
O'Brien, D. P., Walsh, K. J., Morbidelli, A., Raymond, S. N., & Mandell, A. M. 2014, Icarus, 239, 74
Oliveira, C. M., Hébrard, G., Howk, J. C., et al. 2003, Astrophys. J., 587, 235
Owen, T., Bar-Nun, A., & Kleinfeld, I. 1992, Nature, 358, 43
Persson, M. 2015, http://dx.doi.org/10.6084/m9.figshare.1267445
Persson, M. V., Jørgensen, J. K., van Dishoeck, E. F., & Harsono, D. 2014, Astron. Astrophys., 563, A74
Piskunov, N., Wood, B. E., Linsky, J. L., Dempsey, R. C., & Ayres, R. 1997, Astrophys. J., 474, 315
Robert, F. 2003, Space Sci. Rev., 106, 87
Roberts, H., Herbst, E., & Millar, T. J. 2003, Astrophys. J. Lett., 591, L41
Rodgers, S. D. & Charnley, S. B. 2002, Mon. Not. R. Astron. Soc., 330, 660
Rosenberg, H. 1910, Astron. Nachr., 186, 71
San José-García, I., Mottram, J. C., Kristensen, L. E., et al. 2013, Astron. Astrophys., 553, A125
Sarafian, A. R., Nielsen, S. G., Marschall, H. R., McCubbin, F. M., & Monteleone, B. D. 2014, Science, 346, 623
Shu, F. H., Adams, F. C., & Lizano, S. 1987, Ann. Rev. Astron. Astrophys., 25, 23
Stimpfl, M., Walker, A. M., Drake, M. J., de Leeuw, N. H., & Deymier, P. 2006, J. Cryst. Growth, 294, 83
Tielens, A. G. G. M. 1983, Astron. Astrophys., 119, 177
Tielens, A. G. G. M. & Hagen, W. 1982, Astron. Astrophys., 114, 245
van de Hulst, H. C. 1949, The Solid Particles in Interstellar Space (Utrecht, The Netherlands: Drukkerij Schotanus & Jens)
van Dishoeck, E. F. 2004, Ann. Rev. Astron. Astrophys., 42, 119
van Dishoeck, E. F., Herbst, E., & Neufeld, D. A. 2013, Chemical Reviews, 113, 9043
Whittet, D. C. B., Bode, M. F., Longmore, A. J., et al. 1988, Mon. Not. R. Astron. Soc., 233, 321
Williams, J. P. & Cieza, L. A. 2011, Ann. Rev. Astron. Astrophys., 49, 67

2

METHODS: EXPERIMENTAL SOLID-STATE ASTROCHEMISTRY

The knowledge on gas-phase reactions occuring in interstellar clouds cannot be extrapolated as to describe the same reaction taking place on the surface of a dust grain. In the solid state not only more intermolecular interactions can play a role, such as the influence of the neighboring molecules, but reactions are also in competition with the other processes that can take place simultaneously. A study devoted to astrochemically relevant surface reactions is therefore crucial in understanding the key proceses at play for, *e.g.*, water formation and detection in the interstellar medium. In this Thesis we will use precisely such dedicated experiments conducted in an ultra-high vacuum setup equipped with reflection absorption infrared spectroscopy and a quadrupole mass spectrometer. These two analytical techniques are complementary: infrared spectroscopy can be performed in situ, whereas the mass can be detected only if ices are sublimated.

This chapter starts with an overview of the relevant surface science techniques applied in experimental astrochemistry, putting the system and procedures employed in Chapters 6-8 in perspective. Secondly, a detailed description of the used setup, SURFRESIDE^2, is documented.

Based on S. Ioppolo, G. Fedoseev, T. Lamberts, C. Romanzin and H. Linnartz, *SURFRESIDE^2: An Ultrahigh Vacuum System for the Investigation of Surface Reaction Routes of Interstellar Interest*, Rev. Sci. Instrum. 84 (2013) 073112

2.1 INTRODUCTION

The dust grains present in the interstellar medium (ISM) play an important role in the synthesis of saturated species as explained in the Introduction. On average in a relatively cold and dense interstellar region ($n_H = 10^4$ cm^{-3}, 10 K) maximum one hydrogen atom arrives on the grain surface per day (Tielens, 2013) and mimicking such reactions in the laboratory inherently means changing the timescale at which they take place. In other words, reactions on the experimental surface occur rapidly one after the other, or simultaneously. Note that the main assumption made is therefore that thermalization on the surface and in the ice is fast enough to ensure that excess reaction heat cannot be used to overcome reaction barriers. Since many reactions can occur at the same time it is crucial to make use of a bottom-up approach: constructing a reaction network from single well-understood processes. A first step in this direction is to use surface science techniques at cryogenic temperatures to recreate conditions as similar as possible to those in the ISM. The first experiments designed specifically to probe atom-addition reactions against an astrochemical background were performed by Hiraoka et al. (1994) and revolved around the hydrogenation of CO at $10 - 20$ K. In the past decades the number of experimental studies devoted to astrochemistry has increased tremendously.

In general, an experimental setup consists of five parts: (i) a main chamber, (ii) a substrate, (iii) deposition lines, (iv) ice processing techniques, and (v) analytical tools. A division can be made between main chambers under high vacuum (HV, $10^{-5} - 10^{-7}$ mbar at room temperature) and ultra high vacuum (UHV, $10^{-8} - 10^{-11}$ mbar at room temperature). Note that originally all experiments were performed in HV setups, which resulted in the investigation of ices with thicknesses up to several μm. A big disadvantage of the relatively high pressures in the chamber is the continuous deposition of the largest contaminant: water. This can be minimized by reducing the pressure and baking the system, *i.e.*, working under UHV. Another advantage is the possibility to work with thin film ices or even perform sub-monolayer studies. A monolayer corresponds to $0.5 - 1 \times 10^{15}$ molecules cm^{-2}, depending on the species at hand. The deposition lines are typically held under vacuum when they are not used to reduce the number of possible contaminants entering the main chamber. The substrates used, ice processing techniques, and the analytical tools will be reviewed below.

This chapter first focuses on experimental techniques used in astrochemistry in general and then discusses the setup used for this Thesis, SURFRESIDE^2, in particular.

2.2 DEPOSITION AND PROCESSING OF ICES

2.2.1 *Surfaces*

The substrate surfaces used in an experimental setup can be aimed either at reproducing the characteristics of interstellar dust grains or at being advantageous for one particular experimental technique.

Imitating an interstellar surface serves in particular the studies focusing on the surface-molecule interaction and its influence on the reactions at hand, *i.e.*, monolayer and submonolayer studies. Interstellar dust grains are thought to be of carbonaceous and/or silicaceous origin (Hony, 2003; Gibb et al., 2000) and therefore these types of surfaces have been implemented in experimental setups. Highly ordered pyrolytic graphite (HOPG) has been used as a carbonaceous grain analog (Brown et al., 2006; Thrower et al., 2011; Minissale et al., 2014). Amorphous silicate substrates, $(SiO)_x$, have also been employed and the influence of various

structures with respect to H_2 formation has been characterized (Dulieu et al., 2013; Abdulgalil et al., 2013; Sabri et al., 2014).

Substrates made from certain metals can be used intentionally to avoid any interaction between the ice and the surface, such as Au (used as a substrate throughout the work described in this Thesis), Al (Oba et al., 2010), or Cu (Gavilan et al., 2012). An advantage of these substrates is that they are highly reflective, which is exploited by reflection absorption infrared experiments (see Section 2.3.1). However, it can also be desirable to have a substrate that is transparent to infrared radiation, such as CsI, KBr, ZnSe, and Si if spectra are acquired in an infrared transmission mode (Öberg et al., 2009; Palumbo et al., 2010; Islam et al., 2014).

Finally, to ensure the separation between the ice studied and the surface or to study the influence of a particular ice on reaction mechanisms (*e.g.*, polar vs. non-polar ice) an intermediate layer of ice can be deposited on the substrate prior to the experiment.

2.2.2 *Ice deposition*

When ices are deposited at low temperatures, this can be thought of to occur via a ballistic hit-and-stick mechanism, because there is not enough thermal energy available per species to scan the surface and find the most favourable position. This implies that the morphology depends on the angular distribution of the water molecules incident from the gas phase (Stevenson et al., 1999). For water ice, perpendicular deposition results in the lowest porosity, which increases by using more glancing angles. Background deposition, probably most similar to interstellar conditions, leads to the highest porosity. The main disadvantage there is, however, that the main chamber is fully filled with the depositing species.

In general, two types of deposition experiments can be performed: sequential deposition and co-deposition. In the case of sequential deposition, one of the reactants is first deposited on the sample and subsequently exposed to the second reactant (typically a thermal atom-beam, see Section 2.2.3.2). The formation and destruction of intermediates then leads to the creation of final, stable products. Plotting surface abundances versus time allows for the derivation of reaction rates of these products. However, the yields are often limited due to the low penetration depth of the atoms into the ice layer. Moreover, the reactivity of the intermediate species (often radicals) does not allow for their unambiguous identification. During co-deposition, on the contrary, all reactants enter the experimental setup simultaneously. The ratio between them can be varied and in this way either a high yield of final products can be obtained or the formation of intermediate species can be probed. These two types of deposition techniques are complementary.

If ices are thick enough, the laser interference pattern of a He-Ne laser being reflected by both the vacuum-film and the film-substrate interfaces can be used to monitor the thickness of the ice film during ice deposition (*e.g.*, Palumbo et al. (2010)).

2.2.3 *Ice processing*

2.2.3.1 *Thermal processing*

Increasing the temperature of the substrate mimics the evolution of a dark cloud collapsing and leads to the formation of a protostar that heats up its surroundings. The main effects of thermal processing are diffusion, segregation, crystallization, and sublimation. Elevated temperatures are also thought to activate chemistry (Duvernay et al., 2010).

Diffusion increases with increasing temperature because there is more energy available thermally for species to overcome the binding energy to its neighbors. For instance CO diffu-

sion through a H_2O layer can be probed at different temperatures with infrared spectroscopy (Mispelaer et al., 2013; Karssemeijer et al., 2014). Diffusion can ultimately lead to the collapse of originally porous ices (Bossa et al., 2012).

Segregation can occur in mixed ices if the mutual binding energy between two different species is less than the binding energies of those species with themselves. A prominent example in astrochemistry is the segregation of CO_2 and H_2O in originally mixed ices, driven by the strong (hydrogen bonded) interaction between water molecules (Ehrenfreund et al., 1998; Öberg et al., 2009).

The amorphous ices deposited at low temperature can crystallize when given enough time or energetic input. In the case of water, for instance, slow deposition at 10 K results in an amorphous solid. Increasing the temperature to 130 K results first in irreversible annealing of the ice followed by a transformation into polycrystalline cubic ice. At temperatures higher than 150 K the hexagonal structure can be found (Fletcher, 1971; Hagen et al., 1983).

Finally, if temperatures rise high enough, the binding energy to the surface can be overcome and species are sublimated into the gas phase where it can be detected by, *e.g.*, a mass spectrometer.

2.2.3.2 *Atom addition experiments*

The most obvious origin of chemistry taking place on surfaces is by bringing one or more reactive components together. Typical reactive species are radicals and these can be generated in several ways described below.

Thermal cracking is a common practice to generate H (D) atoms from a H_2 (D_2) beam that passes through a tungsten heated hot ($\sim$ 2000 K) capillary (Tschersich & von Bonin, 1998; Tschersich, 2000; Tschersich et al., 2008). Such commercially available systems have been widely used in laboratory astrochemistry (Baouche et al., 2006; Ioppolo et al., 2008; Minissale et al., 2014). In a similar way, oxygen atoms can also be generated, but such thermal cracking beamlines are designed to be used for a single species, either hydrogen (deuterium) or oxygen. For other species the temperatures required for breaking a bond are too high.

A microwave discharge plasma, on the contrary, can be used to generate a range of radicals by cracking molecules in the plasma. In principle a plasma can break the bonds of H_2, D_2, O_2, N_2, H_2O, NH_3, etc, yielding their respective radical fragments. The ions that are simultaneously generated can be deflected after leaving the plasma chamber to assure that they do not reach the sample surface. Such a source is typically operated at 2.45 GHz and is both commercially available, making use of the electron cyclotron resonance effect (Anton et al., 2000), but can also be made in-house (McCullough et al., 1993; Timmermans et al., 1998). Both types of sources have been reported in astrochemical literature (Oba et al., 2010; Minissale et al., 2014).

Alternatively, a radio-frequency generated plasma operating in the MHz regime can also be used (Sibener et al., 1980; Pirronello et al., 1997; He et al., 2014).

Both feedgas molecules and product fragments can be excited, some in (metastable) long lived states. To ensure that this excitation energy is not transferred to the ice, changing the structure, or is used to overcome reaction barriers, such species need to be quenched. This is setup dependent, one example is described in Section 2.4.4.

In order to be able to extrapolate experimental results to interstellar timescales, it is crucial to quantify the atom fluxes and dissociation efficiencies carefully. There is a wide range of possibilities available to do so and here we only summarize several that have been used in the astrochemical community. Quantification of a hydrogen atom beam can be performed by using a quadrupole mass spectrometer (QMS, see below) and comparing masses 1 and 2 with the (microwave) source switched on and off (Hidaka et al., 2004). Nagaoka et al. (2007) used

a time-of-flight setup equipped with a QMS to determine the translational temperature of a cooled atomic hydrogen (deuterium) beam. The presence of OH in a microwave plasma of H_2O has been proven with the use of Resonance Enhanced Multiphoton Ionization (REMPI). Finally, in Section 2.4, we will discuss the reference reaction technique to derive O- and N-atom fluxes based on measuring the yield of products of a barrierless reaction.

2.2.3.3 *Energetic processing*

Interstellar ices can also be subject to particles of a more energetic nature, which is the case for ices that interact with cosmic rays. While cosmic rays are composed primarily of high-energy nuclei, interactions with molecules can result in secondary electrons and photons being generated as well. The energies involved for these three types of irradiation is quite different: UV photons lie in the range of 7-14 eV, electrons around keV and cosmic rays can be mimicked experimentally up to MeV.

In general, the effects of energetic processing are sputtering (or desorption), structural changes, chemistry, (ion) implantation, and residue formation on the substrate. To discuss all of these effects falls outside the scope of this Thesis, but some recent developments in vacuum ultraviolet (VUV) irradiation, ion and electron bombardment experiments will be discussed below.

VUV irradiation of interstellar ice analogs is commonly brought about by so-called microwave discharge hydrogen-flow lamps and have already been used in the early days of laboratory astrochemistry (Hagen et al., 1979). They produce atomic hydrogen Ly-α (121.6 nm) and hydrogen molecular emission in the 110-180 nm regime. Despite its widespread use, the characterization of these lamps in terms of H_2 pressure, lamp geometry, and seed gas is a recent development (Chen et al., 2014).

Studies focusing on the influence of VUV on the chemistry show that irradiating mixed interstellar ice analogs is powerful enough to lead to the formation of complex molecules (Bernstein et al., 2002; Muñoz Caro et al., 2002). A more quantitative investigation of the separate reaction routes is needed in order for the results of laboratory work to be implemented in astrochemical models and new experimental setups aiming to do so have indeed been reported (Paardekooper et al., 2014). Besides inducing chemistry, VUV irradiation can also result in the photodesorption of the top layers of the ice. The desorption efficiency is in fact wavelength dependent which can be probed at the SOLEIL synchrotron facility (Fayolle et al., 2011; Bertin et al., 2012).

Ions can be generated with an ECR ion source, an ion accelerator with a magnetic mass filter or with a commercially available ion source (Sivaraman et al., 2013; Bennett et al., 2014; Raut et al., 2012). Ion irradiation experiments can be performed in three ways: ions passing through the ice-covered sample, irradiation during ice deposition, and ion implantation. The thicker the ice involved, the more ions can be implanted. Many ionization studies (both using ions and electrons) are performed in the light of their relevance to the outer solar system (Raut et al., 2012; Raut & Baragiola, 2013). Although numerous investigations have been performed, again, the quantification of such setups is crucial and to that end, new setups have lately been constructed (Jones & Kaiser, 2013).

A direct comparison between the effects of ion irratiation and UV photolysis, in terms of dose (eV per mass unit), is available for many systems, *e.g.*, CH_4, CH_3OH, and CO (Baratta et al., 2002; Loeffler et al., 2005).

2.3 ANALYTICAL TECHNIQUES

2.3.1 *Infrared spectroscopy*

Surface science traditionally does not particularly make use of vibrational, infrared (IR) spectroscopy as an analytical technique. Astronomy, however, does. Rotational spectroscopy would in fact be preferable, because those states can be thermally excited and can therefore be probed in emission. In the solid state, however, rotation is quenched. Electronic transitions, or UV-Vis radiation, are not typically used, because the energy is too high and destroys both the ice structure as well as the molecules (see Section 2.2.3.3).

Remember that vibrations can be excited only if the transition moment is non-zero, which occurs mainly for molecules with a non-zero electric dipole moment, *i.e.*, a molecule such as O_2 does not absorb IR radiation, whereas H_2O does. The fundamental transitions – those occuring if one quanta of energy is absorbed – correspond to the strongest detected signals. Overtones, where multiple quanta are absorbed, or combination bands, when more than one normal mode is involved, are less intense. The types of vibrations that can occur are for instance symmetrical and antisymmetrical stretching, bending, torsion, and umbrella modes. Molecules that are not infrared active can still be observed in the ISM through quadrupolar and magnetic dipolar transitions. Finally, electronic emission spectroscopy can also be employed.

Here, we highlight two possible experimental types of operation: transmission and reflection as depicted in Fig. 2.1. From the figure it is apparent that in transmission thicker ices are required (HV conditions), while the thin films grown under UHV conditions can only be analyzed if the pathlength is increased via a reflection of the beam on the surface. Changing the angle of incidence also has an effect on the absorption frequency detected. The long-range dipole-dipole coupling can manifest itself in a frequency difference (several cm^{-1}) between the longitudinal and the transverse optical modes. This is a result of the long range electric fields associated with long-wave longitudinal phonons. TO phonon vibrations are characterised by atomic displacements perpendicular to the wavevector whereas for LO vibrations, the atomic displacements are parallel to the wavevector. In transmission at normal incidence, only the TO mode is active, but both modes are active at oblique incidence. In reflection spectroscopy on a metal surface, only the LO mode band is observed, due to the electric field in the metal. See Palumbo et al. (2006) for an in-depth discussion of the LO-TO splitting of the fundamental CO band at 2140 cm^{-1}. Note that originally, all astrochemical experiments were performed in a HV setup and hence made use of transmission infrared spectroscopy (*e.g.*, Sandford & Allamandola (1988); Palumbo & Strazzulla (1993); Ehrenfreund et al. (1997)).

A typical experiment consists of recording absorption spectra at selected time intervals with respect to an initially recorded background spectrum. This background spectrum corrects for the gas-phase absorption that the infrared beam encounters on its way from the source through the vacuum chamber to the detector.

Given a spectrum, both experimentally and observationally, a quantitative analysis in terms of a number of absorbing molecules is needed. This is achieved by integrating a selected infrared absorption band to obtain the band area and subsequently divide this by the so-called band strength. The band strength is a value for the number of molecules corresponding to a fixed amount of absorption. Although these band strengths are readily available for spectra recorded in transmission mode, they depend on the substrate and structure of the sample (Gerakines et al., 1995; Fulvio et al., 2009). Moreover, in the reflection mode, they are highly setup-dependent (see Section 2.4.3).

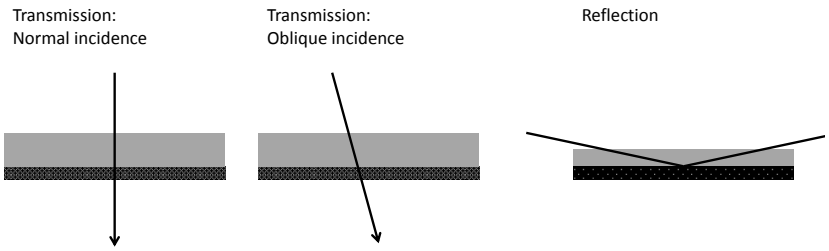

Figure 2.1: Two types of infrared spectroscopy if ice films: transmission and reflection.

Although IR spectroscopy has proven to be of great use in astrochemistry, there are certainly drawbacks. First, mainly particular functional groups are detected, such as -CH or -OH moieties, instead of molecules themselves. Therefore, if the functional group strongly interacts with its surrounding the absorption band is broadened and can easily overlap with that of another molecule. This becomes especially troublesome when dealing with large, but non-abundant species of which the signal would be buried within that of more abundant species. Furthermore, transitions at IR frequencies correspond to intramolecular vibrational modes of the molecules in the ice, and therefore, detects only local changes in structure. TeraHertz (THz) or far-IR spectroscopy, actually probes the lower frequency vibrations that correspond to low energy intra- and, especially, intermolecular modes and as such is sensitive to large-scale structural changes. This also means that, in principle, astronomical THz observations can be obtained in the absence of a background radiation source (Allodi et al., 2014).

Finally, the sensitivity or IR spectroscopy is rather low, even if reflection absorption spectroscopy is used: a minimum of ~ 0.5 ML is needed for a signal to be clearly detected (see for instance Chapter 6). Mass spectroscopy, on the other hand, has a much lower detection limit and as such is more suitable for submonolayer studies (Noble et al., 2011).

2.3.2 *Temperature Programmed Desorption*

Complementary to in situ IR spectroscopy, Temperature Programmed Desorption (TPD) experiments can be performed during which ice sublimation is probed. TPD experiments are usually performed in an UHV set-up equipped with a quadrupole mass spectrometer (see below), but can also be used in conjuction with, *e.g.*, Resonance Enhanced Multiphoton Ionization and Time of Flight spectrometry (REMPI-TOF) (Gavilan et al., 2012).

The experiment consists of two phases: first, the substrate is kept at a constant low temperature and a known quantity of one or multiple species is deposited; during the second phase the temperature is linearly increased and the desorption of surface species is monitored using the mass spectrometer. The measured desorption rate of the species is then plotted as a function of temperature.

In this way, species produced on the surface and in the ice can be detected, usually according to their masses. Knowing the desorption temperature, the corresponding emerging mass and simultaneous disappearing infrared feature often provides enough handles to determine a reaction product.

More quantitative studies can also be performed, aiming to derive a binding energy. One can perform a series of TPD experiments, varying the initial deposited amount, the deposition

temperature, and/or the heating ramp. Often, the resulting TPD spectra are then fitted by the Polanyi-Wigner equation

$$\frac{d}{dT} n_g(A) = n_s(A)^o \frac{\nu \exp(-E_{bind,A}/k_B T)}{\beta} \quad (2)$$

where o is the order of the desorption process and β is the heating rate. Generally the order is assumed and the prefactor, ν, and binding energy, $E_{bind,A}$, are used as fitting parameters. Unfortunately, these two parameters are correlated and it is not straightforward to get accurate values for both parameters simultaneously. Therefore, sometimes the prefactor is assumed as well and only the binding energy is obtained from the fit.

Zeroth order desorption generally occurs when multiple layers of the same species are deposited. During the desorption, the number of surface species available for desorption (the top layer) remains the same. For first order desorption, the temperature for which the desorption rate peaks is independent of the deposited amount. First order desorption generally occurs in the monolayer regime, where all surface species are also available for desorption. Finally, second order desorption is mainly due to two reasons: either desorption of reaction products, that were formed in a second order surface reaction, or the surface exhibits a distribution of binding sites. In the latter case, the stronger binding sites are filled first and the average binding energy decreases with coverage, resulting in TPD curves that resemble second order behavior.

Care has to be taken in concluding which chemistry occurs at low temperature on the surface and during the warm-up phase. Typically, this is done through a variety of control experiments. For instance, an experiment can be performed at different temperatures followed by TPD. If the Langmuir-Hinshelwood mechanism is responsible for a reaction, the results of the TPD should differ. If no difference is found, the spectrum obtained might well be caused by secondary reactions.

The binding energies of a wide collection of stable species have been determined using the TPD technique. Examples are N_2 (Öberg et al., 2005), CO (Öberg et al., 2005), O_2 (Acharyya et al., 2007), H_2O (Bolina et al., 2005; Fraser et al., 2001), and CH_3OH (Green et al., 2009). The binding energies have been mostly determined for the desorption of pure ices from different substrates. Since interstellar ices are not homogeneous the desorption of mixed layers is more relevant for astrochemical modeling. However, the introduction of more species in the ice makes the desorption process immediately much more complex. First, the binding energy of a particle can change depending on its surrounding material. Second, the dominant mantle species can prevent other species from desorbing.

2.3.3 *Mass spectrometry*

As mentioned in the previous section, mass spectrometry is often used in conjunction with a TPD experiment. Its working principle makes use of the interaction of a magnetic and/or electric field with the mass-to-charge ratio of a charged particle. Ionizing a species can be achieved with electrons generated by a hot filament or through single photon ionization (see Section 2.4 and Kaiser et al. (2014)).

A circular path is brought about by a magnetic (Lorentz) force that acts on a moving charged particle. This force depends on the velocity and can be couteracted by an electric force (in the presence of an electric field). Therefore, if the electric and magnetic forces are in equilibrium, only particles with a matching velocity are selected, which in turn depends on the mass-to-charge, m/z, ratio. It is precisely the latter characteristic that can be detected by varying the magnetic field.

In practice it is not straightforward to achieve stable and spatially uniform magnetic fields with permanent magnets. Instead, a quadrupolar electric field can be implemented with the use of four metal rods where two opposing rods have an applied potential negative with respect to that of the remaining two rods. All rods have both an alternating and direct current (AC and DC) potential. The DC components act as a mass filter: the positive component destabilizes low masses, whereas the negative component does the same for high masses. The alternating current allows ions of the right m/z ratio to travel in an oscillatory motion through the rods until the detector is reached. Again, the influence of the electric fields depends on the mass and charge of the species and by tuning the voltages the double mass filter only allows a narrow range of mass-to-charge ratios to pass through the quadrupole. By scanning the voltages, a mass spectrum is generated.

Although a narrow range of m/z ratios can be selected, the uncertainty is typically of the order of 1 amu, *i.e.*, for instance the molecules CO and N_2 cannot be distinguished. An alternative is provided by a time-of-flight (TOF) mass spectrometer. In that case, the generated ions are extracted by a potential into the flight tube where the long pathlength separates the species according to their velocity. The potential energy given to the ions during the extraction depends on the charge and is converted into kinetic energy given its mass, hence again the m/z ratio determines the velocity and therefore the time of arrival at the detector. To increase the pathlength a reflectron can be placed at the end of the tube, reflecting the ions in the direction of the second detector. This increases the separation between the detection of different ions, *i.e.*, the mass resolution.

Possible detectors include secondary electron multipliers, microchannel plate detectors, Daly detectors, and Faraday cups (see Section 2.4.2).

2.3.4 *Other analytical techniques*

To study the effects of sputtering, *i.e.*, acquire knowledge about the mass removed from a target given a particular ion fluence, a quartz-crystal microbalance (QCM) is very useful. Coupling such a QCM to a mass spectrometer allows to distinguish the molecular species emitted from the targets as well (Loeffler & Baragiola, 2010; Raut & Baragiola, 2011).

A clear disadvantage of TPD experiments is the destruction of the ice that is under investigation and the fact that thermal chemistry could be induced. Another approach is to ablate a fraction of the ice, for instance via Matrix-Assisted Laser Desorption/Ionization (MALDI). The resulting plume of molecules can then be analyszed and if a TOF mass spectrometer is coupled to such a setup it is possible to work with large molecules or complex mixtures (Gudipati & Yang, 2012; Paardekooper et al., 2014). REMPI can provide valuable information concerning excited states of species formed on the surface (Watanabe et al., 2010; Gavilan et al., 2012).

2.4 SURFRESIDE^2 - SYSTEM DESCRIPTION

The focus of this section is on a quantitative characterization of the experimental properties of the setup used throughout this thesis: the SURFace REaction SImulation DEvice - 2 or SURFRESIDE^2. A new approach to fully characterize atom fluxes has been used and is outlined below. SURFRESIDE^2 consists of three distinct UHV chambers (Fig. 2.2). In the main chamber, ices are deposited with monolayer precision and processed at astronomically relevant temperatures. Reflection Absorption Infrared (RAIR) spectroscopy and Temperature Programmed Desorption (TPD) are used as analytical tools to characterize the ice composition. In the other chambers different atom sources are mounted for the controlled production of

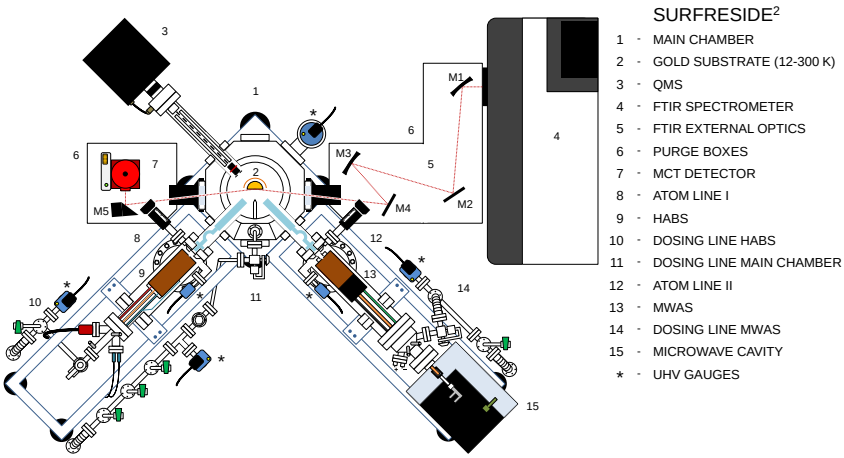

Figure 2.2: A schematic top-view of the experimental apparatus.

well-characterized atom (molecular) beams. Shutters separate the beam line chambers from the main chamber and allow an independent operation of the individual beam lines.

2.4.1 *Main Chamber*

The custom-made ultrahigh vacuum 304 stainless steel main chamber has a diameter of 30 cm and is provided with eight lateral CF 35, two lateral CF 16, one top CF 63 and one bottom CF 200 flange connections (#1 in Fig. 2.2). A gate valve connects the bottom-flange with a 260 l/s (for N_2) turbomolecular pump (Pfeiffer Vacuum, TMU 261P). The CF 35 lateral flanges are used to connect the main chamber to the two atom lines (#8 and #12 in Fig. 2.2), an active cold cathode transmitter (Pfeiffer Vacuum, IKR270) for pressure readings in the $5 \cdot 10^{-11}$ - 0.01 mbar range, and a quadrupole mass spectrometer (QMS; Spectra - Microvision Plus; #3 in Fig. 2.2). Two CF 35 windows are used for in- and out-going light from a Fourier transform infrared spectrometer (FTIR; Agilent Technologies Cary 600 Series; #4 in Fig. 2.2). The two CF 16 flanges are used as inlet for a double ice deposition dosing line (#11 in Fig. 2.2), while a differentially-pumped (Leybold Vacuum, TW 300) ϑ rotatable stage (0°-360°) connects the top-flange to a helium closed-cycle refrigerator (ASR Inc.; #2 in Fig. 2.2).

The room temperature base pressure of the main chamber is in the low 10^{-10} mbar regime. An optically-flat gold-coated copper substrate ($2.5 \cdot 2.5$ cm^2) is placed in the center of the main chamber and is in thermal contact with the cold finger of the helium closed-cycle cryostat. The gold surface is not representative for interstellar grain surfaces, but it is an effective heat conductor, highly reflective in the mid-infrared, and chemically inert, *i.e.*, the substrate plays no role in catalyzing chemical reactions or processes at the substrate surface. Moreover, ice thicknesses are typically more than ten monolayers, reducing the role of the substrate. Therefore, it is well suited to study interstellar relevant reaction routes that occur on and in ice samples. The substrate temperature is varied between 12 and 300 K with a relative precision of 0.5 K through a cryogenic temperature controller (LakeShore model 340). To achieve temperatures as low as 12 K an aluminum thermal shield kept at ~77 K surrounds the cold finger and the back-side of the sample. The temperature of the sample is changed and monitored by means of heating wires and thermocouples, respectively. The heating wires are mounted

around the cold finger close to the substrate, while the two KP-type thermocouples are connected above and below the gold substrate. The absolute temperature accuracy is better than 2 K. This is checked by monitoring the well known desorption temperature of volatile species like for instance CO, N_2, and O_2 (Acharyya et al., 2007).

An all-metal high-vacuum stainless steel ice deposition dosing line is used to prepare, store and introduce gas mixtures into the main chamber. The pressure in the deposition dosing line is monitored mass independently by means of an active capacitance transmitter (Pfeiffer Vacuum, CMR361) in the range between 0.1 and 1100 mbar. Lower pressures are monitored with an active Pirani transmitter (Pfeiffer Vacuum, TPR280) ($5 \cdot 10^{-4} - 1000$ mbar). The deposition dosing line is first pre-pumped with a diaphragm pump (ABM, VDE 0530) and then with a 180 l/s (for N_2) turbomolecular pump (Pfeiffer Vacuum, TPH 180H) to reach low pressures ($< 5 \cdot 10^{-4}$ mbar). Gaseous species are admitted into the main chamber through a dosing line comprising of two separate all-metal leak valves connected to gas reservoirs. Therefore, different gasses can be prepared and stored in two different sections of the dosing line and then deposited separately or simultaneously onto the gold substrate. Deposition proceeds under an angle of 90° and 68°, respectively, and with a controllable flow between 10^{-8} and 10^{-7} mbar s^{-1}, where $1.3 \cdot 10^{-6}$ mbar s^{-1} corresponds to 1 Langmuir (L). Gas-phase species are monitored during deposition mass spectrometrically by means of the QMS, which is placed behind the substrate and mounted opposite to one of the two atom lines.

2.4.2 *Analytical Tools*

Ices are monitored *in situ* by means of RAIR spectroscopy using the FTIR, which covers the range between 4000 and 700 cm^{-1} ($2.5 - 14$ μm). A spectral resolution between 1 and 4 cm^{-1} is generally used and between 128 and 512 scans are co-added. The infrared beam coming from the FTIR is slowly diverging. Therefore, a series of $\lambda/4$ precision gold-coated mirrors (Edmund Optics and Thorlabs) is used to focus the beam onto the gold substrate (#5 in Fig. 2.2). The first one (M1) is a spherical mirror with a diameter of 76.2 mm and an effective focal length (EFL) of 762 mm. This mirror is used to gently converge the beam. The second (M2) and the fourth mirror (M4) are flat mirrors, while the third one (M3) is a spherical mirror with a diameter of 75.0 mm and an EFL of 500 mm. The latter focusses the beam onto the substrate with a glancing angle of $\sim 8°$. The main chamber mounts two Zinc Selenide (ZnSe) CF 35 view ports that act as a vacuum seal and allow the IR beam to enter and leave the chamber with a transmission $> 95\%$ in the range between $4 - 20$ μm. The out-going beam is then focussed into a narrow band and enters a liquid nitrogen cooled Mercury Cadmium Telluride (#7 in Fig. 2.2) detector by means of a 90° off-axis parabolic gold-coated mirror (M5) with a diameter of 50.8 mm and a reflected EFL of 50.8 mm. The external optics and the detector are mounted in metal boxes (#6 in Fig. 2.2). These boxes as well as the FTIR spectrometer are purged with dry-air to minimize atmospheric absorptions.

Two different experimental procedures are applied when using the FTIR. During pre-deposition experiments, ices are first deposited onto the gold substrate and subsequently exposed to atoms. To detect newly formed stable solid species, RAIR difference spectra (ΔAbsorbance) are acquired during atom exposure with respect to a background spectrum of the initial deposited ice. In co-deposition experiments, molecules and atoms are simultaneously deposited onto the substrate. The formation of intermediate species and final products is controlled by changing the deposited molecule/atom ratio. In this case, RAIR difference spectra are acquired during co-deposition with respect to a background spectrum of the bare gold substrate.

At the end of the atom exposure a TPD experiment can be performed: the sample is heated linearly (*i.e.*, with a constant rate between 0.1 and 10 K/min) till the ice is fully desorbed.

The thermal desorption can be followed spectroscopically by using the FTIR. Alternatively, the sample can be turned 135° to face the QMS. In this way, gas-phase species thermally desorbed from the ice are monitored mass spectrometrically. The desorbed species are recorded as a function of temperature by the QMS, which produces a signal proportional to the number of incoming molecules as a function of their mass to charge ratio (m/z). The incoming molecules first enter the ion source of the QMS, where they are ionized through electron bombardment by electrons released from a hot filament. The resulting ions are then focussed, selected and directed onto a Faraday detector, which collects the ions directly, allowing the ion current to be monitored. Alternatively, for higher sensitivity, a Channel Electron Multiplier (CEM) can be used. This type of detector is a Secondary Electron Multiplier (SEM) in which a large negative potential (~ - 2000 V) is used to attract the ions into the channel entrance. The channel is coated with a material that readily releases secondary electrons upon ion/electron impact. This produces a cascade of electrons down to the channel which can be detected, either as an electron current, or as a series of pulses.

TPD combined with a QMS is a sensitive technique, but it has several disadvantages: surface reaction products that remain in the solid phase cannot be probed *in situ*; additional surface reactions during the TPD (*i.e.*, during the linear heating of the ice and before complete desorption of the species) cannot be excluded; quantifying the desorbing species is not trivial as some of the interesting species have equal (*i.e.*, undistinguishable) masses and the analysis of the fractionated components of species upon electronic bombardment is not always straightforward. Finally, a TPD experiment inherently involves the destruction of the ice. Therefore, QMS data are mainly used here to constrain RAIR spectrocopy data acquired during atom exposure of the ice.

2.4.3 *Data Analysis*

After fitting the infrared spectra with connected straight baseline segments, the column densities (molecules cm^{-2}) of newly formed species can be determined from the integrated intensity of their infrared bands using a modified Lambert-Beer equation (Bennett et al., 2004):

$$N_X = \frac{\int A(\nu)d\nu}{S_X}, \tag{3}$$

where $A(\nu)$ is the integrated absorbance and S_X is the corresponding band strength. This equation can, however, only be used for thin ice layers. Teolis et al. (2007) showed that the proportionality between the optical depth and the ice abundance breaks down for thicker layers (~ 20 ML onwards); the integrated band area oscillates as a function of the layer thickness due to optical interference that is caused by the reflection at both the film-vacuum and film-substrate interfaces.

Since literature values of transmission band strengths cannot be used directly in reflectance measurements, an apparent absorption strength of stable species has to be calculated from calibration experiments. The determination of this apparent absorption strength is setup dependent. Therefore we performed a series of isothermal desorption experiments for the new apparatus introduced here to derive these values. Briefly, a layer of the selected ice is deposited at a temperature lower than its desorption temperature. The sample is then linearly heated to a temperature close to its desorption value. Infrared spectra are acquired regularly until the desorption of the ice is complete. The transition from zeroth-order to first-order desorption is assumed to occur at the onset to the submonolayer regime and appears in the desorption curve as a sudden change in slope (see Fig. 2.3). The apparent absorption strength

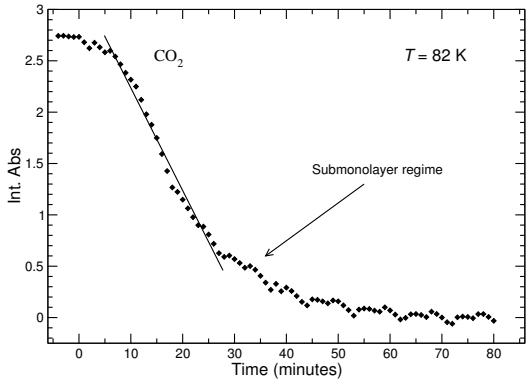

Figure 2.3: The decrease in integrated absorbance of CO_2 following desorption at a constant temperature of 82 K. The arrow indicates the transition point from the multi- to sub-monolayer regime.

in cm^{-1} ML^{-1} is then calculated by relating the observed integrated area to 1 ML in the modified Lambert-Beer equation. We estimate the uncertainty of band strengths determined in this way to be large but within 50% (also see Fuchs et al., 2009; Ioppolo et al., 2010; Fraser et al., 2001).

The determination of the band strength allows for a quantitative study of stable species formed upon atom exposure of the ice. This is mostly the case in pre-deposited experiments. Isothermal desorption experiments of unstable intermediate species cannot be performed and therefore their band strengths cannot be derived. Thus, a qualitative study is generally performed in co-deposition experiments where instable species are frozen in ice matrices and then detected in the infrared. In this case, formation trends of detected species are followed by integrating the corresponding band area as a function of time, *i.e.*, without calculating column densities. As a consequence, only formation trends of the same species obtained under different experimental conditions (*e.g.*, ice temperature, atom flux, ice composition) can be compared, but this still allows us to derive valuable information on the involved reaction network.

2.4.4 *Atom Beam Lines*

Two different atom sources are used, one (HABS) based on thermal cracking, and the other (MWAS) using a microwave discharge (#9 and #13 in Fig. 2.2). The two custom-made atom line chambers present identical geometrical characteristics (see Figs. 2.4 and 2.5): they are both pumped by 180 l/s (for N_2) turbomolecular pumps (Varian, TV 301 NAV); their room temperature base pressure is in the high 10^{-10} mbar regime (micro ion gauges, Granville-Phillips); they both are situated under an angle of 45° with respect to the substrate, both during single or simultaneous operation; a shutter is used to separate the lines from the main chamber; and a quartz pipe is placed after the shutter and along the path of the dissociated beam. The nose-shaped form of the pipe is designed to efficiently quench the excited electronic and rovibrational states of species through collisions with the walls of the pipe before they reach the ice sample. The geometry is designed in such a way that this is realized through at least four wall collisions of the atoms before leaving the pipe. In this way, “hot" species cannot reach the ice directly. In fact, throughout the calibration stage of the setup, several reactions have

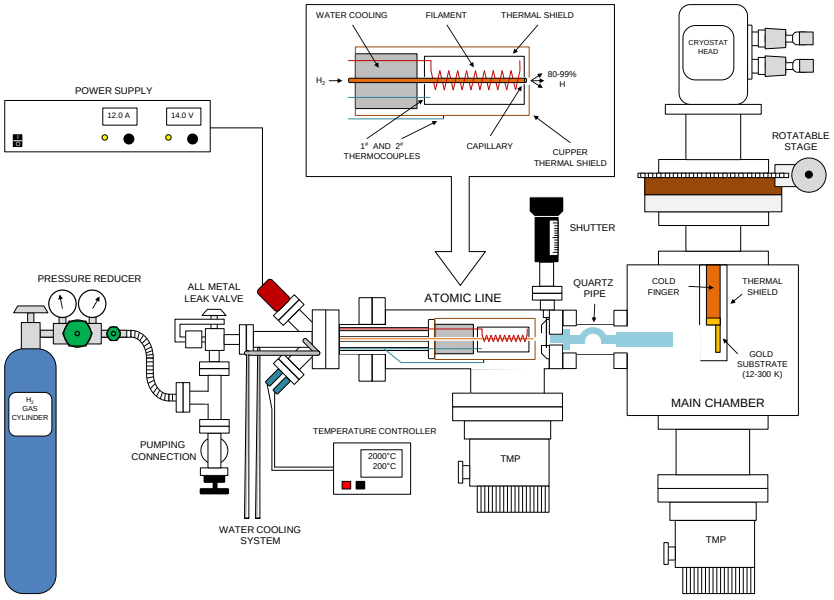

Figure 2.4: A schematic side-view of the atom line (HABS) with the thermal cracking H/D atom source and the main chamber.

been performed to probe the (non-)existence of excited states in the beamline. For example, the reaction $H_2 + O(^1D) \longrightarrow OH(^2\Pi) + H$ is exothermic and posesses no detectable temperature dependence in the gas-phase and is therefore assumed to proceed barrierless (Davidson et al., 1977). The reaction $H_2 + O(^3P) \longrightarrow OH + H$ on the other hand is endothermic and is therefore not expected to proceed. In a codeposition of H_2 and O on a cold surface, no large amount of potential products, OH or H_2O, can be found (Chapter 6). Therefore it is safe to assume that the fraction of $O(^1D)$ deposited on the surface is negligible or, alternatively, energy dissipation is fast enough to ensure that the excess energy cannot be used during reactions.

Two separate all-metal dosing lines are used to prepare and inlet pure gasses and mixtures into each of the atom sources (#10 and #14 in Fig. 2.2). The dosing lines are pre-pumped with the same diaphragm pump that is used for evacuating the deposition dosing line. Each of the atom lines is then pumped with a 70 l/s (for N_2) turbomolecular pump (Pfeiffer Vacuum, TMU 071P). The room temperature base pressure of these lines is $< 1 \cdot 10^{-5}$ mbar and is monitored by means of a compact process ion gauge for each line (Pfeiffer Vacuum, IMR 265).

2.4.4.1 *HABS*

An all-metal precision leak valve is used to admit H_2/D_2 molecules (99.8% purity, Praxair) from the all-metal dosing line into the capillary of a commercially-available and well-characterized thermal cracking source, a Hydrogen Atom Beam Source (HABS, Dr. Eberl MBE-Komponenten GmbH) (Tschersich & von Bonin, 1998; Tschersich, 2000; Tschersich et al., 2008), which is used to hydrogenate/deuterate the sample through heating the capillary from 300 to a maximum of 2250 K by a surrounding tungsten filament (see top-box in Fig. 2.4). During experiments the H + H_2 (D + D_2) flow through the capillary and the temperature of the tungsten filament are controlled and kept constant by adjusting the all-metal valve position and

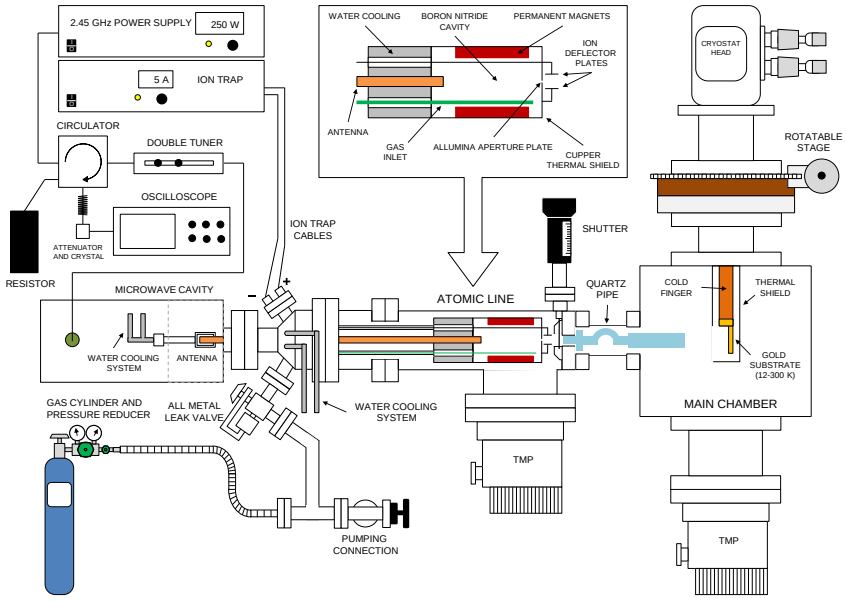

Figure 2.5: A schematic side-view of the atom line (MWAS) with the microwave plasma atom source and the main chamber.

the voltage of the power supply of the HABS (Delta Elektronika, SM 7020-D). The temperature of the filament is monitored by means of a C-type thermocouple placed close to the filament and inside the internal thermal shield. To prevent melting of components a water cooling system is implemented into the source, in thermal contact with an external copper thermal shield. The temperature of this shield is controlled with a second C-type thermocouple. The HABS is used in horizontal mode.

A wide range of atom-beam fluxes is accessible with this source by changing the pressure in the capillary pipe and/or the temperature of the filament. Typically values cover a range from 10^{11} to 10^{13} atoms cm^{-2} s^{-1}. Atom fluxes are measured at the sample position in the main chamber, following a procedure described in Section 2.4.5.1 (also see Bergh et al., 1999; Hidaka et al., 2007; Ioppolo et al., 2010).

As aforementioned, a quartz pipe is placed along the path of the beam (*i.e.*, after the shutter and before the sample in the main chamber) to cool the beam to room temperature. Previous experiments with liquid nitrogen cooled atom beams did not show any H/D-atom temperature dependence in CO hydrogenation reaction processes compared to experiments at room temperature (Watanabe & Kouchi, 2002). It is important to note that the relatively high temperature of 300 K of the incident H/D atoms in our experiments does not affect the experimental results, since H/D atoms are thermally adjusted to the surface temperature before they can react with other species through Langmuir-Hinshelwood mechanism, as shown in Fuchs et al. (2009); Hidaka et al. (2004); Watanabe et al. (2006).

2.4.4.2 *MWAS*

A Microwave Atom Source (MWAS, Oxford Scientific Ltd) is included in the second atom line to produce beams of different atoms and radicals (*e.g.*, H, D, O, OH, OD, N). Figure 2.5 shows

a schematic diagram of the MWAS. A 2.45 GHz microwave power supply (Sairem) produces up to 300 W that are coupled into a microwave cavity. Along this path a circulator is placed to avoid that the back-reflected power enters the power supply. A custom-made double tuner is placed after the circulator and before the microwave cavity to minimize the back-reflected power that ultimately is dissipated in a resistor. Part of the back-reflected signal is monitored by means of an oscilloscope (Tektronix, TDS 2012) connected to an attenuator and a crystal detector (Aertech Industries). An antenna (coaxial transmission line) connects the microwave cavity to a boron nitrite chamber in which gasses enter through the all-metal precision leak valve of the dosing line (see top-box in Fig. 2.5). A plasma is created in a coaxial waveguide by coupling a radially symmetric 2.45 GHz microwave field to ions on the 86 mT surface of a multi-polar magnetic array (permanent magnets). The plasma is enhanced by the electron cyclotron resonance (ECR) effect. A water cooling system keeps the source and particularly the antenna close to room temperature. Moreover, the absence of a hot filament permits operation with most gases including reactive gases such as oxygen and nitrogen.

A specially designed alumina aperture plate allows reactive neutrals to escape from the plasma. The addition of an ion-trap (*i.e.*, two metal plates charged by a Oxford Scientific DC power supplier) can deflect the residual ion content from the beam, preventing ion exposure of the sample. All the electronically and ro-vibrationally excited species coming from the source are quenched through multiple collisions on passing through a quartz pipe before they reach the sample. Different plasma cavity pressures and/or different plasma power values give access to a wide range of atom fluxes, typically between 10^{10} and 10^{13} atoms cm^{-2} s^{-1}. These numbers depend on the dissociated species (see next section).

2.4.5 *Beam Flux Determinations*

In order to measure the absolute D-atom fluxes for HABS and MWAS in the main chamber, the gold substrate is removed and the inlet of the QMS is placed at the center of the chamber facing the two atom lines, exactly at the same position and with the same angle that the substrate has when the ice is deposited and exposed to atom-beam bombardment (see also Ref. (Hidaka et al., 2007; Ioppolo et al., 2010)). Since the sensitivity of the standard $1 - 200$ amu QMS does not allow an accurate measurement at mass 1 amu, we measure the absolute D-atom fluxes instead of the H-atom fluxes for HABS and MWAS by following the aforementioned procedure. H-atom fluxes are then derived from the H/D ratio as obtained in selected experiments discussed in Section 2.4.5.1.

The other MWAS absolute atom fluxes (*e.g.*, oxygen and nitrogen) cannot be measured mass spectrometrically because the background signal from the fractionated molecular species coming from the molecular component of the beam and the residual gas in the main chamber interferes with the signal coming straight from the atom beam. Therefore, effective O/N-atom fluxes are derived at the ice surface by using a new calibration method described here for the first time and based on measuring the formation yield of final products of barrierless surface reactions (see Sections 2.4.5.2 and 2.4.5.3).

2.4.5.1 *H/D-atom beam fluxes*

The D-atom and D_2 molecule fluxes for both HABS and MWAS are measured by monitoring masses 2 and 4 amu, respectively. Once the source is turned on, an increase in intensity of the D atoms is monitored with the QMS. The QMS measurements do not directly give the D-atom

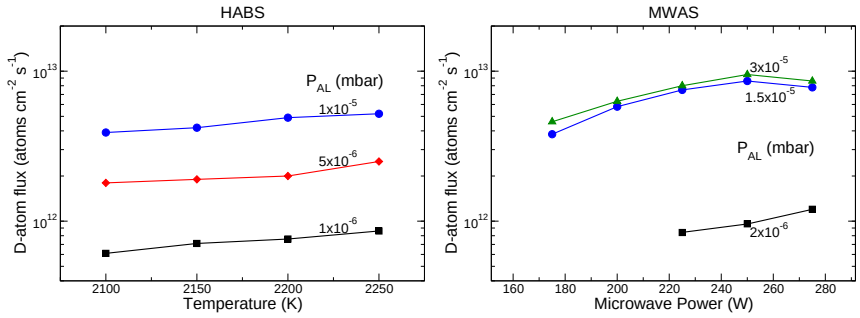

Figure 2.6: D-atom flux values as measured for the HABS (left panel) and the MWAS (right panel) at the substrate place for different parameter settings.

flux values. However, the increase in intensity of the QMS signal, ΔQ_D, is proportional to the increase in pressure in the main chamber, ΔP_D:

$$\Delta P_D = a \Delta Q_D. \tag{4}$$

The setup specific proportionality factor a is measured from eq. (4) by introducing in the main chamber D_2 molecules instead of D atoms. The choice of D_2 is given by the fact that the factor a is independent of gas species, because the density of molecules should be proportional to the density of produced ions in the QMS ion source. Furthermore, the D-atom beam contains a significant amount of undissociated D_2 molecules. Therefore, an exact measurement of ΔP_D is not trivial, while ΔP_{D_2} can be easily measured. The absolute D-atom fluxes are subsequently obtained from the following expression:

$$f_D = \frac{c_D \Delta P_D \langle v \rangle}{4 k_B T} = \frac{c_D a \Delta Q_D \langle v \rangle}{4 k_B T}, \tag{5}$$

where c_D is the calibration factor for the pressure gauge for D atoms taken from the specifications, $\langle v \rangle$ is the thermal velocity of the D atoms at 300 K, k_B is the Boltzmann constant, and T is the D-atom temperature. Different D-atom fluxes are obtained by varying the filament temperature and/or the D_2 inlet flow with the HABS, and by changing the plasma cavity pressure and/or plasma power with the MWAS. Figure 2.6 shows the D-atom flux values produced by the HABS (left panel) and by the MWAS (right panel), as measured at the substrate site for different parameter settings. The relative error for D-atom fluxes (HABS and MWAS) is within 10%. The absolute error is within 50%. These errors may seem large, but it should be noticed that here atom fluxes at the ice surface are actually determined experimentally, whereas in previous studies these numbers are generally only estimated.

Since an absolute H-atom flux cannot be directly measured, the comparison between H- and D-atom fluxes is difficult. We compared the H_2O_2 and D_2O_2 formation rate upon O_2 hydrogenation and deuteration, which is flux dependent, in two identical 25 K experiments for both the HABS and the MWAS. The H_2O_2 formation rate was found to be a factor of ~ 2 higher than the D_2O_2 formation rate for both sources. This value confirms our previous finding (Ioppolo et al., 2010) and is used here to scale H-atom fluxes with an uncertainty of 50%. This simplistic way of measuring a scaling factor between H- and D-atom fluxes does not however take into account that H and D atoms can differ by (*i*) sticking probability onto the surface, (*ii*) hopping rate, (*iii*) HO_2 + H (DO_2 + D) branching ratio and reaction barrier, (*iv*) desorption probability, and (*v*) recombination probability with other H/D atoms. Therefore, a new method for the determination of the H-atom fluxes, based on trapping H and D atoms

inside an O_2 ice matrix, is used by Fedoseev et al. (2015) In brief, the reaction H + O_2 → HO_2 is barrierless under certain incoming angles in the gas phase. During co-deposition experiments, the angle dependence has a negligible physical importance since the oxygen beam provides O_2 molecules with a range of different orientations at the surface before they can align (Chapter 4). Therefore, the amount of HO_2 (DO_2) formed in the ice is proportional to the H- (D)-atom flux, and gives us an estimate of the effective fluxes at the cold surface. Preliminary results show that the trends found in Fig. 2.6 for the D-atom fluxes are reproduced for the H-atom fluxes as well, but the ratio found for the effective H-versus-D flux is equal to one within the experimental uncertainties. Therefore, as mentioned above, the H-atom flux has an uncertainty of 50%.

2.4.5.2 *O-atom beam fluxes*

The effective MWAS O-atom fluxes (*i.e.*, oxygen atoms directly involved in surface reactions) are derived by measuring the final column density of newly formed ozone ice following co-deposition of ^{16}O atoms and $^{18}O_2$ molecules at 15 K. The reaction O_2 + O → O_3 is barrierless (Campbell & Gray, 1973; Lin & Leu, 1982), and therefore, we can safely assume that most of the oxygen atoms available for reaction on the surface will recombine to form ozone ice. Co-deposition experiments are used in order to avoid limitations in penetration depth of oxygen atoms into molecular oxygen ice.

Final fluxes are calculated from the knowledge of the duration of O-atom exposure, the number of monolayers of O_3 formed upon reaction, and assuming 1 ML = 10^{15} molecules cm^{-2}:

$$f_X = \frac{N_{X'} \cdot 10^{15}}{\text{exposure time}}, \tag{6}$$

where f_X is the O-atom flux, and $N_{X'}$ = N_{O_3} = $^{16}O^{18}O^{18}O$ + $^{16}O^{16}O^{16}O$ in monolayers. We do not count the $^{16}O_3$ contribution three times because solid $^{16}O_3$ is not likely to be formed through the sequential merging of ^{16}O atoms on the surface of the ice. Most of the $^{16}O_2$ can indeed form in the quartz pipe through recombination of ^{16}O atoms (see Section 2.4.4.2), or it originates from a not fully dissociated beam, mainly in the case that ^{16}O atoms form through dissociation of $^{16}O_2$ gas molecules. The overall contribution of $^{16}O_2$ originating from the atom line is considerably smaller when N_2O is used instead of $^{16}O_2$ as a precursor gas to produce ^{16}O atoms. This can be checked by comparing the amount of $^{16}O_3$ formed in the ice in co-deposition experiments of ^{16}O (from $^{16}O_2$) + $^{18}O_2$ at 15 K with the amount of $^{16}O_3$ formed in similar co-deposition experiments with ^{16}O from N_2O. Moreover, the amount of $^{16}O_3$ can be controlled by changing the ratio $^{16}O/^{18}O_2$. An over-abundance of $^{18}O_2$ minimizes the amount of $^{16}O_3$ formed in the ice because ^{16}O atoms react mostly with $^{18}O_2$. A negligible amount of $^{16}O_3$ in the co-deposition experiments gives $N_{O_3} \approx {}^{16}O^{18}O^{18}O$, and therefore a more direct and accurate O-atom flux value. This is true, especially when ^{16}O atoms are obtained from N_2O. Finally, the non-detection of the other ozone isotopologues (*e.g.*, $^{18}O^{16}O^{16}O$, $^{18}O^{16}O^{18}O$, or $^{18}O^{18}O^{18}O$) in our experiments indicates that isotopic exchange induced by surface destruction reactions, like O_3 + O → 2 O_2, is under the detection limit. Therefore, our method can be safely used to characterize the O-atom beam fluxes produced by the MWAS.

To quantify the amount of ozone produced in the oxygen flux-determination experiments, we derived the absorption band strength of ozone in two different ways: (i) performing an isothermal desorption experiment as described in Section 2.4.3 ; (ii) measuring the consumption of ozone through hydrogenation reactions and assuming that hydrogen can penetrate

Table 2.1: The effective O- and N-atom fluxes as derived from the formation yields of solid species in the ice upon barrierless reactions (see eq. 6).

Effective atom flux	High (at. cm^{-2} s^{-1})	Diss. ratio (%)	Low (at. cm^{-2} s^{-1})	Diss. ratio (%)
^{16}O from O_2	$9 \cdot 10^{11}$	8	$2 \cdot 10^{11}$	12
^{16}O from N_2O	$7 \cdot 10^{11}$	19	$1 \cdot 10^{11}$	10
^{15}N from $^{15}N_2$	$9 \cdot 10^{10}$	0.4	—	—
^{14}N from $^{14}N_2$	$8 \cdot 10^{10}$	0.4	—	—

only up to 2 ML of ozone ice. In the first case, in order to determine one monolayer of ozone, we first produce $^{16}O^{18}O^{18}O$ during 3 hrs of co-deposition of ^{16}O and $^{18}O_2$ at 35 K. Subsequently, an isothermal desorption experiment is performed at 58.5 K. From the offset between zeroth-order and first-order desorption we estimate the band strength of $^{16}O^{18}O^{18}O$. In the second case, a co-deposition of ^{16}O and $^{18}O_2$ at 15 K is performed for 3 hrs to form again $^{16}O^{18}O^{18}O$. The ice is then annealed to 50 K in order to remove the molecular oxygen and to realize a pure ozone ice. The $^{16}O^{18}O^{18}O$ ice is then exposed to H atoms at 15 K to monitor the destruction of the ozone layer. Assuming that only ~2 ML of ozone ice are fully hydrogenated (Romanzin et al., 2011), we derive the number of ozone molecules destroyed upon hydrogenation per monolayer, which gives us back the apparent band strength for $^{16}O^{18}O^{18}O$. The final band strength for ozone is confirmed within 30% of uncertainty by the two different methods.

The $^{16}O_3$ apparent band strength is obtained from the available data for $^{16}O^{18}O^{18}O$ for our setup and the ratio between the transmission band strengths for $^{16}O_3$ and $^{16}O^{18}O^{18}O$ (for the transmission band strength values see Sivaraman et al., 2011). According to eq. 6 standard O-atom fluxes span in the range between 10^{11} and 10^{12} atoms cm^{-2} s^{-1}. The O-atom flux values shown in Table 2.1 have to be considered as lower limits because (*i*) fluxes are derived indirectly (effective fluxes), (*ii*) some of the ^{16}O can recombine on the surface of the ice, and (*iii*) $^{16}O_2$ can potentially not be further oxygenated to form ozone because it is trapped into the $^{18}O_2$ matrix. The dissociation rates shown in Table 2.1 are obtained by comparing the undissociated molecular component of the beam (*i.e.*, N_2O, O_2, N_2) measured mass spectrometrically (*i.e.*, with the atom source on and the QMS placed at the center of the main chamber) with the O- and N-atom flux values as derived in Sections 2.4.5.2 and 2.4.5.3, respectively.

2.4.5.3 *N-atom beam fluxes*

As for the MWAS O-atom fluxes, the determination of effective nitrogen-atom fluxes is obtained indirectly by measuring the final column density of newly formed dinitrogen trioxide (N_2O_3) ice after co-deposition of ^{15}N atoms and NO molecules at 15 K. In this particular experiment, a sequence of barrierless (or very low barrier) surface reactions is involved in the formation of N_2O_3 (Campbell & Gray, 1973; Schieferstein et al., 1983; Markwalder et al., 1993): N + NO → N_2 + O, NO + O → NO_2, and NO_2 + NO → N_2O_3. Therefore in this specific case, N-atom fluxes are directly proportional to the amount of N_2O_3 formed in the ice, and are determined by using Eqn. 6, where f_X is the N-atom flux, and $N_{X'} = N_{N_2O_3}$ which is the amount of monolayers of N_2O_3 formed in the ice after a certain time of N-atom exposure.

As in Section 2.4.5.2, we use two different methods to obtain the apparent N_2O_3 band strength. In particular, two new co-deposition experiments of NO and O_2 are performed at 15 K. Also in this case N_2O_3 is formed through surface reactions. The ice obtained from these two experiments is in both cases heated up to remove the NO trapped in the ice. In one of the two experiments, the ice temperature is then kept at 121 K to monitor the desorption of N_2O_3 (isothermal desorption experiment). From this experiment we obtain the band strength for N_2O_3, as discussed in the latter sections. In the second experiment, the ice is cooled down again to 15 K and subsequently hydrogenated to see the destruction of N_2O_3. The penetration depth of hydrogen into N_2O_3 ice is expected to involve only a few monolayers, as for O_3, CO, and NO ice (Romanzin et al., 2011; Fuchs et al., 2009; Fedoseev et al., 2012). Therefore, assuming that only ~2 ML of N_2O_3 are consumed by the surface hydrogenation of the ice, we can estimate the band strength of N_2O_3 which is found to be consistent with the value obtained from the isothermal desorption experiment within 40% of uncertainty.

The N-atom flux values are roughly one order of magnitude lower than the O-atom values (see Table 2.1). As explained in Section 2.4.5.2, these values are all lower limits, because of the way the fluxes are derived. In the specific case of nitrogen fluxes, the formation of N_2O_3 is a three step reaction, and therefore the single reactant can further react with the others to form N_2O_3, or alternatively desorb, or be trapped in a NO matrix. Therefore, we expect the O- and N-atom absolute fluxes to be higher than reported in Table 2.1.

BIBLIOGRAPHY

Abdulgalil, A. G. M., Marchione, D., Thrower, J. D., et al. 2013, Royal Society of London Philosophical Transactions Series A, 371, 10586

Acharyya, K., Fuchs, G. W., Fraser, H. J., van Dishoeck, E. F., & Linnartz, H. 2007, Astron. Astrophys., 466, 1005

Allodi, M. A., Ioppolo, S., Kelley, M. J., McGuire, B. A., & Blake, G. A. 2014, Phys. Chem. Chem. Phys., 16, 3442

Anton, R., Wiegner, T., Naumann, W., et al. 2000, Review of Scientific Instruments, 71

Baouche, S., Gamborg, G., Petrunin, V. V., et al. 2006, J. Chem. Phys., 125, 4712

Baratta, G. A., Leto, G., & Palumbo, M. E. 2002, Astron. Astrophys., 384, 343

Bennett, C. J., Ennis, C. P., & Kaiser, R. I. 2014, Astrophys. J., 782, 63

Bennett, C. J., Jamieson, C., Mebel, A. M., & Kaiser, R. I. 2004, Phys. Chem. Chem. Phys., 6, 735

Bergh, H. S., Gergen, B., Nienhaus, H., et al. 1999, Rev. Sci. Instrum., 70, 2087

Bernstein, M. P., Dworkin, J. P., Sandford, S. A., Cooper, G. W., & Allamandola, L. J. 2002, Nature, 416, 401

Bertin, M., Fayolle, E. C., Romanzin, C., et al. 2012, Phys. Chem. Chem. Phys., 14, 9929

Bolina, A. S., Wolff, A. J., & Brown, W. A. 2005, J. Phys. Chem. B, 109, 16836

Bossa, J.-B., Isokoski, K., de Valois, M. S., & Linnartz, H. 2012, Astron. Astrophys., 545, A82

Brown, W. A., Viti, S., Wolff, A. J., & Bolina, A. S. 2006, Faraday Discuss., 133, 113

Campbell, I. M. & Gray, C. N. 1973, Chem. Phys. Lett., 18, 607

Chen, Y.-J., Chuang, K.-J., Muñoz Caro, G. M., et al. 2014, Astrophys. J., 781, 15

Davidson, J. A., Schiff, H. I., Streit, G. E., et al. 1977, J. Chem. Phys., 67, 5021

Dulieu, F., Congiu, E., Noble, J., et al. 2013, Scientific Reports, 3, 1338

Duvernay, F., Dufauret, V., Danger, G., et al. 2010, Astron. Astrophys., 523, A79

Ehrenfreund, P., Boogert, A. C. A., Gerakines, P. A., Tielens, A. G. G. M., & van Dishoeck, E. F. 1997, Astron. Astrophys., 328, 649

Ehrenfreund, P., Dartois, E., Demyk, K., & D'Hendecourt, L. 1998, Astron. Astrophys., 339, L17

Fayolle, E. C., Bertin, M., Romanzin, C., et al. 2011, Astrophys. J. Lett., 739, L36

Fedoseev, G., Ioppolo, S., Lamberts, T., et al. 2012, J. Chem. Phys., 137, 054714

Fedoseev, G., Ioppolo, S., & Linnartz, H. 2015, Monthly Notices of the Royal Astronomical Society, 446, 449

Fletcher, N. H. 1971, Reports on Progress in Physics, 34, 913

Fraser, H. J., Collings, M. P., McCoustra, M. R. S., & Williams, D. A. 2001, Mon. Not. R. Astron. Soc., 327, 1165

Fuchs, G. W., Cuppen, H. M., Ioppolo, S., et al. 2009, Astron. Astrophys., 505, 629

Fulvio, D., Sivaraman, B., Baratta, G. A., Palumbo, M. E., & Mason, N. J. 2009, Spectrochimica Acta Part A: Molecular Spectroscopy, 72, 1007

Gavilan, L., Vidali, G., Lemaire, J. L., et al. 2012, Astrophys. J., 760, 35

Gerakines, P. A., Schutte, W. A., Greenberg, J. M., & van Dishoeck, E. F. 1995, Astron. Astrophys., 296, 810

Gibb, E. L., Whittet, D. C. B., & Schutte et al, W. A. 2000, Astrophys. J., 536, 347

Green, S. D., Bolina, A. S., Chen, R., et al. 2009, Mon. Not. R. Astron. Soc., 398, 357

Gudipati, M. S. & Yang, R. 2012, The Astrophysical Journal Letters, 756, L24

Hagen, W., Allamandola, L. J., & Greenberg, J. M. 1979, Astrophys. & Space Sci., 65, 215

Hagen, W., Tielens, A. G. G. M., & Greenberg, J. M. 1983, Astron. Astrophys. Suppl., 51, 389

He, J., Jing, D., & Vidali, G. 2014, Phys. Chem. Chem. Phys., 16, 3493

Hidaka, H., Kouchi, A., & Watanabe, N. 2007, J. Chem. Phys., 126, 204707

Hidaka, H., Watanabe, N., Shiraki, T., Nagaoka, A., & Kouchi, A. 2004, Astrophys. J., 614, 1124

Hiraoka, K., Ohashi, N., Kihara, Y., et al. 1994, Chem. Phys. Lett., 229, 408

Hony, S. 2003, PhD thesis, University of Amsterdam

Ioppolo, S., Cuppen, H. M., Romanzin, C., van Dishoeck, E. F., & Linnartz, H. 2008, Astrophys. J., 686, 1474
Ioppolo, S., Cuppen, H. M., Romanzin, C., van Dishoeck, E. F., & Linnartz, H. 2010, Phys. Chem. Chem. Phys., 12, 12065
Islam, F., Baratta, G. A., & Palumbo, M. E. 2014, Astron. Astrophys., 561, A73
Jones, B. M. & Kaiser, R. I. 2013, The Journal of Physical Chemistry Letters, 4, 1965
Kaiser, R. I., Maity, S., & Jones, B. M. 2014, Phys. Chem. Chem. Phys., 16, 3399
Karssemeijer, L. J., Ioppolo, S., van Hemert, M. C., et al. 2014, Astrophys. J., 781, 16
Lin, C. L. & Leu, M. T. 1982, Int. J. Chem. Kinet., 14, 417
Loeffler, M. J. & Baragiola, R. A. 2010, The Journal of Chemical Physics, 133,
Loeffler, M. J., Baratta, G. A., Palumbo, M. E., Strazzulla, G., & Baragiola, R. A. 2005, Astron. Astrophys., 435, 587
Markwalder, B., Gozel, P., & van den Bergh, H. 1993, J. Chem. Phys., 97, 5260
McCullough, R. W., Geddes, J., Donnelly, A., et al. 1993, Meas. Sci. Technol., 4, 79
Minissale, M., Fedoseev, G., Congiu, E., et al. 2014, Phys. Chem. Chem. Phys., 16, 8257
Mispelaer, F., Theulé, P., Aouididi, H., et al. 2013, Astron. Astrophys., 555, A13
Muñoz Caro, G. M., Meierhenrich, U. J., Schutte, W. A., et al. 2002, Nature, 416, 403
Nagaoka, A., Watanabe, N., & Kouchi, A. 2007, The Journal of Physical Chemistry A, 111, 3016
Noble, J. A., Dulieu, F., Congiu, E., & Fraser, H. J. 2011, Astrophys. J., 735, 121
Oba, Y., Watanabe, N., Kouchi, A., Hama, T., & Pirronello, V. 2010, Astrophys. J. Lett., 712, L174
Öberg, K. I., Fayolle, E. C., Cuppen, H. M., van Dishoeck, E. F., & Linnartz, H. 2009, Astron. Astrophys., 505, 183
Öberg, K. I., van Broekhuizen, F., Fraser, H. J., et al. 2005, ApJ Suppl., 621, L33
Paardekooper, D. M., Bossa, J.-B., Isokoski, K., & Linnartz, H. 2014, Review of Scientific Instruments, 85,
Palumbo, E. M., Baratta, G. A., Collings, M. P., & McCoustra, M. R. S. 2006, Phys. Chem. Chem. Phys., 8, 279
Palumbo, M., Baratta, G., Leto, G., & Strazzulla, G. 2010, Journal of Molecular Structure, 972, 64 , horizons in hydrogen bond research 2009 A Collection of Papers from the {XVIIIth} International Conference "Horizons in Hydrogen Bond Research", Paris, France, 14âĂŞ18 September 2009
Palumbo, M. E. & Strazzulla, G. 1993, Astron. Astrophys., 269, 568
Pirronello, V., Biham, O., Liu, C., Shen, L., & Vidali, G. 1997, Astrophys. J. Lett., 483, L131
Raut, U. & Baragiola, R. A. 2011, Astrophys. J. Lett., 737, L14
Raut, U. & Baragiola, R. A. 2013, Astrophys. J., 772, 53
Raut, U., Fulvio, D., Loeffler, M. J., & Baragiola, R. A. 2012, Astrophys. J., 752, 159
Romanzin, C., Ioppolo, S., Cuppen, H. M., van Dishoeck, E. F., & Linnartz, H. 2011, J. Chem. Phys., 134, 084504
Sabri, T., Gavilan, L., Jäger, C., et al. 2014, Astrophys. J., 780, 180
Sandford, S. A. & Allamandola, L. J. 1988, Icarus, 76, 201
Schieferstein, M., Kohse-Höinghaus, K., & Stuhl, F. 1983, Ber. Bunsenges. Phys. Chem., 87, 361
Sibener, S. J., Buss, R. J., Ng, C. Y., & Lee, Y. T. 1980, Review of Scientific Instruments, 51
Sivaraman, B., Mebel, A. M., Mason, N. J., Babikov, D., & Kaiser, R. I. 2011, Phys. Chem. Chem. Phys. (Incorporating Faraday Transactions), 13, 421
Sivaraman, B., Raja Sekhar, B. N., Fulvio, D., et al. 2013, J. Chem. Phys., 139, 074706
Stevenson, K. P., Kimmel, G. A., DohnÃąlek, Z., Smith, R. S., & Kay, B. D. 1999, Science, 283, 1505
Teolis, B. D., Loeffler, M. J., Raut, U., Famá, M., & Baragiola, R. A. 2007, Icarus, 190, 274
Thrower, J., Nilsson, L., Jørgensen, B., et al. 2011, European Astronomical Society Publications Series, 46, 453
Tielens, A. G. G. M. 2013, Reviews of Modern Physics, 85, 1021
Timmermans, E., Jonkers, J., Thomas, I., et al. 1998, Spectrochimica Acta Part B: Atomic Spectroscopy, 53, 1553
Tschersich, K. G. 2000, J. Appl. Phys., 87, 2565

Tschersich, K. G., Fleischhauer, J. P., & Schuler, H. 2008, J. Appl. Phys., 104, 034908

Tschersich, K. G. & von Bonin, V. 1998, J. Appl. Phys., 84, 4065

Watanabe, N., Hidaka, H., & Kouchi, A. 2006, in AIP Conf. Ser., Vol. 855, Astrochemistry - From Laboratory Studies to Astronomical Observations, ed. R. I. Kaiser, P. Bernath, Y. Osamura, S. Petrie, & A. M. Mebel, 122–127

Watanabe, N., Kimura, Y., Kouchi, A., et al. 2010, Astrophys. J. Lett., 714, L233

Watanabe, N. & Kouchi, A. 2002, Astrophys. J. Lett., 571, L173

3

METHODS: KINETIC MONTE CARLO

It is not straightforward to disentangle the various processes occuring on grain surfaces and in ices. Deposition, diffusion, reaction and desorption are in competition with each other, while only the net effect can be observed experimentally. To be able to apply the detailed knowledge gained from experiments to astrochemical large scale models, it is essential to have constraints on the numerous process rates. This is where models with microscopic detail come into play. In this thesis we will use the lattice-gas Kinetic Monte Carlo in this context. An advantage of KMC over, for instance, Molecular Dynamics, is the relatively long timescales that can be simulated. Laboratory surface science experiments of several hours can be easily reached with the possibility to include atomistic detail in the simulations. For this reason, KMC is often applied in surface science and catalysis to simulate experimental conditions and determine experimentally measurable quantities. These can then be directly compared to experiments. Lattice-gas KMC is far from being an *ab-initio* method, in the sense that all input parameters need to be given. This can also be an advantage, however, since the effect of these parameters on the output can be tested and different mechanisms can be switched on and off by changing these parameters. By testing different mechanistic scenarios in this way and comparing the results to experiments, insight into the mechanisms can be obtained.

This chapter introduces the microscopic Kinetic Monte Carlo (KMC) method used in Chapters 4-6 and 8 with its main assumptions, puts KMC in both historical and theoretical perspective, outlines the main technical parameters and summarizes several applications in astrochemistry. Particular deviations or additions from what is discussed here are mentioned and explained in the relevant chapters.

Based on H. M. Cuppen, L. J. Karssemeijer and T. Lamberts, *The Kinetic Monte Carlo Method as a way to solve the master equation for interstellar grain chemistry*, Chem. Rev. 113 (2013) 8840

3.1 INTRODUCTION

Different modeling techniques have been applied to grain surface astrochemistry, covering a large range of time- and length scales. More molecular detail comes at the expense of more CPU time to cover the same evolution in real time. How different techniques relate to one other in this respect is indicated in Figure 3.1. Molecular dynamics simulations trace the exact location and orientation of the molecules including lattice vibrations and in some cases even the intramolecular movement, but they typically stay within the picosecond to nanosecond time frame. Rate equations on the other hand can easily handle 10^8 years – much longer than the lifetime of a molecular cloud – but adsorbed molecules are only treated in terms of numbers and their exact locations are not known. Here, the application of the Kinetic Monte Carlo technique (KMC) to interstellar relevant grain surface chemistry is discussed. This method was initially introduced into astrochemistry as a solution to the 'accretion' limit (see Section 3.2), but is now more and more applied to gain insight into the physico-chemical surface processes. The method has, in principle, no real restriction in how molecules are represented: in terms of number densities or with their exact location and orientation. The different implementations of kinetic Monte Carlo can therefore cover a huge time- and length scale range.

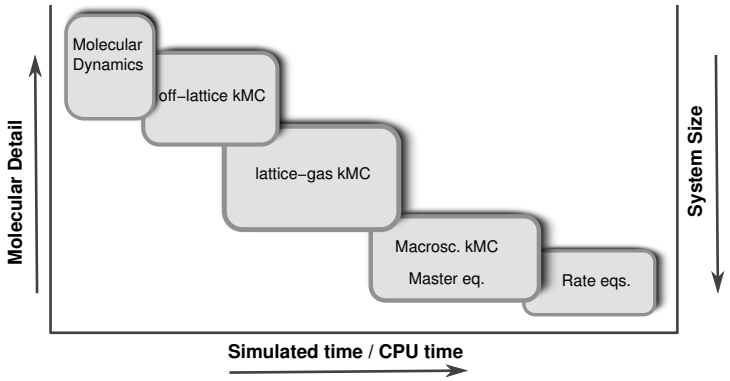

Figure 3.1: Overview of the different simulation methods mentioned in this chapter.

Many processes occurring on the surfaces of grains are in principle stochastic processes. We can describe these systems by a state vector x and a time coordinate t. In this section, x is an abstract quantity which may be some local minimum on the potential energy surface (PES), which is schematically drawn in the left panel of Figure 3.2. Here the black circles represent different states. In many grain surface models a PES is however not explicitly considered and in those cases a state x can be represented by, *e.g.*, the species on the grain, their position, the temperature of the grain, etc., or x can simply contain the coordinates of all particles on the grain.

The kinetic Monte Carlo technique is a way to solve the master equation, a thorough derivation can be found in textbooks such as van Kampen (1992); Gardiner (1994); Gillespie (1992). Here, only the final result is given. On a discrete state space, which is usually used for grain simulations, the equation is written in terms of probabilities, P, in the following way:

$$\frac{d}{dt}P(x_i,t) = \sum_j \left(k(x_i|x_j)P(x_j,t) - k(x_j|x_i)P(x_i,t)\right). \tag{7}$$

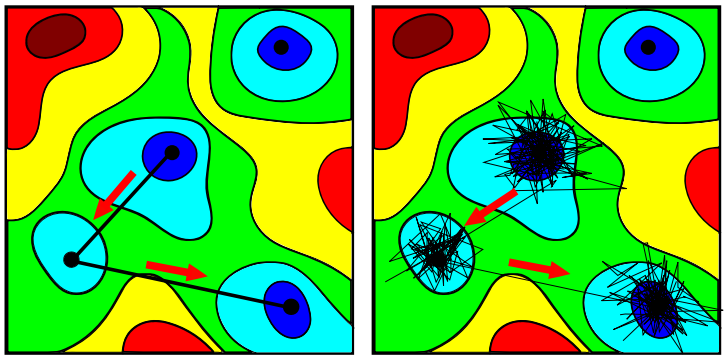

Figure 3.2: Schematic representation of a potential energy surface (PES). The states, local minima on the PES, are indicated by black solid spheres. (left) The system moves from state to state or (right) the vibrational movement is included as well and the trajectories spend most of their time around the local minimum.

The first part of the sum represents the increase in $P(x_i, t)$ because of events that enter state x_i from any other state x_j; the second part is the decrease in $P(x_i, t)$ due to all events leaving x_i. This is intuitive when considering chemistry: reaction creating a molecule are in competition with those destroying it.

In the formal derivation of the master equation the so-called Markov chain assumption is key: the assumption that the probability of arriving in x_n, t_n is only dependent on x_{n-1}, t_{n-1} and not on the states before t_{n-1}. Due to its importance in the derivation it can therefore also be a severe restriction if the assumption is not valid. It is namely valid only for memoryless processes. When simulating grain surface chemistry, we are typically interested in rare events, such as diffusion and desorption. This type of events occur at much longer timescales than the (lattice) vibrations and the event timescale and the vibrational timescale become decoupled. This makes rare events effectively memoryless, since all history about which states where previously visited is lost due to the vibrations between two transitions. This is schematically depicted in Figure 3.2. The residence time of the system in a local minimum of the potential energy surface is several orders of magnitude larger than the vibrational timescale. The system will therefore typically proceed according to a trajectory like the one drawn in the right panel of Figure 3.2. At the time that the system leaves the potential well, all information about the direction from which it initially entered this potential well, is lost. In kinetic Monte Carlo this is approximated by a trajectory as drawn in the left panel. In some cases, when the residence time in a state is short as compared to the vibrational timescale, this approximation breaks down. An example of this is the 'hot' reaction products which move away from each other with a certain momentum upon reaction (Chapters 4 and 5). For such cases, Molecular Dynamics simulations, which use Newton's equations of motion to determine the molecular trajectories, are better suited. These types of simulations would result in trajectories plotted in the panel on the right. A drawback of this technique is however that their simulation timescales do not match astrochemical timescales – they are shorter by roughly twenty orders of magnitude – which makes them less suitable for astrochemical simulations. Individual processes with astrochemical relevance can however be treated with Molecular Dynamics (See Section 3.3.2).

Several modeling methods have been used to simulate grain surface chemistry and Section 3.2 gives a overview of the introduction of these techniques into astrochemistry and

their main advantages and disadvantages. The reason to include a short discussion on these other techniques is that this allows us to put the results on Kinetic Monte Carlo into a better perspective. This chapter will then continue by discussing some of the technical aspects involved in constructing a KMC model and the input parameters that are needed for such a model. Section 3.4 summarize the application of the kinetic Monte Carlo technique in astrochemistry. Here the distinction is made between simulations that try to reproduce astrochemically relevant experimental results and simulations that attempt to predict astrochemical environments. Only models that treat the grain with some microscopic detail will be discussed. Finally, some recent advances in the application of kinetic Monte Carlo are discussed.

3.2 HISTORICAL AND THEORETICAL OVERVIEW OF GRAIN MODELING TECHNIQUES

3.2.1 *Rate equations*

One of the most applied methods in astrochemistry is solving rate equations numerically. These equations model the abundances of species and can be seen as the deterministic counterpart of the stochastic master equation. They do not describe the probabilities, P, to be in individual states, but rather the surface abundances, n_s, of the different species on the grain. Since a similar quantity is used to describe the gas-phase chemistry (the gas-phase abundance n_g), these type of equations can be easily coupled to gas-phase chemistry networks. The first gas-grain simulations were therefore rate equation based (d'Hendecourt et al., 1985; Brown & Charnley, 1990; Hasegawa et al., 1992; Shalabiea & Greenberg, 1994). Rate equations are often applied in chemistry to describe macroscopic (experimental) effects and account for many-body effects with a mean-field approach. A set of rate equations to describe surface reactions in astrochemistry was first constructed by Pickles & Williams (1977) to describe the formation of molecular hydrogen from H atoms and water from O_2 and H through HO_2 and H_2O_2.

Grain species can generally undergo four types of processes: accretion onto the surface, desorption, diffusion, and reaction. This leads to the following expression for the change in surface abundance of species C at time t

$$\begin{aligned}\frac{d}{dt}n_s(C,t) = &\sum_{A,B} k_{react,A,B}\frac{k_{hop,A}+k_{hop,B}}{N_{sites}}n_s(A,t)n_s(B,t)\\ &- n_s(C,t)\sum_{D} k_{react,C,D}\frac{k_{hop,D}+k_{hop,C}}{N_{sites}}n_s(D,t)\\ &+ k_{acc,C}n_g(C)\\ &- [k_{evap,C}+k_{non-th,C}]n_s(C,t),\end{aligned} \tag{8}$$

with N_{sites} the number of sites on the grain. The number of species on the grain is thus averaged both per grain and in time. Here the subscripts s and g of n represent the surface and gas-phase abundances of the species, respectively. The first two terms in this expression denote the gain and loss of species A due to reactions of the types $A + B \longrightarrow C$ and $C + D \longrightarrow E$. These are described in terms of reaction rates k_{react} and hopping rates k_{hop}. The third term accounts for the accretion of new species from the gas phase, through the accretion rate k_{acc}. The final term represents the desorption of the species into the gas phase. This can either be due to thermal desorption (k_{evap}) when the temperature is high enough to overcome the binding energy or be due to non-thermal effects (k_{non-th}) like photodesorption (Westley et al., 1995; Öberg et al., 2007, 2009c,b), sputtering by cosmic rays or grain

heating by cosmic rays (Hasegawa & Herbst, 1993; Herbst & Cuppen, 2006). Here first order kinetics are assumed for the desorption, although experimentally zeroth order kinetics are often observed for the desorption of ices in the multilayer regime (see Chapter 2).

All of the reactions included in Eq. (8) are assumed to occur through the Langmuir-Hinshelwood mechanism. Eley-Rideal is generally considered to be only important for high surface coverages or low surface mobility (Ruffle & Herbst, 2001) and is therefore not explicitly considered in most models. Rate equations that include surface reactions following the Eley-Rideal mechanism contain an additional term that depends on the gas-phase abundance of one reactant, the surface abundance of the other reactant and the rate of reaction between them (Hassel et al., 2010). Furthermore, it is often ignored that reaction is in fact in competition with diffusion and desorption (Herbst & Millar, 2008).

Another disadvantage of the rate equation method is that it does not treat statistical fluctuations. One of the assumptions underpinning the rate equations leads to following:

$$\langle N_A \rangle \langle N_B \rangle \approx \langle N_A N_B \rangle . \tag{9}$$

In other words, the probability of finding both particles A and B on the surface is the probability of having particle A on the surface multiplied by the probability of having particle B on the surface. For a reaction to occur, however, two species should be actually present and for a small number of species the probability of having both species A and B on the surface is much smaller than the multiplication of the individual probabilities. Thus, when the number of species on the surface is small, the assumption breaks down and the systems reaches the accretion limit as it was called by Charnley et al. (1997). In this case the rate limiting step for reaction is not diffusion but the arrival of species on the surface from the gas phase. To account for the accretion limit problem in the rate equations, alternative methods have been proposed which either adjust the rate equations in the accretion limit regime to result in the correct rates (Caselli et al., 1998; Garrod, 2008) or do not use the expectation value assumption and are so-called stochastic methods (Stantcheva & Herbst, 2004).

3.2.2 *Master equation method*

The accretion limit problem led to the realization that grain surface processes can be better described by a master equation. This resulted in the introduction of several techniques that solve this master equation. One of these constructs differential equations for the probabilities to have a certain number of species on the surface and uses a numerical integrator to obtain the average number of species on the grain as a function of time. This method was introduced into astrochemistry to circumvent the accretion limit problem (Biham et al., 2001; Green et al., 2001; Stantcheva et al., 2002) and is usually referred to as the 'master equation method'. This can be confusing since the kinetic Monte Carlo approach, which is discussed in the next section, also solves the master equation. A better description, although rather lengthy, would perhaps be 'numerical integration of master equations', but in line with previous authors we will stick to using the term 'master equation method' in the remainder of this chapter.

Since most gas-phase models also use numerical integration, the master equation approach can again be easily integrated within a gas-phase astrochemical code. If only two types of

species, A and B, are considered, the expressions that have to be integrated become of the type

$$\begin{aligned}\frac{d}{dt}P(x_{A,B}[k,l],t) &= k_{react,A,B}\frac{k_{hop,A}+k_{hop,B}}{N_{sites}}\\ &\times[(k+1)(l+1)P(x_{A,B}[k+1,l+1],t)-klP(x_{A,B}[k,l],t)]\\ &+k_{acc,A}n_g(A)[P(x_{A,B}[k-1,l],t)-P(x_{A,B}[k,l],t)]\\ &+k_{acc,B}n_g(B)[P(x_{A,B}[k,l-1],t)-P(x_{A,B}[k,l],t)]\\ &+[k_{evap,A}+k_{non-th,A}][(k+1)P(x_{A,B}[k+1,l],t)\\ &\qquad -kP(x_{A,B}[k,l],t)]\\ &+[k_{evap,B}+k_{non-th,B}][(l+1)P(x_{A,B}[k,l+1],t)\\ &\qquad -lP(x_{A,B}[k,l],t)]. \end{aligned} \tag{10}$$

Explicit probabilities are listed per type of situation, for instance $P(x_{A,B}[k,l],t)$ denotes the probability that k species A and l species B reside on the grain at time t. One can again recognize the reaction, accretion, and desorption terms. The factors $(k+1)$ and $(l+1)$ in the first reaction term reflect the number of possible combinations to form new molecule AB of $k+1$ species A and $l+1$ species B and leave k species A and l species B behind. In principle, one should construct these expressions for all possible combinations of species A and B ($P(x_{A,B}[0,0],t)$, $P(x_{A,B}[1,0],t)$, $P(x_{A,B}[0,1],t)$, $P(x_{A,B}[1,1],t)$, etc.). Obviously, these expressions become much more involved if more types of species are included in the model. If the number of particles expands, either by a change in physical conditions (N^{max}grows) or by increasing the number of considered species in the model, the number of equations blow up rapidly. Algorithms have been suggested to make the effect less severe and to extend the range in which the master equation method is applicable (Lipshtat & Biham, 2004; Barzel & Biham, 2007).

Theoretically the number of expressions to solve is infinite. However, cutoffs can be used to exclude the higher order terms, if their probability of occurrence becomes very small. In other words, one can set upper limits on the maximum number of particles per species that can reside on the grain, $N^{max}(A)$. The lowest possible cutoff would be $N^{max}=2$ for species that form homonuclear diatomic molecules (H_2, O_2, etc.) and $N^{max}=1$ for all other species, but obviously this would lead to a large error. To make this less dramatic one can convert the original master equations into moment equations (Lipshtat & Biham, 2003; Barzel & Biham, 2007, 2011).

While the constraint that at any given time, at most, two atoms or molecules can be adsorbed simultaneously on the surface can work for a small network under specific physical conditions where the surface density is low, this constraint cannot be obeyed in the general case and application of moment equations to large grain surface networks could result in undesirable effects. For this reason, Du & Parise (2011) introduced a hybrid method that combines moment equations and rate equations. In general, both gas-phase and surface reactions are treated by rate equations, but if the average population of a certain surface species becomes smaller than one per grain, the algorithm switches to moment equations.

3.2.3 *Macroscopic Kinetic Monte Carlo*

The first astrochemical application of simulations based on the Monte Carlo method was performed by Tielens & Hagen (1982). They used the method to simulate the evolution of the grain mantle by one-by-one accretion of gas-phase species and calculating their fate (reac-

tion, desorption, trapping) before a new species would land on the surface. In this way, the time evolution is determined by the accretion rate and the Monte Carlo aspect determines the fate of accreted species. The abundances found are integer numbers, albeit spatially averaged over the ice, which also circumvents the accretion limit problem. Steady-state gas-phase abundances were used to determine the relative accretion rates for each of the gas-phase species. These were obtained from a pure gas-phase model and gas-grain interactions were not directly included in this calculation other than using a depletion parameter which decreases the relative elemental abundance of the heavier species like O, N and C towards clouds with higher densities. Using the resulting gas-phase abundances, the mantle composition was calculated as a function of visual extinction A_V or radiation field, cloud density and depletion factor. Since the results of the simulations were presented as the steady-state fractional composition of the grain mantles, the time evolution of the grain was not discussed.

Charnley (1998, 2001) was the first to introduce the Kinetic Monte Carlo method to determine the chemical evolution of a cloud, including both gas-phase and grain surface. Charnley started from the master equation (Eq. (7)). Using this equation one can derive the time interval between two events, which is one of the fundamental expressions in kinetic Monte Carlo, since it describes how time progresses during a simulation. If one starts from state i at time t (so $P(x_j, t) = 0 \; \forall \; j \neq i$), then for small Δt we have

$$\frac{d}{dt} P(x_i, t + \Delta t) = - \sum_j k(x_j | x_i) P(x_i, t + \Delta t) \tag{11}$$

where $k(x_j|x_i)$ represents the rate of leaving state i and populating state j. Therefore, the probability to remain in state i at time $t + \Delta t$

$$P(x_i, t + \Delta t) = \exp\left(- \int_t^{t+\Delta t} dt' k_{tot}(x_i, t') \right), \tag{12}$$

where $k_{tot}(x_i, t)$ is the total rate leaving state x_i. If we assume stationary rates than Eq. (12) becomes

$$P(x_i, t + \Delta t) = \exp\left(- k_{tot}(x_i) \Delta t \right). \tag{13}$$

Stationary rates are a reasonable assumption for grains of constant temperature. If the surface temperature fluctuates, for instance due to stochastic heating of the grains by incoming UV photos or cosmic rays (Cuppen et al., 2006; Herbst & Cuppen, 2006; Draine, 2003; Hasegawa & Herbst, 1993) or in a Temperature Programmed Desorption experiment, the rates change over time and the time interval Δt should be determined differently (Jansen, 1995). This will be discussed in Section 3.3.

In practice, this means a KMC cycle starting from state x_i consists of three steps if all possible events are known: first a final state x_f is picked with probability that scales the rate $k(x_f|x_i)$ with the total rate leaving state i

$$p_{i \to f} = \frac{k(x_f | x_i)}{k_{tot}(x_i)}, \tag{14}$$

using a random number. Next, the time is advanced where the values for Δt are chosen such that they follow the distribution dictated by Eq. (13). This can be numerically achieved by generating a uniform random number Z in range $(0, 1]$ and equating this to the probability that the reaction has not yet occurred:

$$Z = P(x_i, t + \Delta t), \tag{15}$$

which leads to

$$\Delta t = -\frac{\ln(Z)}{k_{tot}(x_i)} \tag{16}$$

for stationary rates. Finally, the picked transition is evaluated and the transition rates leaving this new state, x_f, are determined. The consequence of Eqs. (14) and (16) is that at each given time all possible transition events leaving the current state and their corresponding rates should be known. This combination of events and rates is often referred to as 'table of events'. For the systems discussed so far, the table of events can be easily constructed, since all possible events are known at the start of the simulation. If we want to look at grain surface chemistry in more microscopic detail, this can become problematic as we will discuss in Sections 3.3 and 3.5.

The KMC realization of the master equation is not as easily implemented in a gas-grain astrochemical code as the rate equation and master equation methods. The reason for this is that for the gas phase usually rate equations are used and the Monte Carlo algorithm cannot be easily coupled with numerical integrators.

3.2.4 *Microscopic Kinetic Monte Carlo*

The methods discussed so far only considered the abundances or numbers of the different surface species and not their exact location and exact movement on the grain. The diffusion of the different species is included in some average way. In microscopic KMC simulations, the location of the particles is known. They undergo a random walk and they can revisit sites multiple times. This revisiting is often referred to as *back diffusion*. In these kind of simulations, accretion, desorption, diffusion, and reaction are again considered, with similar rates to the macroscopic KMC method, but with the difference that for each individual atom or molecule on the surface its specific position on the grain is monitored. Diffusion now occurs through individual hops of the species from one site to the next. This includes hopping back to where it came from. The information of the position of the atoms/molecules on the surface is an advantage over macroscopic KMC.

Another advantage is that the surface structure can be included. The rate of diffusion and desorption can be made site-specific, mimicking steps on the surface, amorphicity of the grain, and/or inhomogeneity of the grain material. The species might undergo a hindered random walk that does not result in an exact second order for reaction. Since in microscopic KMC, only species either in neighboring sites or occupying the same site are allowed to react and the reaction order is not included specifically beforehand, this deviation from second order will come out naturally. In the same way, crossing a reaction barrier is treated in competition with diffusion and desorption automatically in microscopic KMC (Cuppen et al., 2009).

One can imagine that while the grain mantle grows, species can become trapped in the lower layers and are not able to participate in the chemistry that occurs on the surface of the formed ice, or that these species will not be able to desorb. Again this will come out naturally from the microscopic Monte Carlo simulations.

The first implementation of microscopic KMC in astrochemistry was focused on H_2 formation and was called continuous-time, random-walk (CTRW) Monte Carlo (Chang et al., 2005) following the algorithm by Montroll & Weiss (1965). It is also this algorithm in particular that has been used throughout this Thesis.

3.3 TECHNICAL ASPECTS OF MICROSCOPIC KMC

This section will discuss the technical aspects of the Kinetic Monte Carlo technique applied to surface astrochemistry. In this section, we will go more into the details of the implementation of the theory and its technical limitations. As discussed in Section 3.2, the theory behind KMC demands the formation of a table-of-events. We will discuss the type of information that is needed to construct such a table, how this is obtained, and what the common assumptions are. Different applications of the KMC technique require different algorithms, and therefore a wide selection of different algorithms has been developed, usually with only slight variations. Here, only the continuous-time random-walk algorithm used in Chapters 4-6 and 8 will be discussed. Additionally an algorithm which is able to handle non-stationary rates will be discussed as well. But first the representation of the grain in the simulations is explained.

3.3.1 *Representation of the grain*

KMC follows the evolution of a Markov chain from one state, or local minimum on the potential energy surface, to the next. These states are usually put on a regular grid represented by a 2D or 3D array where for each grid point the occupancy is monitored. A reaction or a diffusion from one site to another is then modeled as a sudden change in the occupancy of the sites. A model that puts sites on a grid and registers their occupancies, is often referred to as a *lattice-gas* model.

Since molecules are confined to lattice positions, using realistic molecular potentials can become problematic. Furthermore, making guesses on the possible events is far from straightforward and important mechanisms can be easily missed. So, ideally, one wants to move away from lattice models, but for Kinetic Monte Carlo this is not so obvious. Examples of off-lattice Kinetic Monte Carlo techniques are mentioned in Section 3.5. For now, we will limit ourselves to lattice-gas simulations, since these are most commonly used in astrochemistry and also used throughout this Thesis.

A clear advantage of a lattice-gas model is that one can work with a predefined event table. Since the molecules are confined to a lattice, only a limited amount of events is possible of which the rates can be determined at the start of the simulation. This allows one to cover very large timescales. The simulations can really mimic laboratory experiments of ices, covering hours of simulation time and tracing similar properties.

One of the largest disadvantages of using a lattice model is that a large part of the molecular detail is lost in these models. Because of the amorphous character of the grain and ice, the local environment of the sites probably varies across the surface and the states are most likely not at exact equidistant locations. Nevertheless, the bare grain or its ice mantle is usually considered to have well-defined positions on its surfaces where other species can adsorb and these sites are probably distributed with some limitations in terms of number of neighbors. In this sense, there is some regularity, even for amorphous grain mantles, which would justify the use of lattice-gas models.

3.3.2 *Input parameters in grain models: filling the table of events*

A requirement for KMC is to have a table of events with corresponding rates. For macroscopic KMC this table contains similar processes and input parameters as rate equation and master equation models. These include sticking fractions, diffusion barriers, binding energies, and

activation energies for reaction. These barriers can be converted into diffusion, desorption, and reaction rates respectively by assuming thermal or tunneled activation of the process:

$$k_{process,thermal,A} = \nu \exp\left(-\frac{E_{process,A}}{k_B T}\right), \tag{17}$$

$$k_{process,tunneled,A} = \nu \exp\left(-\frac{2a}{\hbar}\sqrt{2\mu E_{process,A}}\right), \tag{18}$$

where ν is an attempt frequency, a the width of the barrier under consideration, and μ the reduced mass. In Chapter 6 the difference between calculating reaction rates via thermal or tunneled activation is explicitly studied.

Macroscopic KMC requires at least two input parameters per species (diffusion barrier and binding energy) and one per reaction (reaction barrier). If other types of desorption are considered, like photodesorption (Westley et al., 1995; Öberg et al., 2007, 2009c,b), sputtering by cosmic rays, grain heating by cosmic rays (Hasegawa & Herbst, 1993; Herbst & Cuppen, 2006) or desorption upon reaction using the excess energy (Garrod et al., 2007; Dulieu et al., 2013), more input parameters are needed. For microscopic KMC the list is much longer, since the location of each species is known and the exact environment can influence binding energies and barriers.

On of the main aspects of this Thesis concerns filling the table of events. By varying the input parameters and comparing them against experiments an optimal set of rates can be obtained (Chapter 4 and 5) and subsequently used for astrochemical simulations (Chapters 5, 6, and 8). Three main types of parameters have been varied: binding energies, diffusion barriers, and reaction rates. First, the sticking fraction is discussed.

3.3.2.1 *Sticking fractions*

The sticking fraction is the fraction of impingements that leads to adsorption. The sticking fraction S_A of a species A to the surface depends both on the grain and gas temperature and is one of the quantities determining the accretion rate of said species on the grain

$$k_{acc,A} = S_A \nu_A n_{grain} \pi r_{grain}^2 \tag{19}$$

with r_{grain} the average radius of an interstellar grain (~ 0.1 µm) with number density n_{grain}, and with ν_A the average gas-phase speed.

Sticking fractions are often assumed to be equal to unity, which is a good approximation for species other than hydrogen at low gas and grain temperatures (Buch & Czerminski, 1991; Al-Halabi et al., 2003; Al-Halabi et al., 2004). They can deviate from one if the incoming species cannot convert their momentum into phonons or if a barrier for sticking, typically restricted to chemisorption, exists. Fractions lower than one decrease the flux of incoming particles.

Sticking fractions can be theoretically determined by Molecular Dynamics (Buch & Czerminski, 1991; Al-Halabi et al., 2002, 2003; Al-Halabi et al., 2004; Batista et al., 2005), perturbation and effective Hamiltonian theories, close coupling wavepacket, and reduced density matrix approaches (Lepetit et al., 2011) or by the much-more-approximate soft-cube method (Logan & Keck, 1968; Burke & Hollenbach, 1983). Experimental studies on the sticking of H, H_2, D, and D_2 have been performed (Amiaud et al., 2007; Chaabouni et al., 2012).

3.3.2.2 *Binding energies*

The binding energies determine the temperature regime in which the species are on the surface of the grain and are available for reaction. The residence time of a species A on the

surface is predominantly determined by their desorption rates, which, in turn, depends on the binding energy $E_{bind,A}$ via Eqn. 17.

In an off-lattice simulation, one should be able to obtain the binding energy from the potential energy surface; in lattice-gas models this is not possible and the binding energies should be taken from some external source. One of these sources are Temperature Programmed Desorption experiments (See Chapter 2). TPD experiments have yielded accurate binding energies for many species. However, interstellar ices are inherently mixtures of several components. Species can be trapped in ices with predominantly high desorption temperatures and/or can escape via a segregation process. Modeling the desorption of mixed layers depends on a large number of parameters including surface temperature, ice composition and mixing ratio. The effect of trapping due to layering can be easily simulated using microscopic KMC simulations, segregation is harder to model, since the exact mechanism is not yet understood (Öberg et al., 2009a).

3.3.2.3 *Diffusion barriers*

Diffusion barriers are crucial in determining the rate of reaction, since most reactions occur through the diffusive Langmuir-Hinshelwood mechanism. Furthermore, each species has a unique barrier. The determination thereof remains, however, experimentally challenging and is one of the largest origins of uncertainty in the modeling of surface chemistry in general. TPD experiments can also be applied to obtain information on diffusion barriers. This information is however indirect and the result is rather sensitive to the formation mechanism/reaction order that is implicitly assumed in the model used for fitting. Compare for example, Katz et al. (1999), Cazaux & Tielens (2004) and Cuppen & Herbst (2005) who were able to fit the same experimental results from Refs. Pirronello et al. (1997b,a, 1999) applying different models. Furthermore, originally H atoms were assumed to diffuse through quantum tunneling. Nowadays models favor thermal hopping after experimental studies that showed that the diffusion of H atoms is rather slow (Pirronello et al., 1997b,a, 1999; Katz et al., 1999).

Since diffusional barriers are not well defined for most species, often a fixed fraction of the binding energy is taken. This fraction is preferably chosen to be rather high, since a low diffusion barrier slows down the simulations substantially. In that case, the diffusion timescale becomes very small as compared to, for instance, accretion or desorption rates and the simulation spends most of its CPU time on diffusion steps that do not lead to a fast evolution of simulated time. Computational efforts with atomistic models have been reported (Batista & Jónsson, 2001; Al-Halabi & van Dishoeck, 2007; Karssemeijer et al., 2012). In one such studies Karssemeijer, L. J. & Cuppen, H. M. (2014) determined diffusion-desorption ratios of 0.31 for CO and 0.39 for CO_2, hence assuming a high fraction might in fact not be reliable.

On first instance, one would expect the diffusion rate to play a crucial role in the overall evolution of the systems. This depends, however, strongly on the ratio between the reaction partners at play. A faster diffusion rate namely leads to more frequent meetings between both reactants, but per encounter the time to react is shorter with respect to using lower diffusion rates. In simulations of the hydrogenation of pure ices, diffusion rates can have a significant effect on the final yield of many of the species, as is the case for O_2 hydrogenation under laboratory conditions (Chapter 4). Vasyunin & Herbst (2013) showed the impact of the fraction chosen on the outcome of the astrochemical cloud collapse models.

Finally, a requirement for every rate is that it should obey macroscopic reversibility. In equilibrium, the master equation should result in a steady state

$$\sum_{x_f} \left(\tilde{k}(x_i|x_f) P_{eq}(x_f) - \tilde{k}(x_f|x_i) P_{eq}(x_i) \right) = 0, \tag{20}$$

where $\tilde{k}(x_f|x_i)$ denotes the equilibrium rates, which are equal to the transition probabilities times some unit of time. The easiest way to fulfill Eqn. 20 is to require detailed balance or microscopic reversibility, *i.e.*, the net flux between every pair of states is zero

$$\frac{\tilde{k}(x_i|x_f)}{\tilde{k}(x_f|x_i)} = \frac{P_{eq}(x_i)}{P_{eq}(x_f)}. \tag{21}$$

For a canonical ensemble, using Eqn. 17

$$\frac{P_{eq}(x_i)}{P_{eq}(x_f)} = \exp\left(-\frac{E(x_i) - E(x_f)}{kT}\right). \tag{22}$$

For KMC models with homogeneous diffusion and desorption rates, this requirement is met naturally. Only when different types of binding sites are introduced, one should be careful to check whether especially the diffusion rates obey this detailed balance criterion.

3.3.2.4 *Reaction activation barrier*

Finally, the activation barrier for reaction should be given for all reactions in the network. Experimentally it is possible to constrain solid state reaction rates to a certain extent. Barrierless reactions, for instance, can be discriminated by their temperature-independence (Cuppen et al., 2010). Alternatively, species can be intentially placed in an ice in such a way that they are in competition with reactions with known rates, in order to appreciate whether the reaction proceeds faster, with approximately equal rate, or slower than the known reaction (Fedoseev et al., 2012). If reactions are thermally activated, a kinetic study can be performed at several temperatures resulting in an Arrhenius plot through which the activation energy is determined (Mispelaer et al. (2012), Chapter 7). Furthermore, for reactions proceeding via tunneling, product abundances and ratios change upon changing the reactive partner from hydrogen to deuterium (Oba et al., 2012; Oba et al., 2014). In all experimental studies it is important to keep in mind that the activation energies found are influenced by the exact surrounding of the species and, *e.g.*, rates in polar ices may not be directly applicable to non-polar ices.

To circumvent the experimental issues, rates are often guessed from analogous reactions or taken from gas-phase data, ignoring the influence of the grain. The catalytic effect of the grain can namely change the barrier and the branching ratios of reaction products (Goumans et al., 2007; Goumans et al., 2008). High-level theoretical calculations, such as *ab initio* methods are often computationally too expensive to use for barrier calculations due to the system size. Molecular Dynamics and embedded QM/MM methods, are able to deal with larger systems and have been used both for thermally activated and photo-induced reactions (Goumans et al., 2009b,a; Arasa et al., 2013; Koning et al., 2013). Note that gas-phase calculations can still provide useful information on general trends, for instance in the calculation of kinetic isotope effects between hydrogenation and deuteration (Andersson et al., 2011).

In astrochemical models often two possible reactive mechanisms are implemened: thermally induced reactions (Eqn. 17) and quantum tunneling through a square barrier (see also Chapter 6) (Hasegawa et al., 1992).

3.3.3 *Kinetic Monte Carlo algorithms*

The theory behind KMC can be implemented into an algorithm in several ways, common algorithms are that proposed by Nordmeyer & Zaera (1991, 1992), the n-fold algorithm by Bortz et al. (1975), and the continuous-time random-walk (CTRW) algorithm by Montroll & Weiss

(1965). Here we will focus only on the CTRW implementation of which the flow diagram is depicted in Fig. 3.3. It was originally designed to describe noninteracting random walkers on a surface.

The algorithm starts by inputing all rates, *i.e.,* creating the table of events. Then, the surface is initialized by creating an empty matrix, M, where each entry represents a site and the occupancy of this site can be changed by changing the number. In the next step the first deposition is determined with a separate random number. After this deposition, a time for a new deposition is determined followed by a loop in which a separate time line for each individual random walker is determined. The time increment is therefore not determined by the total rate for the whole system, but the total rate for an individual random walker. The event times for each walker are then compared, together with the next deposition time, and the first event is then executed. Only one random number per iteration is needed; two in the case of deposition. In this way when updating the system for the next iteration only the random walker which moved in the previous iteration has to be considered. This random walker will get a new event time and will be placed in the species list which is sorted according to its event time. Because both the event and the location are determined in one step, this is an algorithm that is in principle suitable for inhomogeneous surfaces.

The algorithm works very well for non-interacting species. Obviously when species interact, a move of one random walker can affect the total rate of a neighboring random walker and, in turn, its event time. A good example would be when a stationary species, that has an event time well above the termination time of the simulation, gets a mobile neighbor with which it can undergo reaction. The event time of the stationary species changes drastically. A way to adjust for this is to store for each species, the random number Z_i that was drawn to determine its initial event time, its total rate, and the time at which its last event occurred $t^i_{\text{event,old}}$. The adjusted event time, $t^i_{\text{event,adjust}}$ can than be calculated using

$$\begin{aligned} -\ln(Z_i) =& k^i_{\text{tot,old}}(t_{\text{current}} - t^i_{\text{event,old}}) \\ &+ k^i_{\text{tot,adjust}}(t^i_{\text{event,adjust}} - t_{\text{current}}). \end{aligned} \tag{23}$$

Numerical errors can occur in adjusting this event time, if large time differences are subtracted.

3.3.4 *Simulations with varying rates*

Evaluating the thermal expression that is typically used to calculate reaction rates, Eqn. 17, shows that a temperature fluctuation results in a time-dependent rate. This is the case when TPD experiments are considered, but also in the case of simulating thermalization of reaction products (Chapter 5).

The two main equations on which KMC algorithms rely are Eqs. (12) and (14). While these are relatively straightforward for stationary rates, they become more complex in the case of a varying (surface) temperatures which causes the rates to change in time. Usually, however, we know in advance *how* the temperature will change. For instance for TPD experiments, this is usually $T = T_0 + \beta t$ where T_0 and β are constants. Jansen (1995) has described a way to account for this time dependence and to obtain values for Δt that follow the correct distribution. Both Eqs. (12) and (14) have the term

$$\int_{t_{k-1}}^{t_k} k(t')dt'. \tag{24}$$

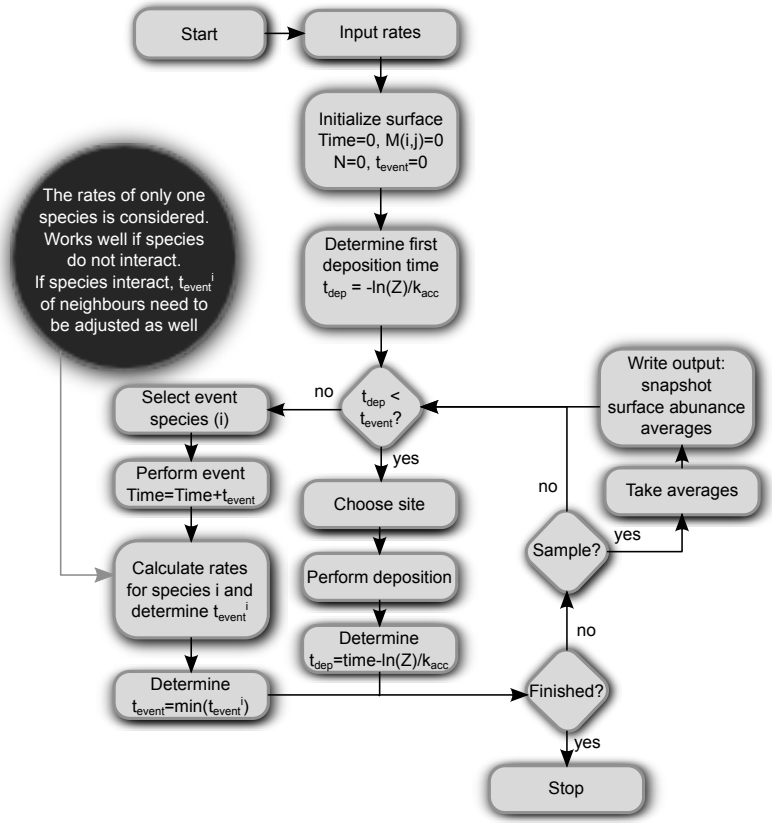

Figure 3.3: Flow diagram of the continuous-time, random-walk KMC algorithm derived from Montroll & Weiss (1965) and adjusted to simulate grain surface chemistry.

For thermal rates and assuming a linear increase in temperature this becomes

$$\int_{t_{k-1}}^{t_k} \nu \exp\left(-\frac{E}{k(T_0+\beta t')}\right) dt' = \Omega(t_k) - \Omega(t_{k-1}) \tag{25}$$

with

$$\Omega(t') = \frac{\nu}{\beta}(T_0+\beta t')E_2\left[\frac{E}{k(T_0+\beta t')}\right]. \tag{26}$$

Here E_2 is an exponential integral Abramowitz & Stegun (1972). Since t_{k-1} is known, it is the current time, and β and T_0 are experimental parameters, *i.e.*, the heating ramp and the initial deposition temperature, respectively. A value for t_k can be obtained by solving

$$Z = \exp(-\Omega(t_k) + \Omega(t_{k-1})). \tag{27}$$

This effectively means finding the root of

$$\Omega(t_k) - \Omega(t_{k-1}) + \ln(Z). \tag{28}$$

This can be most conveniently done with the Newton-Raphson method (Press et al., 1992). Since Ω and $d\Omega/dt$ are both monotonically increasing, the method always succeeds.

The derivation here used a linear increase of the surface temperature. Different time dependences are also possible. The numerical effort is determined by the integration of the expression $\int_0^t \nu \exp\left(-\frac{E}{kT(t)}\right) dt'$.

3.4 KMC SIMULATIONS OF ASTROCHEMICALLY RELEVANT ICE (ANALOGS)

This section highlights several key parameters and processes when simulating ice experiments and ice build-up under astrochemical conditions. This concerns most notably diffusive processes, reaction barriers, and the inclusion of microscopic structure to determine binding energies of the species at hand.

3.4.1 *Simulations of ice experiments*

In all of the KMC simulations simulating experiments bulk diffusion is important in reproducing the experimental results, but is simultaneously still an ill-understood process.

In the framework of thermal processing, the astronomically observed segregation of mixed H_2O and CO_2 ices has been studied in a combined experimental and computational study (Öberg et al., 2009a). Vasyunin & Herbst (2013) used follow-up TPD experiments of the desorption of mixed ices to calibrate their multilayer macroscopic KMC model MONACO. In this model only the outer most layers are chemically active, but they did not allow bulk diffusion to occur.

Diffusion processes covering the penetration of reactive species into the ice can be very similar to the ones that drive segregation of ices. An example of a surface reaction experiment where this is at play is the hydrogenation of solid CO:

$$CO \xrightarrow{+H} HCO \xrightarrow{+H} H_2CO \xrightarrow{+H} H_3CO \xrightarrow{+H} CH_3OH.$$

Experiments performed on this topic have been modeled, and it was found that both the reaction barriers and the diffusion are key parameters, but penetration could be only partially reproduced by the simulations (Fuchs et al., 2009).
The simulations of the hydrogenation of molecular oxygen

$$O_2 \xrightarrow{+H} HO_2 \xrightarrow{+H} H_2O_2 \xrightarrow{+2H} H_2O.$$

are extensively discussed in Chapters 4 and 5 focusing both on the reaction barriers and effects of non-Markovian diffusion. Furthermore, the reaction network derived is also used in Chapter 6 to derive an upper limit for the reaction rate of $H_2 + O \longrightarrow OH + H$.

3.4.2 *Simulations of astrochemical environments*

Typical astrochemical environments, *e.g.*, dark or diffuse clouds, have been simulated to predict or reproduce molecular abundances. Note that apart from the studies mentioned below, Kinetic Monte Carlo models have also been used as a reference model with which less computationally expensive models are compared (Garrod et al., 2009; Hincelin et al., 2014).

Dense molecular clouds provide a surrounding with low temperature, high density, high H_2 abundance and typically high values of A_V (See Introduction). The latter is especially ideal for the formation of icy mantles reaching thicknesses up to 100 ML. The main problem when simulating grain surface chemistry in these dense conditions is that one leaves the submonolayer regime and ice layers build up. The grain is therefore constantly changing and the binding

Table 3.1: Overview of KMC ice studies with some microscopic detail.

Reference	# reactions[a]	Species	gas phase?[b]	D/H?	photo-processes?	comments
Herbst & Cuppen (2006)	0	–	N	N	N	CR desorption
Chang et al. (2007)	12	CH_3OH, H_2O, CO_2	Y	N	N	
Cuppen & Herbst (2007)	10	H_2O_2, H_2O, O_3	N	N	Y	
Muralidharan et al. (2008)	0	–	N	N	N	water chemisorption model
Fuchs et al. (2009)	5	CH_3OH	N	N	N	sequential accretion of CO and H
Cuppen et al. (2009)	5(12)	CH_3OH, (CO_2, H_2O)	N	N	N	one simulation with larger network
Cazaux et al. (2010)	101	H_2O_2, H_2O, O_3	N	Y	Y	
Das et al. (2010)	10	CH_3OH, H_2O, CO_2	N	N	N	
Das & Chakrabarti (2011)	11	CH_3OH, H_2O, CO_2	N	N	Y	
Marseille & Cazaux (2011)	0	–	I	N	N	water accretion timescale
Chang & Herbst (2012)	29	CH_3OH, H_2O, CO_2, CH_4	Y	N	Y	only photodesorption is included
Meijerink et al. (2012)	101	H_2O_2, H_2O, O_3	I	Y	Y	included in XDR model
Vasyunin & Herbst (2013)		full gas-grain network	Y	N	Y	only layers
Garrod (2013)	5	H_2O				off-lattice model
Lamberts et al. (2014)	21	H_2O	N	N	Y	Chapter 5
Chang & Herbst (2014)	238	CH_3OH, H_2O, CO_2, CH_4, NH_3	Y	N	Y	bulk diffusion

[a] Photodissociation reactions are not included in this count. [b] 'I' stands for Indireclty if the results are later fed to another simulation program treating the gas phase.

energies and hopping barriers change consequently. In diffuse clouds, the desorption and diffusion behavior of the hydrogen atoms is mainly determined by the underlying grain and the interaction between absorbates occurs through reaction. Now, in dense clouds newly formed species determine the binding energy, barriers and reaction possibilities of their neighbors. Many more interaction energies are thus needed to describe the system, because there is not only interaction between the different species with the bare substrate, but also with all other adsorbed species. The problem is that many of these interaction energies are unknown or at best poorly constrained. In Table 3.1 16 KMC studies of interstellar ices are summarized. These treat the ice at least in terms of layers, but often with more microscopic detail.

The various papers are not discussed separately for the sake of brevity, but the reader is rather referred to Chapters 5, 6 and 8 for examples of experimentally benchmarked KMC studies under interstellar conditions.

3.5 NEW DIRECTIONS

As a result of the increased computer power, one can see an increase in complexity of the Monte Carlo models that are being reported.

On the one hand, unified gas-grain models are developed in which the complexity of the chemical network is increased or in which gas and grain surface chemistry are combined. As mentioned in Section 3.2.3, the numerical integrators used for rate equation based models cannot be easily coupled to the Monte Carlo algorithm. Another approach to couple gas-phase chemistry and grain surface chemistry is to use the KMC approach for both phases (Vasyunin et al., 2009; Chang & Herbst, 2012; Chang & Herbst, 2014). Furthermore, a macroscopic KMC model that includes 'microscopic' information is achieved by including layering, where the composition of each layer is followed in time (Vasyunin & Herbst, 2013). Introducing more microscopic-detail into macroscopic models can also be done in a more pragmatic way, where microscopic simulation programs are used and the obtained information is then given to the macroscopic model in terms of lookup tables or fitted analytical expressions (Chang et al., 2006; Meijerink et al., 2012).

On the other hand, more molecular detail is introduced which evolves further in off-lattice KMC models One of the main restrictions of traditional KMC methods is the confinement of the system to a predefined lattice. This restricts the amount of physical detail contained by the simulation and makes the use of realistic interaction potentials far from straightforward. In the solid state, the lattice approximation is often well-justified for simple crystalline systems, but the situation already becomes more complicated for molecular crystals which often show some degree of disorder, like many hydrates and the hydrogen bond network in H_2O ices. Small site-to-site differences in these systems affect the rate constants and make the generation of the table of events a tedious task. For amorphous systems, the situation obviously becomes even worse. A second problem with traditional KMC simulations is the need to define the table of events before the start of the simulation. Ideally, one would like to evaluate every process individually, as accurately as possible. This can be done in off-lattice KMC by applying force fields (Much et al., 2002; Middleton & Wales, 2004; Pedersen et al., 2009; Karssemeijer et al., 2012) or even electronic structure methods (Xu & Henkelman, 2008) to calculate individual process rates. As every process is considered to be unique, this evaluation needs to be done on-the-fly, which considerably increases the computational costs. The advantage of not having any *a priori* assumptions about processes in the system is, however, often worth this additional effort.

The continuum Kinetic Monte Carlo Method (Zhang & Jansen, 2010) is a particularly interesting off-lattice KMC method which incorporates diffusion of particles analyticcally into

a continuous time KMC scheme. Reaction rates and diffusion constants still need to be specified before the simulation starts though. The Adaptive Kinetic Monte Carlo (Henkelman & Jónsson, 2001) method is an on-the-fly, off-lattice, KMC method which allows for very high atomistic detail, requiring no other input than an interatomic interaction potential. The first applications of AKMC in an astrochemical context concern CO and CO_2 diffusion on both hexagonal and amorphous ices (Karssemeijer et al., 2012; Karssemeijer et al., 2014),

Finally, the first off-lattice KMC model of interstellar dust grain surface chemistry (including 5 reactions) has recently been published (Garrod, 2013) able to determine the positions of all surface particles according to local potential minima resulting from the pair-wise interactions between atoms and molecules.

BIBLIOGRAPHY

Abramowitz, M. & Stegun, I. A. 1972, Handbook of Mathematical Functions: with formulas, graphs, and mathematical tables (New York: Dover)
Al-Halabi, A., Fraser, H. J., Kroes, G. J., & van Dishoeck, E. F. 2004, Astron. Astrophys., 422, 777
Al-Halabi, A., Kleyn, A. W., van Dishoeck, E. F., & Kroes, G. J. 2002, J. Phys. Chem. B, 106, 6515
Al-Halabi, A., Kleyn, A. W., van Dishoeck, E. F., van Hemert, M. C., & Kroes, G. J. 2003, J. Phys. Chem. A, 107, 10615
Al-Halabi, A. & van Dishoeck, E. F. 2007, Mon. Not. R. Astron. Soc., 382, 1648
Amiaud, L., Dulieu, F., Fillion, J.-H., Momeni, A., & Lemaire, J. L. 2007, J. Chem. Phys., 127, 144709
Andersson, S., Goumans, T. P. M., & Arnaldsson, A. 2011, Chem. Phys. Lett., 513, 31
Arasa, C., van Hemert, M. C., van Dishoeck, E. F., & Kroes, G. J. 2013, The Journal of Physical Chemistry A, 117, 7064
Barzel, B. & Biham, O. 2007, Astrophys. J. Lett., 658, L37
Barzel, B. & Biham, O. 2011, Phys. Rev. Lett., 106, 150602
Batista, E., Ayotte, P., Bilić, A., Kay, B., & Jónsson, H. 2005, Phys. Rev. Lett., 95, 223201
Batista, E. & Jónsson, H. 2001, Comp. Mat. Sci., 20, 325
Biham, O., Furman, I., Pirronello, V., & Vidali, G. 2001, Astrophys. J., 553, 595
Bortz, A. B., Kalos, M. H., & Lebowitz, J. L. 1975, J. Comp. Phys., 17, 10
Brown, P. D. & Charnley, S. B. 1990, Mon. Not. R. Astron. Soc., 244, 432
Buch, V. & Czerminski, R. 1991, J. Chem. Phys., 95, 6026
Burke, J. R. & Hollenbach, D. J. 1983, Astrophys. J., 265, 223
Caselli, P., Hasegawa, T. I., & Herbst, E. 1998, Astrophys. J., 495, 309
Cazaux, S., Cobut, V., Marseille, M., Spaans, M., & Caselli, P. 2010, Astron. Astrophys., 522, A74
Cazaux, S. & Tielens, A. G. G. M. 2004, Astrophys. J., 604, 222
Chaabouni, H., Bergeron, H., Baouche, S., et al. 2012, Astron. Astrophys., 538, A128
Chang, Q., Cuppen, H. M., & Herbst, E. 2005, Astron. Astrophys., 434, 599
Chang, Q., Cuppen, H. M., & Herbst, E. 2006, Astron. Astrophys., 458, 497
Chang, Q., Cuppen, H. M., & Herbst, E. 2007, Astron. Astrophys., 469, 973
Chang, Q. & Herbst, E. 2012, Astrophys. J., 759, 147
Chang, Q. & Herbst, E. 2014, The Astrophysical Journal, 787, 135
Charnley, S. B. 1998, Astrophys. J. Lett., 509, L121
Charnley, S. B. 2001, Astrophys. J. Lett., 562, L99
Charnley, S. B., Tielens, A. G. G. M., & Rodgers, S. D. 1997, Astrophys. J. Lett., 482, L203
Cuppen, H. M. & Herbst, E. 2005, Mon. Not. R. Astron. Soc., 361, 565
Cuppen, H. M. & Herbst, E. 2007, Astrophys. J., 668, 294
Cuppen, H. M., Ioppolo, S., Romanzin, C., & Linnartz, H. 2010, Phys. Chem. Chem. Phys., 12, 12077
Cuppen, H. M., Morata, O., & Herbst, E. 2006, Mon. Not. R. Astron. Soc., 367, 1757
Cuppen, H. M., van Dishoeck, E. F., Herbst, E., & Tielens, A. G. G. M. 2009, Astron. Astrophys., 508, 275
Das, A., Acharyya, K., & Chakrabarti, S. K. 2010, Mon. Not. R. Astron. Soc., 409, 789
Das, A. & Chakrabarti, S. K. 2011, Mon. Not. R. Astron. Soc., 418, 545
d'Hendecourt, L. B., Allamandola, L. J., & Greenberg, J. M. 1985, Astron. Astrophys., 152, 130
Draine, B. T. 2003, Ann. Rev. Astron. Astrophys., 41, 241
Du, F. & Parise, B. 2011, Astron. Astrophys., 530, A131
Dulieu, F., Congiu, E., Noble, J., et al. 2013, Sci. Reports, 3, 1338
Fedoseev, G., Ioppolo, S., Lamberts, T., et al. 2012, J. Chem. Phys., 137, 054714
Fuchs, G. W., Cuppen, H. M., Ioppolo, S., et al. 2009, Astron. Astrophys., 505, 629
Gardiner, C. W. 1994, Handbook of stochastic methods for physics, chemistry and the natural sciences (Berlin: Springer)
Garrod, R. T. 2008, Astron. Astrophys., 491, 239
Garrod, R. T. 2013, Astrophys. J., 778, 158

Garrod, R. T., Vasyunin, A. I., Semenov, D. A., Wiebe, D. S., & Henning, T. 2009, Astrophys. J. Lett., 700, L43
Garrod, R. T., Wakelam, V., & Herbst, E. 2007, Astron. Astrophys., 467, 1103
Gillespie, D. T. 1992, Markov Processes: An Introduction for Physical Scientists (London: Academic Press Limited)
Goumans, T. P. M., Catlow, C. R. A., & Brown, W. A. 2008, The Journal of Chemical Physics, 128,
Goumans, T. P. M., Catlow, C. R. A., Brown, W. A., Kästner, J., & Sherwood, P. 2009a, Phys. Chem. Chem. Phys., 11, 5431
Goumans, T. P. M., Richard, C., Catlow, A., & Brown, W. A. 2009b, Mon. Not. R. Astron. Soc., 393, 1403
Goumans, T. P. M., Wander, A., Catlow, C. R. A., & Brown, W. A. 2007, Mon. Not. R. Astron. Soc., 382, 1829
Green, N. J. B., Toniazzo, T., Pilling, M. J., et al. 2001, Astron. Astrophys., 375, 1111
Hasegawa, T. I. & Herbst, E. 1993, Mon. Not. R. Astron. Soc., 261, 83
Hasegawa, T. I., Herbst, E., & Leung, C. M. 1992, Astrophys. J. Suppl. Ser., 82, 167
Hassel, G. E., Herbst, E., & Bergin, E. A. 2010, Astron. Astrophys., 515, A66
Henkelman, G. & Jónsson, H. 2001, J. Chem. Phys., 115, 9657
Herbst, E. & Cuppen, H. M. 2006, Proc. Natl. Acad. Sci. USA, 103, 12257
Herbst, E. & Millar, T. J. 2008 (London: Imperial College Press)
Hincelin, U., Chang, Q., & Herbst, E. 2014, ArXiv e-prints
Jansen, A. P. J. 1995, Comp. Phys. Comm., 86, 1
Karssemeijer, L. J., de Wijs, G. A., & Cuppen, H. M. 2014, Physical Chemistry Chemical Physics (Incorporating Faraday Transactions), 16, 15630
Karssemeijer, L. J., Pedersen, A., Jónsson, H., & Cuppen, H. M. 2012, Phys. Chem. Chem. Phys., 14, 10844
Karssemeijer, L. J. & Cuppen, H. M. 2014, å, 569, A107
Katz, N., Furman, I., Biham, O., Pirronello, V., & Vidali, G. 1999, Astrophys. J., 522, 305
Koning, J., Kroes, G. J., & Arasa, C. 2013, The Journal of Chemical Physics, 138,
Lamberts, T., de Vries, X., & Cuppen, H. M. 2014, Far. Disc., 168, 327
Lepetit, B., Lemoine, D., Medina, Z., & Jackson, B. 2011, J. Chem. Phys., 134, 114705
Lipshtat, A. & Biham, O. 2003, Astron. Astrophys., 400, 585
Lipshtat, A. & Biham, O. 2004, Phys. Rev. Lett., 93, 170601
Logan, R. M. & Keck, J. C. 1968, J. Chem. Phys., 49, 860
Marseille, M. G. & Cazaux, S. 2011, Astron. Astrophys., 532, A60
Meijerink, R., Cazaux, S., & Spaans, M. 2012, Astron. Astrophys., 537, A102
Middleton, T. F. & Wales, D. J. 2004, J. Chem. Phys., 120, 8134
Mispelaer, F., Theule, P., Duvernay, F., Roubin, P., & Chiavassa, T. 2012, Astron. Astrophys., 540, A40
Montroll, E. W. & Weiss, G. H. 1965, J. Math. Phys., 6, 167
Much, F., Ahr, M., Biehl, M., & Kinzel, W. 2002, Comp. Phys. Comm., 147, 226
Muralidharan, K., Deymier, P., Stimpfl, M., de Leeuw, N. H., & Drake, M. J. 2008, Icarus, 198, 400
Nordmeyer, T. & Zaera, F. 1991, Chem. Phys. Lett., 183, 195
Nordmeyer, T. & Zaera, F. 1992, J. Chem. Phys., 97, 9345
Oba, Y., Osaka, K., Watanabe, N., Chigai, T., & Kouchi, A. 2014, Far. Disc. , 168, 185
Oba, Y., Watanabe, N., Hama, T., et al. 2012, Astrophys. J., 749, 67
Öberg, K. I., Fayolle, E. C., Cuppen, H. M., van Dishoeck, E. F., & Linnartz, H. 2009a, Astron. Astrophys., 505, 183
Öberg, K. I., Fuchs, G. W., Awad, Z., et al. 2007, Astrophys. J. Lett., 662, L23
Öberg, K. I., Linnartz, H., Visser, R., & van Dishoeck, E. F. 2009b, Astrophys. J., 693, 1209
Öberg, K. I., van Dishoeck, E. F., & Linnartz, H. 2009c, Astron. Astrophys., 496, 281
Pedersen, A., Henkelman, G., Schiøtz, J., & Jónsson, H. 2009, New J. Phys., 11, 073034
Pickles, J. B. & Williams, D. A. 1977, Astrophys. & Space Sci., 52, 443
Pirronello, V., Biham, O., Liu, C., Shen, L., & Vidali, G. 1997a, Astrophys. J. Lett., 483, L131
Pirronello, V., Liu, C., Roser, J. E., & Vidali, G. 1999, Astron. Astrophys., 344, 681
Pirronello, V., Liu, C., Shen, L., & Vidali, G. 1997b, Astrophys. J. Lett., 475, L69

Press, W. H., Teukolsky, S. A., Vetterling, W. T., & Flannery, B. P. 1992 (Cambridge: University Press)
Ruffle, D. P. & Herbst, E. 2001, Mon. Not. R. Astron. Soc., 324, 1054
Shalabiea, O. M. & Greenberg, J. M. 1994, Astron. Astrophys., 290, 266
Stantcheva, T. & Herbst, E. 2004, Astron. Astrophys., 423, 241
Stantcheva, T., Shematovich, V. I., & Herbst, E. 2002, Astron. Astrophys., 391, 1069
Tielens, A. G. G. M. & Hagen, W. 1982, Astron. Astrophys., 114, 245
van Kampen, N. G. 1992, Stochastic Processes in Physics and Chemistry (Amsterdam: Elsevier Science)
Vasyunin, A. I. & Herbst, E. 2013, Astrophys. J., 762, 86
Vasyunin, A. I., Semenov, D. A., Wiebe, D. S., & Henning, T. 2009, Astrophys. J., 691, 1459
Westley, M. S., Baragiola, R. A., Johnson, R. E., & Baratta, G. A. 1995, Planet. Space Sci., 43, 1311
Xu, L. & Henkelman, G. 2008, J. Chem. Phys., 129, 114104
Zhang, X.-Q. & Jansen, A. P. J. 2010, Phys. Rev. E, 82, 046704

4

WATER FORMATION AT LOW TEMPERATURES BY SURFACE O_2 HYDROGENATION – MONTE CARLO SIMULATION

Water is the most abundant molecule found in interstellar icy mantles. In space it is thought to be efficiently formed on the surfaces of dust grains through successive hydrogenation of O, O_2 and O_3. The underlying physico-chemical mechanisms have been studied experimentally in the past decade and in this chapter we extend this work theoretically, using Continuous-Time Random-Walk Monte Carlo, or kinetic Monte Carlo (KMC), simulations to disentangle the different processes at play during hydrogenation of molecular oxygen. KMC offers a kinetic approach to compare simulated surface abundances of different species to the experimental values. For this purpose, the results of four key experiments - sequential hydrogenation as well as co-deposition experiments at 15 and 25 K - are selected that serve as a reference throughout the modeling stage. The aim is to reproduce all four experiments with a single set of parameters. Input for the simulations consists of binding energies as well as reaction barriers (activation energies). In order to understand the influence of the parameters separately, we vary a single process rate at the time. Our main findings are: (i) The key reactions for the hydrogenation route starting from O_2 are H + O_2, H + HO_2, OH + OH, H + H_2O_2, H + OH. (ii) The relatively high experimental abundance of H_2O_2 is due to slow destruction. (iii) The large consumption of O_2 at a temperature of 25 K is due to a high hydrogen diffusion rate. (iv) The diffusion of radicals plays an important role in the full reaction network. The resulting set of 'best fit' parameters is presented and discussed for use in future astrochemical modeling.

T. Lamberts, H. M. Cuppen, S. Ioppolo and H. Linnartz, *Water formation at low temperatures by surface O2 hydrogenation III: Monte Carlo simulation*, Phys. Chem. Chem. Phys., 15 (2013) 8287

4.1 INTRODUCTION

Water is an important molecule in molecular astrophysics and a prerequisite for life on Earth; it controls much of the gas-grain chemical interplay in space and is vital to the formation of more complex molecules as star-formation progresses. For this reason, understanding its fundamental properties is vital to disseminating our knowledge of chemical evolution through star and planet formation, and ultimately of the origin of life itself. Yet it has been a perennial question how water forms under the harsh conditions that govern chemistry in the interstellar medium and which physical and chemical processes are most important.

In dense cold regions of the interstellar medium gas-phase formation routes for H_2O and subsequent freeze-out mechanisms cannot explain the large ice abundances observed. Therefore, it is expected that water is formed on surfaces of cold icy dust grains that act as catalytic sites for molecule formation. Indeed water has been identified as the main component of interstellar ices (Gibb et al., 2000). The first reaction scheme for a grain surface formation route of H_2O was theoretically proposed in 1982 by Tielens and Hagen. This scheme focussed on the hydrogenation of atomic oxygen, molecular oxygen and ozone. At that time, only gas-phase data were available to estimate surface reaction rates. In 2007 Cuppen and Herbst showed in a theoretical study that the solid-state reaction H + OH $\rightarrow$ H_2O likely dominates water formation under diffuse cloud conditions, whereas H_2 + OH $\rightarrow$ H_2O + H is prominent in dark molecular clouds (Cuppen & Herbst, 2007).

To test the surface hydrogenation of O, O_2 and O_3, the proposed reaction routes have been experimentally verified in the past decade (Hiraoka et al., 1998; Dulieu et al., 2010; Miyauchi et al., 2008; Oba et al., 2009; Ioppolo et al., 2010; Cuppen et al., 2010; Mokrane et al., 2009; Romanzin et al., 2011). These experiments provide a more detailed understanding of the reaction network involved in water formation, extending the originally proposed network (Tielens & Hagen, 1982) to that depicted in Fig. 4.1. In particular, water formation at low temperatures by surface O_2 hydrogenation has been studied in depth. Ioppolo *et al.* (Part I, Ref. Ioppolo et al., 2010) and Cuppen *et al.* (Part II, Ref. Cuppen et al., 2010) explored the dependency on a variety of experimental conditions, such as temperature, thickness, H-atom flux, etc.. Different experiments have been performed and constraints on several reaction rates could be determined.

The WISH key programme of the space telescope Herschel has recently made observations of gas phase water and species related to its chemistry in prestellar cores and young stellar objects at different evolutionary stages. Hot gas containing O(I) (Baluteau et al., 1997), O_2 (Larsson et al., 2007), cold H_2O (Hogerheijde et al., 2011), HO_2 (Parise et al., 2012) and H_2O_2 (Bergman et al., 2011) as well as OH, OH^+, H_2O^+ and H_3O^+ have been observed in this context (van Dishoeck et al., 2011). The identification of these molecules is fully consistent with the solid state network that has been derived experimentally.

These experimental results are extended here to KMC simulations to disentangle specific reaction mechanisms and to derive more accurate reaction barriers by comparing laboratory surface abundances with those obtained by simulations. These barriers can then be used as an input for astrochemical models in order to meet observational constraints. We show here that through systematical variation of the many input parameters it is possible to extract information concerning key reactions within the full network.

The manuscript is organized in the following way. Section 4.2 summarizes the key experiments that have been described previously and that are used here as reference for the simulations. Section 4.3 provides the details of the applied KMC method and in Section 4.4 the results are presented and extensively discussed. We conclude with recommendations for fu-

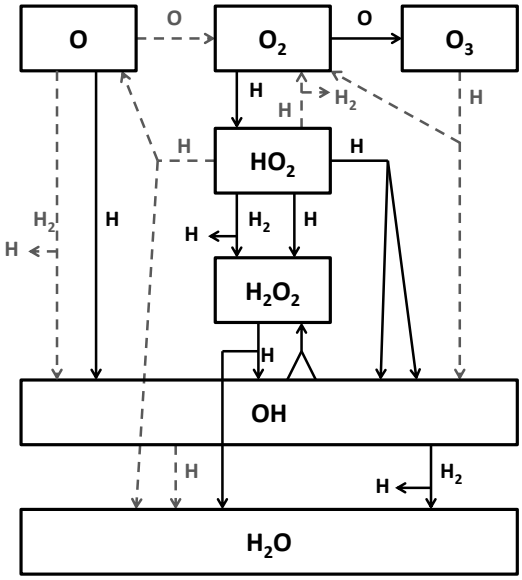

Figure 4.1: A schematic representation of the extended reaction network as obtained in Cuppen et al. (2010). Black, straight lines indicate reactions for which the influence of the barrier is studied here. Grey, dashed lines indicate reactions that are kept constant for all simulations.

ture studies and astrochemical considerations in Section 4.5 as well as with a short summary in Section 4.6.

4.2 EXPERIMENTAL OBSERVATIONS

This section briefly summarizes the previous experimental work that is used here as a starting point. For a detailed description of the used setup, procedures and results we refer to Ioppolo et al. (2008, 2010); Cuppen et al. (2010). Two types of experiments have been performed: sequential hydrogenation of O_2 ice and co-deposition experiments of O_2 molecules and H atoms.

During sequential hydrogenation experiments, an O_2 ice, several monolayers (ML) thick, is first prepared at 15 K and subsequently exposed to hydrogen atoms at various constant ice temperatures. This allows the study of final and stable products of O_2 hydrogenation, i. e., H_2O_2 and H_2O (Fig. 4.1). Quantitative information concerning the surface abundances is obtained by dividing the integrated absorption of a selected infrared band (cm^{-1}) over the so-called band strength (ML/cm^{-1}) as described by Ioppolo et al. (2010). In Part I we showed that during sequential hydrogenation experiments the initial formation rates of H_2O_2 and H_2O are temperature and thickness independent. The final yield, however, does depend on these parameters. Furthermore, due to the competition between reaction of atomic hydrogen with solid oxygen and hydrogen diffusion into the ice, the penetration depth of H atoms was found to span up to 16 ML at 25 K (Ioppolo et al., 2010). We will elaborate on this topic in Section 4.4.3.

Table 4.1: Experimental conditions for the four selected experiments; two sequential hydrogenation and two co-deposition experiments at 15 and 25 K.

	Type	T (K)	H/O_2	H flux (cm^{-2} s^{-1})
1	Seq. hydr.	15	–	2.5×10^{13}
2	Seq. hydr.	25	–	2.5×10^{13}
3	Co-dep.	15	1	2.5×10^{13}
4	Co-dep.	25	1	2.5×10^{13}

During co-deposition experiments, O_2 molecules and H atoms are released onto the cold substrate at the same time and therefore adsorb simultaneously. Different stages of the hydrogenation route, *i.e.*, various reactive intermediates, become experimentally accessible by changing the stoichiometric ratios of O_2 and H (Cuppen et al., 2010) (Fig. 4.1). Due to lacking band strengths for the unstable matrix-isolated reactive intermediates, a quantitative study is not trivial. However, quantification of a single species using the ratio between abundances at different temperatures and/or H/O_2 ratio can be easily performed (Cuppen et al., 2010).

Four of the aforementioned experiments are selected for further comparison to simulated results: sequential hydrogenation and co-deposition experiments both at 15 and 25 K, as listed in Table 4.1. In the following, 15 and 25 K are defined as 'low' and 'high' temperature. These four experiments are considered to be representative for the different experimentally observed features. In Fig. 4.2 the measured surface abundances and integrated absorbances are depicted for the selected sequential hydrogenation and co-deposition experiments. In the following, we consistently separate the discussion between these two types. Important features that need to be reproduced by the MC simulations, are summarized below.

Sequential hydrogenation:

- Evolution of the H_2O_2 abundance in time with a sharp transition between the initial (T-independent) linear and final steady state (T-dependent) regime,
- Increase of the final H_2O_2 production by a factor ~7 between 15 and 25 K, and
- Similar behaviour of the H_2O abundance for both temperatures.

Co-deposition:

- Linearly increasing behaviour of all abundances with time at $t_{exp} < 60$ min,
- Decrease of HO_2 and OH abundances between 15 and 25 K,
- Increase of H_2O_2 abundance between 15 and 25 K,
- Low to zero production of H_2O, and
- Constant ratio of OH/H_2O_2.

It should be noted that the uncertainty of the band strengths is estimated to be within 50% and this affects the accuracy with which the experimental surface abundances can be determined.

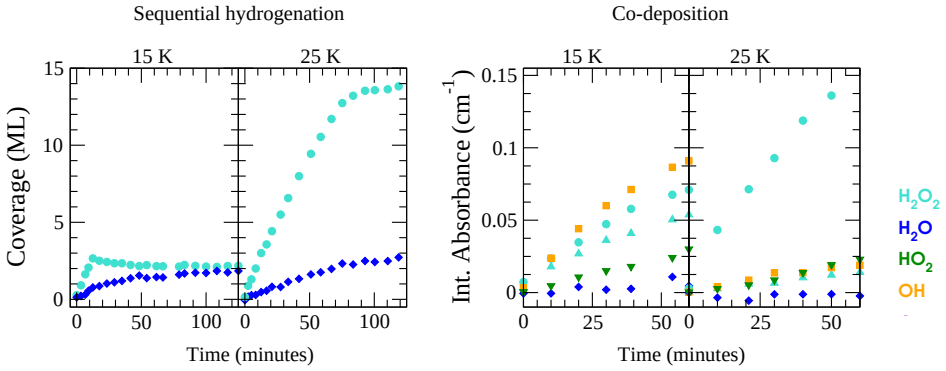

Figure 4.2: Evolution of the experimental surface abundance of O_2 (red), H_2O_2 (light blue), H_2O (dark blue), HO_2 (green), OH (orange) and O_3 (violet) as a function of time for a sequential hydrogenation simulation (left) and a co-deposition simulation (right) at 15 and 25 K.

4.3 THE MONTE CARLO METHOD

This section describes the general Continuous-Time Random-Walk Monte Carlo method used for the simulations, discussing sequentially the simulation of O_2 deposition, the hydrogenation of O_2 ice and the different parameters used for a co-deposition simulation. Subsequently, distinct details of the program are addressed. For a more detailed overview the reader is referred to Chang et al. (2005). The present results are obtained with the program described by Cuppen & Herbst (2007), which has been extended to account for the specific characteristics needed here. The reproducibility of the simulations is monitored by performing each of the standard simulations (see below) three times using different seeds. Standard deviations have typical values of $< 5\%$ for abundant species (*e.g.*, O_2, H_2O_2), $< 10\%$ for less abundant species (*e.g.*, OH) and $< 40\%$ for O_3.

4.3.1 *Deposition of an O_2 surface*

During the deposition phase the O_2 ice is formed starting from a bare surface; the surface used to mimic the experimental gold substrate has a smooth topology and is 2.5% of that depicted in Fig. 1(c) from Cuppen & Herbst (2005). The simulation then starts by the addition of an O_2 molecule to the surface. This occurs at time

$$t_{\mathrm{deposition,O_2}} = \frac{\rho \ln(X)}{F_{O_2}} + t_{\mathrm{current}} \tag{29}$$

where ρ is the surface site density (1×10^{15} sites cm^{-2}), F_{O_2} is the flux of O_2 molecules, X is a random number between 0 and 1, and t_{current} is the current time which is set to 0 at the beginning of the simulation. During the following Monte Carlo cycles a competition between hopping and desorption of the molecules on the surface and deposition of new molecules determines the sequence of events. This sequence is determined by the time at which each event occurs and given by

$$t_{\mathrm{event}} = \frac{\ln(X')}{R_{\mathrm{hop}} + R_{\mathrm{des}}} + t_{\mathrm{current}} \tag{30}$$

where X' is again a random number, and R_{hop} and R_{des} are, respectively, the rates for hopping and desorption to occur. Both rates are assumed to be thermally activated according to

$$R = \nu \exp\left(-\frac{E_{a,Y}}{T}\right) \tag{31}$$

with E_a, Y the activation energy (or barrier) for process Y in Kelvin and ν the pre-exponential factor, which is approximated by the standard value for physisorbed species, $\frac{kT}{h} \sim 10^{12}$ s^{-1}. This factor can be seen as a trial frequency for attempting a new event.

The total binding energy, $E_{tot,bind}$, for each molecule to a site is calculated by additive contributions of its neighbours. Table 4.2 shows the single binding energy values, E, used throughout this chapter. Each species in the lattice has 6 neighbours and 12 nearest neighbours. Nearest neighbours add a contribution of E and next-nearest neighbours of E/8. The latter takes into account the difference in distance of a factor $\sqrt{2}$ and makes use of a distance dependency of $[r^{-6}]$. The neighbour below the particle adds a double contribution (2E) mimicking longer range interactions from the bulk ice layer. Binding energies are typically obtained from desorption barriers determined through so-called Temperature Programmed Desorption (TPD) experiments. These experiments can be reproduced with Monte Carlo simulations when an average number of 0.8 lateral nearest neighbours is taken into account. The single binding energy value, E, is then obtained by dividing the desorption energy by a factor 3.8 (Unpublished work). Note that an order of magnitude difference is applied in binding energy to small molecules (H, H_2 and O) and H_2O like molecules (all the rest). For example, the binding energy of a hydrogen atom binding to a flat surface of O_2 molecules corresponds to the number of neighbours times the contribution: $1 \cdot 2 \cdot 66 + 4 \cdot 2 \cdot 66/8 = 198$ K. Binding to a surface of H_2 molecules yields 19.8 K.

The barrier for hopping from site i to j is given by

$$E_{a,hop}(i,j) = \xi E d^2 + \frac{\Delta E_{bind}(i,j)}{2}, \tag{32}$$

where ξ is an adjustable parameter to change the diffusion, E the single binding energy values, d is the distance between the sites and $\Delta E_{bind}(i,j)$ is the difference in total binding energy between the two sites. This equation is derived from Eq. 10 in Kang & Weinberg (1989). The first term represents the diffusion barrier for equal total binding energies of the sites, while the second ensures microscopic reversibility. Only hopping events between nearest neighbours and next-nearest neighbours are considered.

The barrier for desorption is determined only by $E_{tot,bind}$. Note that the single binding energy value of OH is much smaller than that of H_2O. This will be briefly discussed in Section 4.4.2.3, where the low binding energy is associated with a high diffusion rate.

A total of 10 ML of O_2 is eventually simulated to deposit on top of the bare surface. This results in a smooth ice surface according to the definition from Cuppen & Herbst (2005). In order to compare the results of the different sequential hydrogenation simulations, the same oxygen surface is used for all simulations, except for those that investigate the influence of surface roughness and thickness.

4.3.2 *Sequential hydrogenation*

After deposition of O_2 molecules, the surface is exposed to H atoms and H_2 molecules in a similar manner as before, except that now also reactions can occur and new species are formed. The flux of H atoms and H_2 molecules is set to $S \cdot 2.5 \times 10^{13}$ particles cm^{-2} s^{-1}

Table 4.2: Single binding energy values of a species to one surface site, E, as implemented in the simulations.

Species	H	H_2	O_2	OH	HO_2	H_2O_2	H_2O	O	O_2
E (K)	66	53	240	105	630	1370	1260	260	630

for both species, where the sticking coefficient S equals 0.2. The reaction rates are calculated by using reaction activation energies (or reaction barriers) in Eq. 31 and are listed in Table 4.3. The reaction rates represent the competition between different reactions and therefore the ratio between the rates is used for future reference. Temperature independent reactions are those that have a low to zero barrier. The temperature dependence for the remaining reactions arises from a combination of thermally activated processes and tunneling, *i.e.*, reactions always occur at a higher rate for higher temperatures, not entirely according to Eq. 31, but rather scaling the rates by an arbitrary factor to account for tunneling. Note that tunneling is thus not explicitly included.

Although many reactions leave the products with a large excess energy, this energy is thought to be efficiently dissipated into the ice surface on picosecond timescales, which we conclude from preliminary Molecular Dynamics simulations. Furthermore, in the laboratory the He cryostat provides a suitable dissipation path, while in the interstellar medium the time scales allow thermalization. Since the amount of energy remaining in the molecule does not seem to correlate with the amount of initial excess energy, we include an arbitrary, small excess energy of only 100 K for each reaction product in our model. This excess energy can be applied to overcome barriers for reaction, desorption and/or diffusion. In this way, a chemical desorption mechanism, like the one proposed in Garrod *et al.*, is implicitly included (Garrod et al., 2007). A more accurate implementation of the excess energy, for instance an energy dependence on the exothermicity of a specific reaction, is subject of future studies. Diffusion reduces the excess energy by an arbitrary factor 1.6 for each hop. Furthermore, after 10^{-8} s, the local temperature of the excited species is set back to the temperature of the surface. This is based on the assumption that a molecule on the surface will be thermalized after 10 ns. This rather subjective choice of time scale does not affect the outcome of the simulations, since we find that hot species either react immediately to form a new molecule or remain in their initial configuration for times much longer than 10^{-8} s.

The rates listed in Table 4.3 are explicitly for thermalized reactions only. Consider a hydrogen atom at room temperature (300 K) that lands atop the O_2 surface with a temperature of 15 K. We assume that half of the energy ($\frac{1}{2} \times (300 + 15)$) is immediately dissipated into the surface, leaving the atom with a local temperature of 157.5 K. This energy is dissipated either slowly through hopping or through an immediate step function after 10^{-8} s. All reactions that take place before thermalization have a much higher probability of occurence, according to Eq. 31. This is indeed the case for all reactions with a barrier. The thermalization effect is most pronounced at early times during the simulation, when the surface is not yet filled with molecules preventing fast reactions. Take for example a surface where H_2O has already formed; hydrogen atoms landing on a site next to H_2O are forced to hop in order to meet a reaction partner, thereby losing their energy. The effect is much stronger at 15 K, where the competition between the different processes is small, mainly because the rates are less close to the trial frequency. For instance, for the reaction H + H_2O_2 $\rightarrow$ H_2O + OH, the difference between the hot mechanism and the thermalized reaction is a factor

Table 4.3: List of water formation surface reactions with the used rates for thermalized reactions.

Reaction				R [a] (s^{-1})	R^{high} [b] (s^{-1})	R^{low} [b] (s^{-1})			
Temperature-independent reactions									
H	+ H	→ H_2		1.0×10^{12}					
H	+ O_2	→ HO_2		1.1×10^{5}	6.1×10^{6}	2.1×10^{3}			
H	+ HO_2	→ products		1.0×10^{12}					
		OH	+ OH[c]	56%	91%				
		H_2O_2[c]		35%	0%				
		H_2	+ O_2[c]	2.0%	2.0%				
		H_2O	+ O[c]	7.0%	7.0%				
H	+ O	→ OH		1.0×10^{12}					
O	+ O	→ O_2		1.0×10^{12}					
H	+ O_3	→ O_2	+ OH	1.1×10^{5}					
H	+ OH	→ H_2O		1.1×10^{5}	1.0×10^{12}	2.6			
Temperature-dependent reactions									
				15 K	25 K	15 K	25 K	15 K	25 K
H	+ H_2O_2	→ H_2O	+ OH	6.9×10^{-12}	1.9×10^{-10}	2.6	1.4×10^{1}	1.1×10^{-17}	7.9×10^{-16}
H_2	+ O	→ OH	+ H	2.3×10^{-80}	1.0×10^{-43}				
H_2	+ HO_2	→ H_2O_2	+ H	1.7×10^{-133}	1.4×10^{-75}	1.1×10^{-17}	4.2×10^{-6}		
H_2	+ OH	→ H_2O	+ H	3.3×10^{-3}	1.2×10^{2}	2.1×10^{3}	4.6×10^{3}	6.9×10^{-12}	5.8×10^{-11}
OH	+ OH	→ products		4.2×10^{-6}	1.2×10^{2}	2.1×10^{3}	1.1×10^{5}	8.8×10^{-15}	1.4×10^{-9}
		H_2O_2[d]		100%	100%	90%	90%	75%	75%
		H_2O	+ O[d]	0%	0%	10%	10%	25%	25%
O	+ O_2	→ O_3		3.3×10^{-3}	2.1×10^{3}	1.0×10^{12}	1.0×10^{12}	6.9×10^{-12}	1.3×10^{-2}

NOTE: Rates indicated in GRAY should be used with care, see text.

[a] Standard values used throughout the chapter. [b] Values used to test the effect of the reaction barrier on the overall performance.[c] Total rate of 1.0×10^{12} s^{-1} for H + HO_2. Individual channels are corrected for their branching ratios. [d] Total rate of 4.2×10^{-6} or 1.2×10^{2} s^{-1} for 15 and 25 K, respectively. Individual channels are corrected for their branching ratios.

of $\frac{e^{-E_{a,reaction}/\frac{1}{2}\cdot(300+15)}}{e^{-E_{a,reaction}/15}} \approx 10^{21}$. Reactions that occur easily in the experiment, are therefore not neccessarily accessible under conditions resembling the darker regions of the interstellar medium.

Finally, in this chapter we only consider physisorbed hydrogen atoms, both on the surface as well as trapped in pores. The solid phase interactions are incorporated indirectly through positioning of the hydrogen atoms on the surface and accounting for the binding energy at a specific lattice site. If a species has more neighbours, the cumulative binding energy increases. Furthermore, the effect of the surroundings on the reaction itself is included in the barrier. In this way, a stabilizing effect through for instance hydrogen bonding of a neighboring species is not included explicitly as is the case when real potentials are used. Rather a change to the activation energy is applied. In Section 4.4.2.7 we will briefly talk about the possibility to explicitly incorporate solid state effects involving H atoms.

4.3.3 *Co-deposition*

During a co-deposition simulation, H, H_2 and O_2 all settle on the bare ('gold') surface simultaneously, after which their possible events are determined and evaluated again using the Arrhenius behaviour. Reactions can thus take place from the start. The individual deposition rate of O_2, H and H_2 is set to be 2.5×10^{13}, 5×10^{12} and 5×10^{12} particles cm^{-2} s^{-1}, repectively, assuming again a 1:1 ratio between H and H_2. The sticking coefficient S is thus already accounted for in the fluxes: $S_{H_{(2)}}/S_{O_2} = 0.2$.

4.3.4 *Size and ice morphology*

We use a lattice-gas model, where the lattice surface consists of 50×50 sites. This is large enough to overcome the finite size limit, which is set by the rate of atomic hydrogen desorption, as outlined by Chang et al. (2005). Larger lattices would result in computationally too expensive simulations. We performed one simulation using standard parameters (see below) on a surface of 100×100 sites as a check and found no difference with respect to the smaller surface.

Although experimental surfaces are probably amorphous, the adsorption sites will be clearly defined and likely distributed with some kind of order in terms of number of neighbours. A lattice-gas model can thus be seen as a grid of potential wells, and a process results in a change of the occupancy of the lattice sites. The largest advantage of using a lattice-gas model is the reduction of computational costs as result of working with a predefined event table. Since the molecules are confined to a lattice, only a fixed amount of processes can occur and large time scales can be simulated. The disadvantage is that the level of molecular detail is limited and some mechanisms are not included. These types of models have, however, demonstrated how powerful they can be in mimicking ice chemistry, covering hours of simulated time (Fuchs et al., 2009; Cazaux et al., 2010).

To account for the penetration of H atoms observed experimentally, small species (i. e., H, H_2, OH and O) are allowed to diffuse to interstitial sites in the oxygen ice. For this purpose each monolayer in the ice is represented by two fields in the matrix that holds the ice; one can hold all species present in the simulations, the other contains mainly small species. The diffusion only takes place when an O_2 or a HO_2 molecule is atop the final position, since penetration in water-like structures has not been observed experimentally. Larger species can be present in the intermediate layer, though, as a result of the positioning of reaction products.

4.4 RESULTS AND DISCUSSION

In this section we present and discuss Monte Carlo simulations of the four experiments listed in Table 4.1. The reaction input parameters for these simulations are given in Table 4.3. The second column indicates the settings used for the so-called *standard simulations (*R*).* These are based on *ab initio* barriers, experimental constraints or other models and represent the starting point for optimization. Subsequently, for each reaction with a barrier, this activation energy E_a is either increased or decreased after which the effect of the reaction on the final result is studied. The reaction rates are listed in the third and fourth column of Table 4.3. Note that while changing a rate, all other parameters are kept constant. Decreasing or increasing the reaction rates in a systematic way forms the core of this chapter and is described in Section 4.4.2. The final goal is to see whether these variations bring us closer to the experimental results, simultaneously providing insight in the underlying molecular mechanism. Furthermore, we hope to obtain information on the sensitivity of the system on a specific reaction, *i.e.*, information on the error bar of the barrier. Besides studying the chemistry itself, we also investigate the effect of the diffusion barrier of H and O_2 as well as the effect of the interstitial positioning.

We first discuss the standard simulations and then how the different input parameters affect the production of various species. The simulations are then compared with the experimental results by using the time evolution of the surface abundances of the molecular species, *i.e.*, comparing the simulated trends to the experimental findings shown in Fig. 4.2. For the sequential hydrogenation experiments, the observations are not only based on the absolute abundances, but also take into account the ratio between H_2O and H_2O_2 as well as trends in the time evolution. For the co-deposition experiments, accurate band strengths are not available. Therefore, the approximation is made that each hydroxyl group contributes equally strong to the OH-stretching and bending vibrations, which allows for an estimation of the relative band strengths and therefore relative abundances. To strengthen this analysis, we performed simulations for selected sets of parameters for a H/O_2 ratio of 2. This way, we can compare the molecular abundances between different experiments using infrared features. Furthermore, the OH/H_2O_2 ratio is studied, following the conclusion from Cuppen et al. (2010) that their abundances are correlated. To study the temperature dependence, experiments and simulations are compared at 15 and 25 K. Finally, the effect of the ice structure and the experimentally observed penetration depth is discussed.

4.4.1 *Standard simulations*

4.4.1.1 *Ice structure.*

Figures 4.3 and 4.4 show cross sections of the simulated ice mantle at the end of a simulation for the four different conditions using the standard settings. The colour coding indicates the different molecular species. Each square represents one molecule or atom. The black squares on the bottom represent the initial substrate on which the O_2 ice (red) is deposited. H and H_2 can diffuse into the ice at interstitial positions (intermediate white rows) and form new species there. The sequential O_2 hydrogenation cross sections (Fig. 4.3) show that the penetration of the H atoms at 15 K is less than at 25 K where some hydrogenation has occurred even at the deepest layers. Indeed a larger penetration depth is required to reproduce the 25 K experimental results. The final ice structure at high temperature is more irregular with respect to that at low temperature. Pores (or empty sites) are formed upon reaction in the original O_2 structure. This, combined with the temperature effect of Eq. 31 allows for easier hydrogen

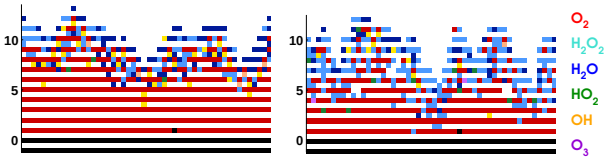

15 K 25 K

Figure 4.3: A cross section of the simulated ice mantle for a hydrogenation simulation of predeposited solid O_2 at 15 K (left) and 25 K (right). Standard values are used for the reaction rates. O_2 is represented by red, H_2O_2 by light blue, H_2O by dark blue, HO_2 by green, OH by orange and O_3 by violet.

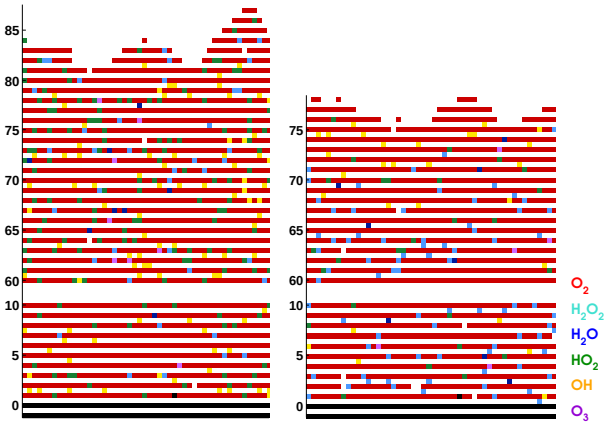

15 K 25 K

Figure 4.4: Similar to Fig. 4.3 for co-deposition simulations. For reasons of clarity, the center 50 ML of the matrix are omitted from the surface.

diffusion. Moreover, at 15 K the top of the surface has been hydrogenated to water almost entirely whereas at 25 K some H_2O_2 in the top layer is still available for hydrogenation.

For the co-deposition simulations (Fig. 4.4), the resulting ice mantle consists mainly of O_2 with other species embedded in the O_2 matrix. The top 5 ML of the matrix have a different composition than the lower layers because the hydrogen atoms landing on the surface can still penetrate some of the ice and induce further reactions. The main difference between the 15 and 25 K ice mantles is in the amount of HO_2 and OH versus H_2O_2. At 25 K most of the small species have reacted further as a result of the higher mobility of H and OH. Finally, the total mantle thickness for a higher temperature is smaller as a result of the higher O_2 desorption probability. The thermal desorption value of pure O_2 ice has been experimentally determined as 31 K (Fuchs et al., 2006; Acharyya et al., 2007).

4.4.1.2 *Time evolution of the surface abundance.*

The solid curves in each of the panels of Figs. 4.5 and 4.6 represent the time evolution of a specific molecular species with respect to the initial conditions before hydrogenation for the standard simulations. In Fig. 4.5 the sequential hydrogenation and in Fig. 4.6 the co-deposition

Table 4.4: Experimental and simulated relative surface abundances.

	T = 15 → 25 K H/O_2 =1		T = 15 → 25 K H/O_2 = 2		T = 15 K H/O_2 = 1 → 2		T = 25 K H/O_2 = 1 → 2	
	Exp.	Sim.	Exp.	Sim.	Exp.	Sim.	Exp.	Sim.
H_2O_2 bulk	↑↑	↑	↑↑	↑	↑	↑	–	↑
H_2O_2 isol.	↓	↓	↓↓	↓	↓	–	↓	↓
HO_2 isol.	↓	↓↓	↑	↓↓	↓	↓	↓	↓
OH isol.	↓↓	↓↓	↓↓	↓↓	↓	↑	↓	↓

Note. Arrows indicate the effect on the molecular surface abundances for an increase in temperature (column two and three) or H/O_2 ratio (last two columns). A double arrow represents a large increase (up) or decrease (down), a single arrow a small increase (decrease) and a hyphen no change.

simulations are shown. The O_2 molecules are consumed and the time evolutions in Fig. 4.5 (red) are therefore negative. O_2 cannot be spectroscopically observed unless it is abundantly mixed with other species since it is infrared inactive. All other species are formed in the process. Note the differences in the vertical scales in Fig. 4.5 between 15 and 25 K as well as between Figs. 4.5 and 4.6.

From these figures we can conclude that the trends in the time evolution of water and hydrogen peroxide surface abundances are in good qualitative agreement with the experimental data. Like for the experimental results (Fig. 4.2), the initial increase in H_2O_2 abundance is similar at low and high temperature and there is a clear transition between the linear increase and final steady state behaviour for sequential hydrogenation simulations. The slight decrease before reaching the steady state for the H_2O_2 signal at 15 K is also reproduced by the standard model. The experimental transition is sharper than the simulated one and the level of the steady state at 25 K is much higher (14 ML vs. 4 ML). The H_2O production at 15 and 25 K follows roughly the same behaviour and the curve shape agrees with the experimental one as well. The H_2O abundance is slightly higher for lower temperature and as a result the H_2O/H_2O_2 ratio is overestimated. During experiments the abundance of O_3 stays below the detection limit and this is in agreement with the low value of the simulated abundances.

The molecular time evolution for the co-deposition simulations is plotted as a solid curve in Fig. 4.6. The final O_2 thickness is of the order of 80 ML, which is beyond the dynamic range of the panels (see also Fig. 4.4). At later times some O_2 is observed experimentally only at 15 K for H-atom rich conditions. The simulations confirm this trend, since the final O_2 abundance at 15 K is higher than at 25 K. The abundance of most species increases linearly in time except for HO_2 which slowly levels off. These abundances are compared to the linear experimental regime ($t < 60$ minutes) where H_2O_2 and OH have not yet reached steady state. H_2O and O_3 remain below the IR detection limit in the experiments and simulated abundances are correspondingly low. From the comparison of the bending and stretching vibration modes it seems that the simulations overproduce the intermediate species HO_2 for both temperatures. This can partially be explained by the hydrogen diffusion rate incorporated in the standard simulations. A higher mobility would allow hydrogen to scan both a larger surface area and bulk volume, hence allowing for the reaction H + HO_2 to take place more often. The dependence of the molecular surface abundances on both temperature and H/O_2 ratio is summarized in Table 4.4. The comparison with the experimental data is also shown and for H_2O_2 a good

agreement is found. The arrows show the influence of increasing temperature or H/O_2 ratio on the amount of species formed. Indeed, the HO_2 and OH production decreases at higher temperature, whereas for H_2O_2 it increases. The OH/H_2O_2 ratio stays equal throughout a single simulation, in accordance with the experiments. From the above, it appears that the main inconsistencies are caused by radical species. The dynamics of these species is not fully understood, but one should keep in mind the experimental error bars involved in this analysis, as stated in Section 4.2.

4.4.2 *Key reactions*

The investigation of the reaction rates is done by varying one reaction barrier at a time with respect to the standard values as indicated in Table 4.3. Figs. 4.5 and 4.6 show the resulting time evolution of the surface abundances. The procedure adopted is as follows: if the difference between a given simulation and the standard simulation is larger than the derived standard deviation, it is considered to be a strong effect. The reactions that exhibit the largest effect upon changing their corresponding barriers, are:

$$H + O_2 \rightarrow HO_2 \tag{R1}$$
$$H + HO_2 \rightarrow \text{products} \tag{R2}$$
$$OH + OH \rightarrow \text{products} \tag{R3}$$
$$H + H_2O_2 \rightarrow H_2O + OH \tag{R4}$$
$$H + OH \rightarrow H_2O\,. \tag{R5}$$

The implications of these reactions, along with those of reactions with H_2, are discussed in the sections below. For reasons of brevity, we will comment only on features that distinctly differ from those in the standard simulations.

4.4.2.1 *H + O_2.*

Since the reaction H + O_2 is the start of the hydrogenation pathway, changing its rate affects the full reaction scheme. In the gas phase the barrier of the reaction depends on the incoming angle of the molecule (Walch & Duchovic, 1991) and a change in the rate can thus be interpreted as a change in the fraction of successful approaches.

In general an increase in the rate results in a different competition between the first reaction in the scheme (Fig. 4.1), H + O_2, and the follow-up reactions. For a higher rate, more HO_2 and subsequently more H_2O_2 is formed. Therefore, less hydrogen atoms are available for other reactions and the formation yields of those products indeed decrease. The lower rate results in more reactions that occur 'deeper' in the reaction network, enhancing for instance H + OH $\rightarrow$ H_2O.

Since the O_2 molecules in the pre-deposited oxygen layers probably have some preferred orientation (local crystallinity), the H atoms approach them under the same angle when penetrating the ice. This is reflected by a certain barrier. For co-deposition experiments, the angle dependence is of less physical importance since the oxygen beam provides O_2 molecules with a range of different orientations at the surface. This means that there are more molecules available for a reaction pathway with a lower barrier. Since in the Monte Carlo simulations the ice geometry is not explicitly taken into account, the barrier can be lowered for co-deposition simulations.

The back reaction (R6) is also allowed in the simulations with a rate of 2×10^{-4} s^{-1}

$$HO_2 \rightarrow H + O_2\,. \tag{R6}$$

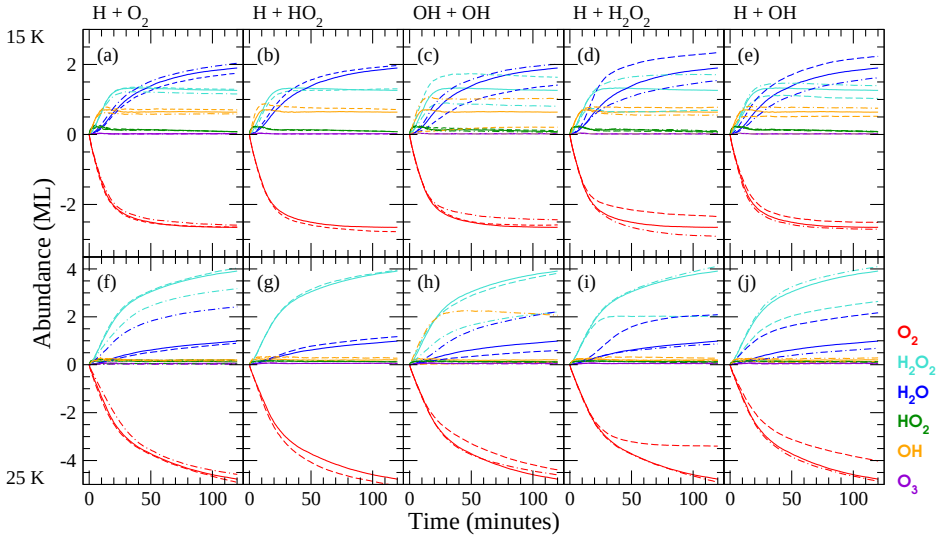

Figure 4.5: Evolution of the surface abundance of O_2 (red), H_2O_2 (light blue), H_2O (dark blue), HO_2 (green), OH (orange) and O_3 (violet) as a function of time for a hydrogenation simulation of predeposited solid O_2 for the five key reactions at 15 K ((a)-(e)) and 25 K ((f)-(j)). Solid curves represent simulation results with the standard value, dashed curves with lower barrier (higher rate), and dash-dotted curves with higher barrier (lower rate).

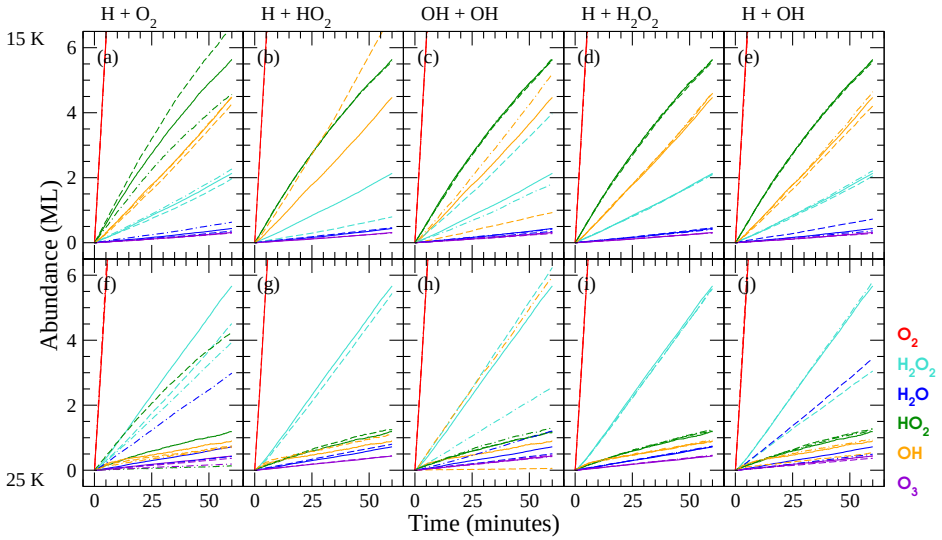

Figure 4.6: Evolution of the surface abundances, as for Fig. 4.5, but applied to the co-deposition simulations.

4.4.2.2 *H + HO_2 branching ratio.*

For the reaction H + HO_2, not the rate, but the branching ratio for the product channels OH + OH and H_2O_2 is varied.

$$H + HO_2 \rightarrow OH + OH \quad \text{(R2a)}$$
$$H + HO_2 \rightarrow H_2O_2 \quad \text{(R2b)}$$
$$H + HO_2 \rightarrow H_2 + O_2 \quad \text{(R2c)}$$
$$H + HO_2 \rightarrow H_2O + O \quad \text{(R2d)}$$

For the analogous gas-phase reaction, H_2O_2 is typically not found as a final product since there is no third body to remove the excess energy (Keyser, 1986; Mousavipour & Saheb, 2007). Since experimentally OH and H_2O_2 were found to behave similarly, a common formation route was suggested (Cuppen et al., 2010). In the standard case, (R2a):(R2b):(R2c):(R2d) is 56:35:2:7. It is found that for a ratio of 91:0:2:7 H_2O_2 is only being indirectly formed by the consecutive reaction of OH + OH $\rightarrow$ H_2O_2.

The latter branching ratio leads to a more open ice structure for the sequential simulations; the regularity of the O_2 matrix is destroyed. This is because HO_2 will split into two species which will take up interstitial space and distort the ice structure. Two OH radicals can then react again to H_2O_2 which forms additional pores. A more open ice structure allows H atoms to penetrate deeper in the ice layers and thus more reactions can take place.

In the co-deposition experiments the changed branching ratio is reflected in the ratio OH/H_2O_2 at 15 K. At 25 K most of the formed OH immediately reacts to H_2O_2 and little to no difference is observed in the final abundances. In the experiments approximately 3 times more OH is formed than H_2O_2 at low temperature. In the simulations this is a factor 2 for the standard simulations and 9 for the changed branching ratio. The real branching ratio is therefore probably in between the two adopted values. This value can only be quantitatively constrained in combination with the reaction rate of OH + OH $\rightarrow$ H_2O_2, that is discussed in the following subsection.

4.4.2.3 *OH + OH.*

Branching ratio.
The competing reactions (R3a) and (R3b) have reaction enthalpies of -210 and -70 kJ/mol, respectively, and have small to zero gas-phase reaction barriers (Atkinson et al., 2004)

$$OH + OH \rightarrow H_2O_2 \quad \text{(R3a)}$$
$$OH + OH \rightarrow H_2O + O\,. \quad \text{(R3b)}$$

The results from the simulations are trivial in the sense that an increase in the fraction of reaction (R3b) results in an increase of the H_2O and O_3 and a decrease in H_2O_2 abundances for all parameter settings.

Using a non-zero contribution of reaction (R3b), we are able to correctly reproduce the trend in H_2O abundance at 25 K for sequential hydrogenation, in particular the initial rise. Based on the small abundance of O_3 found in the experiments, we expect that reaction (R3a) is strongly favoured, which is reflected by a branching ratio of (R3a):(R3b) = 90:10.

Diffusion and reaction.
Since OH is formed through the same reaction as H_2O_2 but can still be detected in the ice, there must exist a mechanism that prohibits recombination to peroxide.

Experimentally, OH is only observed during co-deposition where it eventually freezes out in the O_2 matrix. When two OH radicals are formed from the reaction H + HO_2 the excess energy of the reaction allows the radicals to move away from each other on the surface just before thermalizing and subsequently freezing out in the matrix. Diffusion of thermalized OH at a later stage is not expected. If (R3) takes place, it immediately follows reaction (R2). This makes the two reactions hard to constrain separately.

To model the possibility of two products separating upon reaction is non-trivial, due to the lack of directionality in our simulations, *i.e.*, a high diffusion rate allows fast hopping in all directions, both back and forth. This would allow two species to separate quickly followed by a fast recombination as a result of hopping back. To prevent recombination, we introduce a relatively high diffusion rate and, contrary to current gas-phase studies, an effective barrier for the reaction OH + OH $\rightarrow$ H_2O_2. Different barrier heights are used for the reactions at 15 and 25 K in order to reproduce the experimental features.

The rate of this reaction has a strong effect on the appearance of the ice in the sequential simulations. For a high rate, H_2O_2 is formed both at the surface and deep in the ice and the small amount of OH resides in the top layers. For a low rate, a layer of H_2O covers the surface and OH occupies a large fraction of interstitial positions in the top layers of the matrix. For both the sequential and co-deposition simulations the OH/H_2O_2 ratio decreases with increasing reaction rate. The decrease in OH also has an effect on the final H_2O yield which decreases as well.

The intermediate reaction rate employed in the standard simulations reproduces the experiments best. The high rate reproduces the sequential simulations but overproduces H_2O_2 in the co-deposition simulations and the low rate overproduces OH in the sequential simulations but is in better agreement with the co-deposition experiment. As mentioned above, the exact rate can only be determined considering multiple input parameters of which the OH diffusion and the H + HO_2 branching ratio are the most important.

Note, however, that OH diffusion inside the pre-deposited O_2 matrix is not likely. Therefore, in reality the OH fragments formed during sequential hydrogenation will react and the H_2O_2 abundance correspondingly increases whereas the H_2O abundance decreases. Indeed, this corresponds with a scenario where the H_2O/H_2O_2 fraction gets closer to the experimental value.

4.4.2.4 *H + H_2O_2.*

H_2O production can proceed through various reactions, of which H + H_2O_2 is a special case as a result of the high barrier associated with it. Gas-phase calculations suggest a barrier of approximately 2000 K (Koussa et al., 2006). The barriers used in our simulations are considerably lower since we include a tunneling contribution as suggested by Miyauchi et al. (2008).

In general the H_2O/H_2O_2 ratio increases with increasing rate. In the sequential simulations this mainly occurs at later times, at the expense of H_2O_2 of which the abundance declines in time. By increasing the H + H_2O_2 reaction rate, more H atoms are consumed in this reaction on top of the surface; less of the initial O_2 is thus affected upon hydrogenation. A decrease in the rate allows for the build-up of hydrogen peroxide and therefore a more correct ratio with respect to H_2O at 15 K. However, the leveling off of the peroxide signal occurs at later times, contrary to the sharp transition observed experimentally.

For the co-deposition simulations, H_2O is predominantly formed through (R2d) and (R3b) and the change in H + H_2O_2 reaction rate only has an effect upon significant decrease of the barrier. The latter, however, results in an overestimation of H_2O.

Additional simulations are performed to focus only on the H + H_2O_2 reaction. A surface consisting only of H_2O_2 molecules (20 K) is used on top of which H and H_2 (300 K) are de-

posited. Using a reaction barrier of 1000 K indeed results in a reasonable correspondence to the hydrogenation experiment performed by Cuppen et al. (2010). However, on closer inspection of the dynamics, it becomes clear that all reactions between hydrogen and peroxide occur through the hot mechanism. We therefore expect this reaction to be rather inefficient in the dense interstellar medium.

4.4.2.5 *H + OH.*

The reaction H + OH is barrierless, but with a very large excess energy of more than 5 eV. The dissipation of this energy with only one reaction product, H_2O, might be problematic, although some of the excess energy is probably absorbed by the ice surface. Changing the rate of this barrierless reaction, should therefore be interpreted as changing the efficiency by which the excess energy of this reaction can be dissipated. For a more in depth discussion see Romanzin et al. (2011).

An increase in rate leads to a higher water production. At the same time the production of H_2O_2 goes down since less OH is available for its formation. The low and intermediate rate results appear to be in better agreement with the selected experiments since the H_2O/H_2O_2 ratio is better reproduced.

4.4.2.6 *H_2 + HO_2 and H_2 + OH.*

Reactions involving molecular, rather than atomic, hydrogen are of great importance in an astrochemical context due to the large abundance of H_2 in the interstellar medium. Molecular hydrogen that has been formed on the surface via

$$H + H \rightarrow H_2^* \tag{R7}$$

is formed with an excess energy of 4.5 eV and we assume that it therefore desorbs upon formation, *i.e.* the fraction that stays on the surface, μ, is 0. Only a very small fraction of gas-phase H_2 is hot, both experimentally and in the interstellar medium, and in our simulations it is implemented without substantial excess energy. Runs with $\mu = 0.5$ resulted in abundances within the limits of the standard deviations.

The reaction H_2 + HO_2 has a large barrier (Tsang & Hampson, 1986) and is even endothermic, therefore it is not expected to proceed at these low temperatures. However, co-depostion experiments with the same H fluence but with ten times higher H_2 fluence show an increase in H_2O_2 and decrease in HO_2 in agreement with the proposed reaction. Also in Romanzin et al. (2011) an observed isotope effect between hydrogenation and deuteration of ozone suggested this reaction to occur under laboratory conditions. It was therefore hypothesized that the excess energy from the reaction H + O_2 can be used to overcome both the reaction barrier and the endothermicity of the H_2 + HO_2 reaction since the total reaction H + H_2 + O_2 $\rightarrow$ H_2O_2 + H is exothermic.

In the simulations this reaction is included with a high barrier and as a result the reaction does not contribute to the H_2O_2 production. If the activation energy is substantially lowered, a small increase in the H_2O_2 is observed for the co-deposition simulation at 25 K. The current simulations cannot constrain the value of the reaction barrier.

The reaction H_2 + OH has a gas-phase barrier of 2700 K (M. Yang and D. H. Zhang and M. A. Collins and S.-Y. Lee, 2001). Gas-phase experiments indicate that tunneling starts to play a role for OH + H_2 for temperatures below 250 K Orkin et al. (2006). Recently, Oba *et al.* performed solid state experiments confirming a dependency of the reaction rate on effective mass (Oba et al., 2012). The reaction rate at $15 - 25$ K should therefore be substantially raised through tunneling. In the present simulations the reaction only plays a minor role in the

water production regardless of the barrier for reaction. Even in the low barrier case, the H_2O formation rate is only slightly changed by this reaction. However, on closer inspection of the different contributions to the H_2O formation rate, one notices that the fraction of water that is produced through H_2 + OH increases with reaction rate. The contribution of H + OH declines at the same time, resulting in a zero net effect.

4.4.2.7 *Potentially important reactions.*

To conclude this section, we discuss the reactions that have not been included in the standard and optimization simulation runs, namely

$$O + OH \rightarrow HO_2 \tag{R8}$$
$$OH + H_2O_2 \rightarrow H_2O + HO_2 \tag{R9}$$
$$HO_2 + HO_2 \rightarrow H_2O_2 + O_2 \tag{R10}$$
$$HO_2 + OH \rightarrow H_2O + O_2 \tag{R11}$$
$$HO_2 + O_2 \rightarrow O_2 + HO_2 \tag{R12}$$
$$OH + H_2O \rightarrow H_2O + OH\,. \tag{R13}$$

Where possible, we performed several test runs including one of these aforementioned reactions in the standard simulation scheme.

Adding the first reaction, (R8), to the scheme with zero barrier has a negligible effect, since it accounts at most for 3% of the total HO_2 budget as a result of the low O production.

Concerning reaction (R9), Vakhtin et al. (2003) reported an empirical relation with a negative barrier in the gas-phase at relatively low temperatures (96-296 K). This would render the reaction effectively barrierless for our purpose. However, a kinetic isotope effect was previously found, suggesting in fact the presence of an activation energy (Vaghjiani et al., 1989). Liquid-phase studies of this reaction indicate that the reaction rate can be decreased by as much as a factor of 1840 with respect to the gas phase (Atadinç et al., 2005; Buszek et al., 2012). The presence of water can thus have a large effect on the probability for this reaction to occur. Moreover, a mechanism involving a reorientation into a five-membered prereactive complex was predicted (Atadinç et al., 2005; Buszek et al., 2012), but efficient reorientation is not likely in the solid state. Therefore, we exclude reaction (R9) from our simulations. Test runs were performed by using various settings and unequivocally poor reproductions of the experimental results were found through overproduction of water.

Reactions (R10) to (R13) should be considered part of the same train of thought, namely that hydrogen atoms are not all physisorbed but some are trapped in a chemical bond with for instance O_2. These complexes or molecules can then continue to react with other species. Only incorporating reaction (R10) (with E_a = 0 K (Kircher & Sander, 1984)) has little effect, except for co-deposition at 15 K, where the OH/H_2O_2 ratio changes to a large extent. This can be easily overcome through changing the branching ratio of (R2). Incorporating also reaction (R11) (with E_a = 0 K) results in a heavy overproduction of water. Reactions (R12) and (R13) allow for a type of proton exchange and may be considered as an alternative to hydrogen diffusion. Since these are reactions that go back and forth, they strongly increase the computational costs for barriers below 2500 K. Preliminary results show a decreased penetration depth for both temperatures as well as underproduction of H_2O_2. We postpone this concept for the time being (see Chapter 8) and continue using our assumption of physisorbed hydrogen atoms diffusing on and through the ice.

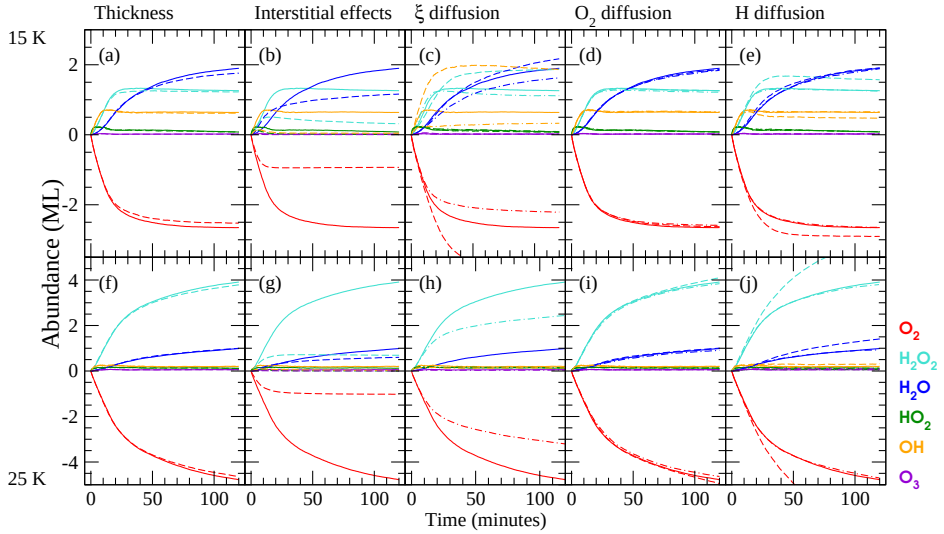

Figure 4.7: As for Fig. 4.5, but investigating different parameters relating to penetration depth. Solid curves represent simulation results with standard values. Dashed curves in panel (a) represent standard values applied to a 16 ML surface and in panel (b) easy access to interstitial positions was switched off. For panel (c) dashed curves represent a low ξ value (Eq. 32) and dashed-dotted curves a high value. For panels (d) and (e) dashed curves represent a lower barrier of diffusion and dashed-dotted curves represent easier access to interstitial positions for O_2 and H, respectively. Panels (f)-(j) give the 25 K situation.

4.4.3 *Penetration depth*

In Section 4.4.2.4 we mentioned that the standard simulations cannot reproduce the large experimental surface abundance of H_2O_2, 14 ML, at 25 K for sequential hydrogenation. This large abundance can accumulate in time through different mechanisms, for instance: (1) replenishing of the top layers by O_2 mobility and (2) competition between reaction and diffusion of H atoms. Several control experiments have been performed and it was established in Part I that the most likely scenario is the second mechanism, where hydrogen atoms can either react with a partner (initially O_2) or diffuse deeper into the ice. The extent to which the atoms enter the icy mantle is called penetration depth. The reaction H + O_2 is (close to) barrierless and temperature independent. Diffusion, however, is enhanced with increasing temperature and hydrogen atoms are thus able to reach deeper layers in the ice at higher temperature. In Fig. 4.7 a summary of the study on diffusive effects and penetration depth is presented, depicting the influence of initial ice thickness, availability of interstitial positions, the diffusion parameter ξ, and the diffusion and positioning of H and O_2 in the ice.

The effect of the surface itself is discussed first. Increasing the initial surface roughness allows a higher production of both water and hydrogen peroxide, simply as a result of a larger surface area available for hydrogenation. Starting from a more porous ice, *i.e.*, 10% pores in the standard surface, there is no significant effect on the penetration. The most probable explanation is that during the course of the simulation, pores are created as a result of products that continue to react further. A possibility for the low simulated use-up of O_2 could be the

initial ice thickness, since the final experimental H_2O_2 abundance is 14 ML which is more than our initial surface thickness (10 ML). This is illustrated in Figs. 4.7(a) and (f), and no dependence on ice thickness can be concluded. The fact that the ice thickness does not change abundances significantly is a sign of a lacking penetration mechanism. After all, if hydrogen atoms penetrate deeply into the matrix, a large O_2 reservoir would allow for more reactions to occur. The lack of this effect urges further investigation of diffusive effects with the purpose of understanding how we can increase the consumption of O_2.

First of all, in the standard simulations there is already a mechanism included to account for some form of penetration, namely the availability of interstitial positions for small species, in particular hydrogen atoms. If this penetration mechanism is switched off, hydrogenation only occurs in the top layer of the ice and the final abundances drop to unrealistically low values as shown in Figs. 4.7(b) and 4.7(g). Furthermore, the shape of the H_2O_2 curves changes and the sharp transition from linear growth to steady state is no longer present. Also, OH cannot be properly produced since it needs a second lattice site upon production.

The parameter ξ, in Eq. 32 is used to determine the ease with which molecules can diffuse, which regulates the diffusion both on the surface and into the bulk. A value higher than for the standard simulations decreases the diffusion rate, which leads to a low penetration depth since molecules are not formed deep in the ice and the top layers therefore easily block further reactions. A value of ξ lower than for the standard simulations increases the diffusion rate; this allows for more HO_2 production deeper in the ice. The abundance of stable species increases and that of the intermediates decreases as they are more accessible. A high diffusion rate, however, overestimates the abundance of OH and H_2O for the sequential simulations and changes the OH evolution in the co-deposition simulations (not shown) so that it no longer follows the same trend as H_2O_2. Therefore, we conclude that the intermediate diffusion rate reproduces the experiments best.

This brings us back to the two possible scenarios suggested in the experimental paper (Ioppolo et al., 2010). A higher O_2 mobility is obtained through a lower barrier of O_2 diffusion or by easier access to interstitial positions. From Figs. 4.7(d) and 4.7(i) it is clear that both have no effect. Therefore, the second scenario was tested by varying the H mobility as depicted in Figs. 4.7(e) and 4.7(j). A lower barrier results in a steeper increase in the abundances of H_2O and H_2O_2 at 25 K and reproduces the transition between the initial rise and subsequent steady state behaviour at 15 K. Since this leads to a higher penetration depth at 25 K, we conclude that fast hydrogen diffusion could be a key feature in reproducing the competition between the reaction H + O_2 and diffusion into the ice, confirming the suggestions made by Ioppolo et al. (2010).

4.5 RECOMMENDATIONS FOR FUTURE STUDIES

We have gained insight in the surface processes linked to the formation of water ice by simulating previous experimental results with Continuous-Time Random-Walk Monte Carlo simulations and explicitly taking into account relevant surface effects. A systematic approach to varying reaction barriers is applied here to obtain a best fit model and characterize the sensitivity of the full reaction network to the various reactions. With this model experimental trends are reproduced and specific reaction barriers have been obtained as given in Table 4.5. These rates are compared to literature values and recommended for future use in astrochemical models. Below, we describe the best fit found by using our simulations and we highlight some astrochemical considerations.

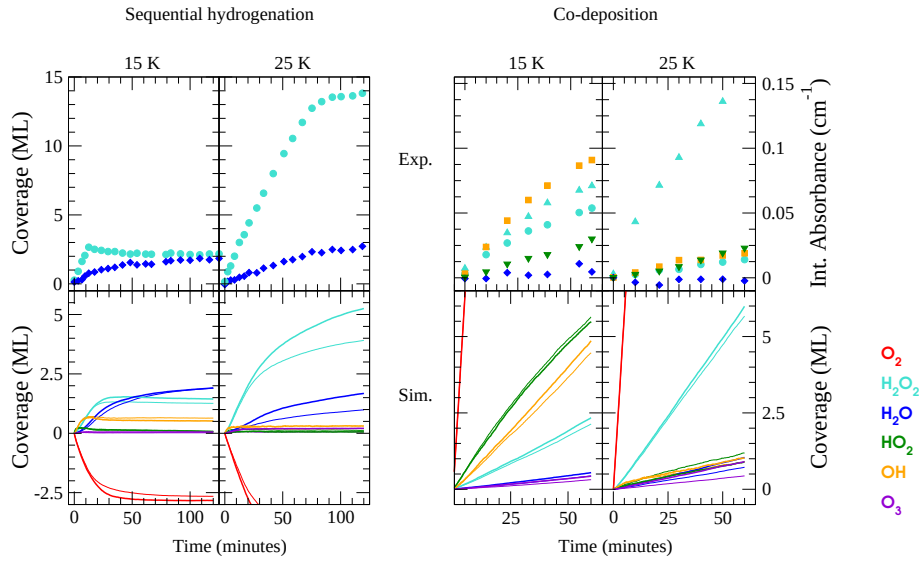

Figure 4.8: Evolution of the surface abundance of O_2 (red), H_2O_2 (light blue), H_2O (dark blue), HO_2 (green), OH (orange) and O_3 (violet) as a function of time for a sequential hydrogenation simulation (left) and a co-deposition simulation (right) at 15 and 25 K compared to the experimental values. The thin lines represent the standard simulations, whereas the thick lines represent the simulation connected to the best fit parameters of Table 4.5. Note that the experimental surface abundances for the co-deposition simulations are in units of integrated absorbance, due to a lack of available band strengths for matrix isolated species.

4.5.1 *Best fit*

The activation energies given in Table 4.5 are largely similar to those of the standard simulations, except for:

- The reaction barrier for the reaction H + O_2 in the case of co-deposition simulations,
- The branching ratio of the reaction OH + OH, which is set to (R3a):(R3b) = 90:10,
- The binding energy of hydrogen atoms to the surface, E, is lowered to 53 K.

Key reactions are indicated in boldface in Table 4.5. In Fig. 4.8 the surface abundances as obtained by the best fit simulation are plotted versus time and can be compared to both the standard simulations and the experimental trends.

In general, a clear agreement between experimental and simulated data can be observed. Prominent is the reproduction of the H_2O_2 abundance evolution where the shape of the curves for sequential hydrogenation is correct as well as the overall behaviour under influence of a change in temperature. Moreover, with the 'best fit' settings the H_2O production is roughly similar at 15 and 25 K, as it should be. Note that water does remain slightly overproduced at low temperature, likely due to the dynamics of the OH radical (diffusion versus a barrier for (R3)). Furthermore, the best fit settings are used to test once more the influence of the initial ice thickness. With these improved settings, indeed a small increase in H_2O_2 abundance is found at 25 K using a 16 ML thick surface indicating an enhancement of hydrogen penetration.

Table 4.5: Parameters that reproduce the selected experiments the best. A comparison to (mean) gas-phase literature values is also included. Key reactions are listed in bold face.

Reaction					R (s^{-1}) [a]	Lit. E_a (K)
Temperature independent reactions						
H	+ H	→ H_2			1×10^{12}	
H	**+ O_2**	→ **HO_2**			1.1×10^{5} [b]	~ 0 (Walch & Duchovic, 1991; Sellevåg et al., 2008)
H	**+ HO_2**	→ **products**			1×10^{12}	T indep. (Keyser, 1986)
		OH	+ OH		56%	
		H_2O_2			35%	
		H_2	+ O_2		2%	
		H_2O	+ O		7%	
H	+ O	→ OH			1×10^{12}	–
O	+ O	→ O_2			1×10^{12} [c]	–
H	+ O_3	→ O_2	+ OH		1.1×10^{5}	450 (Lee et al., 1978)
H	**+ OH**	→ **H_2O**			1.1×10^{5}	~ 0 (Sellevåg et al., 2008)
Temperature dependent reactions						
H	**+ H_2O_2**	→ **H_2O**	**+ OH**		800	1280	2000 (Koussa et al., 2006)
H_2	+ O	→ OH	+ H		3165 [c]	3165 [c]	3165 (Baulch et al., 1992)
H_2	+ HO_2	→ H_2O_2	+ H		5000 [c]	5000 [c]	13100 (Tsang & Hampson, 1986)
H_2	+ OH	→ H_2O	+ H		500 [c]	800 [c]	2100 (Atkinson et al., 2004; Oba et al., 2012)
OH	**+ OH**	→ **products**			– [d]	– [d]	0 (Atkinson et al., 2004)
		H_2O_2			90%	90%	0 (Atkinson et al., 2004)
		H_2O	+ O		10%	10%	0 (Atkinson et al., 2004)
O	+ O_2	→ O_3			500	500	0 (Atkinson et al., 2004)

NOTE: The hydrogen diffusion barrier used was 53 K instead of the value listed in Table 4.2.

[a] This work. [b] A value of 8.3×10^{5} used for the co-deposition simulations. [c] Reaction practically does not take place in our simulations. [d] See Section 4.4.2.3.

Considering the co-deposition simulations, the 'best fit' runs are performed with parameters equal to those for sequential hydrogenation, except for the rate of the reaction of H + O_2. As mentioned in Section 4.4.2.1, the angle dependence of this reaction is less of a restriction during co-deposition and a lower barrier for this reaction is better at reproducing the HO_2 abundances. The overproduction of HO_2 decreases slightly and the production of H_2O_2 increases with respect to the standard simulations. Moreover, the production of O_3 is enhanced, which is in agreement with the experimental results, judging by Fig. 5.3 from Cuppen et al. (2010). Furthermore, the branching ratio of the reaction H + HO_2 is found to be within the following range (R2a):(R2b):(R2c):(R2d) = (56-65):(35-26):(2):(7). The effect of changing this translates into a changed OH/H_2O_2 ratio for co-deposition at 15 K while no change is observed for co-deposition at 25 K or sequential hydrogenation simulations. Note that the uncertainty in the dynamics of the OH radical can also affect the time evolution of the abundance of this species. The comparison made in Table 4.4 between different temperatures and H/O_2 ratio remains unchanged.

Finally, we tried to reproduce the sequential hydrogenation study performed by Miyauchi et al. (2008) using the best fit parameters combined with their experimental conditions. We corrected for the different band strengths used as well as the systematic shift in temperature reading of 2 K (compare Fig. 2.6 in Fuchs et al. (2009) and Fig. 3 in Watanabe et al. (2006)). Our simulations confirm their experimentally observed trends to within 50%, in terms of H_2O and H_2O_2 abundance as well as evolving trends in time.

4.5.2 *Astrochemical Considerations*

Monte Carlo simulations have the potential to bridge the difference in conditions (time constraints, abundances and fluxes) between experiments and the interstellar medium by investigating surface reaction mechanisms under, first laboratory, and then interstellar medium conditions.

For instance, a high hydrogen diffusion rate in O_2 ice is necessary to reproduce the large penetration depth observed experimentally. However, the penetration depth is a bulk effect, which is largely absent under astrochemical conditions. A pure O_2 ice is not likely to be present in space and diffusion will be restricted mainly to the surface layers. In this work the goal is to understand the physico-chemical principles and therefore the penetration depth is an effect that does need to be investigated.

Penetration depth plays a somehow less important role for the co-deposition simulations and since most features are correctly reproduced, we are confident that this set of parameters can be used in astrochemically relevant simulations to reproduce observations of water in different regions of the interstellar medium. This will be also the topic of a future study in which the influence of directionality in a hot diffusion mechanism will be incorporated.

Another important difference between experiments and astronomical observations is the abundance of formed solid H_2O_2 with respect to H_2O. Starting from O_2, a high abundance of H_2O_2 is found. Here we show that a relatively slow destruction of H_2O_2 explains the high accumulation of this species. Figure 2 in Cuppen et al. (2010) indicates that a high and more interstellar relevant H/O_2 ratio in co-deposition experiments is in favor of water formation. A more detailed study of the role of the H_2O_2 surface destruction channel (R4) within the whole reaction network under interstellar conditions is highly needed. Du *et al.* used a gas-grain model to reproduce the observed gas-phase abundance of H_2O_2 in ρ Oph A using a low barrier of 92 K for the surface reaction (R4) (Du et al., 2012b). They see a very high gas-phase H_2O_2 abundance for a range of physical conditions, which could be explained by the lack of gas-phase destructive mechanisms. Moreover, the abundance of surface H_2O_2 as obtained in their

model is affected by the height of the barrier of reaction (R4) (Du et al., 2012a). Increasing the barrier for reaction (R4) to our values would result in higher solid H_2O_2 abundances, further strengthening their and our suggestion to investigate the surface formation and destruction of H_2O_2 under interstellar relevant conditions in more depth.

The unknown diffusive behaviour of radical species, such as OH and H, is key to predict water formation under conditions relevant to the interstellar medium. However, experiments investigating diffusion are scarce due to the non-trivial competition with the high reaction probabilities involved. In the present study the two most relevant species in this respect are OH and H. The first because the experimental detection in co-deposition experiments poses a challenge as reaction (R3) was initially thought to occur barrierless. Furthermore, the diffusion of hydrogen on a surface was studied experimentally only by Katz *et al.* in 1999 and barriers found on carbon and silicate surfaces are not necessarily applicable to icy grains as well (Katz et al., 1999; Matar et al., 2008). Although the H diffusion is not fully constrained, it is a key parameter for our simulations as we extensively discussed in Section 4.4.3.

Finally, for astrochemical applications, the reactions with H_2, discussed in Section 4.4.2.6, are actually relevant to dark cloud conditions (Cuppen & Herbst, 2007). Since molecular hydrogen posesses a rather strong intramolecular bond, barriers are typically high and tunneling is required to increase the rate of reaction with other ice species. This tunneling should scale with the so-called effective mass of the total system, since the system needs to be considered as a whole as outlined in Oba et al. (2012). This is by no means trivial and depends strongly on the binding of the molecule with the surface as well as on the evolution of the effective mass with reaction coordinate (Bell, 1980). Also here further dedicated experimental research as well as (theoretical) modeling to study reactions with H_2 is needed for a deeper understanding of the full reaction scheme.

4.5.3 *Practical use of the best fit parameters*

In our Monte Carlo simulations the competition between different processes for a single species is explicitly taken into account. This is not easy to implement in classic rate equation models. However, in the interstellar medium, ice chemistry is limited by diffusion of surface species. Especially in dark molecular clouds species on the surface are thermalized before engaging in reactions. Therefore, reactions with high rates (either due to a low activation energy or the result of tunneling) will dominate.

Here we find a number of key reactions for the O_2 + H route, as summarized in Table 4.5. When implementing these reaction rates in (astrochemical) models, the rates and activation energies given in Table 4.5 need to be considered in such a way that (i) the ratio between two reaction rates corresponds to the ratio found here and (ii) the rates are scaled according to the prefactor being used that amounts here to 1×10^{12} s^{-1}.

4.6 CONCLUSIONS

Solid state hydrogenation reactions of O_2 ice have been simulated with a Continuous-Time Random-Walk Monte Carlo method, explicitly taking into account the recent findings of a number of experimental studies. A strategy of systematically varying the different processes at play in the simulations, and comparing the outcome with experimental values, allows to derive the key processes. In this way, we can gain insight in the actual processes taking place. Our model consists of a combination of reaction barriers (or activation energies) and binding energies for all species present in the reaction network (Fig. 4.1). In order to probe the large

parameter space, we selected four previously performed different experiments. These are sequential hydrogenation and co-deposition experiments at 15 and 25 K that are all reproduced with a single set of parameters. The best fit model reproduces experimentally observed trends using the binding energies given in Table 4.2, complemented with the reaction barriers given in Table 4.5. From an extensive set of simulations, we conclude the following:

- The key reactions for the reaction route starting from O_2 are (R1) H + O_2, (R2) H + HO_2, (R3) OH + OH, (R4) H + H_2O_2 and (R5) H + OH,
- A relatively slow destruction of H_2O_2 explains the high accumulation of this species,
- A high hydrogen diffusion rate is necessary to reproduce the large penetration depth of H into the O_2 ice observed experimentally, and
- The diffusive behaviour of radical species, such as OH and H, is a key parameter.

BIBLIOGRAPHY

Acharyya, K., Fuchs, G. W., Fraser, H. J., van Dishoeck, E. F., & Linnartz, H. 2007, Astron. Astrophys., 466, 1005
Atadinç, F., Günaydin, H., Özen, A. S., & Aviyente, V. 2005, Int. J. Chem. Kinet., 37, 502
Atkinson, R., Baulch, D. L., Cox, R. A., et al. 2004, Atmos. Chem. Phys., 4, 1461
Baluteau, J.-P., Cox, P., Cernicharo, J., et al. 1997, Astron. Astrophys., 322, L33
Baulch, D. L., Cobos, C. J., Cox, R. A., et al. 1992, J. Phys. Chem. Ref. Data, 21, 411
Bell, R. P. 1980, The tunnel effect in chemistry (London: Chapman and Hall)
Bergman, P., Parise, B., Liseau, R., et al. 2011, Astron. Astrophys., 531, L8+
Buszek, R. J., Torrent-Sucarrat, M., Anglada, J. M., & Francisco, J. S. 2012, J. Phys. Chem. A, 116, 5821
Cazaux, S., Cobut, V., Marseille, M., Spaans, M., & Caselli, P. 2010, Astron. Astrophys., 522, A74+
Chang, Q., Cuppen, H. M., & Herbst, E. 2005, Astron. Astrophys., 434, 599
Cuppen, H. M. & Herbst, E. 2005, Mon. Not. R. Astron. Soc., 361, 565
Cuppen, H. M. & Herbst, E. 2007, Astrophys. J., 668, 294
Cuppen, H. M., Ioppolo, S., Romanzin, C., & Linnartz, H. 2010, Phys. Chem. Chem. Phys., 12, 12077
Du, F., Parise, B., & Bergman, P. 2012a, Astron. Astrophys., 544, C4+
Du, F., Parise, B., & Bergman, P. 2012b, Astron. Astrophys., 538, A91+
Dulieu, F., Amiaud, L., Congiu, E., et al. 2010, Astron. Astrophys., 512, A30+
Fuchs, G. W., Acharyya, K., Bisschop, S. E., et al. 2006, Far. Disc., 133, 311
Fuchs, G. W., Cuppen, H. M., Ioppolo, S., et al. 2009, Astron. Astrophys., 505, 629
Garrod, R. T., Wakelam, V., & Herbst, E. 2007, Astron. Astrophys., 467, 1103
Gibb, E. L., Whittet, D. C. B., Schutte, W. A., et al. 2000, Astrophys. J., 536, 347
Hiraoka, K., Miyagoshi, T., Takayama, T., Yamamoto, K., & Kihara, Y. 1998, Astrophys. J. , 498, 710
Hogerheijde, M. R., Bergin, E. A., Brinch, C., et al. 2011, Science, 334, 338
Ioppolo, S., Cuppen, H. M., Romanzin, C., van Dishoeck, E. F., & Linnartz, H. 2008, Astrophys. J., 686, 1474
Ioppolo, S., Cuppen, H. M., Romanzin, C., van Dishoeck, E. F., & Linnartz, H. 2010, Phys. Chem. Chem. Phys., 12, 12065
Kang, H. C. & Weinberg, W. H. 1989, J. Chem. Phys., 90, 2824
Katz, N., Furman, I., Biham, O., Pirronello, V., & Vidali, G. 1999, Astrophys. J., 522, 305
Keyser, L. F. 1986, J. Phys. Chem., 90, 2994
Kircher, C. C. & Sander, S. P. 1984, J. Phys. Chem., 88, 2082
Koussa, K., Bahri, M., Jaïdane, N., & Ben Lakhdar, Z. 2006, J. Mol. Struct.:THEOCHEM, 770, 149
Larsson, B., Liseau, R., Pagani, L., et al. 2007, Astron. Astrophys., 466, 999
Lee, J. H., Michael, J. V., Payne, W. A., & Stief, L. J. 1978, J. Chem. Phys., 69, 350
M. Yang and D. H. Zhang and M. A. Collins and S.-Y. Lee. 2001, J. Chem. Phys., 115, 174
Matar, E., Congiu, E., Dulieu, F., Momeni, A., & Lemaire, J. L. 2008, Astron. Astrophys., 492, L17
Miyauchi, N., Hidaka, H., Chigai, T., et al. 2008, Chem. Phys. Lett., 456, 27
Mokrane, H., Chaabouni, H., Accolla, M., et al. 2009, Astrophys. J. Lett., 705, L195
Mousavipour, S. H. & Saheb, V. 2007, Bull. Chem. Soc. Jpn., 80, 1901
Oba, Y., Miyauchi, N., Hidaka, H., et al. 2009, Astrophys. J., 701, 464
Oba, Y., Watanabe, N., Hama, T., et al. 2012, Astrophys. J., 749, 67+
Orkin, V. L., Kozlov, S. N. P. G. A., & Kurylo, M. J. 2006, J. Phys. Chem. A, 110, 6978
Parise, B., Bergman, P., & Du, F. 2012, Astron. Astrophys., 541, L11+
Romanzin, C., Ioppolo, S., Cuppen, H. M., van Dishoeck, E. F., & Linnartz, H. 2011, J. Chem. Phys., 134, 084504
Sellevåg, S. R., Georgievskii, Y., & Miller, J. A. 2008, J. Phys. Chem. A, 112, 5085
Tielens, A. G. G. M. & Hagen, W. 1982, Astron. Astrophys., 114, 245
Tsang, W. & Hampson, R. F. 1986, J. Phys. Chem. Ref. Data, 15, 1087
Vaghjiani, G. L., Ravishankara, A. R., & Cohen, N. 1989, J. Phys. Chem., 93, 7833
Vakhtin, A. B., McCabe, D. C., Ravishankara, A. R., & Leone, S. R. 2003, J. Phys. Chem. A, 107, 10642

van Dishoeck, E. F., Kristensen, L. E., Benz, A. O., et al. 2011, Publ. Astron. Soc. Pac., 123, pp. 138

Walch, S. & Duchovic, R. 1991, J. Chem. Phys., 94, 7068

Watanabe, N., Hidaka, H., & Kouchi, A. 2006, in AIP Conf. Ser. , Vol. 855, Astrochemistry - From Laboratory Studies to Astronomical Observations, ed. R. I. Kaiser, P. Bernath, Y. Osamura, S. Petrie, & A. M. Mebel, 122–127

5

THE FORMATION OF ICE MANTLES ON INTERSTELLAR GRAINS REVISITED – THE EFFECT OF EXOTHERMICITY

Modelling of grain surface chemistry generally deals with the simulation of rare events. Usually deterministic methods or statistical approaches such as the kinetic Monte Carlo technique are applied for these simulations. All assume that the surface processes are memoryless, the Markov chain assumption, and usually also that their rates are time independent. In this paper we investigate surface reactions for which these assumptions are not valid and we discuss what the effect is on the formation of water on interstellar grains. We will particularly focus on the formation of two OH radicals by the reaction $H + HO_2$. Two reaction products are formed in this exothermic reaction and the resulting momentum gained causes them to move away from each other. What makes this reaction special, is that the two products can undergo a follow-up reaction to form H_2O_2. Experimentally OH has been observed, which means that the follow-up reaction does not proceed with a 100 % efficiency, even though the two OH radicals are formed in each other's vicinity in the same reaction. This can be explained by a combined effect of directionality of the OH radical movement together with energy dissipation. Both effects are constrained by comparison with experiments and the resulting parametrised mechanism is applied to simulations of the formation of water ice under interstellar conditions.

T. Lamberts, X. de Vries, and H. M. Cuppen, *The formation of ice mantles on interstellar grains revisited - the effect of exothermicity*, Far. Disc. 168 (2014) 327

5.1 INTRODUCTION

Water is one of the molecules most vital for life on Earth. How water was delivered to Earth is not completely clear. Different pathways have been suggested; including scenarios where Earth's water is of extraterrestrial origin (Drake, 2005). Water frozen on interstellar dust particles could have been trapped during the accretion of dust to form our planet, or water may have been transported by comets in a later stage. In both cases, interstellar ices are at the origin of the mechanism (Muralidharan et al., 2008; Bockelée-Morvan et al., 2000). In the cold regions of molecular clouds, water is formed through grain surface reactions. On the grain surface, water can be formed through simple exothermic addition reactions, where the grain serves as a third body to take up the excess energy (van Dishoeck et al., 2013).

In 2007, we performed the first microscopic astrochemical simulations on the surface formation of water in different environments: diffuse, translucent, and dense clouds (Cuppen & Herbst, 2007). This model was based on the physical and chemical information that was available at the time, which was rather poor, but it triggered many experimental studies by several different laboratories (Miyauchi et al., 2008; Matar et al., 2008; Ioppolo et al., 2008; Oba et al., 2012). Because of these new experiments the surface reaction network is now much better constrained and the understanding of solid water and its precursors has improved in general. Recently, a new microscopic kinetic Monte Carlo (KMC) model was developed (Chapter 4) that is capable of simulating different types of water formation experiments (Ioppolo et al., 2010; Cuppen et al., 2010) and that put constraints on the reaction rates of many of the reactions within the surface network. Table 5.2 gives an overview of this network as it is currently understood (Ioppolo et al., 2010; Cuppen et al., 2010; Oba et al., 2012; Dulieu, 2011). In the present discussions, the new KMC model will be the basis for simulations under interstellar conditions. We further aim to show the importance of exothermicity of reactions and how this leads to non-Markovian behaviour and chemical desorption.

Grain surface chemistry is generally simulated by either rate equations or a stochastic method that solves the master equation. The master equation describes the change in probability to be in a certain state at a certain time. In these simulations a state is often represented by, *e.g.*, the species on the grain, their position, the temperature of the grain, etc. One of the assumptions at the root of the derivation of the master equation is that the events bringing the system from one state to the next are memoryless: the Markov chain assumption. Typical grain surface processes such as diffusion and desorption of thermalised species are effectively memoryless: they occur at much longer time scales than the (lattice) vibrations and all history about which states where previously visited is lost due to the vibrations between two transitions. For a more in-depth discussion see Cuppen et al. (2013). Newly formed reaction products can behave differently however. Most grain surface reactions are highly exoergic. Part of this exothermicity will be immediately transferred to the icy mantle, but likely a substantial fraction of it remains in the reaction products making them 'hot'. For reactions with two or more reaction products the energy gain is distributed as momentum over the products. This will have two effects: the hot species are more likely to move and desorb than thermalised species and because they have some momentum, their movement will not be memoryless and their trajectory will therefore not follow a random walk. The energy responsible for this behaviour eventually dissipates through collisions with the grain and/or ice mantle. The extend of this effect will therefore strongly depend on the time scale for energy dissipation, which in turn depends on the local environment. Collisions with molecules making up the ice mantle are much more effective than collisions with the harder grain material which does not absorb the energy as easily.

A clear example of a reaction where non-Markovian behaviour becomes important, is the formation of two OH radicals by the reaction $H + HO_2$. This one of the few significant surface reactions in the water network that leads to two reaction products. The formed radicals will move away from each other due to their opposite relative momenta. If this reaction occurs on top of an ice or a grain surface, the species will continue to diffuse on the surface. If the reaction occurs in the bulk phase, however, they can loose their directionality through collisions with neighbouring molecules. What makes this reaction special, is that the two products can undergo a follow-up reaction to form H_2O_2. In a co-deposition experiment of O_2 and H with an overabundance of O_2 the most-likely pathway to OH formation is through this $H + HO_2$ reaction. Experimentally OH has been observed under these conditions, which means that the follow-up reaction of $OH + OH$ does not proceed with a 100 % efficiency, even though the two OH radicals are formed close together in the same reaction.

In Chapter 4 we already suggested that one of the reasons why the KMC simulations cannot reproduce an appreciable amount of OH, without artificially changing physical parameters, is their inherent Markovian behaviour. Because of the assumption that the processes are memoryless, the OH radicals can travel in all directions, including towards the location where the OH radicals were initially formed. It is relatively straightforward to give reaction products some extra energy in the simulations, to alter their trajectory and not make it a random walk, is much harder. Without this change, however, newly formed OH radicals can easily meet again and react.

To constrain the time scale for energy dissipation is not straightforward. Some information is available for photoproducts of water ice photodissociation by Molecular Dynamics simulations (Andersson et al., 2006; Arasa et al., 2010, 2011), which are determined by Newton's equations of motion and do not assume Markovian behaviour. But these results are limited to a water-rich environment and they may not be applicable to the formation of the first monolayers of the water ice mantle. Dulieu et al. (2013) showed in a combined experimental and simulation study that the chemical desorption of water-related species can be much higher in the monolayer regime. Garrod et al. (2006) already suggested the importance of chemical desorption for, *e.g.*, the gas phase detection of methanol in cold dark clouds. This work was based on the Rice-Ramsperger-Kessel (RRK) theory which relates the excess energy and the binding energy of species to a desorption probability. They modified this theory by adding an unconstrained α parameter which they chose to be 0.1. Later Cazaux et al. (2010) studied the influence of chemical desorption on the gas phase composition by applying a KMC model, similar to one of Cuppen & Herbst (2007), but specifically focusing on the impact on the gas phase and on fractionation. In the present paper, we vary the time scale for thermalisation and we will show how this affects the overall evolution of the grain mantle. We will not only focus on chemical desorption but also on its influence on the grain surface chemistry and ice structure. The parameters that corresponds best to our experiments will be applied in Section 5.4 to model the evolution of a grain in diffuse cloud, translucent cloud and dense cloud conditions.

5.2 METHODOLOGY

The formation of water is simulated by microscopic kinetic Monte Carlo simulations. For a detailed description of the method we refer to Cuppen et al. (2013). The program and its parametrisation are described in detail in Chapter 4 and in Cuppen & Herbst (2007). Here, we briefly describe the main characteristics of these models. This is followed by a description of the adaptations that were implemented to overcome the use of empirically fitted parame-

ters, replacing them by more physically relevant values. Finally we highlight the differences between experimental and astrochemical simulation runs.

The grain is represented by a lattice model in which each lattice site can be occupied by one of the species from Table 5.1. Each species in the lattice has 6 neighbours and 12 nearest neighbours, corresponding to a primitive cubic lattice. The total binding energy, $E_{tot,bind}$, for each species to a site is calculated by additive contributions of its neighbours. Nearest neighbours add a contribution of E and next-nearest neighbours of E/8. Values for E are quoted in Table 5.1. The neighbour below the particle adds a double contribution (2E). Small species, *i.e.*, H, H_2, OH, and O, are allowed to occupy interstitial sites in the ice. This is included to account for the experimentally observed penetration of H atoms into solid O_2. Diffusion of these species to subsurface positions only occurs when an O_2 or a HO_2 molecule is atop the final position, since penetration in water-like structures has not been observed experimentally. Larger species can be present in the intermediate layer, though, as a result of the positioning of reaction products.

Table 5.1: Species in the model and their corresponding binding energy contribution, E, in Kelvin depending on the specific environment.

	Grain	H, H_2, O	Rest
H	105	10	70
H_2	80	10	50
O_2	240	240	240
OH	210	20	210
O_2H	630	60	630
H_2O_2	1370	140	1370
H_2O	1260	130	1260
O	260	30	260
O_3	630	60	630

After the deposition of a species on the grain, it can desorb, diffuse, react or dissociate. Each event is assumed to be thermally activated and the event rate is calculated using

$$k = \nu \exp\left(-\frac{E_{a,i}}{T}\right) \tag{33}$$

with $E_{a,i}$ the activation energy (or barrier) for process i in Kelvin and ν the attempt frequency, which is approximated by the standard value for physisorbed species, $\frac{kT}{h} = 10^{12}\ s^{-1}$. Desorption can only occur if a species is positioned in the top layer and depends on the total binding energy of the site. Diffusion can occur to each of the 18 neighbouring sites, provided that this site is empty. If the site is full, the small species have a probability to move to a corresponding interstitial site. Hopping events are calculated taking into account the binding energy contribution to the site as well as a term to ensure microscopic reversibility. Reactions can occur with co-reactants occupying one of the 6 nearest-neighbour and interstitial sites. Photodissociation only occurs in the interstellar simulations under the influence of the interstellar radiation field (IRF) with

$$k = \alpha_{photo} \exp(-\gamma_{photo} A_V)\ , \tag{34}$$

or through cosmic-ray induced photons

$$k = \alpha_{\text{cr photo}} \zeta \,, \tag{35}$$

where ζ is the cosmic ray ionization rate which is taken to be $1.3 \cdot 10^{-17}$ s^{-1}. Table 5.2 presents an overview of the chemical and photodissociation reactions included in our model. Surface reaction rates can be found in Chapter 4 and photodissociation rates in van Dishoeck et al. (2006). Deviations from these literature values are discussed in Section 5.2.1.

Table 5.2: List of surface and photodissociation reactions used in the current model. For their corresponding rates we refer to Chapter 4 and Cuppen & Herbst (2007).

Temperature-independent reactions					
H	+	H	→	H_2	
H	+	O_2	→	HO_2	
H	+	HO_2	→	products	
				OH	+ OH
				H_2O_2	
				H_2	+ O_2
				H_2O	+ O
H	+	O	→	OH	
O	+	O	→	O_2	
H	+	O_3	→	O_2	+ OH
H	+	OH	→	H_2O	
Temperature-dependent reactions					
H	+	H_2O_2	→	H_2O	+ OH
H_2	+	O	→	OH	+ H
H_2	+	HO_2	→	H_2O_2	+ H
H_2	+	OH	→	H_2O	+ H
OH	+	OH	→	products	
				H_2O_2	
				H_2O	+ O
O	+	O_2	→	O_3	
Photodissociation reactions					
OH			→	O	+ H
H_2O			→	OH	+ H
O_2			→	O	+ O
O_3			→	O_2	+ O

5.2.1 *Adaptations of the Monte Carlo routine*

The KMC simulation study in Chapter 4 could only reproduce the experimental observation of significant OH abundances, if the mobility of OH radicals and the barrier for OH + OH reaction were artificially increased. The values required were not consistent with other independent estimates of the OH mobility and OH + OH reaction barrier (Atkinson et al., 2004), but were necessary to prevent immediate recombination of the two OH radicals to form H_2O_2. Moreover, to ensure the correct ratio between formed OH and H_2O_2 a fixed branching ratio for the reaction $H + HO_2$ leading to 2 OH and to H_2O_2 was chosen. The latter might, however, be the result of a two step process: $H + HO_2 \rightarrow$ 2 OH $\rightarrow H_2O_2$.

In the present paper, both the diffusion and activation barrier have been adjusted to values of 210 and 0 K, respectively, and the product channel $H + HO_2 \rightarrow H_2O_2$ is removed. A physical explanation for the experimental detection of OH is the initial opposite relative momentum that two reaction products get upon reaction. To emulate this, we made two additional adaptations to the program described in Chapter 4. The two reaction products in the first reaction will be allowed to react or move with a directional bias, such that a higher probability is given to moving in the opposite direction of the other OH radical. The total hopping rate remains the same. The directionality is retained as long as the species is excited, *i.e.*, when the temperature of the species is higher than the temperature of the surface. Typically this allows for one to three directional hops to be performed.

Furthermore, species that are formed during an exothermic reaction resulting in two or more reaction products get a certain energy gain that can be utilized to enhance their mobility: increased hopping and desorption rates. The excess energy is expressed in terms of temperature, T_{ex} and is distributed over the produced species inversely proportional to their masses, following conservation of momentum (Arasa et al., 2011), and the energy gained by species A in a reaction with products A and B is therefore $T_{gain,A} = T_{ex}\frac{m_B}{m_A+m_B}$. We use the following notations: T_{ex} is the excess energy of the reaction, T_{gain} is the energy given to a specific reaction product directly after reaction and $T_{species}$ is the temperature of a species at any given time. For the experimental simulations, the energy is distributed (almost) equally between two products for the dominant reactions, since these products are of (nearly) equal mass. For the interstellar conditions where photodissociation reactions and the reaction $H_2 + OH \longrightarrow H_2O + H$ determine the chemistry to a large extend, T_{gain} becomes very different for the two products.

In the original simulations in Chapter 4 an arbitrary, small excess energy of only 100 K for each reaction product, regardless of their number, was included in the model. The event time of the next event for reaction product was then calculated using

$$\Delta t = -\frac{\ln X}{k_{tot}(T_{species})} \tag{36}$$

with X a pseudo-random number between 0 and 1 and k_{tot} the sum of all rates (diffusion, desorption, and reaction) for this molecule. These rates were considered constant during Δt for a temperature $T_{species}$, that was set equal to $T_{gain} = 1/2\ T_{ex}$ after reaction. This energy was dissipated through hopping events, where each diffusion step reduces $T_{species}$ by an arbitrary factor of 1.6. After 10^{-8} s, the local temperature of the excited species was set back to the temperature of the surface. This assumes that a molecule on the surface will be thermalised after 10 ns. The species were found to either react immediately to form a new molecule or remain in their initial configuration for times much longer than 10 ns. The outcome of the simulation results is therefore not too sensitive to the exact choice of this time scale.

The assumption that the rates remain stationary during Δt is a rather crude approximation. To be able to study the effect of thermalisation, the algorithm which determines Δt has been

changed to accommodate the effect of changing rates, *i.e.*, including energy dissipation. The dissipation of the energy is expected to be exponential (Shalashilin & Jackson, 1998). To reduce the computational complexity of an exponential energy loss, a simpler expression (Eq. (37)) was suggested by Cuppen & Hornekær (2008). The sensitivity of the model to the exact functional form was checked and found to be small. The initial temperature gain is assumed to decay following

$$T'(t) = \max\left(T_{surf}, \frac{T_{gain}}{(1 + B\,(t_r - t_a))^2}\right) \tag{37}$$

where t_r is the time at which the reaction occurred. A similar model was applied by Cuppen & Hornekær (2008). The parameter B can be chosen freely. Here two types of B parameters are used: B to describe the decay in the presence of an ice mantle and B_{grain} the decay on a bare grain surface. The varying temperature leads to non-stationary rates and the KMC time step cannot be determined in the usual way for this situation (see also Cuppen et al., 2013). We applied the method of Jansen (1995) to obtain the time step, using Eq. (37) instead of a linearly increasing temperature.

We assume that the total T_{ex} that is distributed over the two reaction products is smaller than the maximum exothermicity of the reactions included in the network. The main effect that we believe the excess energy has on the evolution of the ice species is by moving reactants over a large enough distance that they will not be able to react together. A large part of the energy is thought to be dissipated through (internal) rotational and vibrational modes and interaction with the substrate, but the time scales involved in this dissipation are expected to be considerably smaller than those for the translational excitation. Rotational excitation may change the reaction rates because of a change in incoming angle and, moreover, rotational and/or vibrational excitation will most likely affect the energetics involved in the reaction. However, most ice reactions are diffusion limited and we expect these effects not to dominate.

5.2.2 *Experimental vs. Interstellar simulations*

There are a few differences between the simulations of the experimental conditions and the simulations of interstellar ices. One of the differences is the composition of the gas phase (see also Section 5.4). The H-atom flux for experimental conditions is chosen to be $5{\times}10^{12}$ atoms $cm^{-2}\ s^{-1}$, in agreement with the experimental fluxes used in Ioppolo et al. (2010) and Cuppen et al. (2010) multiplied by a sticking fraction of 0.2. The other species arriving at the surface are H_2 and O_2, for an experimental simulation and H_2 and O under interstellar conditions. In the interstellar medium (ISM) the flux is determined by

$$f_A = \frac{v_A n(A) n_H}{4} \tag{38}$$

with $n(A)$ the relative gas phase abundance of species A, n_H the total hydrogen density, and v_A the mean velocity of species A in the gas. For a cloud with a temperature of 20 K and a density of $n_H = 10^4\ cm^{-3}$ and half of its in hydrogen in the form of H atoms, the H atom flux is 1.6×10^8 atoms $cm^{-2}\ s^{-1}$. The initial oxygen atom abundance is $3 \times 10^{-4}\ n_H$ and slowly diminishes over the course of the simulation to account for the freeze-out of the O atoms in terms of the newly formed surface species.

Besides the large difference in order of magnitude between the fluxes, there is also a change in the time scale over which the simulation is run. Experimental simulations last up to the length of the experiment (an hour), whereas astrochemical simulations are associated with

Table 5.3: Summary of the parameters chosen for all experimental simulations.

#	$H + HO_2$	$E_{a,\,OH\,diff}$	$E_{a,\,OH+OH}$	B	B_{grain}	T_{ex}	Directionality
	%	(K)	(K)	(s^{-1})	(s^{-1})	(K)	
I (1)	56:32:2:7	105	600	–	–	100[a]	off
II	91:0:2:7	210	0	–	–	100[a]	off
III	91:0:2:7	210	0	10^{12}	10^{12}	200	on
IV	91:0:2:7	210	0	10^{12}	10^{12}	1000	on
V	91:0:2:7	210	0	10^{12}	10^{12}	1400	on
VI	91:0:2:7	210	0	10^{12}	10^{12}	2000	on
VII	91:0:2:7	210	0	10^{11}	10^{11}	1400	on
VIII	91:0:2:7	210	0	10^{13}	10^{13}	1400	on
IX	91:0:2:7	210	0	10^{13}	10^{13}	2000	on

[a] A $T_{gain} = \frac{1}{2}T_{ex}$ of 100 K is given to each product, regardless of the number of products and their masses. (1) Chapter 4

time scales typical for dense clouds, *i.e.*, $10^5 - 10^6$ years (Bergin & Tafalla, 2007). Here we can cover between 4×10^4 and 2.5×10^5 years. Finally, the photodissociation events occur only in the interstellar simulations, where H_2O, H_2O_2, O_3, HO_2, and OH are allowed to photodissociate with a rate similar to their gas phase rate.

5.3 SIMULATIONS OF EXPERIMENTS

Here, we present and discuss kinetic Monte Carlo simulations of the following four experiments: sequential hydrogenation of O_2 at 15 K and 25 K and codeposition of O_2 and H at 15 K and 25 K. Following the approach from Chapter 4 we have chosen to reproduce these experimental results since they are representative for different experiments of the $O_2 + H$ reaction route. The experimental surface abundances are reproduced as closely as possible, but using parameters based on chemical and physical arguments rather than empirical ones which was done in the previous study. As mentioned above, one of the crucial parameters was found to be the OH mobility rate combined with the OH + OH reaction barrier. These, as well as different choices for T_{ex} and B and B_{grain} (Eq. 37) are changed in the current study to obtain a set of, physico-chemically acceptable, best fit parameters that can be implemented in simulations run over astrochemically relevant time scales. The parameters chosen for all simulations are summarized in Table 5.3. The experimental simulations were performed on a more smooth surface, analogous to the polished gold substrate used in the experimental set-up. Since the experimental studies are all bulk studies, the exact nature of the initial substrate is only of marginal influence.

Figure 5.1 shows a comparison of the time evolution of surface abundances that are experimentally obtained (Cuppen et al., 2010) with simulated results for runs I, II and V. Changing the set of parameters from simulation I to II encompasses the use of more realistic values. For instance, the barrier for the OH + OH reaction is removed following the recommended gas phase value from Atkinson et al. (2004). The new value, however, results in a poorer agreement with the experimental results for the co-deposition simulations. In general, this is due to the fact that all OH radicals produced by the reaction $H + HO_2$ are used in a follow-up

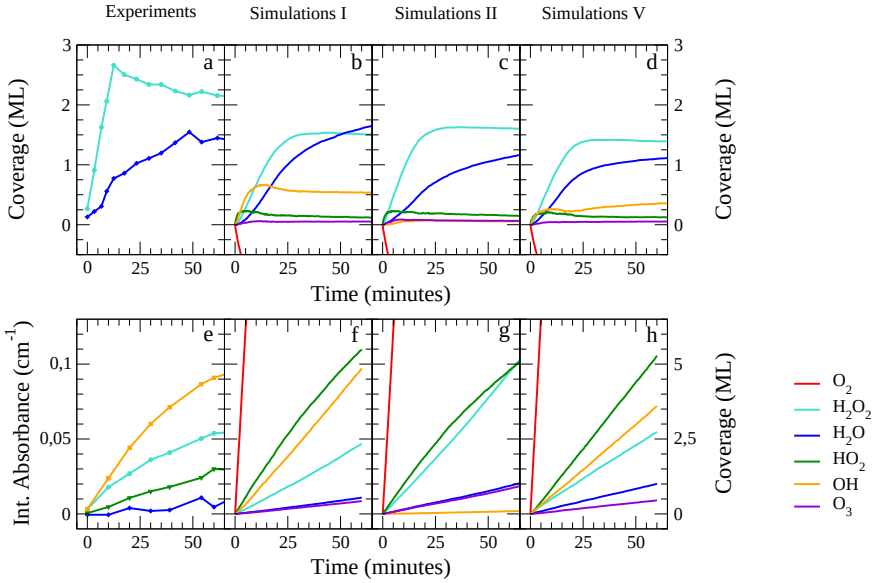

Figure 5.1: Evolution of the surface abundances of O_2, OH, HO_2, H_2O, H_2O_2 and O_3 as a function of time; (a) and (e) experimentally (Cuppen et al., 2010), (b) and (f) simulations I from Table 5.3, using the parameters from Chapter 4, (c) and (g) simulations II, using only physical parameters, (d) and (g) simulations V, using best fit parameters from this work (d).

reaction to subsequently produce H_2O_2 since there is no preventing mechanism. This is clear from the decrease of the OH surface abundance by 5 ML and the simultaneous increase of the H_2O_2 abundance by 2.5 ML. For the sequential hydrogenation at 15 K, a similar effect is observed and all H_2O is subsequently formed through the reactions $H + H_2O_2 \rightarrow H_2O + OH$ and $H + OH \rightarrow H_2O$. H_2O is slightly underproduced since there are not enough OH radicals available for reaction, but no large discrepancies with respect to the experiment are observed.

To improve the reproduction of the experimental co-deposition surface abundances, directional hopping is included as well as the use of non-stationary excess energy. In Figure 5.2 co-deposition simulations III and V-VIII are presented for 15 K and 25 K.

Firstly, the dependence of the surface abundances on T_{ex} is manifested mainly through a difference in the OH versus H_2O_2 production. A higher mobility of the reaction products from the reaction $H + HO_2$ allows them to move away from each other and prevent subsequent reaction to H_2O_2. This can also be seen in Table 5.4 where the ratio of follow-up reactions over the initial $H + HO_2 \longrightarrow 2\,OH$ reaction is given. This ratio decreases with T_{ex}. The overall $\frac{[2OH]}{[H_2O_2]}$ abundance ratio is also affected by other reactions and desorption and can therefore not be directly derived from the first ratio. It is, however, more easily comparable to experimentally measurable quantities. Cuppen et al. (2010) determined this ratio to be 1.6 $\pm$ 0.2 for 15 K and less than 0.5 for 25 K. The assumption was made that the bandstrength of the OH stretch mode of H_2O_2 is twice the bandstrength of that of the OH radical. If this assumption is indeed valid, a T_{ex} of 200 K is obviously not enough to allow for sufficient build-up of OH in the ice. A value of 1400 K or 2000 K appears to describe this experimental observable best.

Panels (a) and (c) in Figure 5.2 give the results of runs V, VII, and VIII and show the influence on B. Similar trends are observed when simulations VI and IX are compared. Again the

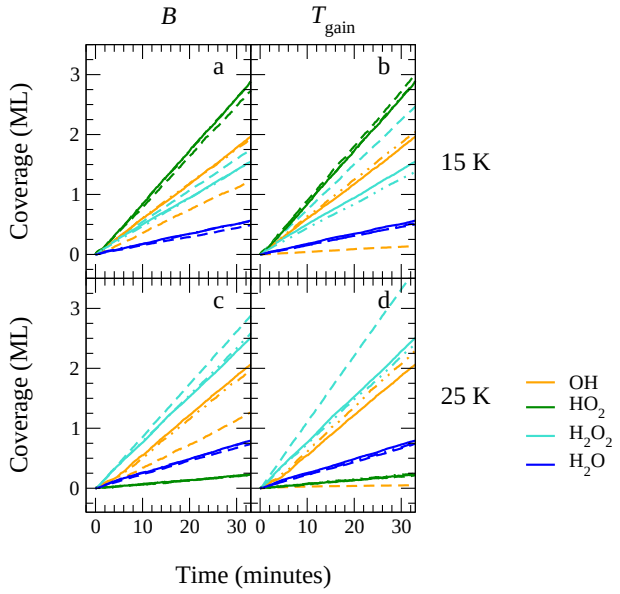

Figure 5.2: Evolution of the surface abundances of OH, HO_2, H_2O, H_2O_2 and O_3 as a function of time for 15 K and 25 K with different values for B and T_{ex}. Solid lines indicate $B = 10^{12}$ s^{-1} and $T_{ex} = 1400$ K. Dashed lines indicate the lower value for B or T_{ex}, dashed-dotted lines indicate the higher value. Simulations V, VII and VIII are depicted in panels (a) and (c), runs III, V and VI in panels (b) and (d).

results are also summarized in Table 5.4. The $\frac{2OH \rightarrow products}{HO_2 + H \rightarrow 2OH}$ ratio remains more or less unaffected with varying B, as expected since this is almost purely determined immediately after the formation of the two OH radicals. The influence of the B parameter becomes most apparent if one considers the number of diffusion events during thermalisation of a single species which is presented in the last column of Table 5.4. These diffusion events can bring the OH radicals to nearest-neighbour sites over a distance of approximately 3 Å, using a site density of 10^{15} sites cm^{-2}, or to next-nearest-neighbour sites over a distance of 4.5 Å. The number of diffusion events increases with decreasing B for the same T_{ex} since B controls how fast thermalisation occurs. The initial momentum of the particle is, however, determined by T_{ex} and the number of diffusion events is therefore a function of both. The average diffusion of a single species with an initial T_{ex} value of 1400 K ranges between 1.1 and 4.4 hops. Since we use a directionality for the mobility, OH will have more or less travelled in a straight line, in the opposite direction of the other OH radical formed. The OH radicals have therefore covered a spatial range of 3.3 to 20 Å. Molecular Dynamics simulations by Andersson et al. (2006) and Arasa et al. (2011) show that the distance travelled by an excited OH radical inside bulk, non-porous ice is approximately 2 Å. The distance travelled on top of a surface can range up to 80 Å. In our simulations, species are always restricted by either bulk molecules or neighbours residing on step edges and islands. Therefore we expect the distance travelled by a hot reaction product to be larger than 2 Å, but considerably smaller than 80 Å. We expect a value of 10^{12} s^{-1} for the B parameter therefore to be most realistic.

Experimentally, a large drop in the HO_2 and OH surface abundances accompanied by a strong increase in H_2O_2 is observed upon increasing the temperature from 15 to 25 K. The decreasing OH abundance is only reproduced by simulations III; the decrease in HO_2 and

Table 5.4: Summary of the effect of the B and T_{ex} parameters on the formation of OH and subsequent behaviour in the experimental simulations.

#	T_{ex} (K)	B (s^{-1})	T_{surf} (K)	$\frac{2OH \rightarrow products}{HO_2 + H \rightarrow 2OH}$	$\frac{[2OH]}{[H_2O_2]}$	Diffusion ('hot' events/sp)
III	200	10^{12}	15	0.90	0.03	1.0
IV	1000	10^{12}	15	0.62	0.49	1.1
V	1400	10^{12}	15	0.55	0.66	1.4
VI	2000	10^{12}	15	0.50	0.75	2.2
VII	1400	10^{11}	15	0.62	0.35	4.4
VIII	1400	10^{13}	15	0.55	0.66	1.1
IX	2000	10^{13}	15	0.50	0.79	1.1
III	200	10^{12}	25	0.90	0.01	1.0
IV	1000	10^{12}	25	0.69	0.32	1.2
V	1400	10^{12}	25	0.63	0.42	1.4
VI	2000	10^{12}	25	0.60	0.49	2.2
VII	1400	10^{11}	25	0.72	0.22	4.8
VIII	1400	10^{13}	25	0.64	0.40	1.1
IX	2000	10^{13}	25	0.62	0.42	1.1

increase in H_2O_2 are seen in all simulations. Experimentally, at 15 K OH is more abundant, whereas at 25 K H_2O_2 is more abundant. Taking this into account leads to best fit parameters of B = 10^{12} in combination with T_{ex} = 1400 or 2000 K. In conclusion, our simulations of the codeposition experiments show that thermalisation is indeed an important effect which can help explain the observed behaviour.

Simulations of sequential hydrogenation experiments show, however, that the produced H_2O/H_2O_2 ratio for the low T_{ex} value reflect the experimental results better. Moreover, the slight decrease of the H_2O_2 abundance around 10-20 minutes od experiment is best reproduced by an excess energy of 1400 K. For this reason, we will continue to use the parameters of simulations V throughout the remainder of the paper, but we will comment in the text how the other parameter choice affects the obtained experimental simulation results.

Finally, as mentioned in the introduction, Dulieu et al. (2013) studied the importance of chemical desorption of reaction products through sequential O_2 hydrogenation experiments where the amount of deposited O_2 remained in the (sub)monolayer regime. Their underlying substrate was an amorphous silicate or a graphite surface. They find substantial desorption of the formed H_2O molecules. This is caused, at least in part, by the lack of binding with surrounding molecules. Their (sub)monolayer system is fundamentally different from our bulk studies. Using our optimised model we indeed find a similar trend, albeit only concerning desorption of formed OH radicals. Desorption of OH radicals for a surface covered with $\sim$ 0.5 ML O_2 is a factor of 2.5–5 larger than on a surface covered with $\sim$ 3.5 ML O_2 for T_{ex} values of 1400 and 2000 K. Desorption of H_2O is not prominent, as expected, since a water molecule atop a water surface with one H_2O neighbour has a total binding energy of 5020 K in our simulations, comparable to the value reported by Dulieu et al. (2013).

5.4 SIMULATIONS OF INTERSTELLAR CONDITIONS

We have chosen to run simulations under interstellar conditions, using a T_{ex} of 1400 K and $B_{ice} = 10^{12}$ s^{-1} and $B_{grain} = 10^{11}$ or 10^{12} s^{-1}. The physical conditions and relative fluxes of the different species are given in Table 5.5 along with the values used in the laboratory. The physical conditions are chosen equal to those in Cuppen & Herbst (2007) for A2, D2, E2 and F2, representing a diffuse, translucent and two dense clouds, respectively. Also the same initial grain surface was used as in this previous study. This initial grain surface possesses a high degree of surface roughness and is therefore thought to be representative for the irregularly formed interstellar grains. For dense cloud condition II, H-atom diffusion is rapid and H-atom desorption is slow. Simulations can therefore not be run for astrophysically relevant timescales. We can however comment on the relative contribution of the H_2O production channels, since we find that these do not change beyond the production of one monolayer. Figure 5.3 shows the surface abundances for all species for two simulation runs of a typical diffuse cloud, Figure 5.4 for the translucent and dense cloud I conditions. Figure 5.5 gives cross sections of the resulting three simulated grains. Tables 5.6 and 5.7 summarize the contributions of the different reaction routes to OH and H_2O formation, respectively, for all four conditions.

5.4.1 *Diffuse clouds*

The simulations of the diffuse cloud conditions reach within 2×10^4 years an almost steady state situation of a more or less empty grain with a H_2O surface abundance of 1×10^{-3} ML and a OH surface abundance of 0.01 ML. Deposited oxygen atoms are efficiently converted into H_2O through reactions with H atoms. Due to the strong radiation field for these conditions all formed water molecules are photodissociated into OH which desorbs in 48 % of the photodissociation events during steady state. The remaining OH either reacts again with H atoms to H_2O or is further dissociated to O and H. This cycle results in this low surface coverage of H_2O and OH; the total ice coverage is lower than the equivalent simulations in Cuppen & Herbst (2007) (0.05 ML) and in the previous simulations H_2O was the dominant species. The reason for this discrepancy is the high OH photodesorption rate. We will come back to this issue later. The species that stay on the surface, fill the vacancies of the grain surface or reside near the step edges as can be seen in the left panel of Fig. 5.5, which shows cross sections of the simulated grain surfaces. The photodesorption rate of OH radicals on top of a grain fluctuates as function of time and appears to depend on the time-dependent, local configuration of the grain. If the water molecules are mostly present in a local configuration where the photodesorption rate is lower, their oxygen atoms will repeatedly undergo the formation-dissipation cycle resulting in lower average desorption rate. Once these atoms have desorbed the time-dependent photodesorption rate increases again until such a favourable configuration is again obtained. However, considering all dust grains in a typical diffuse cloud, these fluctuations will average out.

The photodesorption efficiency (amount of hot desorbed OH radicals devided by the number of H_2O photodissociation events) fluctuates between 28 and 80 % with a median value of 48 %. This is significantly higher than the values obtained by Andersson et al. (2006): 9 and 2 % for OH desorption *in* the first monolayer of crystalline and amorphous ice, respectively. In their case, the efficiency also depends on the local configuration. One would expect the desorption rate on top of a grain to be higher than from bulk ice because excess energy is probably easier to transfer to an molecular environment than to a more brittle grain surface. For this reason we ran additional simulations with a B_{grain} parameter of 10^{11} s^{-1}. This B_{grain}

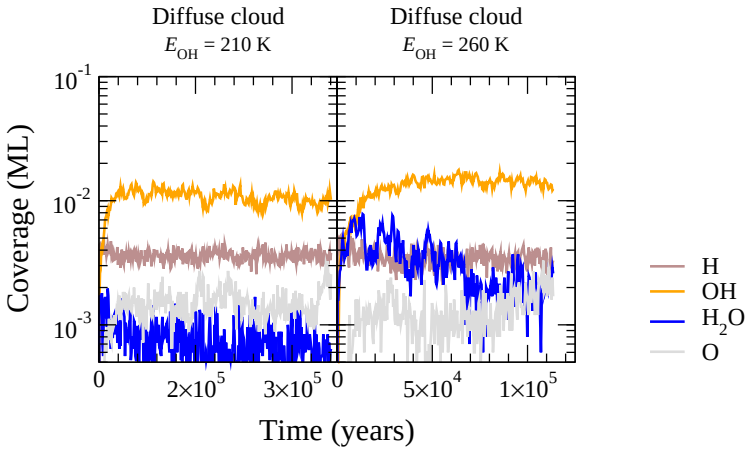

Figure 5.3: Simulated surface abundances of ice species in monolayers as a function of time under two diffuse cloud conditions. Panel (a) shows the abundances for a standard run with $E_{OH} = 210$ K, panel (b) for a run with $E_{OH} = 260$ K.

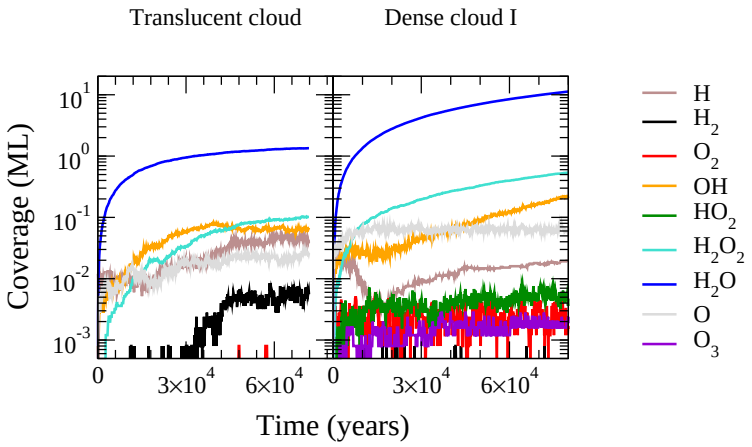

Figure 5.4: Simulated surface abundances of ice species in monolayers as a function of time under (a) translucent and (b) dense cloud I conditions.

Figure 5.5: Cross sections of simulated grains for the three cloud conditions: diffuse, translucent, and dense I, respectively. The grain sites are represented by black, orange is H_2, dark blue H_2O, light blue H_2O_2, yellow OH, and grey O.

Table 5.5: Physical conditions and initial fluxes of the reactants in the simulations under laboratory and interstellar conditions.

Parameter		Lab	Diffuse	Translucent	Dense I	Dense II
A_V (mag)		–	0.5	3	5	10
n_H (cm^{-3})		–	1×10^2	1×10^3	5×10^3	2×10^4
T_{gas} (K)		300	80	40	20	10
T_{grain} (K)		15	18	14	12	10
f_A (# cm^{-2} s^{-1})						
	H	2.5×10^{13}	3.2×10^6	2.3×10^5	3.2×10^4	2.3×10^4
	H_2	2.5×10^{13}	–	8.0×10^6	2.9×10^7	8.0×10^7
	O	–	2.4×10^2	1.7×10^3	6.1×10^3	1.7×10^4
	O_2	2.5×10^{13}	–	–	–	–

Table 5.6: Contributions of the different surface reaction routes to OH formation.

	T_{ex} (K)	$H + HO_2$	$H + O$	$H + O_3$	$H + H_2O_2$
Diffuse	1400	0.0	100.0	0.0	0.0
	2000	0.0	100.0	0.0	0.0
Translucent	1400	0.5	89.7	0.0	9.8
	2000	0.7	92.2	0.0	7.1
Dense I	1400	13.2	82.7	0.9	3.2
Dense II	1400	31.6	55.1	6.6	6.6

parameter is used for energy dissipation of species that do not have any molecule in their immediate vicinity. For these simulations the photodesorption efficiency of OH upon H_2O photodissociation behaves very similar (51 %). The steady state coverages of OH and H_2O remain the same for this case as can be seen in Fig. 5.3. Our values may be much higher, but concern an almost empty grain surface. The binding energy of an OH radical on top of a surface is most likely lower than of an OH embedded in a water layer. We ran some additional simulations in which we increased the binding energy of OH to the surface from $E = 210$ K to $E = 260$ K. In this case the photodesorption efficiency of OH ranges between 5 and 17 % with an average efficiency of 9 %, which is comparable to the results of Andersson et al. (2006). The steady state surface abundance is now 6×10^{-3} ML for H_2O and 0.02 ML for OH. Using this increased binding energy, the experimental simulations remain very similar and still reproduce the experimental observations. Finally, another parameter that is of influence on the photodesorption efficiency is T_{ex}, increasing its value to 2000 K also increases the photodesorption. In the following, all discussed simulations are parametrised according to T_{ex} of 1400 K and $B_{ice} = 10^{12}$ s^{-1} and $B_{grain} = 10^{11}$ s^{-1} and using the standard OH binding energy.

During the simulations, not only H_2O is formed, but H_2 as well. We see here that because of our rough surface, the residence time of the hydrogen atoms is not the rate limiting step, but rather the sticking probability of the hydrogen atoms to the surface. Since under these conditions the gas phase has a relatively high temperature of 80 K, the sticking probability of

Table 5.7: Contributions of the different reaction routes to H_2O formation.

	T_{ex} (K)	$H + OH$	$H_2 + OH$	$H + H_2O_2$	$OH + OH$	$H + HO_2$
Diffuse	1400	99.5	0.0	0.0	0.5	0.0
	2000	99.8	0.0	0.1	0.1	0.0
Translucent	1400	85.4	2.4	10.4	1.8	0.0
	2000	87.6	2.2	8.7	1.5	0.0
Dense I	1400	76.7	17.6	4.0	1.0	0.7
Dense II	1400	22.5	61.6	11.3	2.4	2.2

H atoms to the surface is relatively low ($\sim$ 33 %), but more than 47 % of all H atoms remaining on the surface react to form H_2, leading to an H_2 formation efficiency of 15 %. This is in good agreement with the results from Chang et al. (2005), who found a recombination efficiency of $\sim$ 10 % for temperatures as high as 21.8 K, which is enough to account for significant H_2 production in diffuse interstellar clouds. Again we can observe a time-dependent H_2 formation rate in the beginning of the simulation when the ice develops. This is because of similar arguments as for the time-dependent OH photodesorption rate. Lower E for H binding to the bare grain than 105 K results in lower H_2 formation rates, mainly because of the reduced sticking. Since we know observationally that H_2 has to be formed under these conditions, we have chosen to use this value for E. Lower values of E result in a similar production of H_2O and all other species, except H_2.

5.4.2 *Translucent clouds*

In general we observe a similar behaviour compared to the results from Cuppen & Herbst (2007), *i.e.*, the competition between photodissociation and surface reaction is key. The new photodissociation rates, following van Dishoeck et al. (2006), are higher than those previously used, but attenuate faster with visual extinction which results in lower rates at $A_V = 3$ mag.

In our present simulations the growing ice layer reaches a thickness of slightly more than a monolayer after 7×10^4 years, where a steady state seems to have been reached. Cuppen & Herbst (2007) obtained surface coverages of a few monolayers under equivalent circumstances. They found that the bottom layers are heavily processed and contain more oxygen-rich species like OH, O_2, and O_3 , since these layers lose part of their hydrogen due to the photoprocessing. Here, we stay around the monolayer regime and we therefore do not see the same effect. One of the reasons for this is the higher photodesorption rate. The ice structure found in the previous work was very porous due to the heavy processing. Figure 5.5b a cross section of the ice surface is depicted, where only some small pores can be found. The lack of strong porosity upon processing is in agreement with experimental work on ion irradiation of water ices by Palumbo (2006) and is probably caused by the exothermicity of the photoproducts that allows for restructuring.

The contribution of the various reaction routes (Tables 5.6 and 5.7) shows that most of the OH is formed through the reaction $O + H$, although the dissociation of H_2O also plays a role (see below). Even though the amount of H_2 is high, the $H_2 + OH$ route is less efficient in the formation of water ice, since the reaction is not barrierless. We observe H_2O_2 as a result of the reaction route $OH + OH$. The follow-up reaction $H + H_2O_2$ is consequently also more

important for both OH and H_2O formation, more than in the previous 2007 work. The H_2O production rate decreases for increasing times. We also observe that the contributions of the various reaction routes change with time, before the steady state is reached OH is formed only through H + O and H_2O only through H + OH. At later times, however, the contribution of H + H_2O_2 becomes stronger. Both the evaporation and dissociation rate of the various species also increase up to the point where the total surface coverage is ~ 0.6 ML, then the rates stabilize.

To distinguish between desorption originating from photodissociation events and from reaction heat is not trivial, hence we will only comment on it qualitatively. The largest part of the desorbing OH radicals originates from photodissociation of water. Changing the exothermicity to 2000 K leads to a larger amount of chemical desorption events, whereas increasing the binding energy of OH to the surface decreases this amount. Even though the relative contributions of the various reaction routes do not change upon changing these parameters, the final amount of (water) ice produced does. An increased desorption, regardless of the origin, decreases the ice thickness since less radicals are available for reaction.

5.4.3 *Dense clouds*

The right panel of Fig. 5.4 shows the surface abundance of a water covered grain for dense cloud condition I. For both dense cloud conditions I and II water ice is efficiently formed, more efficiently than in the Cuppen & Herbst (2007) simulations. The main reasons for this are that H_2 does not stick to the surface as easily, which prevented many surface reactions in the earlier work, and that the ice is more compact because of the use of excess energy. The latter can be seen in the right panel of Fig. 5.5, where a very compact ice is formed; much more compact than in Cuppen & Herbst (2007) where towers of H_2O were formed, typical for ballistic deposition (Kimmel et al., 2001). In the present simulations, the formed species have some momentum to move around and find a more favourable binding site, which leads to a smoothing of the formed ice. Oba et al. (2009) indeed find that ice that is formed on a surface shows more characteristics of a compact ice than ice that is deposited at similar low surface temperatures.

Under dense cloud conditions, the O_2 route becomes increasingly important, since the O/H flux ratio increases going from diffuse, to translucent to dense I and finally dense II. This can be seen in Table 5.6. The contribution of the H + HO_2 reaction to the formation of the hydroxyl radical increases. The intermediate HO_2 is formed from H + O_2. At the same time, we see the related reaction O_3 + H increases as well. A clear difference with the Cuppen & Herbst (2007) simulations is that now the O_2 channel does not exclusively proceed with H_2O_2 as an intermediate for H_2O formation. Table 5.7 shows that its contribution increases with density (O/H flux ratio), but not to the same extend as in the previous simulations. In the present work, most of the OH formed through the O_2 formation channel is transformed into water through the follow-up reactions OH + H and OH + H_2. Since the first has no barrier, this reaction is preferred under most circumstances. However, under dense cloud II conditions water ice is predominantly formed through the latter reaction, since the H_2 flux becomes much higher than the H flux and the surface residence time of H_2 increases at the same time because of the low surface temperature. Indeed, the main differences between the two dense cloud conditions are the density and the grain temperature. The percentage of intermediate species is higher for dense cloud II than for dense cloud I. This is probably because H atoms cannot convert these intermediate species into stable species as easily under these conditions. A lower temperature namely results in less H diffusion and the H-atom flux relative to the H_2 flux and O-atom flux is lower than for dense cloud I.

Photodesorption is not important here due to the high visual extinctions involved. Part of the formed water ice is returned into the gas phase, however, by chemical desorption. The 1400 K excess energy can be used for desorption when two reaction products are formed and therefore we see that chemical desorption is more efficient for the dense cloud II simulations since the contribution of reactions with two products ($H_2 + OH$ and $H + H_2O_2$) is larger here. Roughly, desorption of OH is 10 and 29 % respectively, for H_2O it amounts to 5 and 13 %.

In our current model, it is not possible for intermediate species HO_2 and H_2O_2 to desorb, although these species have been observed in the gas phase (Bergman et al., 2011; Parise et al., 2012; Du et al., 2012). Desorption mechanisms, other than chemical desorption, could be responsible for these observations. These mechanisms include photodesorption through cosmic ray photons or cosmic ray desorption, where a cosmic ray hit of a grain results in the desorption of most of the mantle material (Hasegawa & Herbst, 1993; Herbst & Cuppen, 2006). This stochastic rare event is rather hard to simulate considering a single grain, but integrated over a large cloud with many dust grains the effect can be significant. Another possible desorption mechanism that is not included here is the so-called kick-out mechanism, where a cold species desorbs as a result of a hit by a hot species. This was observed in Molecular Dynamics simulations to be important (Andersson et al., 2006; Arasa et al., 2010, 2011). Experimentally this mechanism was confirmed by time-of-flight measurements of the desorption fragments of water ice photodissociation (Yabushita et al., 2009). Similar conclusions were drawn for the photodesorption of N_2 in the presence of CO, where the excited CO kicks out N_2 which has no absorbance in applied photon range (Öberg et al., 2009b).

5.4.4 *Comparison to observations and other models*

Much of the work done since Cuppen & Herbst (2007) has focussed their attention on the importance of the molecular oxygen route for water formation. Here we found that this route has the largest implications in dense clouds, as expected. A particularly interesting region to study the influence of O_2 in dense clouds is ρ Oph A, where O_2, HO_2 and H_2O_2 have been detected in recent years (Larsson et al., 2007; Bergman et al., 2011; Parise et al., 2012; Du et al., 2012; Liseau et al., 2012). The derived abundances with respect to hydrogen are 5×10^{-8}, 1×10^{-10} and 1×10^{-10}, respectively. The hybrid moment equation approach was applied by Du & Parise (2011) to model the production of H_2O_2 on the surface of dust grains in the ISM. They ran a model for a range of different physical conditions and found reasonable agreement with observations for a time of 6×10^5 years, with abundance ratios of the three species of 60:3:1 in the gas phase for O_2:HO_2:H_2O_2. They use the chemical desorption mechanism introduced by Garrod et al. (2006) and see that the exact setting of the α parameter has a large influence on the gas phase composition. Furthermore, the reaction $OH + OH$ is excluded from their network and the reaction $H + H_2O_2$ has a lower barrier than adopted here. Both factors could increase their H_2O_2 abundance.

In our model we do not calculate any gas phase abundances, but as outlined by Öberg et al. (2009a) the gas phase abundance seems to reflect the composition of the co-existing ice mantles (see also Fig. 1 in Du & Parise (2011)). The dense cloud simulation runs do indeed produce O_2, HO_2, H_2O_2 next to H_2O where we do not see that the O_2 abundance is much higher than for HO_2 and H_2O_2, which is likely caused by the much lower desities considered. The physical parameters determined for ρ Oph A (T = 21 K and $n_H = 6 \times 10^5$ cm^{-3}) are not typical for dense clouds and lead to an atomic oxygen abundance of $3 \times 10^{-4} n_H$ corresponding to a flux of 7.5×10^5 atoms cm^{-2} s^{-1}. Comparing this to our values of 6.1×10^3 and 1.7×10^4 atoms cm^{-2} s^{-1} it is clear that much more O_2 and HO_2 can be produced. Results of our optimised model run with parameter settings as close as possible to those of ρ Oph A

show the following behaviour for the ice abundances $O_3 \gg O_2 > HO_2 > H_2O_2$. If we assume that the species H_2O_2 and HO_2 are predominantly formed on the grain surface and that the gas phase is a good reflection of the ice composition, our H_2O_2/HO_2 abundance ratio of 0.6 is in good agreement with the observed ratio presented by Parise et al. (2012) of 1.

As compared to the previous simulations of Cuppen & Herbst (2007), our final amount of produced H_2O is similar and varies as a function of A_V. Since the 2007 results were in good agreement with the observations by Whittet et al. (2001) of water ice in Taurus dark clouds in terms of the water ice threshold value of $A_V = 3.2$ K and linear growth of the column density of water ice above this value. The present results offer a similar agreement. The main differences between the studies are the formation routes for water ice. We expect this to have consequences for the deuterium fractionation of the ice species, although this was unexplored in the present paper. Since some of the channels like $H_2 + OH$ posses a barrier, which can be overcome through quantum chemical tunneling the formation of H_2O will be favoured over HDO. For other channels this might the reverse. Cazaux et al. (2010) included deuteration reactions in their water ice network to study this effect, unfortunately there is not enough experimental and quantum chemical evidence available to back up this network and to make it predictive.

5.5 DISCUSSIONS AND CONCLUSIONS

In the present paper, exothermicity of reactions is used to increase the momentum of the final products by increasing the hopping and desorption rates. Garrod et al. (2007) showed that chemical desorption can play an important role in explaining the observed abundance of different gas phase chemical species. Later Cazaux et al. (2010) and Dulieu et al. (2013) made similar conclusions. Here we see again the same effect. But exothermicity cannot only lead to desorption but can also lead to a more compact ice which has an effect on many diffusion properties and it can allow reactants to meet. In our simulations, we indeed see this compactification.

Here the exothermicity is only considered for reactions with two or more reaction products and the excess energy is only employed for diffusion and desorption and not to overcome chemical reactions. Allowing also single reaction products to desorb with a higher probability, leads to too much desorption under interstellar conditions: even in dense clouds hardly any ice is formed. Applying the excess energy to overcome reactions as well leads to too many $H + H_2O_2$ under experimental conditions. If the energy is not partitioned between the two products according to their relative masses, the desorption rate of OH upon H_2O photodissociation becomes near unity. Our set-up in the current paper therefore best describes experimental and astronomical observations as well as Molecular Dynamics simulations. Moreover, we believe this to be a rather accurate description of the underlying physics and chemistry, where the exothermicity is transferred into kinetic energy. Because of conservation of momentum this can only be done for reaction of multiple products and the energy is distributed considering their relative masses. How excess energy can be applied to overcome chemical barriers is not clear and this mechanism is currently missing in our models. With this Discussions we hope to trigger new dedicated studies and discussions on this topic and on the role of exothermicity in general. Also the role of a kick-out mechanism remains unexplored in this work.

BIBLIOGRAPHY

Andersson, S., Al-Halabi, A., Kroes, G.-J., & van Dishoeck, E. F. 2006, J. Chem. Phys., 124, 064715
Arasa, C., Andersson, S., Cuppen, H. M., van Dishoeck, E. F., & Kroes, G. 2010, J. Chem. Phys., 132, 184510
Arasa, C., Andersson, S., Cuppen, H. M., van Dishoeck, E. F., & Kroes, G. J. 2011, J. Chem. Phys., 134, 164503
Atkinson, R., Baulch, D. L., Cox, R. A., et al. 2004, Atmos. Chem. Phys., 4, 1461
Bergin, E. A. & Tafalla, M. 2007, Ann. Rev. Astron. Astrophys., 45, 339
Bergman, P., Parise, B., Liseau, R., et al. 2011, Astron. Astrophys., 531, L8
Bockelée-Morvan, D., Lis, D. C., Wink, J. E., et al. 2000, Astron. Astrophys., 353, 1101
Cazaux, S., Cobut, V., Marseille, M., Spaans, M., & Caselli, P. 2010, Astron. Astrophys., 522, A74
Chang, Q., Cuppen, H. M., & Herbst, E. 2005, Astron. Astrophys., 434, 599
Cuppen, H. M. & Herbst, E. 2007, Astrophys. J., 668, 294
Cuppen, H. M. & Hornekær, L. 2008, J. Chem. Phys., 128, 174707
Cuppen, H. M., Karssemeijer, L. J., & Lamberts, T. 2013, Chem. Rev., in press
Cuppen, H. M., Kristensen, L. E., & Gavardi, E. 2010, Mon. Not. R. Astron. Soc., 406, L11
Drake, M. J. 2005, Meteor. Planet. Sci., 40, 519
Du, F. & Parise, B. 2011, Astron. Astrophys., 530, A131
Du, F., Parise, B., & Bergman, P. 2012, Astron. Astrophys., 538, A91
Dulieu, F. 2011, in IAU Symposium, Vol. 280, IAU Symposium, ed. J. Cernicharo & R. Bachiller, 405–415
Dulieu, F., Congiu, E., Noble, J., et al. 2013, Sci. Reports, 3, 1338
Garrod, R., Park, I. H., Caselli, P., & Herbst, E. 2006, Faraday Discussions, 133, 51
Garrod, R. T., Wakelam, V., & Herbst, E. 2007, Astron. Astrophys., 467, 1103
Hasegawa, T. I. & Herbst, E. 1993, Mon. Not. R. Astron. Soc., 261, 83
Herbst, E. & Cuppen, H. M. 2006, Proc. Natl. Acad. Sci. USA, 103, 12257
Ioppolo, S., Cuppen, H. M., Romanzin, C., van Dishoeck, E. F., & Linnartz, H. 2008, Astrophys. J., 686, 1474
Ioppolo, S., Cuppen, H. M., Romanzin, C., van Dishoeck, E. F., & Linnartz, H. 2010, Phys. Chem. Chem. Phys., 12, 12065
Jansen, A. P. J. 1995, Comp. Phys. Comm., 86, 1
Kimmel, G. A., Dohnálek, Z., Stevenson, K. P., Smith, R. S., & Kay, B. D. 2001, J. Chem. Phys., 114, 5295
Larsson, B., Liseau, R., Pagani, L., et al. 2007, Astron. Astrophys., 466, 999
Liseau, R., Goldsmith, P. F., Larsson, B., et al. 2012, Astron. Astrophys., 541, A73
Matar, E., Congiu, E., Dulieu, F., Momeni, A., & Lemaire, J. L. 2008, Astron. Astrophys., 492, L17
Miyauchi, N., Hidaka, H., Chigai, T., et al. 2008, Chem. Phys. Lett., 456, 27
Muralidharan, K., Deymier, P., Stimpfl, M., de Leeuw, N. H., & Drake, M. J. 2008, Icarus, 198, 400
Oba, Y., Miyauchi, N., Hidaka, H., et al. 2009, Astrophys. J., 701, 464
Oba, Y., Watanabe, N., Hama, T., et al. 2012, Astrophys. J., 749, 67
Öberg, K. I., Bottinelli, S., & van Dishoeck, E. F. 2009a, Astron. Astrophys., 494, L13
Öberg, K. I., van Dishoeck, E. F., & Linnartz, H. 2009b, Astron. Astrophys., 496, 281
Palumbo, M. E. 2006, Astron. Astrophys., 453, 903
Parise, B., Bergman, P., & Du, F. 2012, Astron. Astrophys., 541, L11
Shalashilin, D. V. & Jackson, B. 1998, J. Chem. Phys., 109, 2856
van Dishoeck, E. F., Herbst, E., & Neufeld, D. A. 2013, Chemical Reviews, 113, 9043
van Dishoeck, E. F., Jonkheid, B., & van Hemert, M. C. 2006, Faraday Disc., 133, 231
Whittet, D. C. B., Gerakines, P. A., Hough, J. H., & Shenoy, S. S. 2001, Astrophys. J., 547, 872
Yabushita, A., Hama, T., Yokoyama, M., et al. 2009, Astrophys. J. Lett., 699, L80

6

RELEVANCE OF THE H_2 + O PATHWAY FOR THE SURFACE FORMATION OF INTERSTELLAR WATER

The formation of interstellar water is commonly accepted to occur on the surfaces of icy dust grains in dark molecular clouds at low temperatures (10-20 K), involving hydrogenation reactions of oxygen allotropes. As a result of the large abundances of molecular hydrogen and atomic oxygen in these regions, the reaction $H_2 + O$ has been proposed to contribute significantly to the formation of water as well. However, gas-phase experiments and calculations, as well as solid-phase experimental work contradict this hypothesis. Here, we use precisely executed temperature-programmed desorption (TPD) experiments in an ultra-high vacuum setup combined with kinetic Monte Carlo (KMC) simulations to establish an upper limit of the water production starting from H_2 and O. These reactants were brought together in a matrix of CO_2 in a series of (control) experiments at different temperatures and with different isotopological compositions. The water detected with the quadrupole mass spectrometer upon TPD was found to originate mainly from contamination in the chamber itself. However, if water is produced in small quantities on the surface through $H_2 + O$, this can only be explained by a combined classical and tunneled reaction mechanism. An absolutely conservative upper limit for the reaction rate was derived with a microscopic kinetic Monte Carlo model that converts the upper limit into the highest possible reaction rate. Incorporating this rate into simulation runs for astrochemically relevant parameters shows that the upper limit to the contribution of the reaction $H_2 + O$ in OH, and hence water formation, is 11% in dense interstellar clouds. Our combined experimental and theoretical results indicate, however, that this contribution is most likely much lower.

T. Lamberts, H. M. Cuppen, G. Fedoseev, S. Ioppolo, K.-J. Chuang, and H. Linnartz, *Relevance of the $H_2 + O$ reaction pathway for the surface formation of interstellar water*, Astronomy and Astrophysics 570 (2014) A57

6.1 INTRODUCTION

The formation of interstellar water is commonly believed to occur mostly on the surfaces of icy dust grains in dark molecular clouds where the temperatures typically range between 10 and 20 K. In recent years, several studies have been focusing on the reaction of atomic hydrogen with O, O_2, and O_3 in interstellar ice analogs, both experimentally and through surface models (Chapter 4 and Hiraoka et al., 1998; Dulieu et al., 2010; Miyauchi et al., 2008; Ioppolo et al., 2008; Oba et al., 2009; Ioppolo et al., 2010; Cuppen et al., 2010; Mokrane et al., 2009; Romanzin et al., 2011; Oba et al., 2012). A possibly interesting alternative pathway to form water under interstellar conditions starts from the reaction

$$H_2 + O \rightarrow OH + H \tag{R1}$$

and is followed by

$$OH + H \rightarrow H_2O \tag{R2}$$

or

$$OH + H_2 \rightarrow H_2O + H. \tag{R3}$$

Reaction R1 has been proposed to contribute significantly to the formation of water since molecular hydrogen and atomic oxygen are both abundantly present in the dense regions of the interstellar medium (Cazaux et al., 2010, 2011). Additionally, Cazaux et al. (2010) proposed this reaction to be important for deuterium enrichment during water formation. Conceptually, the interaction between H_2 and the surface could aid in breaking the H-H bond. The reaction is, however, endothermic by 960 K, making it intuitively unlikely to occur in the low-temperature regime. Moreover, a theoretical barrier in the gas phase of approximately 7000 K is predicted for the case that both O and H_2 are in the ground state (Rogers et al., 2000). Gas-phase experimental work also predicts high barriers (~3000 K), as reviewed by Baulch et al. (1992). Barriers of this order of magnitude lead to thermally induced reaction rates that are so slow that their contribution to the full chemical reaction network becomes negligible even over the long interstellar timescales of several million years (Bergin & Tafalla, 2007). It should be noted that at low temperatures tunneling may play an important role, but tunneling through the barrier of an endothermic reaction can only take place if the reactants have an initial energy equal to or higher than the endothermicity (Arnaut et al., 2006).

For these reasons, reaction R1 was excluded in the reaction scheme used by Cuppen & Herbst (2007), who studied the formation of ice mantles on interstellar grains. Recent solid-state laboratory studies by Oba et al. (2012) showed no detectable production of H_2O by means of infrared spectroscopy upon co-deposition of H_2 and O atoms, which motivated Taquet et al. (2013) to exclude it from their ice chemistry reaction network as well.

Here ultra-high vacuum (UHV) surface chemistry experiments are carried out at low temperature in conjunction with KMC modeling to clarify the ambiguity in the importance of the reaction H_2 + O under interstellar conditions.

6.2 CALCULATION OF THE REACTION RATE

Reactions are often considered to take place along pathways such as those shown in Fig. 6.1. The reaction coordinate is depicted on the horizontal axis, energy on the vertical axis, ΔE indicates the difference in potential energy between reactants (A + B) and products (C + D), and the reaction rate is determined by the barrier or activation energy, E_a.

In astrochemical models it is common to use a straightforward expression to calculate a reaction rate as a result of the large chemical networks involved (Garrod & Herbst, 2006). Calculating the reaction rates therefore often involves a rather arbitrary choice between the expression for classically (*i.e.*, thermally) activated reactions

$$k_{\text{therm.}} = \nu \exp\left(-\frac{E_a}{T}\right) \tag{39}$$

and the expression for tunneling of a free particle through a rectangular barrier (Bell, 1980)

$$k_{\text{exo. tunn.}} = \nu \exp\left(-\frac{2\,a}{\hbar}\sqrt{2\,\mu\,E_a}\right). \tag{40}$$

Typically, the trial frequency ν is approximated by the standard value for physisorbed species, $kT/h \approx 10^{12}\ s^{-1}$ and a barrier width a of 1 Å is chosen. In the expression for the tunneling rate the reduced mass, μ_{red}, is usually taken to be the reduced mass of the total reacting system without taking into account the mutual orientation of the reactants. The mass should, however, be affiliated with the reaction coordinate involved, as was done in recent work of a linear bimolecular atom-transfer reaction leading to an effective mass, μ_{eff} (Oba et al., 2012). In the case of reaction R1 the difference between the reduced and the effective mass gives rise to a substantial increase of the reaction rate (see also Table 6.1).

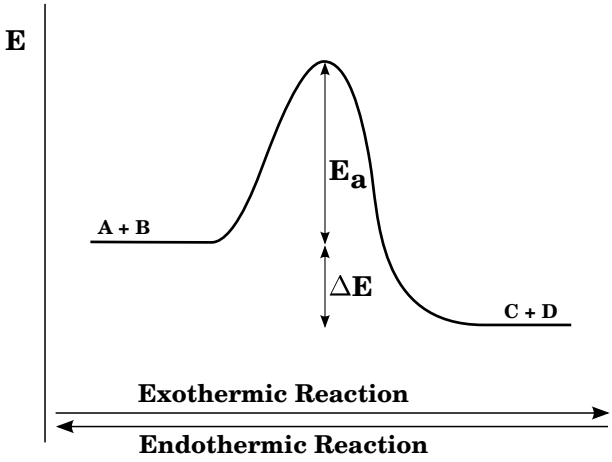

Figure 6.1: Schematic representation of the energy level diagram of an exothermic and endothermic reaction.

Tunneling rates for endothermic reactions, $k_{\text{endo. tunn.}}$ (see Fig. 6.1), need to be calculated as a combination of Eqs. 39 and 40, where the classical contribution accounts for the part of the reaction barrier that lies below the endothermicity and the tunneled contribution for that above (Arnaut et al., 2006). This can be derived from arguments of detailed balance (or microscopic reversibility): in equilibrium the net flux between every pair of states is zero. The reaction rates should then obey the condition

$$\frac{k_{\text{endo. tunn.}}}{k_{\text{exo. tunn.}}} = \exp\left(-\frac{\Delta E}{T}\right), \tag{41}$$

and hence, following the definition for E_a from Fig. 6.1,

$$k_{\text{endo. tunn.}} = k_{\text{exo. tunn.}} \exp\left(-\frac{\Delta E}{T}\right) = \nu \exp\left(-\frac{2a}{\hbar}\sqrt{2\mu E_a}\right) \exp\left(-\frac{\Delta E}{T}\right) . \quad (42)$$

The comparison between these various ways of calculating the reaction rate spans a wide range. as outlined in Table 6.1. A more accurate way to calculate reaction rates also takes into account the shape of the barrier, examples of which are the usage of the Eckart model by Taquet et al. (2013) or the implementation of instanton theory by Andersson et al. (2011). This results in modified tunneling reaction rates with differences of up to several orders of magnitude. Depending on the expression used, the resulting reaction rate can be substantially different. The ambiguity makes it hard to interpret these values in terms of their astronomical relevance. One way to partially circumvent this is to make use of upper (or lower) limits, determined experimentally.

In the following sections we use laboratory experiments combined with microscopic kinetic Monte Carlo simulations to constrain the reaction rate of reaction R1. Subsequently, the resulting reaction rate is incorporated into the same KMC model, but run with physical parameters relevant to the interstellar medium to test its astronomical significance.

Table 6.1: Calculated reaction rates for the reaction $H_2 + O$ assuming classical and tunneled contributions.

Eqn. used	T (K)	ΔE (K)	E_a (K)	μ	Rate (s^{-1})
(39) $k_{\text{therm.}}$	10	960	(...)	(...)	5.2×10^{-119}
(39) $k_{\text{therm.}}$	13.5	960	(...)	(...)	3.1×10^{-85}
(42) $k_{\text{endo. tunn.}}$	10	960	2040[a]	$\mu_{\text{eff}} = 0.47$	5.0×10^{-36}
(42) $k_{\text{endo. tunn.}}$	13.5	960	2040[a]	$\mu_{\text{eff}} = 0.47$	3.2×10^{-25}
(40) $k_{\text{exo. tunn.}}$	(...)	(...)	3000	$\mu_{\text{red}} = 1.78$	1.2×10^{-1}
(40) $k_{\text{exo. tunn.}}$	(...)	(...)	3000	$\mu_{\text{eff}} = 0.47$	$2.3 \times 10^{+5}$

[a] The total barrier of the reaction is the combination of the endothermicity, ΔE, and the barrier itself, E_a, which amounts in total to ~ 3000 K Baulch et al. (1992)

6.3 EXPERIMENTS

6.3.1 *Methods*

Experiments were performed using the SURFRESIDE^2 setup, which allows for the systematic investigation of solid-state reactions leading to the formation of molecules of astrophysical interest at cryogenic temperatures. SURFRESIDE^2 consists of three UHV chambers with a room-temperature base-pressure between $10^{-9} - 10^{-10}$ mbar. The setup has already been extensively described in Ioppolo et al. (2013) and therefore only a brief description of the procedure is given here. A rotatable gold-coated copper substrate in the center of the main chamber is

cooled to 13.5-14.0 K using a He closed-cycle cryostat with an absolute temperature accuracy of $\leqslant$ 2 K. This temperature is around the lower limit of what can be reached under our experimental conditions and was chosen to minimize the diffusion of the oxygen atoms, but simultaneously have a long lifetime of H_2 and O on the surface. To study the solid-state reaction pathway $H_2 + O$, the reactants need to be deposited on a surface while simultaneously preventing the competing reactions $O + O \longrightarrow O_2$ and $O + O_2 \longrightarrow O_3$. This was achieved by using a matrix consisting of CO_2 molecules and an overabundance of molecular hydrogen. A full experiment starts with the preparation of all selected gases in separate pre-pumped ($\leqslant 10^{-5}$ mbar) dosing lines. Then a co-deposition of H_2, O and CO_2 is performed. Room-temperature carbon dioxide (Praxair 99.996%) is deposited through a metal deposition line under an angle of 90°. Room-temperature molecular hydrogen (Praxair 99.999%) is deposited on the surface through an UHV beam line with an angle of 45° with respect to the surface. Oxygen atoms are generated from $^{18}O_2$ (Aldrich 99%) in another UHV beam line in a microwave plasma atom source (Oxford Scientific Ltd, see (Anton et al., 2000)) with an angle of 135° with respect to the surface. A custom-made nose-shaped quartz-pipe is placed in between the atom sources and the substrate. The pipe is designed in such a way that all chemically active species that are in their electronic and/or ro-vibrationally excited states are quenched to room temperature before being deposited to the surface. In addition to ^{18}O atoms a (large) fraction of non-dissociated $^{18}O_2$ is also present in the beam. The UHV beam lines can be operated independently and are separated from the main chamber by metal shutters. All experiments and the corresponding atomic and molecular fluxes are listed in Table 6.2. The effective O flux determination by Ioppolo et al. (2013) was repeated and found to be reproducible: 2×10^{11} at cm^{-2} s^{-1} (uncertainty ~30%). Each (control) experiment was performed for 75 minutes. Experiments 1, 2, and 3 were performed twice to check their reproducibility. The aim of these experiments is to determine an upper limit for the production of water during co-deposition.

SURFRESIDE^2 has two main analytical tools: (i) the ice composition is monitored *in situ* by means of reflection absorption infrared QMS spectroscopy in the range between 4000 and 700 cm^{-1} with a spectral resolution of 1 cm^{-1}; (ii) the main chamber gas-phase composition is monitored by a quadrupole mass spectrometer (QMS) that is placed behind the rotatable substrate. Here, we deposited a total of 0.9 ML O atoms per experiment, meaning that RAIR spectroscopy could only be used if the reaction is indeed as efficient as claimed by the exothermic tunneled rate. RAIR difference spectra with respect to the bare substrate were recorded every 5 minutes, averaging over 512 scans. After the co-deposition was finished, the sample was rotated to face the QMS and a temperature-programmed desorption (TPD) experiment at 1 K min^{-1} was performed to monitor the desorption of the ice constituents. The QMS is typically used for the study of species that fall below the detection limit of RAIR spectroscopy, that is, submonolayer experiments.

To convert the integrated area of the current (pressure) read by the QMS to a number of molecules desorbing from the sample, we performed several calibration experiments. First, to relate the ice thickness to a QMS signal, we deposited layers of water of three different thicknesses at 13.5-14 K, followed by a TPD at the usual ramp of 1 K min^{-1}. Following this, the water RAIR spectral signal at 3280 and 1660 cm^{-1} of these three experiments was converted into a number of monolayers using the IR bandstrength. This is, however, because of the reflection mode of the IR spectrometer, which is setup dependent. The bandstrength of CO_2 in reflection mode was determined through an isothermal desorption experiment by Ioppolo et al. (2013). A similar calibration experiment cannot be easily performed for H_2O, because of the rearrangement of hydrogen bonds at high temperatures, which changes the desorption profile. Therefore, the ratio between the transmission bandstrengths of CO_2 and H_2O was taken from Gerakines et al. (1995) to derive the bandstrengths in reflection mode for the 3280

and 1660 cm^{-1} bands of water. Finally, the value for the integrated QMS signal, corresponding to one monolayer of desorbing water molecules, is determined by averaging over the three deposited water layers.

The experiments were analyzed by first performing a linear baseline correction between 115 and 195 K. Then, the mass 20 amu signal was integrated over two ranges; one centered on the CO_2 desorption (~80 K) and one at the H_2O desorption (~140 K) given in Table 6.2. The combined signal was converted into a number of produced monolayers, averaged over the two experiments and given in the last column of Table 6.2.

In previous experiments not listed in Table 6.2, we used a different CO_2 flux and another source of atomic oxygen, $N_2{}^{16}O$. The latter has the main advantage that the competing ozone channel is less likely to occur since there is only little O_2 present in the plasma source. It does yield regular water ($H_2{}^{16}O$), which is hard to distinguish from the contamination present in all parts of the experimental setup. The use of $^{18}O_2$ as a precursor of atomic oxygen would lead to the formation of $H_2{}^{18}O$, which can be better distinguished from background water contamination. However, as previously mentioned, the resulting O-atom beam would have an overabundance of undissociated O_2 that might react with atomic oxygen to form $^{18}O_3$. The amount of $^{18}O_3$ produced in this way was calculated using the band strength determined by Ioppolo et al. (2013).

We stress that even a low efficiency of the reaction $H_2 + O$ may have a substantial impact on water formation for the timescales relevant in space. The nature of the system (low reaction probability as well as the low oxygen flux) requires several control experiments to identify the contribution of background water deposition from the different parts of the experimental setup. Therefore, special care has to be taken to exclude any experimental contaminations. To ensure that the amount of background water deposition is as equal as possible on a day-to-day basis, all (control) experiments were preceded by a day during which the experimental setup was used only running the $^{18}O_2$ plasma for three hours, allowing the fragments to enter the main chamber as well to obtain stable experimental conditions. Furthermore, the timing of the sequential experimental actions was kept equal throughout all experiments.

6.3.2 *Results and discussion*

This section explains the principle behind the ten experiments mentioned in Table 6.2. We also discuss, the RAIR spectroscopy results and QMS data and several ways to establish an upper limit of water production. We show that with our set of experiments a conservative upper limit of 0.09 ML is found over an experimental duration of 75 minutes.

To distinguish the origin of the different contributions from the detected 20 amu mass signal in the QMS (experiment 1), three control experiments were performed, as indicated in Table 6.2: (a) to see the amount of $H_2{}^{18}O$ produced inside the plasma (experiment 2), (b) to find the influence of the high H_2 pressure inside the main chamber that can potentially result in sputtering of water off the walls of the UHV system (experiment 3), and (c) to check on the background deposition of water without any atoms or molecules in the setup (experiment 4). The upper limit to water production is then determined by

$$[H_2{}^{18}O]\,((1) - (2) - (3) + (4)) \ . \tag{43}$$

Table 6.2: List of (control) experiments and integrated baseline-corrected QMS signals for m/z = 20 and 22, *i.e.* $H_2{}^{18}O$ and $D_2{}^{18}O$, and the calculated $H_2{}^{18}O$ abundance in ML.

Nr.	Experimental parameters							Integrated QMS signal		
	T (K)	Time (min)	CO_2 flux (mol cm^{-2} s^{-1})	$^{18}O_2$ flux (mol cm^{-2} s^{-1})	^{18}O flux (at cm^{-2} s^{-1})	H_2/D_2 flux	(mol cm^{-2} s^{-1})	70-105 (K)	125-175 (K)	$H_2{}^{18}O$ (ML)
1[a]	14	75	1.6×10^{14}	1.7×10^{12}	2×10^{11}	H_2	2.2×10^{14}	2.1×10^{-9}	2.1×10^{-9}	0.26
2[b]	14	75	1.6×10^{14}	1.7×10^{12}	2×10^{11}	–	–	9.6×10^{-10}	6.4×10^{-10}	0.10
3[b]	14	75	–	–	–	H_2	2.2×10^{14}	2.2×10^{-10}	4.2×10^{-10}	0.03
4[b]	14	75	–	–	–	–	–	~ 0	1.3×10^{-10}	~ 0
5[a]	14	300	1.6×10^{14}	1.7×10^{12}	2×10^{11}	H_2	2.2×10^{14}	–[c]	–[c]	~ 1 [d]
6[a]	17	75	1.6×10^{14}	1.7×10^{12}	2×10^{11}	H_2	2.2×10^{14}	1.2×10^{-9}	1.3×10^{-9}	0.15
7[a]	35	75	1.6×10^{14}	1.7×10^{12}	2×10^{11}	H_2	2.2×10^{14}	1.7×10^{-9}	8.4×10^{-10}	0.16
8[a]	50	75	1.6×10^{14}	1.7×10^{12}	2×10^{11}	H_2	2.2×10^{14}	1.6×10^{-9}	4.2×10^{-10}	0.12
9[a]	14	75	1.6×10^{14}	1.7×10^{12}	2×10^{11}	D_2	1.2×10^{14}	– [e]	5.0×10^{-11} [f]	–
								1.8×10^{-9} [g]	9.4×10^{-10} [g]	0.17
10[a]	14	75	1.6×10^{14}	1.7×10^{12}	2×10^{11}	D_2	2.2×10^{14}	– [e]	1.5×10^{-10} [f]	–
								2.7×10^{-9} [g]	9.4×10^{-10} [g]	0.22

Note. The baseline-corrected QMS signals are integrated over two different temperature ranges covering the CO_2 and the H_2O desorption peaks, 70-105 K and 125-175 K.

[a] Experiment. [b] Control experiment. [c] Different ramp rate. [d] from RAIR spectroscopy. [e] Overlaps with doubly ionized CO_2. [f] m/z = 22. [g] m/z = 20.

Experiment 4 is added here, not subtracted. The reason behind this is that experiment 4 gives a contribution that is already included in each other experiment. Therefore if we subtract experiments 2 and 3 from 1, the contribution of experiment 4 is subtracted twice and should therefore be added once to obtain the correct number. Apart from the control experiments, a series of other experiments were performed and added to Table 2 (experiments 5-9). First, we expect the amount of water formed on the sample to be very small. Therefore, we performed experiment 1 for a four times longer duration (experiment 5) to allow for a possible detection of water ice with RAIR spectroscopy. Second, we conducted experiments 6, 7, and 8 at different temperatures to retrieve information on the nature of the surface reaction that may lead to the formation of water ice. For instance, the so-called Langmuir-Hinshelwood (LH) mechanism is temperature dependent, whereas the Eley-Rideal (ER) and hot atom (HA) mechanisms are much less so. Finally, we performed two more experiments (9 and 10) with D_2 instead of H_2 to test to which extent a reaction occurs via (partial) tunneling. Changing the mass of a reactant is a well-established experimental technique generally used to verify whether or not a reaction is classically (thermally) activated or proceeds through tunneling (Oba et al., 2012, 2014) .

6.3.2.1 *RAIR spectroscopy*

In all the experiments where the plasma source was operated, ozone formation was confirmed through RAIR spectroscopy, but no significant difference could be found between the production in experiments 1 and 2. The amount of O_3 detected in both cases is equal to the total amount of O atoms deposited on the surface within the 30% uncertainty in the flux. Therefore, this leaves a maximum of 30% of the O flux to be used for reaction with H_2, that is, an upper limit to water production of

$$30\% \cdot \frac{2 \times 10^{11} \text{at cm}^{-2}\ \text{s}^{-1} \cdot 75\ \text{min} \cdot 60\ \text{s min}^{-1}}{1 \times 10^{15}\ \text{at ML}^{-1}}$$

amounting to 0.27 ML in 75 minutes.

Experiment 1 does not result in a detectable amount of formed OH or H_2O on the basis of their infrared solid-state spectral features. Moreover, there is no significant difference between RAIR spectra of experiments 1 and 2, as demonstrated in Fig. 6.2. The small features visible in the 1600-1800 cm^{-1} range are due to water vapor, and they in fact determine the detectable level. Comparing these spectra with a spectrum obtained from a previous co-deposition experiment of H:O_2 = 1:1 (Cuppen et al., 2010), where OH, OH·H_2O and H_2O spectral bands were found at 3548, 3463, 3426, and 1590 cm^{-1}, we conclude that the maximum water production falls below the detection limit of RAIR spectroscopy during a 75 minutes experiment. Therefore, we performed a 300 minutes co-deposition (experiment 5 in Table 6.2). In this case, the water peak at 1590 cm^{-1} was clearly visible and, moreover, after gently annealing to 110 K at a ramp of 0.5 K min^{-1} to remove CO_2 and O_2 from the ice, a RAIR spectrum was recorded where approximately 1 ML of water was visible. The upper limit to water production seen with RAIR spectroscopy thus remains ~ 0.25 ML for an experiment of 75 minutes.

6.3.2.2 *QMS*

Quadrupole mass spectroscopy allows one to better constrain an upper limit for water formation thanks to its higher sensitivity. Table 6.2 summarizes the integrated baseline-corrected QMS signals for mass 20 amu ($H_2^{18}O$). Figure 6.3 shows the baseline-corrected QMS traces of experiments 1-4 from Table 6.2, both the co-desorption with CO_2 and the thermal desorption of H_2O are visible. Experiments 1-3 were performed twice and both traces are shown. The desorption in the region between 14 and 70 K was not taken into further consideration. This

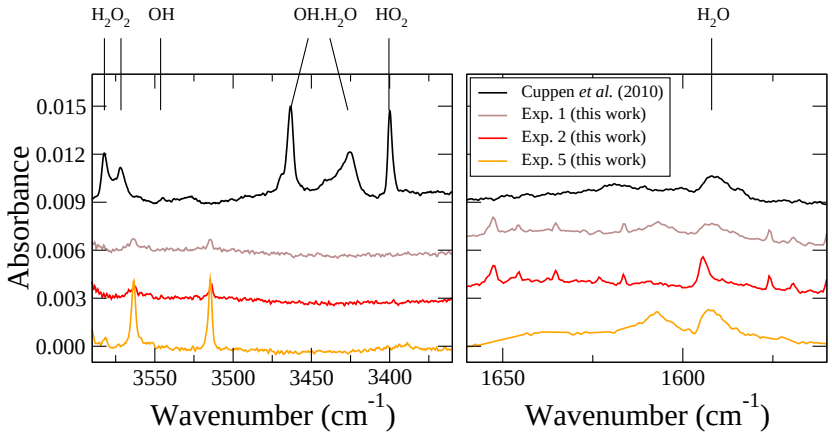

Figure 6.2: RAIR difference spectra from a co-deposition of H and $^{16}O_2$ from Cuppen et al. (2010), H_2, CO_2 and ^{18}O (experiment 1), CO_2 and ^{18}O (experiment 2). Spectra are baseline corrected and offset for clarity. The spectra corresponding to experiments 1, 2 and 5 are scaled with a factor 3. Note that the multitude of peaks in the right panel for experiments 1 and 2 are due to water vapor in the setup, and the peaks at 3515 and 3564 cm^{-1} are also visible in a 'pure' CO_2 spectrum.

is because of the contribution from the species desorbing from the heating tape area in proximity of the substrate, and also because of the oversaturation of the signal by desorption of H_2 or D_2, as can be concluded from comparing experiments 1 and 3. Experiments 1, 2, and 3 all were performed twice, and the difference between the sum of the integrated signals of two identical experiments is 16, 5, and 26% respectively, indicating that the overall uncertainty is on the order of 25% or smaller.

The upper limit to water production, calculated with Eqn. 43, is about a factor 2 lower than concluded from the RAIR spectral data: 0.14 ML during a 75-minute experiment. The m/z = 20 signal of both the co-desorption with CO_2 and pure desorption of water was taken into account.

Species that react via the LH mechanism are thermalized and stay on the surface, where they diffuse until they meet. This mechanism can be tested by changing the temperature of the ice. In this case, the production of water is expected to decrease with increasing temperature because of a lower surface abundance of H_2 and, moreover, no products should be detected at temperatures above the desorption temperature of one of the reactants. For this reason, the experimental temperatures employed here were 17, 35, and 50 K (experiments 6, 7, and 8). All detected m/z = 20 signals in these experiments are close to the background level determined at 14 K by experiments 2 and 3. We assume that the observed water is indeed formed - even though this not necessarily has to be the case - and below we discuss various mechanisms. The detected amounts at 17 and 35 K are equal, implying that the LH mechanism probably does not govern any potential reaction, because of the temperature dependence of the residence time at the surface. Moreover, the integrated m/z = 20 signal decreases further when increasing the temperature to 50 K, but it still remains non-negligible. This means that the ER and/or HA mechanisms probably are responsible for any H_2O formation, at least in part and most likely even at 14 K. For both mechanisms one or more reaction partners are not thermalized. For the HA mechanism again both reaction partners are present on the surface, but at least one of them is in some excited state (*i.e.*, not thermalized), whereas ER assumes that one

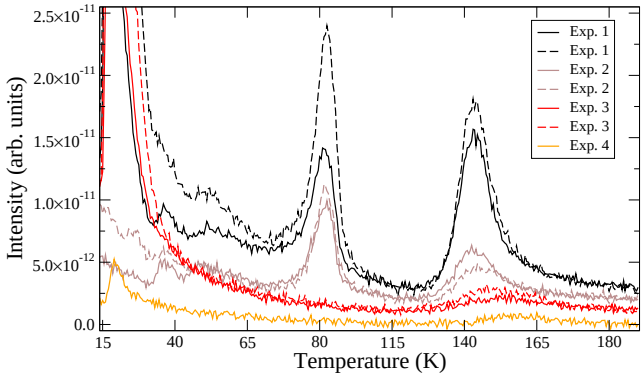

Figure 6.3: QMS traces of mass 20 amu for experiments 1-4 from Table 6.2. Spectra are baseline corrected, offset for clarity, and binned by averaging 5 points. Experiments 1-3 have been performed twice, hence two traces are depicted by the solid and dashed lines.

reaction partner is present on the surface and the second comes directly from the gas phase and therefore must have a temperature of ~300 K. Both mechanisms in combination with excitation are not expected to be astronomically important because of the longer timescales and the much lower gas-phase temperature in dense molecular clouds. The significance of this reaction pathway in the interstellar medium (ISM), therefore, will be negligible.

The reaction itself can proceed either classically activated or through a combination of both a classical and tunneled contribution (*e.g.*, Eqn. 42). Tunneling depends on the mass of the reactants involved. Exchanging hydrogen for deuterium would result in a decrease of the tunneled reaction rate of $D_2 + O$ and therefore a decrease in the production of m/z = 22 ($D_2{}^{18}O$) compared to m/z = 20 ($H_2{}^{18}O$). Comparing the integrated QMS signals of m/z = 22 in experiments 9 and 10 with m/z = 20 in experiment 1 at 125-175 K, we indeed see a large drop up to barely no signal. Therefore, $H_2{}^{18}O$ formation in experiment 1 through a mechanism in which tunneling plays a role cannot be eliminated. Because of the endothermicity of the reaction, this has to be a combination of classical and tunneling behavior. As explained above, the classical part can be overcome by some excitation effect.

Finally, even in the experiments performed with D_2 still $H_2{}^{18}O$ was detected, which can only be caused by water contamination. From the result found in experiment 9 it is possible to directly estimate the upper limit with

$$[H_2{}^{18}O]\,((1)-(9)) \tag{44}$$

instead of with Eqn. 43. The difference in signal between experiments 1 and 9 was therefore taken as the final range for the upper limit to water production for our KMC model, that is, 0.09 ML in 75 minutes. Because we wish to determine an upper limit here, we worked with the outcome of experiment 9 and not 10 to guarantee that we remained on the conservative side.

6.4 THEORETICAL

6.4.1 *Kinetic Monte Carlo model*

This section describes the specific kinetic Monte Carlo procedure used for the simulations and focuses on the difference between modeling experimental results and modeling under interstellar relevant conditions. For a more detailed overview of the method we refer to Chang et al. (2005) and Cuppen et al. (2013). The code we used is described in Chapters 4, 5, and Cuppen & Herbst (2007).

The grain is represented by a lattice of 50×50 sites with periodic boundary conditions, in which each lattice site can be occupied by one of the following species: H, H_2, O, O_2, O_3, OH, HO_2, H_2O, and H_2O_2. Interstitial sites can be only occupied by H, H_2, O, and OH. Processes incorporated in the simulations are (i) deposition from the gas phase to the surface, (ii) desorption from the surface back into the gas phase, (iii) diffusion on the surface, (iv) reaction, when two species meet each other, and (v) (photo)dissociation upon energy addition to the species. Each of these processes is simply modeled as a change in the occupancy of the sites involved. The event rates are assumed to be classically activated and are calculated using (a form of) Eqn. 39. The barrier for desorption and diffusion depends on the binding energy of the species to the specific site it occupies. The reaction network consisting of 16 surface reactions and their corresponding rates is taken from Chapter 5. Photodissociation is implemented only in the interstellar simulations to investigate the influence of the interstellar radiation field. In this case, the five relevant reactions and their rates are taken from van Dishoeck et al. (2006).

The following strategy was applied: first KMC calculations were used to reproduce the experiments with the aim to find an upper limit for the reaction rate (Section 6.4.2). The resulting rate was then used to simulate the formation of interstellar ice on astrochemical timescales with a full water surface reaction network to determine the contribution of the $H_2 + O$ reaction to the total production of water ice on interstellar grains in dense clouds (Section 6.4.3). Note that, again, this is a conservative method since we already attributed any possible H_2O formation to mechanisms not relevant in the ISM. Below, however, we assume an LH type mechanism. Our reaction network neither includes any species with C or N atoms, which will also consume hydrogen. Here we specifically compare the contributions of the reactions $H + O$ and $H_2 + O$.

6.4.2 *Experimental modeling*

All surface abundances increase linearly with time, similar to those for co-deposition experiments in Chapters 4 and 5. The final abundances mentioned here were determined after 75 simulated experimental minutes. In all experimental simulations water was produced by the immediate follow-up reaction R2, $H + OH \longrightarrow H_2O$, because of our implementation of zero excess energy for the reaction $H_2 + O \longrightarrow OH + H$. H and OH remain in each other's vicinity and can thus easily react. The uncertainty in the H_2O surface abundance was derived from two different simulations that were each repeated three times. We find values decreasing in time from roughly 25 to 7%, where the largest error bar thus corresponds to the lowest amount of species on the surface.

The values for the fluxes used in the simulations are equal to those listed in Table 6.2 for the used experiments. The sticking coefficients were assumed to be unity for the heavier species (^{18}O, $^{18}O_2$ and CO_2), but was set to a conservative value of 0.2 for H_2. Experimental results on the sticking of H_2 at 300 K to a 10 K surface indeed indicate such low coefficients (Chaabouni et al., 2012). The CO_2 flux may be lower because of freeze-out on the cold finger of the cryostat,

Table 6.3: Lowest, highest and standard parameters used and varied in the experimental simulations.

$E_{diff,\,H_2}$ (K)	$E_{diff,\,O}$ (K)	T_{surf} (K)	T_{gas} (K)	k_{O_2+O} (s^{-1})	k_{H_2+O} (s^{-1})
195	330	13.5	300	8.2×10^{-5}	1.35×10^{-1}
250	1100	13.5	300	1×10^{12}	9.8×10^{2}
220	1100	13.5	300	8.2×10^{-5}	5.1×10^{1} / 2.2×10^{2}

but, again, to remain on the conservative side, we took the highest value of 1.6×10^{14}. The remaining parameter settings used here are listed in Table 6.3. In general, the values for the input parameters are subject to some arbitrary choices. Here, all input variables were chosen such that they would result in a high reaction rate of the reaction $H_2 + O$. This is illustrated by the H_2 sticking coefficient and the flux of CO_2: a low sticking coefficient results in fewer $H_2 + O$ encounters and therefore would require a faster reaction rate to produce a result equal to that with a higher coefficient. The same holds for a decrease of the CO_2 flux.

The approach taken here is to find a set of parameters that allows reproducing the experimental upper limit of 0.09 ML (see Section 6.3.2) in 75 minutes of experiment. To do this, we varied several parameters, as mentioned in Table 6.3. First, the diffusion barrier of H_2 was set to 195, 220 and 250 K. Next, we performed simulations using barriers for oxygen atom diffusion with 330, 555, and 1100 K. The latter value has been used in earlier studies (Chapters 4 and 5) and the second value is half of this number. Very recently, literature values have become available (*e.g.*, Lee & Meuwly (2014); Congiu et al. (2014)) that predict values between 350 and 1000 K, the domain embedded by our chosen barrier values. The reaction rates of the reactions $O_2 + O$ and $H_2 + O$ were also varied. The first reaction rate was set to the value used in a previous study (Chapter 4, 8.2×10^{-5} s^{-1}) and to a value corresponding to a barrierless reaction (1.0×10^{12} s^{-1}). The second rate was set to 1.35×10^{-1}, 5.5, 5.1×10^{1}, 2.2×10^{2}, and 9.8×10^{2} s^{-1}. These values represent exactly the range in which the reaction $H_2 + O$ becomes effective in competing with diffusion and other reactions. In other words, for reaction rates below 1.35×10^{-1} s^{-1} the reaction does not occur at all. This sensitive window of reaction rates was found by performing several test simulations used to probe the influence of the parameters. We started with two models for each parameter, using the lowest and highest value while keeping all other parameters constant to their standard value, as indicated in the final row of Table 6.3. Because of the dominant role of k_{H_2+O}, the influence of any other parameter was typically checked at two different reaction rates. Only when a dependence on a particular parameter was found, we varied that specific parameter to other values in additional simulations while keeping other parameters constant to their standard value. Therefore, we did not use a full grid of models, but performed a total of 15 simulations. The resulting O_3 and H_2O abundances are summarized in Table 6.4.

The diffusion rates of both O and H_2 only play a role when the reaction with the O atom is almost prohibited. In this case, a high diffusion rate leads to a lower water production because of the favorable competition with respect to reaction. The amount of O_3 produced in the simulations does not depend on the diffusion rate of oxygen atoms, but shows a strong dependence on the reaction rate of $O_2 + O$. We previously used a reaction rate of 8.2×10^{-5} s^{-1} (Chapters 4). Here we see that a faster rate is needed to reproduce the amounts detected by RAIR spectroscopy. We return to this in the next section.

From Table 6.4 it can be deduced that for the production of water the reaction rate itself has the strongest impact on the final abundances, that is, k_{H_2+O}. For most simulations the

Table 6.4: Summary of the impact of each parameter on the O_3 and H_2O abundances in the ice.

no.	k_{O_2+O} (s^{-1})	k_{H_2+O} (s^{-1})	$E_{diff,\,H_2}$ (K)	$E_{diff,\,O}$ (K)	H_2O (ML)	O_3 (ML)
1	9.8×10^2	8.2×10^{-5}	220	1100	0.15	0.01
2	2.2×10^2	8.2×10^{-5}	195	1100	0.09	0.01
3	2.2×10^2	8.2×10^{-5}	220	1100	0.09	0.01
4	2.2×10^2	1.0×10^{12}	220	1100	0.10	0.05
5	2.2×10^2	8.2×10^{-5}	220	555	0.10	0.01
6	2.2×10^2	1.0×10^{12}	220	555	0.08	0.06
7	2.2×10^2	8.2×10^{-5}	220	330	0.07	0.01
8	2.2×10^2	8.2×10^{-5}	225	1100	0.09	0.01
9	5.1×10^1	8.2×10^{-5}	220	1100	0.05	0.01
10	5.5×10^0	8.2×10^{-5}	195	1100	0.02	0.01
11	5.5×10^0	8.2×10^{-5}	220	1100	0.03	0.01
12	5.5×10^0	8.2×10^{-5}	220	555	0.03	0.01
13	5.5×10^0	8.2×10^{-5}	220	330	0.02	0.00
14	5.5×10^0	8.2×10^{-5}	225	1100	0.03	0.01
15	1.35×10^{-1}	8.2×10^{-5}	220	1100	0.00	0.02

Note. Abundances given here are scaled to 75 minutes where appropriate.

final H_2O abundance remains below the experimental upper limit of 0.09 ML. In Fig. 6.4, the surface abundances of O, O_2, O_3, H_2 and H_2O are depicted over a simulated period of 37.5 minutes for simulation 3 in Table 6.4, which we define as the upper-limit simulation. This was a co-deposition experiment, therefore the profile of surface abundances is increasing linearly with time. The high amount of H_2 should be interpreted as 1.1 ML distributed over the total ice thickness of 360 ML. The total ice thickness is mainly determined by the high CO_2 flux, and therefore a deposited H_2 molecule either reacts, desorbs, or is covered by another CO_2 molecule. This means that on average there is 0.003 ML of H_2 in each monolayer, and thus this corresponds to the average surface coverage at any given time. The final H_2O abundance in this figure is 0.045 ML because of the reduced time scale. The value of $k_{exp.\,max}(13.5\ K) = 2.2 \times 10^2\ s^{-1}$ leads to this H_2O production, which corresponds to the experimentally determined value. This rate was be used to simulate water formation in the ISM through $H_2 + O$.

6.4.3 *Astrochemical modeling*

Two dense clouds with different temperature, density, and UV field were studied. Their physical parameters were chosen to be identical to those of dense clouds I and II in Chapters 5, as summarized in Table 6.5. The high densities n_H and simultaneous low temperatures, but high A_V values mimic typical values found in dense clouds. A major difference between the present and previous work is the inclusion of endothermicity of reaction R1. In the preceding study, we included an excess energy of 1400 K for each reaction in the water formation

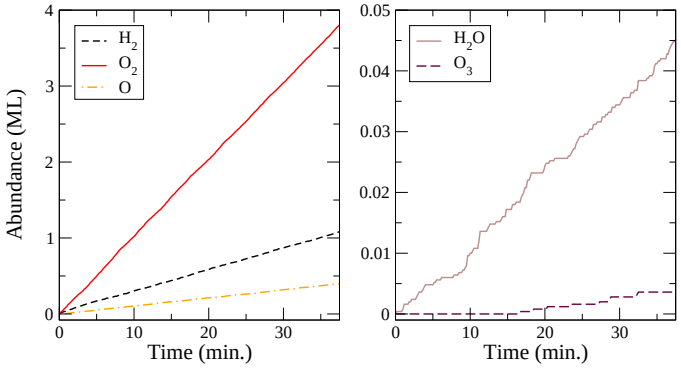

Figure 6.4: Surface abundances of O, O_2, O_3, H_2, and H_2O in time for the upper-limit simulation. One should realize that the total amount of deposited ice over the course of this simulation is 360 ML. The dominant component, by far, is CO_2 (not shown) because of its high flux.

network with two reaction products, and the energy was spread over these products. The excess energy for the endothermic reaction $H_2 + O$ was therefore explicitly set to 0 K, all other two-product reactions obtain a reaction heat of 1400 K. We used the same full water reaction network, but following the outcome of Chapters 4 and 5, we omitted the reaction channel $H + HO_2 \longrightarrow H_2O_2$. The network consisted of 16 reactions.

The main parameter varied in the astrochemical simulations is the rate of reaction R1, ranging between the fastest $k_{exo.\ tunn.}$ and the slowest $k_{endo.\ tunn.}$, as explained in Section 6.2. From the experiments we deduced in Section 6.3.2 that *if* water is produced starting from $H_2 + O$, it can only be by a mechanism that overcomes the endothermicity classically followed by tunneling through the barrier, as indicated in Fig. 6.1 and Eqn. 42. We scale the reaction rate determined experimentally at 13.5 K to rates relevant at 10 and 12 K - the surface temperatures of the grains in the dense cloud studied here - with the approach outlined below:

$$\begin{aligned} k_{exp.\ max}(13.5\ K) &= C \cdot \exp\left(-\frac{\Delta E}{T}\right) \\ 2.2 \times 10^2 &= C \cdot \exp\left(-\frac{960}{13.5}\right) \\ \Rightarrow C &= 1.68 \times 10^{33} \\ k_{exp.\ max}(T) &= 1.68 \times 10^{33} \cdot \exp\left(-\frac{960}{T}\right) . \end{aligned} \tag{45}$$

Here, we assumed that the endothermicity of the reaction, ΔE, is well constrained by the gas-phase value of 960 K. The tunneling mechanism, activation energy, and pre-exponential factor were not specifically considered (compare to Eqn. 42), but were all combined in the factor *C*, which was considered temperature independent over the small temperature range studied here.

Table 6.6 gives the contributions of the different surface reaction routes to OH and H_2O formation and the total amount of H_2O produced per kyr in the simulations. Three different reaction rates were considered: (i) assuming exothermic tunneling with Eqn. 40, (ii) using the experimentally determined highest rate with Eqn. 45, and (iii) assuming that $E_a + \Delta E = 3000$ K in Eqn. 42. The results presented here were obtained at a time of $\sim 2.0 \times 10^4$ and $\sim 3.5 \times 10^3$ years for the two clouds. This may seem too short to be relevant on an interstellar

Table 6.5: Parameters used in the astrochemical simulations, *i.e.,* dense clouds I and II from Chapter 5.

	A_V	n_H (cm^{-3})	$n_{H(I)}$ (cm^{-3})	$n_{O(I)}$ (cm^{-3})	T_{gas} (K)	T_{grain} (K)
I	5	5×10^3	2	1.5	20	12
II	10	2×10^4	2	6	10	10

scale, and is due to the high computational costs, but all abundances increase linearly or reach a steady-state abundance before this time. Moreover, all values were calculated after the grain was already covered with a total of 1 ML of species.

The following reaction channels are considered in Table 6.6: First, the production of the OH radical was broken down into the separate contributions of five reaction routes, namely $H_2 + O$, $H + O$, $H + HO_2$, $H + O_3$, and $H + H_2O_2$. For cloud I, changing the reaction rate of R1 simply shifts the main production route from $H_2 + O$ to $H + O$ for decreasing rates. For cloud II, however, there is more oxygen than atomic H present in the cloud. Allowing the reaction $H_2 + O$ to proceed thus leads to a much higher OH production.

Water can also be formed by multiple reaction routes, but the important two here are $H + OH$ and $H_2 + OH$. For lower densities, the total water production rate does not change substantially between the three rates. At higher densities, the larger abundance of OH translates immediately into more produced H_2O, since the products of reaction R1, that is, H and OH, remain again in each other's vicinity.

Furthermore, table 6.6 clarifies that using $k_{exp.\,max.}$ leaves reaction $H_2 + O$ to contribute at most 11% to the formation of OH on the surface of dust grains in cloud I and does not contribute at all in cloud II. Since we chose all parameters conservatively, this is an absolute upper limit. Higher H_2 sticking probabilities, lower CO_2 flux due to freeze-out on the cold finger or nonthermalized effects as detailed in Sections 6.3.2 and 6.4.2 all lead to lower rates.

The effect of the O diffusion barrier was investigated by simulating with the values 555 and 1100 K. Although the total water production does not change much, the relative contributions of the reactions that produce OH radicals do: with a faster O diffusion, the competition between diffusion and the reaction $H_2 + O$ favors diffusion, leaving O free on the surface to react with other species. Consequently, the reactions $H + O$, $O + O$ or $O + O_2$ play a larger role, the extent of which depends on the density. Furthermore, increasing the reaction rate for O_3 formation results in a larger contribution of the reaction channel $H + O_3$. In the end, these effects will also decrease the efficiency of the reaction $H_2 + O$.

6.5 ASTROPHYSICAL IMPLICATIONS

Since the reaction $H_2 + O$ only contributes to at most 11% to the formation of OH, water formation is dominated by the other reaction routes, such as $O + H$, $O_2 + H$, $OH + H$ and $OH + H_2$. This implies that depending on the ratio of O/H in the gas phase, the limiting factor to the water formation rate in dark clouds is the amount of H atoms available. Additionally, for high O/H ratios, a higher diffusion rate of O atoms can lead to more reactions of the type $O + O$ (Congiu et al., 2014). This does not mean that water formation is prohibited, since the reaction channel $O_2 + H$ can also lead to efficient water formation (Chapter 4 and Ioppolo et al., 2010; Cuppen et al., 2010).

Table 6.6: Contributions of the different surface reaction routes to OH and H_2O formation after a coverage of 1 ML is reached, and the total produced water rate for dense clouds I and II for different values of k_{H_2+O}.

Cloud		$H_2 + O \rightarrow OH + H$	$H + O \rightarrow OH$	$H + HO_2 \rightarrow OH + OH$	$H + O_3 \rightarrow OH + O_2$	$H + H_2O_2 \rightarrow OH + O$	$H + OH \rightarrow H_2O$	$H_2 + OH \rightarrow H_2O + H$	H_2O prod.
	k_{H_2+O} (s^{-1})	(%)	(%)	(%)	(%)	(%)	(%)	(%)	(ML kyr^{-1})
I	$k_{exo.\ tunn.}$ [a] $= 2.3 \times 10^5$	95.0	4.5	~0	~0	~0	~100	~0	0.19
I	$k_{exp.\ max.}$ [b] $= 3.0 \times 10^{-2}$	**11.0**	74.0	12.0	0.5	2.5	86.5	9.0	0.15
I	$k_{endo.\ tunn}$ [c] $= 4.4 \times 10^{-29}$	0	82.0	14.0	1.0	3.0	75.5	19.5	0.14
II	$k_{exo.\ tunn.}$ [a] $= 2.3 \times 10^5$	98.5	1.5	~0	0	~0	99.0	1.0	0.54
II	$k_{exp.\ max.}$ [b] $= 3.5 \times 10^{-9}$	**1.0**	56.0	31.0	6.0	6.0	26.0	60.0	0.24
II	$k_{endo.\ tunn}$ [c] $= 5.0 \times 10^{-36}$	0	54.0	35.0	5.5	5.5	20.5	63.5	0.24

[a] Eqn. 40, with E_a equal to $E_a + \Delta E$ from Fig. 6.1, *i.e.* 3000 K. [b] Eqn. 45. [c] Eqn. 42, with E_a = 2040 K and ΔE = 960 K.

The experimentally found upper limit for the reaction rate, Eqn. 45, can be compared with the values of the reaction rates where exothermic tunneling was assumed. The final two entries of Table 6.1 show that these rates (at 10 K) are always higher. Therefore, the assumed importance of the reaction $H_2 + O$ for the deuterium fractionation ratios of water on the surfaces of dust grains has to be considered with care (Cazaux et al., 2010, 2011). Their HDO/H_2O ratio found at low temperatures results from the assumption that the reaction $HD + O$ proceeds via tunneling and therefore mainly produces OH + D. There might be much more HDO formed on the surface of dust, depending on the main water formation route in the specific region in the interstellar medium (through atomic or molecular oxygen).

6.6 CONCLUSIONS

We studied experimentally and by modeling the significance of the reaction $H_2 + O \longrightarrow H + OH$ in the framework of solid-state water formation in interstellar ice (analogs).

From precisely executed temperature-programmed desorption experiments in an UHV setup that brought together H_2 and O in a matrix of CO_2, we established an experimental upper limit of the water production. If this amount of water is indeed produced on the surface instead of coming from an additional source of contamination, this can only be caused by a combined classical and tunneled reaction mechanism, based on Eqn. 42. An upper limit for the reaction rate was found using a microscopic kinetic Monte Carlo model that converts the maximum number of molecules formed into a possible reaction rate: $1.68 \times 10^{33} \cdot \exp(-960/T)\ s^{-1}$. By incorporating this rate into simulations ran under astrochemically relevant parameters, we found that the reaction $H_2 + O$ does not contribute more than 11% to the formation of water in dense clouds in the interstellar medium.

This number is an absolute upper limit, because all numbers used are conservative estimates. It is likely that in space the efficiency is substantially lower.

BIBLIOGRAPHY

Andersson, S., Goumans, T. P. M., & Arnaldsson, A. 2011, Chem. Phys. Lett., 513, 31
Anton, R., Wiegner, T., Naumann, W., et al. 2000, Rev. Sci. Instrum. , 71, 1177
Arnaut, L. G., Formosinho, S. J., & Barroso, M. 2006, J. Mol. Struct. , 786, 207
Baulch, D. L., Cobos, C. J., Cox, R. A., et al. 1992, J. Phys. Chem. Ref. Data, 21, 411
Bell, R. P. 1980, The tunnel effect in chemistry (London: Chapman and Hall)
Bergin, E. A. & Tafalla, M. 2007, Annu. Rev. Astron. Astrophys., 45, 339
Cazaux, S., Caselli, P., & Spaans, M. 2011, Astrophys. J. Lett. , 741, L34
Cazaux, S., Cobut, V., Marseille, M., Spaans, M., & Caselli, P. 2010, Astron. Astrophys., 522, A74
Chaabouni, H., Bergeron, H., Baouche, S., et al. 2012, Astron. Astrophys., 538, A128
Chang, Q., Cuppen, H. M., & Herbst, E. 2005, Astron. Astrphys., 434, 599
Congiu, E., Minissale, M., Baouche, S., et al. 2014, Far. Disc., 168
Cuppen, H. M. & Herbst, E. 2007, Astrophys. J., 668, 294
Cuppen, H. M., Ioppolo, S., Romanzin, C., & Linnartz, H. 2010, Phys. Chem. Chem. Phys., 12, 12077
Cuppen, H. M., Karssemeijer, L. J., & Lamberts, T. 2013, Chemical Reviews, 113, 8840
Dulieu, F., Amiaud, L., Congiu, E., et al. 2010, Astron. Astrophys., 512, A30
Garrod, R. T. & Herbst, E. 2006, Astron. Astrophys., 457, 927
Hiraoka, K., Miyagoshi, T., Takayama, T., Yamamoto, K., & Kihara, Y. 1998, Astrophys. J. , 498, 710
Ioppolo, I., Fedoseev, G., Lamberts, T., Romanzin, C., & Linnartz, H. 2013, Rev. Sci. Instrum. , 84, 073112
Ioppolo, S., Cuppen, H. M., Romanzin, C., van Dishoeck, E. F., & Linnartz, H. 2008, Astrophys. J., 686, 1474
Ioppolo, S., Cuppen, H. M., Romanzin, C., van Dishoeck, E. F., & Linnartz, H. 2010, Phys. Chem. Chem. Phys., 12, 12065
Lee, M. W. & Meuwly, M. 2014, Far. Disc., 168
Miyauchi, N., Hidaka, H., Chigai, T., et al. 2008, Chem. Phys. Lett., 456, 27
Mokrane, H., Chaabouni, H., Accolla, M., et al. 2009, Astrophys. J. Lett., 705, L195
Oba, Y., Miyauchi, N., Hidaka, H., et al. 2009, Astrophys. J., 701, 464
Oba, Y., Osaka, K., Watanabe, N., Chigai, T., & Kouchi, A. 2014, Far. Disc. , 168, 185
Oba, Y., Watanabe, N., Hama, T., et al. 2012, Astrophys. J., 749, 67
Rogers, S., Wang, D., Kuppermann, A., & Walch, S. 2000, J. Phys. Chem. A, 104, 2308
Romanzin, C., Ioppolo, S., Cuppen, H. M., van Dishoeck, E. F., & Linnartz, H. 2011, J. Chem. Phys., 134, 084504
Taquet, V., Peters, P. S., Kahane, C., et al. 2013, Astron. Astrophys., 550, A127
van Dishoeck, E. F., Jonkheid, B., & van Hemert, M. C. 2006, Far. Disc., 133, 231

7

THERMAL H/D EXCHANGE IN POLAR ICE – DEUTERON SCRAMBLING IN SPACE

We have investigated the thermally induced proton/deuteron exchange in mixed amorphous H_2O:D_2O ices by monitoring the change in intensity of characteristic vibrational bending modes of H_2O, HDO, and D_2O with time and as function of temperature. The experiments have been performed using an ultra-high vacuum setup equipped with an infrared spectrometer that is used to investigate the spectral evolution of homogeneously mixed ice upon co-deposition in thin films, for temperatures in the 90 to 140 K domain. With this non-energetic detection method we find a significantly lower activation energy for H/D exchange – 3840 ± 125 K – than previously reported. Very likely this is due to the amorphous nature of the interstellar ice analogues involved. This provides reactive timescales ($\tau < 10^4$ years at $T > 70$ K) fast enough for the process to be important in interstellar environments. Consequently, an astronomical detection of D_2O will be even more challenging because of its potential to react with H_2O to form HDO. Furthermore, additional experiments, along with previous studies, show that proton/deuteron swapping also occurs in ice mixtures of water with other hydrogen bonded molecules, in particular on the OH and NH moieties. We conclude that H/D exchange in ices is a more general process that should be incorporated into ice models that are applied to protoplanetary disks or to simulate the warming up of cometary ices in their passage of the perihelion, to examine the extent of its influence on the final deuteron over hydrogen ratio.

T. Lamberts, H. M. Cuppen, S. Ioppolo and H. Linnartz, *Thermal H/D exchange in polar ice - deuteron scrambling in space*, Mon. Not. R. Astron. Soc. 448 (2015) 3820

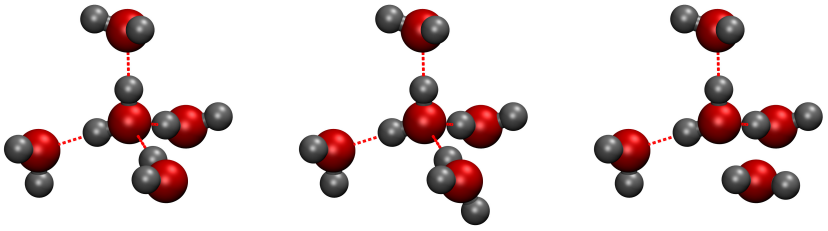

Figure 7.1: (a) Water molecule surrounded by four hydrogen bonded molecules as in an ideal crystal structure, (b) water molecule surrounded by four hydrogen bonded water molecules, where one of those contains an extra proton: ionic defect, and (c) water molecule surrounded by four water molecules, with one of those rotated causing a missing hydrogen bond: 'L-defect'.

7.1 INTRODUCTION

The delivery of water to Earth is far from understood. Several hypotheses have been put forward, among which delivery by comets and/or asteroids during the so-called 'late veneer' stage (Morbidelli et al., 2000; Cleeves et al., 2014), direct adsorption of water onto grains prior to planetary accretion (Muralidharan et al., 2008), and in the recent 'Grand Tack' model, water delivery during the formation phase of terrestrial planets (O'Brien et al., 2014). Since the ratio between deuterons and protons incorporated in water molecules is elevated in the Earth Ocean with respect to that of the initial bulk solar composition, the D/H fraction in various molecules is a logical tracer for the proposed origins. This concerns particularly the ratio of HDO over H_2O. The D_2O abundance is expected to be low, because the amount of deuterium present in the interstellar medium is a factor 100 000 less than that of hydrogen. In fact the number of astronomical D_2O detections is very limited: in the cold envelope layer surrounding solar-type protostar IRAS 16293-2422 (Butner et al., 2007; Vastel et al., 2010; Coutens et al., 2013) and in the warmer regions surrounding the Class 0 protostar NGC 1333 IRAS2A (Coutens et al., 2014).

It should be noted, though, that a direct comparison of observed D/H ratios between different locations may be a too naive approach, to identify the origin of our water, as obviously a number of processes are at play that may scale differently over time for different conditions. For example, investigating molecules other than water, it has been found that deuterium fractionation in low-mass protostellar envelopes and molecular outflows for H_2CO and CH_3OH are higher than those for H_2O and NH_3 as summarized in Fig. 11 by Caselli & Ceccarelli (2012). This difference is argued to reflect the temporal sequence in which the species are formed, as with decreasing gas-phase CO (increasing frozen out solid CO) abundances the gas-phase atomic D/H ratio is found to increase. Final values may also be different in different environments, *e.g.*, low- vs. high-mass protostellar envelopes. In order to interpret molecular D/H ratios correctly, it is important to investigate all impacting processes. In the past, the focus has been on isotope dependent gas-phase chemical processes. So far, the two main routes are first gas-phase isotope dependent reactions with H_2D^+ transferring its deuterium atom and second the enhanced gas-phase D/H ratio after CO freeze-out that impacts on ice chemistry by the higher probability of deuterium deposition (Tielens, 1983; Caselli & Ceccarelli, 2012). In the solid state, on the grains, deuterium fractionation is further determined by the chem-

ical surface reaction networks. These involve both hydrogenation and deuteration pathways and the crosslinks between them. This paper focuses in detail on one particular process only: thermally induced proton/deuteron exchange reactions in the ices.

In general, the grain temperature during the formation of the icy mantles in the dense and dark regions of the interstellar medium is low, between 10-20 K (Bergin & Tafalla, 2007). The exact temperature determines the surface reaction routes taken, by, *e.g.*, sticking coefficients and the relative importance of tunneling transmission coefficients, that lead eventually to the formation of species like CH_3OH and H_2O (Hiraoka et al., 1998; Watanabe & Kouchi, 2002; Fuchs et al., 2009; Miyauchi et al., 2008; Ioppolo et al., 2008). At later evolutionary stages in the star forming sequence, surface temperatures are no longer homogeneously distributed throughout the core or disk and can range up to 100 K (van der Tak et al., 2000; Jørgensen et al., 2002; Aikawa et al., 2002; Nomura & Millar, 2005; Bergin & Tafalla, 2007; Launhardt et al., 2013). At 100 K, ices are expected to have been fully evaporated, thus transferring molecules from the grains to the gas phase.

Within the astrochemical community, proton exchange in polar (*i.e.*, water-rich) ices has attracted special attention. In the context of ion formation at low and higher temperatures, Grim et al. (1989) discuss the proton hopping between the hydrogen bonded molecules leading to the formation of NH_4^+ and OCN^-. As stated by Tielens (2013) heating and sublimation seem to be important in interstellar ices near young stars in modeling the warm gas; non-energetic thermal reactions may therefore be relevant as well. Proton exchange can be important in particular since the main component of ices is H_2O and, moreover, the main reservoir of deuterium is HDO (Rodgers & Charnley, 2002). If indeed such a scrambling of protons and deuterons occurs efficiently, this implies that not the low-temperature reaction routes are decisive for final HDO/H_2O ratio, but rather the total number of H and D atoms incorporated in hydrogen bonded molecules. Ratajczak et al. (2009) showed that the hydroxyl group in a methanol molecule exchanges its proton or deuteron with surrounding water molecules and proposes this as one of the possible explanations for the deviation between modeled and observed CH_2DOH/CH_3OD ratios (Ratajczak et al., 2011).

Interstellar or circumstellar ices and cometary ices are thought to have a common chemical origin (Bockelée-Morvan et al., 2000), but the temperature processing of ices in comets is of an intrinsically different nature. Ices are typically much thicker, *i.e.*, orders of magnitude compared to the layer thicknesses of several tens of monolayers typical for interstellar ices. Moreover, each passage through the perihelion can have a large impact on the temperature depending on the distance to the central object. In the cometary community, however, H/D exchange is often modeled only in the coma gas-phase chemistry via several reactions (Rodgers & Charnley, 2002) following sublimation of ices.

The mechanisms underlying proton/deuteron scrambling have already been studied extensively in the 1980's in the physical chemical community, in particular by Devlin and coworkers (Thornton et al., 1981; Bertie & Devlin, 1983; Collier et al., 1984; Wooldridge & Devlin, 1988) who studied H/D exchange in water ices as well as water-ammonia mixtures with different isotopic compositions. For the case of water ice, exchange has been found to occur both in the bulk (Collier et al., 1984) and on the surface (Uras-Aytemiz et al., 2001; Park et al., 2004; Moon et al., 2010). In the case of isolated D_2O molecules in a H_2O environment, the prevailing mechanism is often referred to as the so-called 'hop-and-turn' mechanism. In Fig. 7.1, three scenarios of the local ice structure are depicted: (a) a perfect crystalline structure, (b) an ionic defect, *i.e.*, the presence of H_3O^+, and (c) an L-defect, *i.e.*, the lack of an expected hydrogen bond. Under influence of an ionic defect, the heavy water is converted into two coupled HDO entities that share a hydrogen bond. These can be converted into two nearest-neighbour HDO molecules by passage of an L defect. Finally, two isolated molecules are created after an addi-

tional proton transfer. Such a detailed mechanism, with corresponding distinct infrared (IR) spectra (in the O-D stretching region) cannot be resolved for current astronomical IR spectra. For astrochemical purposes, the overall reaction can therefore be summarized as

$$H_2O + D_2O \xrightarrow{k_f} 2HDO \tag{R1}$$

$$2HDO \xrightarrow{k_r} D_2O + H_2O. \tag{R2}$$

Collier et al. (1984) and Wooldridge & Devlin (1988) studied cubic ices with D_2O concentrations of several percent in a high vacuum setup. The activation energy for proton exchange was found to be ~5000 K, which means that the process is not likely to be relevant on interstellar time scales at grain temperatures up to the sublimation temperature of ice at 90-100 K. Since the proposed hop-and-turn mechanism depends on the existence of point defects present in the ice and on the defect concentrations, the study was extended to amorphous water samples by Fisher & Devlin (1995). Indeed, they found a much lower activation energy of the turn step involved, ~3000 K. Studies of exchange on ice surfaces – also subject to larger structural defects – indicated an enhanced L-defect activity (Uras-Aytemiz et al., 2001). These studies were performed, however, using ices doped with HCl in order to have a higher sensitivity. Protons are generated via the reaction $HCl + H_2O \longrightarrow H_3O^+ + Cl^-$, the exothermicity of which could influence the local processes that occur (Kim et al., 2009). Doping creates additional (shallow) proton traps in the ice in the vicinity of the counterion (Uras-Aytemiz et al., 2001), and proton films can remain inactive up to around 125 K (Lee et al., 2007), both of which can influence the reaction rates detected. Moon et al. (2010) showed that doping lowers the activation energy found for H/D exchange on surfaces by almost a factor 2.

A similar situation applies to space. In the ISM ices do not have a perfectly ordered structure, partially because they are (i) not condensed at high enough temperatures, (ii) comprised of many species that are formed on the surface, (iii) composed of more molecules than only water, and (iv) subject to structural changes upon energetic processing of the ice. These effects will contribute to a high defect concentration in interstellar ices.

In this paper, we aim to bring together the previous results of these scientific communities – physical chemistry, cometary chemistry and (laboratory) astrochemistry – while presenting several new experimental results of which the relevance to astronomy is discussed. We discuss amorphous D_2O:H_2O ices with mixing ratios around 1:1. Although such ratios are not astrochemically relevant, they do allow for a higher sensitivity of the proton exchange process at lower temperatures, without the neccessity to use doping. We mimic the high expected amount of defects in the ISM by intentionally growing amorphous ice structures at temperatures of 15 K and probe whether this higher defect concentration in the ice structure, see Fig. 7.1, leads to an increase of the reaction rate for reaction R1. The results are extended to a more general concept taking into account 'all' hydrogen bonded molecules. Subsequently, the astrochemical implications are discussed focussing on the relevance of proton/deuteron swapping at long time scales, but at temperatures below full ice desorption.

7.2 METHODS

All experiments studied here consist of two sequential steps: (a) the simultaneous deposition of H_2O (Milli-Q) and D_2O (Sigma-Aldrich 99.96%) on the substrate at 15 K and subsequently (b) an isothermal experiment at a given temperature ($T_{iso} \geqslant 90$ K) during which the level of proton exchange is probed by means of reflection absorption infrared (RAIR) spectroscopy. In one experiment (Section 7.3.2) also a quadrupole mass spectrometer (QMS) is used. Below, the experimental procedure is described first, followed by an explanation of the calibration

experiments performed, the analysis of the spectra, and the analysis of the temporal evolution of the surface abundances of H_2O, HDO and D_2O.

7.2.1 *Experimental*

Experiments are performed using the SURFRESIDE^2 setup, which has been constructed to systematically investigate solid-state reactions leading to the formation of molecules of astrophysical interest at cryogenic temperatures. The setup has been extensively described in Ioppolo et al. (2013) and therefore only a brief description of the procedure is given here. All performed experiments and the corresponding molecular deposition rates are listed in Table 7.1. The results of experiments 1-10 are discussed in Section 7.3.1. Experiment 11 follows a procedure similar to that for the water experiments described below and is discussed in Section 7.3.2. The method used for experiment 12 deviates and is discussed in Section 7.3.2.

SURFRESIDE^2 consists of three UHV chambers: one main chamber for ice growth, ice processing, and ice diagnostics, and two chambers comprising atom beam lines. All have a room-temperature base-pressure between $10^{-9} - 10^{-10}$ mbar. A rotatable gold-coated copper substrate in the center of the main chamber is cooled to the desired temperature using a He closed-cycle cryostat with an absolute temperature accuracy of $\leqslant$ 2 K. Both water and heavy water are prepared in a separate pre-pumped ($\leqslant 10^{-5}$ mbar) dosing line and after several freeze-pump-thaw cycles a co-deposition of room-temperature vapor H_2O and D_2O is performed. One species is deposited through a metal deposition line under an angle of 90° and the other through one of the separate UHV beam lines at an angle of 135° with respect to the plane of the surface, see Table 7.1. This UHV beam line can be operated independently and can be separated from the main chamber by a metal shutter. Deposition takes place at a surface temperature of 15 K to ensure a large amount of amorphicity of the ice (see discussion above).

After approximately 60 minutes of co-deposition at low temperature, yielding 45-65 ML, the substrate is heated up to the desired temperature, T_{iso}, between 90 and 140 K. Note that in the laboratory ices sublimate not at 100 K, but rather between 145-165 K, hence the higher temperatures employed here. The warm-up phase clearly affects the porosity of the ice (Bossa et al., 2012) and therefore also the ice structure. However, using H_2O:D_2O mixing ratios around 1:1, each molecule initially has at least one neighbor of its isotopic counterpart, which renders the degree of porosity less important. Note also that the extra collapse of the pores at 120 K with respect to that at 90 K is only 3% (Bossa et al., 2012). Thus, assuming locally distorted hydrogen bonded structures (Karssemeijer et al., 2014; Karssemeijer, 2014), the exact structure of the ice and/or diffusion mechanisms (Jung et al., 2004; Oxley et al., 2006) do not play a role here. A RAIR difference spectrum with respect to the background is acquired every 5 or 10 minutes up to the final time of the experiments, t_{iso} in Table 7.1. The background spectrum is acquired from an empty surface prior to the co-deposition at low temperature. RAIR spectra comprise a spectral range between 4000 and 700 cm^{-1} with a spectral resolution of 1 cm^{-1} and are averaged over 512 scans. Exchange occurs faster at higher temperatures, therefore those experiments have a shorter duration. Pure component calibration spectra are used for the analysis of the experiments, see Section 7.2.2.

The deposition rates mentioned in Table 7.1 are calculated using the following relation

$$\frac{c_{X_2O} P_{X_2O} \langle \nu \rangle}{4 k_B T} \tag{46}$$

where c_{X_2O} is the calibration factor for the pressure gauge for the three isotopologues of water (X_2O = H_2O, HDO, or D_2O), ν is the thermal velocity of the vapor molecules at 300 K, k_B is the Boltzmann constant, and T corresponds to the (room) temperature.

Table 7.1: List of (calibration) experiments and corresponding parameters; temperature (T), beamline angle to the plane of the surface, and molecular flux (f).

	Experiments					
	T_{iso} (K)	90°	f_{dep} ($cm^2\ s^{-1}$)	135°	f_{dep} ($cm^2\ s^{-1}$)	t_{iso} (min)
1	90	D_2O	$10^{(12)}$	H_2O	$10^{(12)}$	270
2	100	D_2O	$10^{(12)}$	H_2O	$10^{(12)}$	270
3	120	D_2O	$10^{(12)}$	H_2O	$10^{(12)}$	360
4	125	D_2O	$10^{(12)}$	H_2O	$10^{(12)}$	270
5	130	D_2O	$10^{(12)}$	H_2O	$10^{(12)}$	210
6	130	D_2O	$4^{(12)}$	H_2O	$10^{(12)}$	190
7	135	D_2O	$10^{(12)}$	H_2O	$10^{(12)}$	150
8	140	D_2O	$10^{(12)}$	H_2O	$10^{(12)}$	110
9	140	D_2O	$4^{(12)}$	H_2O	$10^{(12)}$	120
10	140	H_2O	$4^{(12)}$	D_2O	$10^{(12)}$	120
11	130	D_2O	$10^{(12)}$	NH_3	$7^{(12)}$	120
12 [a]	TPD	D_2O	-	NO + H	-	-
	Calibration experiments					
1	var. [b]	H_2O	$20^{(12)}$	-	-	-
2	var. [b]	HDO	$10^{(12)}$ [c]	-	-	-
3	var. [b]	D_2O	$19^{(12)}$ [d]	-	-	-
4	var. [b]	-	-	-	-	-

Note. The notation $\alpha^{(\beta)}$ implies $\alpha \times 10^{\beta}$.

[a] Instead of a full co-deposition, a layered experiment was performed, first co-depositing NO + H to prepare a NH_2OH layer, which was then covered by D_2O. [b] Spectra were acquired at all temperatures relevant for the experiments, *i.e.* 90-140 K. [c] Due to the mixture preparation of HDO, the statistical ratio between the constituents H_2O:HDO:D_2O is 1:2:1. [d] The effective deposition rate is somewhat lower as a result of HDO contamination in the D_2O sample, this is estimated to be $\leqslant$ 5% from the OH stretching mode.

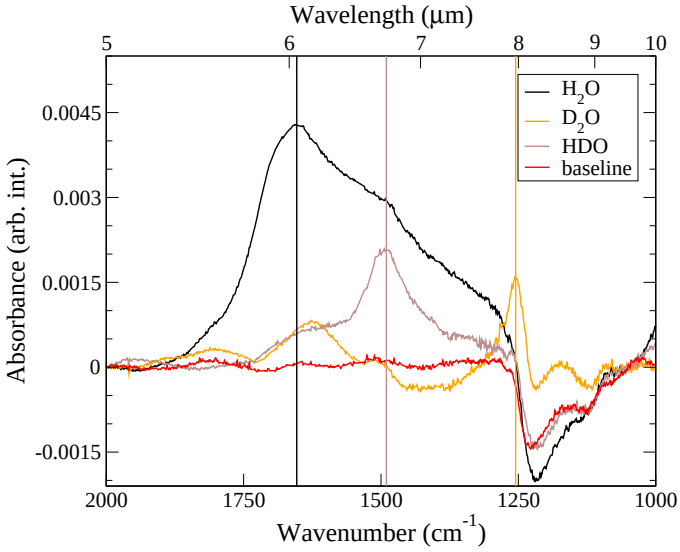

Figure 7.2: Bending region of the calibration spectra used for fitting the experiments, all spectra are recorded at 130 K. See text concerning the 1625 cm^{-1} band in the D_2O spectrum, the contamination in the HDO band, and the baseline artifact around 1200 cm^{-1}.

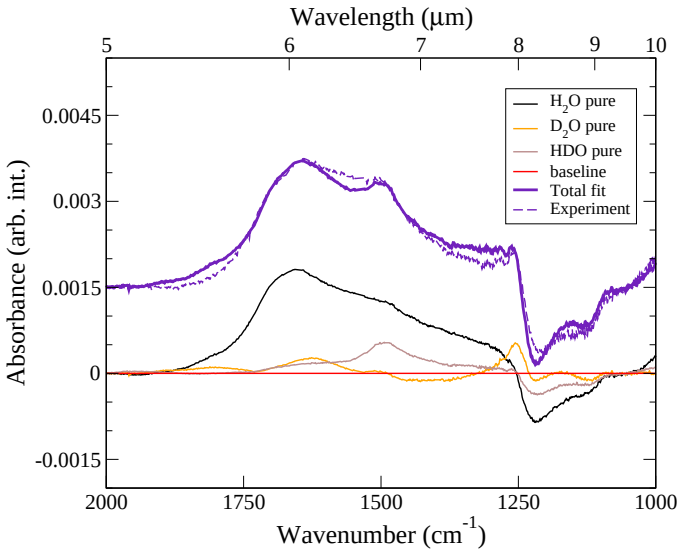

Figure 7.3: Example of a recorded spectrum in the water bending region (130 K) and its best fit, decomposed into the separate components (H_2O, HDO, and D_2O - see Fig. 7.2), recorded after 210 minutes. Note: this concerns experiment 5 from Table 7.1. Pure spectra themselves compensate for the baseline artifact at 1200 cm^{-1}.

The calibration factor for water is 1/0.9. Since there is no significant difference found between the absolute partial cross sections for electron-impact ionization of H_2O and D_2O (influencing the pressure reading of the gauge) (Straub et al., 1998; Itikawa & Mason, 2005), we assume that this is also the case for HDO and all calibration factors for the pressure are taken to be equal.

Note that the initial spectra of experiments 1-5, 7 and 8 at 15 K after deposition are compared with each other to confirm the reproducibility: each low-temperature spectrum is analyzed with the fitting procedure described below and the initial surface abundances of water and deuterated water are found to be reproducible with a standard deviation of $\sim 5\%$.

7.2.2 *Spectral Fitting*

Each spectrum is the sum of the pure H_2O, HDO, and D_2O components along with their intermolecular interactions. The intermolecular interactions cannot be captured in pure calibration spectra and they are stronger in the IR stretching than bending region. Futhermore the bending region is less sensitive to crystallization effects. Therefore, our region of interest lies in the 2000-1000 cm^{-1} range, where the H_2O, HDO and D_2O molecules vibrate in their respective bending modes: 1660, 1490, 1250 cm^{-1}. Upon proton/deuteron exchange the H_2O and D_2O intensities decrease, whereas the HDO intensity increases.

The integrated area of each mode can be converted into a number of mole-cules, assuming that band strengths are available, but in reflection mode these are typically ill-constrained. To be able to quantify the dynamics at work, a spectral fitting procedure is needed to separate the three components. For this purpose, also three calibration experiments are performed.

A calibration experiment, see final rows of Table 7.1, consists of the deposition of a 'pure' X_2O component for 30 minutes at 15 K and spectrum acquisition thereafter at all temperatures relevant for the experiments performed, *i.e.*, 90, 100, 120, 125, 130, 135, and 140 K. At each temperature, the spectrum looks slightly different and therefore pure spectra for each temperature are necessary for the fitting procedure. Furthermore, in the spectral region between $\sim$1050 and $\sim$1250 cm^{-1} a known temperature-dependent artifact is present, which makes it neccessary to record blank spectra at all relevant temperatures as well. It is most likely caused by a temperature dependence in the absorption of our background sample. These spectra are also included in the fits (calibration experiment 4), but do not fully correct for the effect, as explained below.

Using the pure components, we avoid having to correct for the difference in band strengths: each pure spectrum consists of a known amount of deposited H_2O, HDO, and D_2O. A second band around 1625 cm^{-1} in the D_2O spectrum has its origin in the combination mode $\nu_{bending} + \nu_{libration}$ (Bertie & Whalley, 1964). There is also a small OH stretching signal present in the spectrum , but it is $\leqslant 5\%$ with respect to the OD stretching signal. HDO was prepared by mixing equal amounts of H_2O and D_2O vapors into a pre-pumped ($\leqslant 10^{-5}$ mbar) dosing line. We expect the hydrogen and deuterium atoms to be distributed statistically, resulting in a statistical 1:2:1 mixture. That means that the effective HDO deposition rate is only half of the total deposition rate for this particular experiment. The spectra shown in Fig. 7.2 are used for the fitting procedure. The HDO spectrum cannot be obtained pure, due to the way it is produced in the dosing line. In the fitting procedure we used both the original spectrum as well as a spectrum corrected for the H_2O and D_2O contamination in the HDO contribution, see Section 7.2.4.

Every separate experiment is composed of a time-resolved series of recorded spectra, each providing a snapshot of the ongoing proton exchange process. A non-negative least squares solver is used to fit the pure components to the spectrum only in the bending range of 2000-

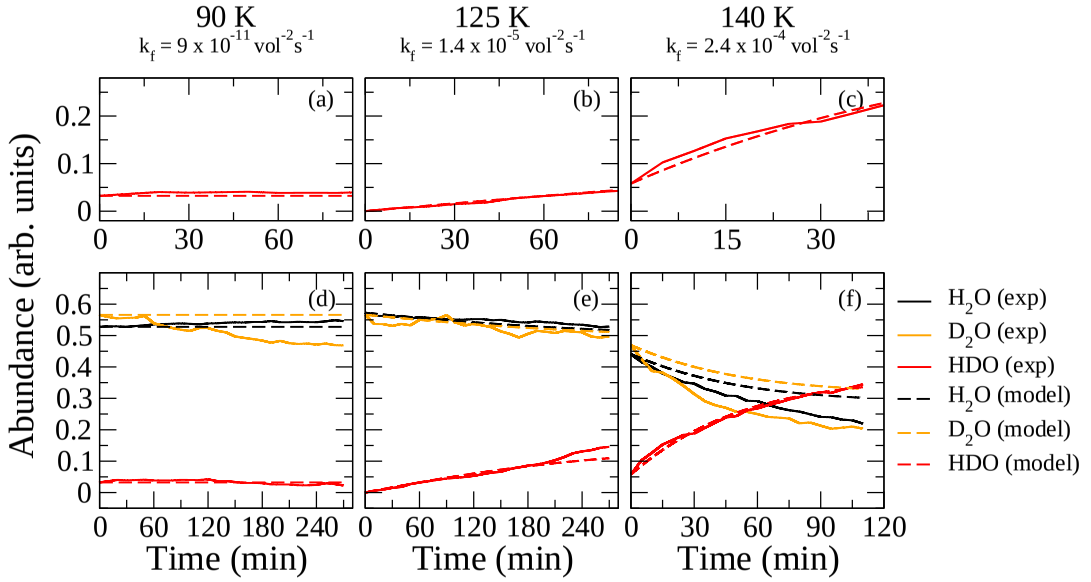

Figure 7.4: Modeled H_2O, D_2O, and HDO concentrations for experiments 1 (a and d), 4 (b and e), and 8 (c and f) (Table 7.1). The top row, panels (a)-(c), are zoom-ins of the HDO experimental and modeled abundance for the first 33% of the experimental duration. The bottom row, panels (d)-(f), depicts the evolution of all three components for the entire duration.

1000 cm^{-1}. Figure 7.3 depicts an example of such a fit for the final spectrum (recorded after 210 min) recorded during experiment 5 from Table 7.1. In this case, the baseline does not contribute to the fit since the sum of the pure components themselves already compensate for the artifact. Usually, however, the temperature-dependent baseline is needed to take care of this artifact.

7.2.3 *Reaction dynamics*

The total contribution of each pure component to the fit is subsequently plotted versus time in order to resolve the dynamics. We are not able to observe the isolated HDO entities in a water matrix that have been proposed to be produced through a hop-and-turn mechanism (Collier et al., 1984), because both reaction partners are present in the ice with mixing ratios between 1:2 to 2:1. Because of this, our system is intrinsically easier to model, since we observe only the proton or deuteron hopping, leading to a reaction system of the forward and backward reactions, R1 with rate k_f and R2 with rate k_r. They can be evaluated in terms of a mean field approximation. The temporal evolutions of the concentrations (or abundances) can be described with a set of ordinary differential (rate) equations

$$\frac{d[H_2O]}{dt} = -k_f[H_2O][D_2O] + k_r[HDO]^2 \tag{47}$$

$$\frac{d[D_2O]}{dt} = -k_f[H_2O][D_2O] + k_r[HDO]^2 \tag{48}$$

$$\frac{d[HDO]}{dt} = 2\,k_f[H_2O][D_2O] - 2\,k_r[HDO]^2\,. \tag{49}$$

Where $\frac{d[H_2O]}{dt} + \frac{d[D_2O]}{dt} + \frac{d[HDO]}{dt} = 0$. We assume desorption to be negligable at these temperatures. Using an optimization algorithm in conjuction with a least-square ODE solver, k_f and k_r can be extracted for each experiment. $[H_2O]_0$, $[HDO]_0$, and $[D_2O]_0$ are taken equal to the values found for each experiment. Section 7.2.4 discusses several examples of both the temporal evolution of the pure components as well as the modeled result via the rate equations. Note that the start of each experiment is almost exclusively sensitive to k_f, since $[HDO]_0$ is always low. We therefore chose to use the first 33% in time, while still in the linear regime, of the experiment to determine k_f. A discussion on this topic is given in the section below.

7.2.4 *Optimization procedure*

Figure 7.4 depicts three examples of our modeled results, for temperatures of 90, 125, and 140 K (experiments 1, 4, and 8 in Table 7.1). The top row, panels (a)-(c), shows the HDO fit to the experiments for the first 33% of the experiment, and from the (near-) linearity of the experimental slopes it can be deduced that it is indeed sensitive mainly to k_f. In panels (d)-(f) the time evolution of the experimental and modeled abundances (Eqns. 47-49) for all three species is plotted for the entire experimental time.

Analyzing the abundances at 90 K we find an apparent discrepancy for the temporal evolution of D_2O. While the recorded H_2O and HDO abundances remain constant in time, since there is no proton exchange at this low temperature, the D_2O abundance does not. Inspection of the IR spectra shows that this is likely caused by the spectroscopic artifact between ~1050 and ~1250 cm^{-1} mentioned above. This artifact actually partially overlaps with the D_2O signal. We therefore decided not to include the heavy water abundance explicitly in the determination of the optimal reaction rates, but to check in retrospect whether or not the modeled abundance is in approximate agreement with the experiments.

Furthermore, the graphs at high temperature (140 K) show that both modeled H_2O and D_2O abundances deviate somewhat from the experiment. We have studied two limiting cases of the dependence of the H_2O and D_2O abundances on the HDO calibration spectrum: (a) assuming a 'pure' HDO calibration spectrum and (b) assuming a statistical 1:2:1 distribution between H_2O:HDO:D_2O for the deposited HDO. Unfortunately, the HDO ice which we deposited to obtain our HDO calibration spectrum did not only contain HDO, but also H_2O and D_2O. If we do not account for this in our calibration spectrum (case (a)), the water and heavy water contribution are decreased during the fitting procedure. Accounting for the presence of both contaminants in the HDO calibration spectrum by assuming a statistical distribution (case (b)) will on the contrary lead to an overestimation of the H_2O and D_2O abundances. Therefore, we decided to optmize the model obtaining k_f and k_r using only the HDO abundance. Subsequently, we verify that using the obtained values for k_f and k_r the modeled water and heavy water abundances fall within the range determined by the two limiting cases.

Thus, the optimization sequence used for modeling the HDO abundance is as follows:

1. k_f is optimized by modeling the first 33% in time of the experiment with $k_r = 0$
2. k_r is optimized by modeling the final 33% in time of the experiment with k_f fixed to the value found in (i)
3. k_f is optimized again by modeling the full experiment with k_r fixed to the value found in (ii).

The error function used for this optimization is

$$E_{HDO} = \sum_{t_1}^{t_2} \frac{1}{\Delta t} \frac{\left([HDO]_{model}(t) - [HDO]_{exp}(t)\right)^2}{\left\langle [HDO]_{model}(t) + [HDO]_{exp}(t) \right\rangle} . \tag{50}$$

The reaction rates leading to the lowest error are selected to be used in next iterations or are stored as the optimum rates.

Finally, the activation energy of R1 is determined by an Arrhenius fit of the different reaction rates versus temperature. The error associated with this fit is determined with the stats subpackage of scipy in python and corresponds to the standard error of the slope.

7.3 RESULTS AND DISCUSSION

7.3.1 *Activation energy of proton exchange in H_2O:D_2O mixtures*

The reaction rates obtained from the reaction dynamical fitting by a simple rate equation model are converted into an activation energy with the use of an Arrhenius expression:

$$k = \nu \, \exp\left(\frac{-E_a}{k_B T}\right) . \tag{51}$$

In this expression the pRactor, ν, represents a trial frequency related to the vibrations of a species in a local potential well and corresponds to values between 10^{12} and 10^{13} s^{-1} (Hasegawa et al., 1992). Figure 7.5 depicts $\ln(k_f)$ versus 1/T. If experiments 2-10 are included in the determination of the activation energy, a value of 3840 ± 125 K is found. The error given here is the error of the slope. The exact value found for the activation energy changes when the amount of assumed contamination in the HDO spectrum is varied, *i.e.*, going from case (a) to (b). The resulting values, however, are not significantly different as assessed by a two-sided student's t-test ($p < 0.05$).

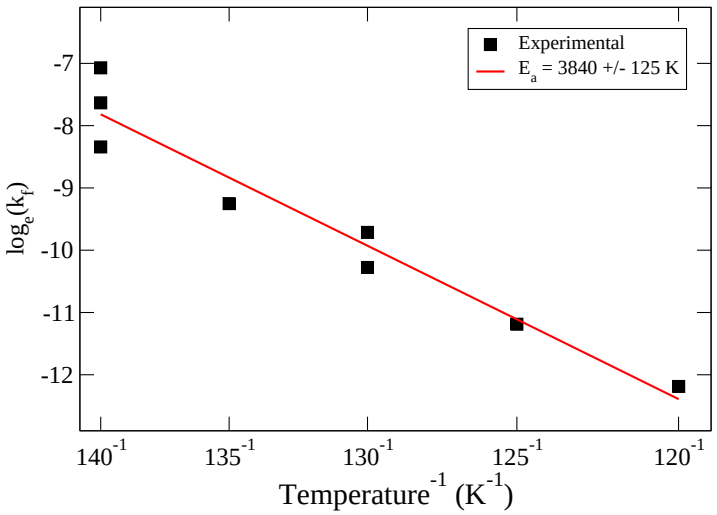

Figure 7.5: Arrhenius plot for k_f.

As stated before, Wooldridge & Devlin (1988) found a substantially higher activation energy of ~5000 K associated with reaction R1. They proposed a mechanism of proton transfer that occurs via ionic defects in the ice. These defects will be more prominent in an amorphous ice and indeed the rate increases drastically; $e^{-3840/T}/e^{-5000/T} > 4000$ for $T \leqslant 140$ K. The specific implications of this for astrochemical environments are discussed in Section 7.5.

Experiments below 130 K are not sensitive to k_r, because the situation in which enough HDO molecules are next to each other is never reached within the experimental duration. For our experiments at 130-140 K it is not possible to find any correlation between k_r and the temperature, again because for the largest part of the experiment there are not enough HDO molecules close to each other. However, Collier et al. (1984) suggested that $k_r < k_f$ in the case of an isolated D_2O molecule in an H_2O surrounding, as a result of the local structure. This can also be explained from a more theoretical free energy point-of-view. The total Gibbs free energy of the reaction, G, is determined by the enthalpies, H, and entropies, S, of the molecules:

$$\Delta G(2\,\mathrm{HDO\text{-}H_2O\text{-}D_2O}) = \Delta H_f - T \cdot \Delta S_f\,. \tag{52}$$

Using the gas-phase data reviewed in Chase (1998) this leads to the following expression

$$\Delta G = 290 - T \cdot 11.86 \quad \mathrm{J\ mol^{-1}} \tag{53}$$

$$= 34.88 - T \cdot 1.43 \quad \mathrm{K}\,. \tag{54}$$

Although the thermochemistry in the solid state is affected by the local structure, the gas-phase expression given above does show that the driving force is the entropy change and that the reaction becomes clearly exogonic at higher temperatures only, hence we also expect that $k_r < k_f$. If this relation is incorporated into the optimization procedure, the activation energy found does not differ significantly from 3840 K.

Finally, note that here no conclusions can be drawn concerning the prefactor ν, because accurate values for the band strengths are lacking.

7.3.2 *Proton exchange in other hydrogen bonded molecules*

As mentioned in the Introduction, proton exchange in ices has been studied previously for several (mixtures of) hydrogen-bonded molecules. Here, we mention these studies specifically and extend the studies of water to a more general ice theme: proton exchange in hydrogen bonded molecules. As long as so-called proton wires exist between the hydrogen bonded molecules, exchange is expected to be rapid (Bertie & Devlin, 1983). A proton wire can be thought of as a chain of hydrogen bonded molecules that has the flexibility to transfer protons from one to the next molecule. In such a way, any ionic defect in the ice can be easily passed on to the neighboring molecule and hence protons and deuterons can move efficiently. The following ice mixtures are briefly discussed: NH_3:D_2O, CD_3OD:H_2O, CD_3ND_2:H_2O, and NH_2OH:D_2O.

Exchange between isolated NH_3 in an amorphous D_2O ice was found to be faster than in pure water ice and much faster than for crystalline ammonia (Thornton et al., 1981; Bertie & Devlin, 1983). We have performed a similar experiment, co-depositing NH_3 and D_2O (2:3) at low temperature and heating to 130 K, experiment 11 in Table 7.1. Indeed rapid exchange of protons can be confirmed. A steady-state HDO concentration is reached at least three times faster than in the case of water (experiment 5). This shows once more that amorphicity can enhance the exchange rates.

Concerning the case of isolated amorphous d4-methanol mixed with water both Ratajczak et al. (2009) and Souda et al. (2003) confirmed thermal exchange to be efficient at laboratory time scales starting from 120 K. Note that this exchange concerns specifically the hydroxyl group of methanol. The C-D (or C-H) bonds do not participate in any hydrogen bonding network and are therefore not exchanged via this mechanism. They can, however, be exchanged via deuterium bombardment of CH_3OH as discussed by Nagaoka et al. (2005).

Ratajczak (2012) also studied the exchange of isolated CD_3ND_2 (methyl-amine) with water and found similar results as for methanol: exchange takes place only on the amine entity of the molecule and is detectable from 110 K onwards.

Here, in light of recent studies highlighting the hydrogenation of NO molecu-les and the subsequent formation of NH_2OH (Congiu et al., 2012; Fedoseev et al., 2012), we also performed an experiment probing the exchange between D_2O and NH_2OH (Experiment 12, Table 7.1). In this case both hydrogen bearing groups are able to form hydrogen bonds. A layer of NH_2OH is grown following a similar procedure as described by Fedoseev et al. (2012) and capped with a layer of D_2O at 15 K. Increasing the sample temperature to 130 or 140 K could lead to exchange of protons and deuterons on the interface of the two molecular layers. However, proton exchange is not clearly visible by RAIR spectroscopy due to overlapping band frequencies between the NH(D) and OD(H) groups. Therefore, a temperature programmed desorption (TPD) experiment is performed, during which the molecules gain more mobility increasing the probability that NH_2OH and D_2O meet, albeit for a short time until full desorption takes place. This experiment resulted in the detection of mass to charge ratios of 19, 34, 35, and 36 in the QMS, see Fig 7.6. In this Figure, the intensity does not reflect the in situ infrared intensity, but the intensity of gas-phase species after evaporation from the surface during a linear heating of the substrate. The temperature indicates the surface temperature at which this evaporation occurs. These masses correspond to the molecules HDO, singly and doubly deuterated NH_2OH, and ND_2OD. This confirms proton exchange in the amine and hydroxyl groups, both of which have hydrogen bonds.

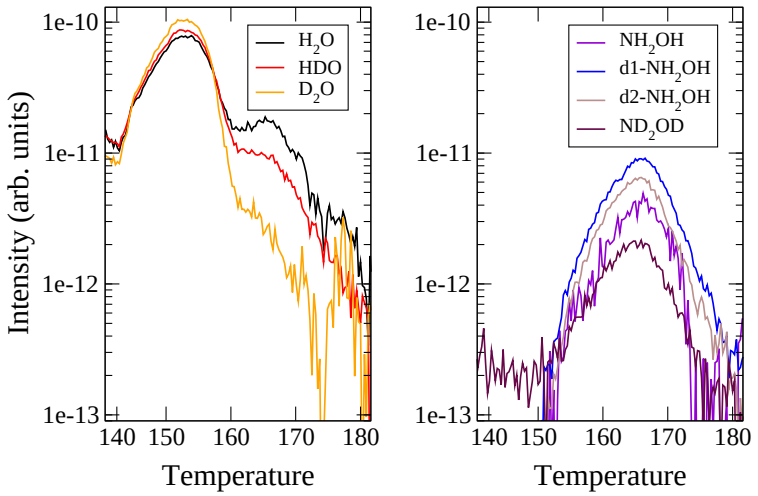

Figure 7.6: QMS traces for TPD experiments of mass to charge ratios of 18, 19, 20, 33, 34, 35, and 36 probing exchange in a layered NH_2OH:D_2O ice. Note that the x-axis unit changed to temperature.

7.4 EXPERIMENTAL CONCLUSIONS

The thermal process of proton/deuteron exchange between water and its isotopologues has been studied in mixed ices. Using RAIR spectra the time evolution of the characteristic vibrational bending modes of H_2O, HDO, and D_2O has been monitered as a function of temperature. In particular H_2O and D_2O have been grown at 15 K and heated up to a desired temperature where the occurence of HDO has been probed, signalling that the reaction $H_2O + D_2O \longrightarrow 2HDO$ takes place. Temperatures between 90 and 140 K have been considered and with the use of a simple rate equation model, a reaction rate for each temperature has been determined. The linearity of the resulting Arrhenius plot in Fig. 7.5 shows that it is reasonable to express the rate through thermal activation and an activation energy of 3840 K has been found.

Ratajczak (2012) suggests that proton exchange coincides with crystallization. However, exchange has been found to take place prior and post crystallization, both in the work presented here as well as by Wooldridge & Devlin (1988); Fisher & Devlin (1995); Gálvez et al. (2011). In the ISM, (F)UV radiation would in fact render the ices largely compact amorphous by destruction of local molecules and recombination of its fragments and exothermic energy release upon molecule formation is likely to have the same effect (Palumbo, 2006; Oba et al., 2009).

In this study, we mimic the lack of long-range order in interstellar ices by intentionally growing amorphous ice structures. The aim is to investigate whether a higher concentration of structural defects (see Fig. 7.1) in amorphous ices with respect to crystalline structures leads to exchange rates high enough to become relevant on interstellar time scales. We indeed find a lower overall (or rate-determining) activation energy associated with the exchange in non-doped amorphous ices with non-energetic detection methods compared to crystalline ices: 3840 versus 5000 K. This corresponds to the quantitative findings of Fisher & Devlin (1995) for doped ices, those of Moon et al. (2010) for pure ice surfaces and to the qualitative results

Table 7.2: Typical thermal exchange timescales at various grain temperatures and activation energies.

T (K)	E_a = 5000 K [1]	E_a = 3840 K [2]
70	3.3×10^{11} yr	2.1×10^{4} yr
80	4.4×10^{7} yr	2.2×10^{1} yr
90	4.2×10^{4} yr	1.1×10^{-1} yr

[1] Wooldridge & Devlin (1988). [2] This work

mentioned by Gálvez et al. (2011). The latter paper also discusses H/D exchange in water ices, but from the point of view to investigate whether HDO detections in ice are possible.

Assuming a values of 10^{12} s^{-1} for the prefactor ν in Eqn. 51, this corresponds to typical timescales as summarized in Table 7.2. The large differences covering orders of magnitude of the typical timescales of proton exchange clearly show the importance of incorporating the correct activation energy.

7.5 ASTROCHEMICAL IMPLICATIONS

Interstellar ices are likely to be defect-rich by nature because of the many ice components and various types of (energetic) processing. Furthermore, since ices consist mainly of water, the hop-and-turn mechanism is likely to dominate proton exchange, while, simultaneously, the existence of the proton wires mentioned above is key to efficient transfer.

7.5.1 *Protostellar and protoplanetary environments*

The typical timescales derived with the experimentally found activation energy can be compared to interstellar timescales, *i.e.*, those mentioned in Table 7.2 and those obtained for protostellar and protoplanetary disk environments. Schöier et al. (2002) showed that the transit time for grains and molecules through the warm, dense region around the hot core IRAS 16293-2422 is of the order of several hundred years. Ices present at temperatures above 80 K can thus be influenced by scrambling. Furthermore, although the high dust-temperature regions in disks concern only the inner few mid-plane AU (Walsh et al., 2010), turbulent vertical and radial mixing can result in transportation of water from the midplane to disk surface (Furuya et al., 2013; Albertsson et al., 2014). This is part of a cycle in which atomic oxygen is transported to the midplane and reforms water and/or other molecules. Since the grains are transported, also the time they pass at higher temperatures is longer, hence allowing proton scrambling to take place. This then applies to all hydrogen bonded molecules. Mixing timescales are determined by the ratio between the column density of water and the flux in upward or radial direction (Furuya et al., 2013). They find that typical timescales range between 10^4 and 10^7 yrs for radii between 1 and 200 AU and that the radial accretion timescale is of a similar order of magnitude and are long enough to allow scrambling to take place.

Comparing typical dynamical timescales in protostellar and protoplanetary disk environments to the values listed in Table 7.2, we find that an activation energy of 3840 K renders the thermally activated H/D exchange relevant at static dust temperatures of 70 K and above.

We would therefore expect a D_2O detection probability lower than determined statistically in high-temperature regions, because any D_2O available in the ice is likely to be converted into two HDO molecules given enough time.

In fact, consistent with this conclusion, in the warmer regions surrounding NGC 1333 IRAS2A Coutens et al. (2014) found a lower D_2O/HDO ratio than in the cold envelope layer around IRAS 16293-2422 (Coutens et al., 2013). The higher D_2O/HDO than HDO/H_2O ratios reported in both cases are currently under debate. Two possible causes are that either (i) the surface deuteration chemistry network is ill-constrained or (ii) that both sublimation of grain mantles and water formation at higher gas-phase temperatures takes place in the inner regions of this source. Alternatively, if high D_2O abundances compared to modeled results turn out to be common (Coutens et al., 2013, 2014), it must be because the ice mantle does not encounter high temperatures for long enough times. This means that the timescales derived here can also be used in the opposite way, to determine an upper limit for the time that an icy grain resides in an area of a certain temperature. Currently, the limited number of observations does not allow us to draw such a conclusion.

7.5.2 *Cometary ices*

Shifting focus towards the application of exchange in cometary ices, we note that to the best of our knowledge no large ice chemistry models of comets exist. In the gas-phase coma model of Rodgers & Charnley (2002) a high ice abundance is sublimated as a given initial condition. The ice itself, however, is not modeled. They found that the D/H ratio in gas-phase coma species is determined by the ratio in their parents. Thus, the ice in fact does determine the deuterium fractionation found in the coma. Ideally, ice abundances should be determined by a cometary ice chemistry model incorporating low- and high-temperature chemistry, as well as sublimation effects to investigate the effect of accumulative heating on ices.

Thermal chemistry, in particular H/D transfer, can play a major role in the thick cometary ices, changing the deuterium fractionation of many species, because HDO is the main deuterated component of these ices.

The recent results on the HDO/H_2O ratio in the coma of comet 67P/Churyu-mov-Gerasimenko and the discrepancy with respect to the D/H ratios in other Jupiter family comets shows that it is crucial to understand the effect of thermal processing of ice constituents (Altwegg et al., 2015).

7.5.3 *Proof-of-principle modeling*

Scrambling of deuterons at high temperatures can alter the D/H ratios and therefore should be taken into account, when using D/H ratios to determine the cosmic origin of the water on Earth. This holds not only for the main component of interstellar ice, water, but especially also for any species that has an N-H or O-H bond that can participate in hydrogen bonding. Molecules detected in the ISM with such functional groups, most of which are though to have been formed on the surface of dust grains, are *e.g.* HNO, HNC, HNCO, HNCS, NH_3, NH_2OH, CH_3OH, $HCONH_2$, CH_3NH_2, NH_2CH_2CN,
CH_3CH_2OH, $(CH_2OH)_2$.

In all examples mentioned in Section 7.3.2 the hydrogen bonded network for OH and NH moieties plays a crucial role in H/D exchange. Moreover, functional groups with CH that do not participate in hydrogen bonds do not exchange their proton thermally.

We emphasize that as a first approximation exchange of protons and deuterons between water

and other hydrogen bonded species should be modeled using an activation energy of ~3840 K both in disk structures as well as in cometary ices.

Note that as discussed above, the forward and backward reaction rates are not expected to be equal, due to a more favorable entropy for the reaction $H_2O + D_2O \longrightarrow 2HDO$ with respect to the backward reaction. Although the activation energy itself is constrained only for the case of water and its deuterated analogues, arguments of enthalpy and entropy can also aid in constraining the reaction rates of H/D transfer for other molecules, as suggested by our experiments listed in Table 7.1. Finally, reactions with no net effect, such as $H_2O + HDO \longrightarrow HDO + H_2O$, only have meaning in a microscopic model, where they can be seen as analogues of diffusion. Thus, in a rate equation based model, they can be omitted.

BIBLIOGRAPHY

Aikawa, Y., van Zadelhoff, G. J., van Dishoeck, E. F., & Herbst, E. 2002, Astron. Astrophys., 386, 622
Albertsson, T., Semenov, D., & Henning, T. 2014, Astrophys. J., 784, 39
Altwegg, K., Balsiger, H., Bar-Nun, A., et al. 2015, Science, 347, A387
Bergin, E. A. & Tafalla, M. 2007, Annu. Rev. Astron. Astrophys., 45, 339
Bertie, J. E. & Devlin, J. P. 1983, 78, 6203
Bertie, J. E. & Whalley, E. 1964, 40, 1637
Bockelée-Morvan, D., Lis, D. C., Wink, J. E., et al. 2000, Astron. Astrophys., 353, 1101
Bossa, J.-B., Isokoski, K., de Valois, M. S., & Linnartz, H. 2012, Astron. Astrophys., 545, A82
Butner, H. M., Charnley, S. B., Ceccarelli, C., et al. 2007, Astrophys. J. Lett., 659, L137
Caselli, P. & Ceccarelli, C. 2012, Astron. Astrophys. Rev., 20, 56
Chase, M. W. 1998, Journal of physical and chemical reference data, Monograph, no. 9. (Washington DC: American Chemical Society)
Cleeves, L. I., Bergin, E. A., Alexander, C. M. O., et al. 2014, Science, 345, 1590
Collier, W. B., Ritzhaupt, G., & Devlin, J. P. 1984, The Journal of Physical Chemistry, 88, 363
Congiu, E., Fedoseev, G., Ioppolo, S., et al. 2012, Astrophys. J. Lett., 750, L12
Coutens, A., Jørgensen, J. K., Persson, M. V., et al. 2014, Astrophys. J. Lett., 792, L5
Coutens, A., Vastel, C., Cazaux, S., et al. 2013, Astron. Astrophys., 553, A75
Fedoseev, G., Ioppolo, S., Lamberts, T., et al. 2012, J. Chem. Phys., 137, 054714
Fisher, M. & Devlin, P. 1995, J. Phys. Chem., 99, 11584
Fuchs, G. W., Cuppen, H. M., Ioppolo, S., et al. 2009, Astron. Astrophys., 505, 629
Furuya, K., Aikawa, Y., Nomura, H., Hersant, F., & Wakelam, V. 2013, Astrophys. J., 779, 11
Gálvez, Ó., Maté, B., Herrero, V. J., & Escribano, R. 2011, Astrophys. J., 738, 133
Grim, R. J. A., Greenberg, J. M., de Groot, M. S., et al. 1989, Astron. Astrophys. Suppl. Ser., 78, 161
Hasegawa, T. I., Herbst, E., & Leung, C. M. 1992, Astrophys. J. Suppl. Ser., 82, 167
Hiraoka, K., Miyagoshi, T., Takayama, T., Yamamoto, K., & Kihara, Y. 1998, Astrophys. J. , 498, 710
Ioppolo, I., Fedoseev, G., Lamberts, T., Romanzin, C., & Linnartz, H. 2013, Rev. Sci. Instrum. , 84, 073112
Ioppolo, S., Cuppen, H. M., Romanzin, C., van Dishoeck, E. F., & Linnartz, H. 2008, Astrophys. J., 686, 1474
Itikawa, Y. & Mason, N. 2005, J. Phys. Chem. Ref. Data, 34
Jørgensen, J. K., Schöier, F. L., & van Dishoeck, E. F. 2002, Astron. Astrophys., 389, 908
Jung, K.-H., Park, S.-C., Kim, J.-H., & Kang, H. 2004, J. Chem. Phys., 121, 2758
Karssemeijer, L. J. 2014, based on the ASW samples used in (Karssemeijer et al., 2014)
Karssemeijer, L. J., Ioppolo, S., van Hemert, M. C., et al. 2014, Astrophys. J., 781, 16
Kim, J.-H., Kim, Y.-K., & Kang, H. 2009, 131, 044705
Launhardt, R., Stutz, A. M., Schmiedeke, A., et al. 2013, Astron. Astrophys., 551, A98
Lee, C.-W., Lee, P.-R., Kim, Y.-K., & Kang, H. 2007, 127, 084701
Miyauchi, N., Hidaka, H., Chigai, T., et al. 2008, Chem. Phys. Lett., 456, 27
Moon, E.-S., Yoon, J., & Kang, H. 2010, J. Chem. Phys., 133, 044709
Morbidelli, A., Chambers, J., Lunine, J. I., et al. 2000, Meteoritics and Planetary Science, 35, 1309
Muralidharan, K., Deymier, P., Stimpfl, M., de Leeuw, N. H., & Drake, M. J. 2008, Icarus, 198, 400
Nagaoka, A., Watanabe, N., & Kouchi, A. 2005, Astrophys. J. Lett., 624, L29
Nomura, H. & Millar, T. J. 2005, Astron. Astrophys., 438, 923
Oba, Y., Miyauchi, N., Hidaka, H., et al. 2009, Astrophys. J., 701, 464
O'Brien, D. P., Walsh, K. J., Morbidelli, A., Raymond, S. N., & Mandell, A. M. 2014, Icarus, 239, 74
Oxley, S. P., Zahn, C. M., & Pursell, C. J. 2006, The Journal of Physical Chemistry A, 110, 11064
Palumbo, M. E. 2006, Astron. Astrophys., 453, 903
Park, S.-C., Jung, K.-H., & Kang, H. 2004, 121
Ratajczak, A. 2012, Phd thesis, Université de Grenoble
Ratajczak, A., Quirico, E., Faure, A., Schmitt, B., & Ceccarelli, C. 2009, Astron. Astrophys., 496, L21

Ratajczak, A., Taquet, V., Kahane, C., et al. 2011, Astron. Astrophys., 528, L13
Rodgers, S. D. & Charnley, S. B. 2002, Mon. Not. R. Astron. Soc., 330, 660
Schöier, F. L., Jørgensen, J. K., van Dishoeck, E. F., & Blake, G. A. 2002, Astron. Astrophys., 390, 1001
Souda, R., Kawanowa, H., Kondo, M., & Gotoh, Y. 2003, 119
Straub, H. C., Lindsay, B. G., Smith, K. A., & Stebbings, R. F. 1998, 108
Thornton, C., Khatkale, M. S., & Devlin, J. P. 1981, 75
Tielens, A. G. G. M. 1983, Astron. Astrophys., 119, 177
Tielens, A. G. G. M. 2013, Rev. Mod. Phys., 85, 1021
Uras-Aytemiz, N., Joyce, C., & Devlin, J. P. 2001, 115
van der Tak, F. F. S., van Dishoeck, E. F., Evans, II, N. J., & Blake, G. A. 2000, Astrophys. J., 537, 283
Vastel, C., Ceccarelli, C., Caux, E., et al. 2010, Astron. Astrophys., 521, L31
Walsh, C., Millar, T. J., & Nomura, H. 2010, Astrophys. J., 722, 1607
Watanabe, N. & Kouchi, A. 2002, Astrophys. J. Lett., 571, L173
Wooldridge, P. J. & Devlin, J. P. 1988, 88, 3086

8

LOW-TEMPERATURE CHEMISTRY BETWEEN WATER AND THE HYDROXYL RADICAL – H/D ISOTOPIC EFFECTS

Sets of systematic laboratory experiments are presented - combining UHV cryogenic and plasma-line deposition techniques - that allow to compare H/D isotopic effects in the reaction of H_2O (D_2O) ice with the hydroxyl radical OD (OH). The latter is known to play a key role as intermediate species in the solid state formation of water on icy grains in space. The main finding of our work is that the reaction $H_2O + OD \longrightarrow OH + HDO$ occurs and that this may affect the HDO/H_2O abundances in space. The opposite reaction $D_2O + OH \longrightarrow OD + HDO$ is much less effective, and also given the lower D_2O abundances in space not expected to be of astronomical relevance. The experimental results are extended to the other four possible reactions between hydroxyl and water isotopes and are subsequently used as input for kinetic Monte Carlo simulations. This way we interpret our findings in an astronomical context, qualitatively testing the influence of the reaction rates, excess energy, and cloud extinction.

T. Lamberts, G. Fedoseev, F. Puletti, S. Ioppolo, H. M. Cuppen, and H. Linnartz, *Low-temperature chemistry between water and hydroxyl radicals; H/D isotopic effects*, submitted to Mon. Not. R. Astron. Soc. (2015)

8.1 INTRODUCTION

Surface reactions on grains have been proposed as an effective way to form water at the low temperatures typical for the interstellar medium (van de Hulst, 1949; Tielens & Hagen, 1982). Over the last ten years many of the possible reactions have been tested in various laboratories and reaction routes, rates, and branching ratios have been determined (Hiraoka et al., 1998; Miyauchi et al., 2008; Ioppolo et al., 2008, 2010; Cuppen et al., 2010; Romanzin et al., 2011). The general conclusions obtained in these studies are in line with each other (Dulieu, 2011) and have been summarized by van Dishoeck et al. (2013).

A detailed characterization of the solid state formation of water also holds the potential to study deuteration effects. With the goal to understand how water was delivered to Earth, there has been much interest in linking the HDO/H_2O ratio in cometary, interstellar, and laboratory ices as well as astronomical (gas-phase) observations to ratios as found in our oceans (Rodgers & Charnley, 2002; Hartogh et al., 2011). Therefore, both the origin of the HDO/H_2O ratio in the ices and their subsequent chemical and thermal processing are currently widely studied (Caselli & Ceccarelli, 2012). It is in fact during the water formation on dust surfaces when the deuterium fractionation commences. This preferential incorporation of D over H in molecules can lead to D/H ratios in molecules that are much larger than the primordial ratio of $\sim 1.5 \times 10^{-5}$ (Piskunov et al., 1997; Oliveira et al., 2003). To understand the origin of this fractionation, it is neccessary to consider both the gas-phase and solid-state processes that are at play. The driving forces behing these processes are the lower zero-point energy of an X-D bond with respect to an X-H bond and the difference in tunneling behavior, both as a result of the larger mass of deuterium (Roberts et al., 2003; Tielens, 1983; Caselli & Ceccarelli, 2012; Lipshtat et al., 2004). One of the possible enhancement routes for hydrocarbon bonds is the simple replacement of a hydrogen by a deuterium *via* a deuterium mediated abstraction mechanism: $-CH + D \longrightarrow -C + HD$ followed by $-C + D \longrightarrow -CD$ (Nagaoka et al., 2005, 2007). An example is substitution of H for D in solid methanol, which has been found to be efficient, whereas the reverse reaction (substituting D for H) is not. Note that Nagaoka et al. (2005) have also attempted to substitute hydrogen in water by the same process, but did not find any deuteration upon D exposure. The non-occurence of reaction $H_2O + D$ has been confirmed in our laboratory (unpublished data).

Another abstraction process, so far studied in less detail, involves OH and OD radicals. Hydroxyl radicals play an important role as reactive intermediates in water formation (see e.g. Cuppen et al., 2010; Chapter 5). Furthermore, recent microscopic models have shown that the radical concentration in the ice can be very high if photon penetration is included (Chang & Herbst, 2014). Garrod (2013) indicated the importance of abstraction reactions by the hydroxyl radical in the framework of complex hydrocarbon molecules. Such an OH induced abstraction mechanism is particularly important in water-rich ices, because both OH and OD radicals are produced on the surface by radical chemistry and by photodissociation of water isotopologues (Ioppolo et al., 2008; Andersson & van Dishoeck, 2008; Öberg et al., 2009).

Considering again the formation of HDO in the ice, the water surface reaction network needs to be duplicated, involving both reactions with hydrogen and deuterium. As a result of the large number of reactions that are in competition with each other and with diffusion, it is experimentally challenging to study hydrogenation and deuteration simultaneously. Therefore, in the past, either the deuteration pathways have been studied separately, *e.g.*, $O_2 + D$ (Chaabouni et al., 2012), or specific reaction routes are tackled theoretically and experimentally, *e.g.*, OH (OD) + H_2 (HD or D_2) and H_2O_2 (D_2O_2) + H (D) (Kristensen et al., 2011; Oba et al., 2012, 2014). Here, we add to these studies and investigate the cross links between the

hydrogenation and deuteration networks by the following four hydrogen abstraction reaction *via* hydroxyl radicals:

$$H_2O + OD \xrightarrow{k_1} OH + HDO \quad (R1)$$

$$HDO + OD \xrightarrow{k_2} OH + D_2O \quad (R2)$$

$$HDO + OH \xrightarrow{k_3} OD + H_2O \quad (R3)$$

$$D_2O + OH \xrightarrow{k_4} OD + HDO \quad . \quad (R4)$$

Hydrogen abstraction of OH from H_2O (or the fully deuterated analog) can also take place

$$H_2O + OH \xrightarrow{k_5} OH + H_2O \quad (R5)$$

$$D_2O + OD \xrightarrow{k_6} OD + D_2O \quad (R6)$$

and although this does not have a net effect on the abundances in the ice, it can be seen as an analog of bulk diffusion, of which models indicate it is of great importance in ice chemistry (Vasyunin & Herbst, 2013; Chang & Herbst, 2014; Chapter 5).

Reactions R2 and R3 cannot be studied in the laboratory, because it is not feasible to deposit pure HDO. Room-temperature rapid proton transfer reactions scramble the protons and deuterons and yield a statistical ~ 1:2:1 mixture of H_2O:HDO:D_2O if one were to start from a pure HDO liquid. Such scrambling has been found to take place efficiently even in ices at temperatures far below room temperature (Chapter 7). Therefore, here, only reactions R1 and R4 are tested experimentally, at low temperature and using reflection absorption infrared (RAIR) spectroscopy as an in-situ diagnostic tool.

Note that from an astrochemical point-of-view, reactions R2, R4, and R6 are unlikely to be relevant as a result of the low concentrations of the reactants (D_2O and OD) present in the ice. Nevertheless, we put efforts in characterizing R4, as an understanding of the underlying mechanism helps in painting the full picture. Reactions R1 and R3, on the contrary, could occur in regions with a high photon flux as this causes water and isotopologues to dissociate, thus generating additional hydroxyl radicals.

In the following, we outline the experimental setup and sets of experiments performed (Section 8.2), the analysis of the resulting RAIR spectra (Section 8.3), the astrochemical implications by means of a kinetic Monte Carlo model (Section 8.4), and we conclude with summarizing remarks (Section 8.5).

8.2 EXPERIMENTAL METHODS

Two sets of representative experiments and their corresponding control experiments are summarized in Table 8.1. All measurements are performed at a surface temperature of 15 K for a duration of 90 minutes. The two experiments that are used for this study are part of a larger set, varying mixing ratios and temperatures, and found to be optimum for the goals set in this work. The findings of the other experiments are largely in line with the ones discussed here, but do not add additional information.

Experiments are performed using the SURFRESIDE^2 setup, which was constructed to systematically investigate solid-state reactions leading to the formation of molecules of astrophysical interest at cryogenic temperatures. The setup has already been extensively described in Ioppolo et al. (2013) and therefore only a brief description of the procedure is given here.

SURFRESIDE^2 consists of three UHV chambers with a room-temperature base-pressure between $10^{-9} - 10^{-10}$ mbar. A rotatable gold-coated copper substrate in the center of the

Table 8.1: Summary of the performed experiments with additional calibration and control experiments and corresponding parameters, $T_{surf} = 15$ K and $t_{exp} = 90$ min in all cases. The deposition rate of the species is denoted as f_{dep} and the angle represents the angle of the deposition line with respect to the surface.

	90°	f_{dep} ($cm^2\ s^{-1}$)	45°	Discharge	f_{dep} ($cm^2\ s^{-1}$)
1a	$H_2{}^{18}O$	4×10^{12}	D_2O	↯	$\leqslant 1 \times 10^{13}$ [a]
1b	$H_2{}^{18}O$	4×10^{12}	D_2O	–	1×10^{13}
1c	–	–	D_2O	↯	$\leqslant 1 \times 10^{13}$ [a]
1d	$H_2{}^{18}O$	4×10^{12}	–	–	–
2a	D_2O	4×10^{12}	$H_2{}^{18}O$	↯	$\leqslant 1 \times 10^{13}$ [a]
2b	D_2O	4×10^{12}	$H_2{}^{18}O$	–	1×10^{13}
2c	–	–	$H_2{}^{18}O$	↯	$\leqslant 1 \times 10^{13}$ [a]
2d	D_2O	4×10^{12}	–	–	–

[a] The upper limit is derived from the D_2O and $H_2{}^{18}O$ deposition rate when the microwave source is turned off.

main chamber is cooled to the desired temperature using a He closed-cycle cryostat with an absolute temperature accuracy of $\leqslant 2$ K.

Both reactions R1 and R4 require a water isotopologue to be co-deposited along with a hydroxyl isotopologue. The former are deposited through a metal deposition line under an angle of 90° and are prepared in a separate pre-pumped ($\leqslant 10^{-5}$ mbar) dosing line. After undergoing several freeze-pump-thaw cycles room-temperature vapor of H_2O or D_2O can partake in the co-deposition. Secondly, the hydroxyl radicals are generated in a Microwave Atom Source (MWAS, Oxford Scientific Ltd, Anton et al. (2000)) using a microwave discharge (300 W at 2.45 GHz) of pure water or heavy water. This discharge is located in a separate UHV beam line with an angle of 45° with respect to the surface. This beam line can be operated independently and is separated from the main chamber by a metal shutter. We cannot quantify the relative deposition rates of all fragments – O, O_2, H, H_2, OH, HO_2, and H_2O (or deuterated equivalents). However, an upper limit can be derived from the H_2O deposition rate when the microwave source is turned off: $\sim 10^{13}$ $cm^2\ s^{-1}$. Many discharge products are thus deposited onto the surface, but only one reacts with D_2O (or H_2O). First, during the calibration stage of our setup the reaction $O + H_2O$ is found not to take place, indicating that discharge fragments that reach the surface are no longer in an excited state (Ioppolo et al., 2013). Both H_2 and O_2 are inert to reactions with other non-radical species as confirmed previously (Ioppolo et al., 2010). The reaction of H with water isotopologues has been dicussed in the Introduction and does not take place in ices for which the water molecules are hydrogen bonded (Nagaoka et al., 2005). The reaction of HO_2 with water is endergonic and has been found to occur in the gas phase only with high barriers (several thousand Kelvin) (Lloyd, 1974). This leaves only the hydroxyl radical to react with a water isotopologue.

To confirm the presence of OH among the H_2O discharge products, we co-deposited H_2O discharge dissociation products with N_2 in a $\sim$ 1:20 ratio during a separate experiment (not listed in Table 8.1). The presence of the OH radical is confirmed *via* its infrared absorption

at 3547 cm^{-1} (Cheng et al., 1988). Furthermore, both $O + H \longrightarrow OH$ and $O_2 \xrightarrow{H} HO_2 \xrightarrow{H} OH + OH$ can lead to additional hydroxyl radicals on the surface, which we expect to thermalize quickly on a picosecond timescale (Arasa et al., 2013; Meyer & Reuter, 2014). Finally, the produced H_2O_2 that forms upon OH recombination on the surface exhibits a comparable temperature dependent behavior to the H_2O_2 features apparent after depositing H_2O dissociation fragments from a similar microwave-discharge plasma by Oba et al. (2011).

A RAIR difference spectrum with respect to the background is acquired every 5 minutes up to the final time of the experiment, 90 minutes. RAIR spectra comprise a spectral range between 4000 and 700 cm^{-1} with a spectral resolution of 1 cm^{-1} and are averaged over 512 scans. Our region of interest lies in the 2000-1000 cm^{-1} range, *i.e.*, the bending modes of H_2O, HDO and D_2O: 1660, 1490, and 1250 cm^{-1}, respectively. Although the bands are broad, the modes are relatively well separated and can be distinguished from each other, whereas that is not the case in the stretching regions. To further enhance the peak separation between the bands of different species we made use of $H_2{}^{18}O$ instead of regular $H_2{}^{16}O$. In the end the effect was limited as in matrix isolation experiments the bending mode of $H_2{}^{18}O$ is redshifted instead of blueshifted with respect to that of $H_2{}^{16}O$. In the following, we will refer to all species without mentioning explicitly the oxygen isotope at hand. Band strengths for the bending modes are typically ill-constrained and therefore we focus here on drawing qualitative conclusions.

The fluxes mentioned in Table 8.1 are calculated using the following relation

$$f_{X_2O} = \frac{c_{X_2O}\, P_{X_2O}\, \langle v \rangle}{4\, k_B\, T} \tag{55}$$

where P_{X_2O} is the pressure, c_{X_2O} is the calibration factor for the pressure gauge for the isotopologues of water, v is the thermal velocity of the vapor molecules at 300 K, k_B is the Boltzmann constant, and T corresponds to the (room) temperature. The calibration factors for both water and heavy water are found to be equal (Straub et al., 1998; Itikawa & Mason, 2005) and we assume here that this also holds for $H_2{}^{18}O$.

The separate experiments within a series, 1a – 1d and 2a – 2d (Table 8.1), are performed sequentially, *i.e.*, on top of each other to make sure that the plasma conditions and deposition rates do not vary between experiments focusing on the abstraction process and the corresponding control experiments. The order in which the measurements are performed is (c)-(a)-(b)-(d). In this particular way first the plasma is able to stabilize before experiment (c) is started. During experiment (c) only the plasma products are deposited and spectra of the accumulated products are recorded. Subsequently the shutter of the plasma chamber is closed, while the plasma remains switched on and a new background spectrum is recorded. It is then possible to perform experiment (a), simply by opening the shutter of both the plasma chamber and the regular deposition line. At the end of this experiment, the discharge is switched off, the shutters of both beamlines are closed and another background spectrum is recorded. By opening the shutters, experiment (b) is performed, *i.e.* no plasma fragments are deposited, but rather the parent molecule itself. Finally, both shutters are closed and a background spectrum is recorded, followed by recording the deposition of non-dissociated species, experiment (d).

8.3 RESULTS AND DISCUSSION

In Figures 8.1 and 8.2 the RAIR spectra recorded after 90 minutes of co-deposition are depicted for experiments 1a - 1c (to investigate reaction R1) and 2a - 2c (idem reaction R4) mentioned in Table 8.1. An overview of the products found in the various spectra and their respective origins is given in Table 8.2. A clear finding is that HDO is only seen in Figure 8.1 and not in Figure 8.2, indicative for different reaction efficiencies.

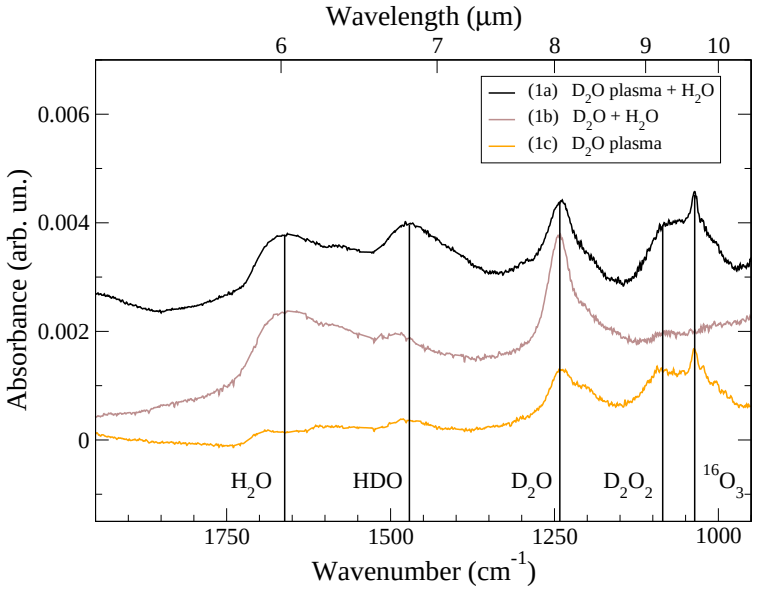

Figure 8.1: $H_2O + OD$. RAIR spectra acquired after 90 minutes of co-deposition for experiments (1a)-(1c), Table 8.1. Graphs are offset for reasons of clarity.

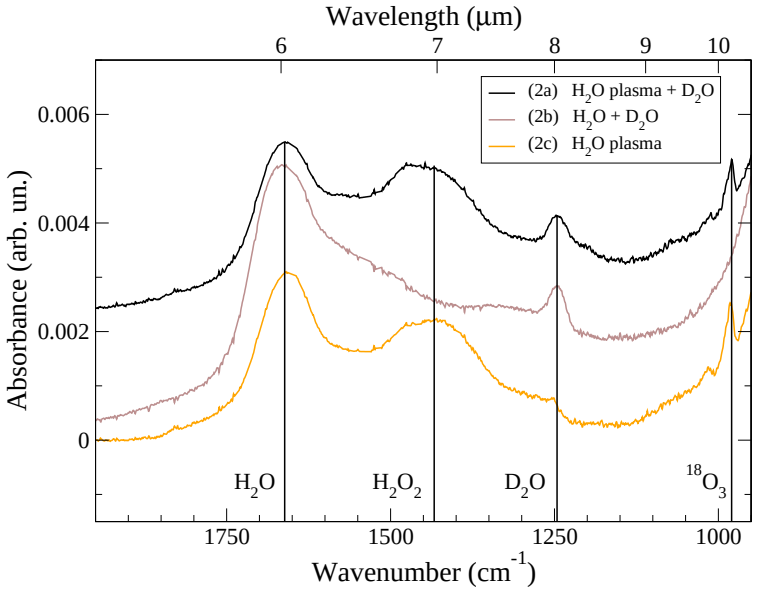

Figure 8.2: $D_2O + OH$. RAIR spectra acquired after 90 minutes of co-deposition for experiments (2a)-(2c), Table 8.1. Graphs are offset for reasons of clarity.

In Figure 8.1, five characteristic infrared features are visible, namely for H_2O, HDO, D_2O, D_2O_2, and $^{16}O_3$. The presence of these species can be explained either by deposition, by (re-)combination of discharge products, or through additional reactions. During experiment 1a ($H_2O + OD$), three molecules are formed in the course of the co-deposition: HDO, D_2O_2, and O_3. Both deuterated peroxide and ozone are also visible in experiment 1c when only dissociated D_2O is deposited on the surface. This indicates that reactions between discharge fragments are responsible for the production of these species. The formation of HDO is, however, observed as a result of reaction R1 which only takes place when the plasma is switched on. The small amount of HDO observed in control experiment 1b, is attributed to contamination in the D_2O sample and is clearly much weaker compared to the feature present in experiment 1a.

In Figure 8.2, four characteristic infrared features are observed, corresponding to H_2O, H_2O_2, D_2O, and $^{18}O_3$. Here, the ozone consists of ^{18}O atoms, as a result of the $H_2{}^{18}O$ plasma that produces both $^{18}O_2$ and ^{18}O. Again, ozone and hydrogen peroxide are generated as a result of discharge fragment (re-)combinations. Throughout experiment 2a ($D_2O + OH$), these are the only two molecules that are formed while HDO production seems to be lacking. However, the peak positions of hydrogenperoxide and singly deuterated water in water-rich environments are very close to each other: ~1435 versus ~1475 cm^{-1} (Devlin, 1990; Oba et al., 2014). Therefore special care is needed to conclude that HDO is not formed efficiently, as its absorption feature may be buried in the H_2O_2 signal. For a detectable level one expects to see a clear shift and a change in total integrated intensity of the peak. In Figure 8.3 a direct comparison between experiment 2a and control experiment 2c is shown. The right panel zooms in on the region of the OH bending mode of both HDO and H_2O_2 (discussed here), while the left panel zooms in on the $\nu_2 + \nu_6$ combination band of H_2O_2 at 2860 cm^{-1}. The latter is the only H_2O_2 band which does not overlap with other species (Lannon et al., 1971) and, as such, can be used as a reference point.

The figure shows that the spectra shift. The OH bending mode band shifts by about 20 cm^{-1}, halfway the peak positions of the H_2O_2 and HDO bands. This would be consistent with HDO formation, but a closer look learns that this shift is due to the changing matrix environment, *i.e.*, the presence of D_2O in experiment 2a or lack thereof in experiment 2c, rather than a detectable amount of HDO formation. The first argument to support this is that also the combination band shifts, roughly 7 cm^{-1}, but in this case the band does not overlap with HDO and is therefore expected not to shift unless the matrix plays a role.

Second, to further study the influence of a mixed HDO and H_2O_2 ice on the bandwidth of the OH bending mode, we artificially added an HDO component to the H_2O_2 component of the H_2O plasma deposition. This is done by selecting specifically the HDO band in experiment 1a in Fig. 8.1, setting its baseline to zero around 1350 and 1530 cm^{-1} and adding it to the same region of the spectrum obtained in experiment 2c. This shows that the final band should then exhibit a larger bandwidth. Clearly the observed band in Fig. 8.3 seems to have shifted rather than to have changed its profile because of merging features. This is only possible when the reaction $D_2O + OH \longrightarrow OD + HDO$ is not efficient.

The third argument follows from a comparison of the integrated band areas (A) of the OH bending mode in experiments 1a, 2a and 2c. Since this involves the rather arbitrary choice of the range over which to integrate, the three experiments were all integrated over several ranges. The first point was chosen between 1340 and 1365 cm^{-1} and the second point between 1520 and 1550 cm^{-1}. Subsequently, the ratio between ($A_{\text{exp. 2a}} - A_{\text{exp. 2c}}$) and $A_{\text{exp. 1a}}$ is derived for all possible combinations of the two limits for the integration range. The maximum ratio poses a strict upper limit on the ratio k_4/k_1 = 0.2. We therefore conclude that the observed

Table 8.2: List of assigned species in the experiments and their respective origins.

Products	Origin	Reaction
Experiment 1		
H_2O	Deposition	
HDO	H_2O reacts with discharge fragments:	$H_2O + OD \longrightarrow OH + HDO$
		$OH + D \longrightarrow HDO$
D_2O	Undissociated molecules in the discharge	
D_2O_2	Reaction of discharge fragments:	$OD + OD \longrightarrow D_2O_2$
		$O_2 + D + D \longrightarrow D_2O_2$
O_3	Reaction of discharge fragments:	$O + O \longrightarrow O_2$
		$O + O_2 \longrightarrow O_3$
Experiment 2		
H_2O	Undissociated molecules in the discharge	
H_2O_2	Reaction of discharge fragments:	$OH + OH \longrightarrow H_2O_2$
		$O_2 + H + H \longrightarrow H_2O_2$
D_2O	Deposition	
O_3	Reaction of discharge fragments:	$O + O \longrightarrow O_2$
		$O + O_2 \longrightarrow O_3$

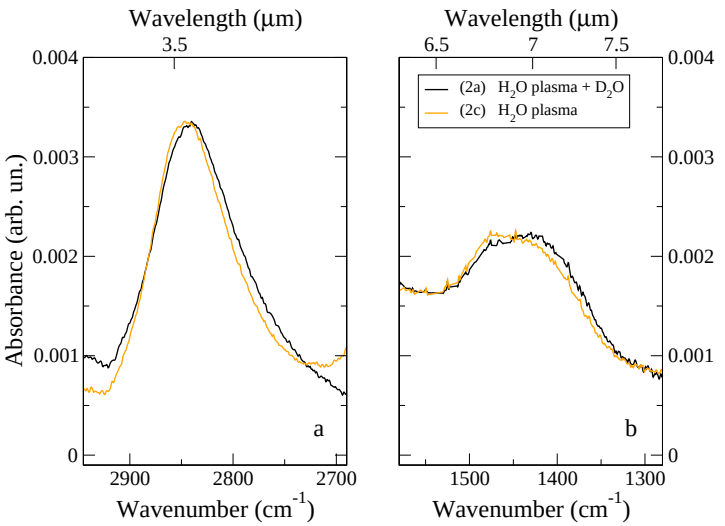

Figure 8.3: Comparison of H_2O_2 RAIR spectra acquired after 90 minutes of co-deposition for experiments (2a) and (2c), Table 8.1. The right panel shows the wavelength domain studied here. The left panel is an additional spectrum in a combination band domain. Graphs are offset in such a way that the bands in both experiments overlap regardless of the baseline.

shift in Fig. 8.3 largely must be due to a matrix effect, ruling out an effective HDO formation in the reaction R4.

A final, independent argument comes from theory. From the experimental set presented here, we conclude that reaction R1 does, and reaction R4 does not efficiently take place at a detectable level for the specific conditions studied. To understand this difference and the overall likelihood of the reactions to take place at low temperatures, the gas-phase Gibbs free energies at 15 K are calculated using the enthalpies and entropies given by Chase (1998):

R1: -1.21 kJ mol^{-1} = -145.66 K

R2: -1.32 kJ mol^{-1} = -159.15 K

R3: 1.21 kJ mol^{-1} = 145.66 K

R4: 1.32 kJ mol^{-1} = 159.15 K.

The experimentally found difference in reaction probability for reactions R1 and R4 is in line with the predictions from gas-phase Gibbs free energies. Extrapolating the experiments, a similar behavior for reactions R2 and R3 is expected.

Additionally, from a tunneling point-of-view, the first two reactions transfer a hydrogen atom, whereas the final two reactions transfer a deuteron. Calculating the effective mass, μ, for this system as outlined by Oba et al. (2012) to find the kinetic isotope effect involved, we find a ~25% decrease in the reaction probabilities assuming that the tunneling rate is well-described by the Wentzel-Kramers-Brillouin or square-potential with width a and height E approximation:

$$k_{\text{tunneling}} \propto \exp\left(-\frac{2a}{\hbar}\sqrt{2\mu E}\right) . \tag{56}$$

This is in agreement with our experimental comparison between the first and the last reaction. Note, however, that the endergonicity still plays a role when tunneling is considered to further decrease the reaction probability (Chapter 6).

To summarize all experimental and theoretical findings and considerations, we expect the following relations to hold:

$$k_4 \ll k_1 \text{ (with an absolute upper limit } k_4 < 0.2\, k_1)$$
$$k_1 \approx k_2 \text{ (assuming thermal activation only)}$$
$$k_1 > k_2 \text{ (assuming that tunneling plays a role)}$$
$$k_3 \approx k_4 .$$

We cannot draw any definitive conclusions concerning reactions R5 and R6, although it is important to note that the change in Gibbs free is zero on average and if tunneling is involved $k_6 < k_5$.

8.4 ASTROCHEMICAL IMPLICATIONS

The key to the astrochemical relevance of the reactions studied here lies in the relative abundances of the water isotopes ($N(H_2O) > N(HDO) > N(D_2O)$) and the ice abundance of both hydroxyl radical isotopes, OH and OD. These species can be either formed on the interstellar dust surfaces *via* O + H and O + D reactions or *via* photodissociation of frozen H_2O, HDO or D_2O. Therefore, especially in rather low-A_V, and relatively high density regions such as translucent clouds the deuterium enrichment effect of the reactions studied here can be substantial. In these regions water is continuously formed and destroyed on the surface until a steady state is reached (Cuppen & Herbst (2007); Cazaux et al. (2010), Chapter 5). Each

time a formed HDO molecule is dissociated into OH + D or, more likely, OD + H (Koning et al., 2013), there is a chance that the hydroxyl radical evaporates. The OD evaporation is in competition with three solid-state reactions creating or recreating HDO:

$$H + OD \rightarrow HDO \tag{R7}$$
$$H_2 + OD \rightarrow H + HDO \tag{R8}$$
$$H_2O + OD \rightarrow OH + HDO \tag{R1}$$

To further characterize this, a previously-used continuous-time random-walk KMC model for water formation is adapted here (Chapters 4 and 5) with an extension of the chemical surface network including all deuteration reactions. All hydrogenation reactions are duplicated and replaced with deuterium analogue(s), initiated by surface reactions with HD or D. If tunneling is expected to be involved, the activation energies are altered accordingly (Oba et al., 2012, 2014). Furthermore, for reactions that can result in more than one product, the branching ratios between the product channels are distributed statistically. We realize that this model is a rather crude approximation, which is necessary, however, as a full model has to take into account too many aspects. It merely serves to test which parameters are crucial when including OH and OD abstraction reactions in the solid state water formation network.

The parameters of the 'translucent cloud' studied here are summarized below. They are chosen such to have a high enough photon flux to induce photodissociation of water, but simulatenously to allow for a minimal build-up of an icy layer. First, a low H_2 gas-phase abundance of 4 cm^{-3} is chosen to minimize the computational cost related to H_2 diffusion on the surface. The validity of this assumption has been tested by changing the H_2 abundance to 500 cm^{-3} and indeed we find no significant difference between the simulations. Second, a high D abundance (one or two orders of magnitude higher compared to Figure 4 in Le Petit et al. (2002) for a molecular fraction of $\sim$ 0.9) is adapted to enhance the HDO abundance on the surface to reduce the total simulation time. The atomic hydrogen density is chosen to be 2 cm^{-3} (Goldsmith & Li, 2005). The remaining fractional densities of the species involved have been chosen typical for a cloud with n_H = 1000 cm^{-3}, *i.e.*, $n_{HD}/n_H = 8 \times 10^{-7}$ and $n_{O(I)}/n_H = 3 \times 10^{-4}$ (Le Petit et al., 2002; Nguyen et al., 2002). Several simulation runs have been performed three times, from which the uncertainty in the HDO/H_2O ratio is found to be $\sim 10 - 30$ % as a result of the low HDO abundances.

An intricate interplay is brought about between several of the simulation input parameters regarding their respective impact on the HDO/H_2O ice ratio, the evaporation of hydroxyl radicals, and the total ice thickness. This is discussed qualitatively below.

Influence of including reactions R1-R6

Reactions R1 and R3 become important after sufficient HDO has been produced on the surface, *i.e.*, either at later stages in the simulation ($> 5 \times 10^4$ years) or upon artificial increase of the D abundance. Indeed, reactions R2, R4 and R6 do not take place efficiently in the simulations, as a result of the low concentrations.

The relations for $k_1 - k_4$ derived experimentally are implemented in the Monte Carlo routine in two ways. First, all reactions are incorporated with a non-zero rate, assuming a conservative upper limit corresponding with $(k_3,\ k_4) < 0.2\ (k_1,\ k_2)$. Second, as experimentally no clear evidence of the occurence of reaction R4 is found, therefore both k_3 and k_4 are set to zero. These simulations are compared to runs where reactions R1-R6 are excluded from the network. We find that the HDO/H_2O ice ratio increases in both cases, since each time that an HDO molecule dissociates, the OD fragment can easily regenerate deuterated water. This is because the likelihood of an OD radical finding an H_2O neighbor is larger than that of finding an H atom. Furthermore, if several values of the ratio $(k_3,\ k_4)/(k_1,\ k_2)$ are tested, the

highest ratio results in the lowest amount of fractionation as a result of the allowed reverse reaction R3. Note that it is often implicitly assumed that the ratios in the ice and in the gas are coupled. This is, however, not always the case (Taquet et al., 2014; Furuya, 2015) and this should be kept in mind.

Excess energy - heat of reaction

All simulations include an excess heat given to each reaction product of a two-product atom addition or photodissociation reaction. For reactions R1 and R2 this value is set to 150 K, whereas reactions R3-R6 receive no excess energy as a result of their endergonicity or net zero Gibbs free energy (Chapter 5). For all other two-product reactions we chose two values, namely 150 and 700 K.

Firstly, a high excess energy allows for more desorption of photodissociation products and therefore the ice thickness decreases by $\sim$ 20%. Furthermore, since reaction R1 provides its products with excess energy this is another source of OH evaporation. Coutens et al. (2014) found a discrepancy between the modeled, predicted D_2O/HDO and HDO/H_2O ratios and the limited set found observationally. They indicated that a possible explanation may be following a higher gas-phase production of H_2O starting from OH. Here, we find that the excess energy is a important parameter in leading to an enhancement of OH in the gas phase.

A lower excess energy keeps more products on the surface and therefore they recycle creating more HDO thus increasing the HDO/H_2O ratio.

Cloud extinction

The cloud extinction also plays an important role in determining the HDO/H_2O ratio, because a lower A_V is associated with a higher degree of photodissociation and therefore more hydroxyl radicals are created. These species can evaporate depending on the excess energy they obtain. Therefore, a low extinction decreases the thickness of the ice, especially when combined with a high excess energy. As a consequence, the HDO/H_2O ratio increases at low A_V as a result of the recycling of OD radicals.

8.5 CONCLUSIONS

We demonstrated experimentally that the reaction between water and a deuterated hydroxyl radical produces singly deuterated water, but the deuterated analogue of this reaction does not proceed with the same efficiency:

$$\mathrm{H_2O + OD \xrightarrow{k_1} OH + HDO}$$
$$\mathrm{D_2O + OH \xrightarrow{k_4} OD + HDO}$$
$$\text{with } k_4 < 0.2\ k_1$$

This result is theoretically supported by the difference in gas-phase Gibbs free energy of the reactions which renders the reaction R1 exergonic, but the reaction R4 endergonic. If such a proton/deuteron transfer reaction was to occur (partially) *via* tunneling, the kinetic isotope effect also points towards a lower reaction rate for the deuteron transfer, *i.e.*, $k_4 < k_1$.

Furthermore, a deuterated-water-formation KMC model shows that including reactions between water and hydroxyl radical isotopes can change the ice ratio of HDO/H_2O with respect to its surface formation. The extend of this change depends on the exact parameters included as well as on the astronomical conditions. More information on the exact role of crucial parameters, such as precise values for the reaction rates and the role of the excess heat upon reaction, in general, is needed before this model can be further extended.

Placing this in context with other studies, we want to stress that the previous experimental solid-state reactions involving different reaction efficiencies for different isotopologues all point towards the involvement of tunneling in overcoming the reaction activation barrier (Oba et al., 2012, 2014). This essentially results in H-enrichment of the ices since tunneling favors reactions with hydrogen over those with deuterium. The reactions discussed in the present work, however, could offer a pathway to D-enrichment. In the light of the recent investigations of the HDO/H_2O and D_2O/H_2O ratios it is thus pivotal to understand the isotopic effect of all single reactions included in the water formation network (van Dishoeck et al., 2013). The present study adds one specific reaction channel that is relevant within the large picture.

Finally, the importance of the abstraction reactions induced by the hydroxyl radical previously reported (Oba et al., 2012; Garrod, 2013) is reinforced by the present results especially since this radical plays an important role as reactive intermediate in water formation. Such reactions can strongly affect the local OH (and OD) abundance in interstellar ices, not only *via* abstraction reactions, but also influence, *e.g.*, CO_2 formation, *via* the diffusion analog reaction R5 ($H_2O + OH \longrightarrow H_2O + OH$), in the case that CO_2 forms through $CO + OH$ recombination (Mennella et al., 2004). In this light, further efforts are needed to establish an accurate estimate of the comparison of the reaction rates of reactions R5 to R1.

BIBLIOGRAPHY

Andersson, S. & van Dishoeck, E. F. 2008, Astron. Astrophys., 491, 907
Anton, R., Wiegner, T., Naumann, W., et al. 2000, Rev. Sci. Instrum. , 71, 1177
Arasa, C., van Hemert, M. C., van Dishoeck, E. F., & Kroes, G. J. 2013, The Journal of Physical Chemistry A, 117, 7064
Caselli, P. & Ceccarelli, C. 2012, Astron. Astrophys. Rev., 20, 56
Cazaux, S., Cobut, V., Marseille, M., Spaans, M., & Caselli, P. 2010, Astron. Astrophys., 522, A74
Chaabouni, H., Minissale, M., Manicò, G., et al. 2012, J. Chem. Phys., 137, 234706
Chang, Q. & Herbst, E. 2014, Astrophys. J., 787, 135
Chase, M. W. 1998, Journal of physical and chemical reference data, Monograph, no. 9. (Washington DC: American Chemical Society)
Cheng, B.-M., Lee, Y.-P., & Ogilvie, J. 1988, Chemical Physics Letters, 151, 109
Coutens, A., Jørgensen, J. K., Persson, M. V., et al. 2014, Astrophys. J. Lett., 792, L5
Cuppen, H. M. & Herbst, E. 2007, Astrophys. J., 668, 294
Cuppen, H. M., Ioppolo, S., Romanzin, C., & Linnartz, H. 2010, Phys. Chem. Chem. Phys., 12, 12077
Devlin, J. 1990, Journal of Molecular Structure, 224, 33
Dulieu, F. 2011, in IAU Symposium, Vol. 280, IAU Symposium, ed. J. Cernicharo & R. Bachiller, 405–415
Furuya, K. 2015, article in preparation
Garrod, R. T. 2013, The Astrophysical Journal, 765, 60
Goldsmith, P. F. & Li, D. 2005, Astrophys. J., 622, 938
Hartogh, P., Lis, D. C., Bockelée-Morvan, D., et al. 2011, Nature, 478, 218
Hiraoka, K., Miyagoshi, T., Takayama, T., Yamamoto, K., & Kihara, Y. 1998, Astrophys. J. , 498, 710
Ioppolo, I., Fedoseev, G., Lamberts, T., Romanzin, C., & Linnartz, H. 2013, Rev. Sci. Instrum. , 84, 073112
Ioppolo, S., Cuppen, H. M., Romanzin, C., van Dishoeck, E. F., & Linnartz, H. 2008, Astrophys. J., 686, 1474
Ioppolo, S., Cuppen, H. M., Romanzin, C., van Dishoeck, E. F., & Linnartz, H. 2010, Phys. Chem. Chem. Phys., 12, 12065
Itikawa, Y. & Mason, N. 2005, Journal of Physical and Chemical Reference Data, 34
Koning, J., Kroes, G. J., & Arasa, C. 2013, The Journal of Chemical Physics, 138,
Kristensen, L. E., Amiaud, L., Fillion, J.-H., Dulieu, F., & Lemaire, J.-L. 2011, Astron. Astrophys., 527, A44
Lannon, J. A., Verderame, F. D., & Anderson, R. W. 1971, The Journal of Chemical Physics, 54
Le Petit, F., Roueff, E., & Le Bourlot, J. 2002, Astron. Astrophys., 390, 369
Lipshtat, A., Biham, O., & Herbst, E. 2004, Mon. Not. R. Astron. Soc., 348, 1055
Lloyd, A. C. 1974, International Journal of Chemical Kinetics, 6, 169
Mennella, V., Palumbo, M. E., & Baratta, G. A. 2004, Astrophys. J., 615, 1073
Meyer, J. & Reuter, K. 2014, Angewandte Chemie International Edition, 53, 4721
Miyauchi, N., Hidaka, H., Chigai, T., et al. 2008, Chem. Phys. Lett., 456, 27
Nagaoka, A., Watanabe, N., & Kouchi, A. 2005, Astrophys. J. Lett., 624, L29
Nagaoka, A., Watanabe, N., & Kouchi, A. 2007, The Journal of Physical Chemistry A, 111, 3016
Nguyen, T. K., Ruffle, D. P., Herbst, E., & Williams, D. A. 2002, Mon. Not. R. Astron. Soc., 329, 301
Oba, Y., Osaka, K., Watanabe, N., Chigai, T., & Kouchi, A. 2014, Far. Disc. , 168, 185
Oba, Y., Watanabe, N., Hama, T., et al. 2012, Astrophys. J., 749, 67
Oba, Y., Watanabe, N., Kouchi, A., Hama, T., & Pirronello, V. 2011, Phys. Chem. Chem. Phys., 13, 15792
Öberg, K. I., Linnartz, H., Visser, R., & van Dishoeck, E. F. 2009, Astrophys. J., 693, 1209
Oliveira, C. M., Hébrard, G., Howk, J. C., et al. 2003, Astrophys. J., 587, 235
Piskunov, N., Wood, B. E., Linsky, J. L., Dempsey, R. C., & Ayres, R. 1997, Astrophys. J., 474, 315
Roberts, H., Herbst, E., & Millar, T. J. 2003, Astrophys. J. Lett., 591, L41
Rodgers, S. D. & Charnley, S. B. 2002, Mon. Not. R. Astron. Soc., 330, 660
Romanzin, C., Ioppolo, S., Cuppen, H. M., van Dishoeck, E. F., & Linnartz, H. 2011, J. Chem. Phys., 134, 084504
Straub, H. C., Lindsay, B. G., Smith, K. A., & Stebbings, R. F. 1998, The Journal of Chemical Physics, 108

Taquet, V., Charnley, S. B., & Sipilä, O. 2014, Astrophys. J., 791, 1
Tielens, A. G. G. M. 1983, Astron. Astrophys., 119, 177
Tielens, A. G. G. M. & Hagen, W. 1982, Astron. Astrophys., 114, 245
van de Hulst, H. C. 1949, The solid particles in interstellar space (Utrecht: Drukkerij Schotanus & Jens)
van Dishoeck, E. F., Herbst, E., & Neufeld, D. A. 2013, Chemical Reviews, 113, 9043
Vasyunin, A. I. & Herbst, E. 2013, Astrophys. J. , 762, 86

SAMENVATTING

INLEIDING

Dit proefschrift gaat over het ontrafelen van de vorming van water op het oppervlak van koude stofdeeltjes die zich bevinden in het InterStellair Medium (ISM). In het Sackler Laboratorium voor Astrofysica van de Universiteit Leiden zijn daartoe experimenten uitgevoerd onder condities die zo dicht mogelijk in de buurt komen van die in de ruimte. Bij de afdeling voor Theoretische Chemie aan de Radboud Universiteit Nijmegen is een complementair computermodel gebruikt om de verschillende processen die op het oppervlak plaatsvinden te kunnen onderscheiden van elkaar.

De studie naar water in het ISM heeft in het afgelopen decennium veel vooruitgang geboekt, niet in de minste plaats dankzij de ruimtemissie van de Herschel Space Observatory. Eén van de belangrijke vragen waarvoor een antwoord werd gezocht is die naar de oorsprong van water op onze eigen planeet. Water is belangrijk voor het leven op aarde, maar het is vooralsnog onduidelijk waar het precies vandaan komt. Dit komt deels door de energetische botsingen tijdens het ontstaan van de aarde en deels doordat de korte afstand van de aarde tot de zon, dat het water op de jonge planeet verdampt zou moeten zijn. Een hypothese is dat water op aarde is gebracht door asteroïdes of komeetinslagen. Om er achter te komen wat de precieze oorsprong van water is, wordt gebruik gemaakt van de verhouding tussen regulier water, H_2O, en zwaarder water, HDO. Zwaarder water bevat één deuteriumatoom in plaats van een waterstofatoom. Deze verhouding is in het oceaanwater een factor 10 hoger dan de D/H verhouding in de gasfase zoals ontstaan in de jonge jaren van het universum. Deze verhoging is het gevolg van de verhoging van de zogenaamde nulpuntsenergie van de OD versus OH binding. Door HDO/H_2O in verschillende regio's van het ISM te vergelijken met dat op aarde is er duidelijkheid te krijgen over de meest waarschijnlijke oorsprong van het (oceaan)water.

WATER IN HET ISM

Op verschillende plekken in de ruimte is water waargenomen, bijvoorbeeld in de geboorteplekken van sterren – prestellaire kernen – en in geëjecteerde gasstromen rondom net gevormde sterren, maar ook in de resulterende schijven waarin planeten ontstaan. In de recente ruimtemissie naar de komeet 67P/Churyumov-Gerasimenko is water ook gezien als bestanddeel van de coma. Dit is de materie van de komeet die verdampt door de toename in temperatuur naarmate ze dichterbij de zon komt. Hoewel water kennelijk tijdens het gehele ster- en planeetvormingsproces kan worden gezien, zijn dit veelal waarnemingen in de gasfase. De meest voor de hand liggende reacties om gasvormig water te produceren zijn echter niet efficiënt genoeg om de hoge concentraties te verklaren: $H + O \longrightarrow OH$ gevolgd door $H + OH \longrightarrow H_2O$.

Het bestaan van interstellair water in de vaste fase, als ijs, werd al gesuggereerd in 1937. Vervolgens werd het in 1946 aannemelijk gemaakt dat water op het *oppervlak* van stofdeeltjes wel kan vormen via de eerder genoemde reacties, bij temperaturen van zo'n -260 °C. Pas in 1973 is waterijs ook daadwerkelijk waargenomen in de ruimte en paradoxaal genoeg is het juist deze ontdekking die een verklaring biedt voor de eerder genoemde hoge concentraties water in de gasfase. Sterker nog, water is het meest voorkomende vastgevroren molecuul in

het ISM. Verder wordt ook gedacht dat de laag waterijs op stofdeeltjes een rol speelt bij het ontstaan van planeten.

De vorming van water op het oppervlak van stofdeeltjes in de donkere wolken die aan de voet staan van het stervormingsproces is heel efficiënt: er kunnen tot zo'n 100 lagen watermoleculen geproduceerd worden gedurende de eerste miljoen jaar. Op kometen kan de dikte van de laag ijs zelfs oplopen tot meters of kilometers. Om de verschillende processen die daarbij een rol spelen goed te kunnen doorgronden, kan gebruik worden gemaakt van de combinatie van oppervlakte-experimenten bij lage temperatuur en theoretische modellen.

ONDERZOEKSMETHODEN

De experimentele proefopstelling die gebruikt is voor de studies beschreven in dit proefschrift is weergegeven in figuur 1 (Hoofdstuk 2). De naam van de opstelling, SURFRESIDE^2, is afgeleid van het Engelse 'SURFace REaction SImulation DEvice'. Het bestaat onder andere uit een roestvrijstalen kamer onder ultrahoog vacuüm met een gouden substraat in het midden. Dit substraat kan gekoeld worden tot temperaturen vergelijkbaar met die in de donkere wolken in het ISM, tot -263 °C. Om de vorming van water te bestuderen moeten atomen en/of moleculen die bestaan uit waterstof (H) en zuurstof (O) met elkaar kunnen reageren op dit oppervlak. Daartoe zijn verschillende atomaire en moleculaire bundellijnen aangebracht. Aan de hand van absorptie van infrarode straling door het ijs en het bepalen van de massa van de gevormde moleculen kan informatie worden verkregen over de reacties die plaatsvinden.

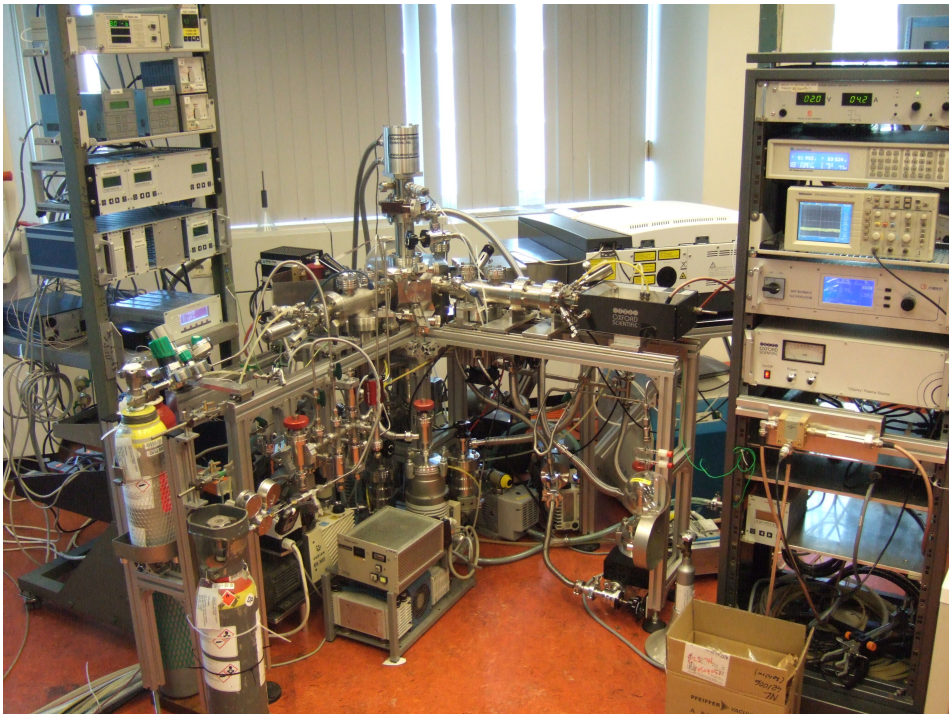

Figuur 1: Experimentele proefopstelling – SURFRESIDE^2 – in het Sackler Laboratorium voor Astrofysica in Leiden.

Het theoretische model (Hoofdstuk 3), kinetische Monte-Carlosimulaties (KMC), maakt het mogelijk om de verschillende oppervlakteprocessen afzonderlijk te bestuderen: vastvriezen en verdampen van atomen en moleculen, diffusie van reactanten op een oppervlak en de mogelijke reacties wanneer twee deeltjes elkaar 'ontmoeten'. KMC berekent de snelheden van de afzonderlijke processen aan de hand van de waarschijnlijkheid dat ze plaatsvinden en zorgt zo voor een beschrijving van de competitie tussen deze processen. Specifieke informatie over de structuur van het oppervlak kan ook worden meegenomen in de berekening.

De aanpak die in dit proefschrift gekozen is voor de combinatie van theorie en experiment begint met het uitvoeren van specifieke experimenten onder gecontroleerde condities. Vervolgens worden diezelfde experimenten gemodelleerd, waarbij de set parameters die de experimenten het best beschrijven wordt opgeslagen. Tot slot wordt het 'beste' model gebruikt om uitspraken te doen over reacties in ijs in het ISM.

KMC-SIMULATIES VAN WATERVORMING

De computersimulaties resulteren in een dieper inzicht in het reactienetwerk, bestaande uit 17 reacties (zie ook figuur 2) van de oppervlaktevorming van water. Hieruit is geconcludeerd wat de belangrijkste routes zijn voor het ontstaan van water wanneer moleculair zuurstof (O_2) en atomair waterstof (H) met elkaar reageren (Hoofdstuk 4). Uit de simulaties blijkt verder dat het zogenaamde hydroxyl radicaal, OH, een cruciaal tussenproduct is. De reactie $H + HO_2 \longrightarrow OH + OH$ kan direct gevolgd worden door $OH + OH \longrightarrow H_2O_2$, wat betekent dat er effectief geen OH meer in het ijs te vinden zou zijn. Dit is echter in tegenspraak met experimenten. Dankzij een uitbreiding van het model kan worden vastgesteld dat de twee gevormde OH radicalen van elkaar wegbewegen als gevolg van de reactiewarmte waarmee ze ontstaan. Daardoor komen ze toch geïsoleerd voor in het ijs. Dit uitgebreide model is vervolgens gebruikt om interstellaire watervorming onder de loep te nemen. Dit is gedaan voor drie interstellaire omgevingen: diffuse, transparante en donkere wolken. Afhankelijk van de omgeving verschilt de hoeveelheid UV-straling en daarmee ook de reactanten die beschikbaar zijn. Daarom is niet in elke wolk dezelfde route voor watervorming dominant (Hoofdstuk 5).

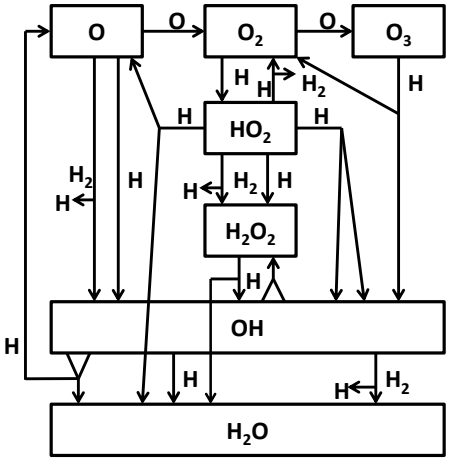

Figuur 2: Reactienetwerk voor watervorming vanuit zuurstof (O, O_2 en O_3) en waterstof (H en H_2).

EEN ENKELE REACTIEROUTE

Naast de studie naar het hele reactienetwerk is ook gekeken naar één enkele reactieroute daarbinnen, namelijk $H_2 + O \longrightarrow OH + H$ (Hoofdstuk 6). De reden daarvoor is dat H_2 heel veel voorkomt in de donkere wolken waar de dikste lagen ijs gevonden worden. Wanneer de genoemde reactie efficiënt zou zijn, zou deze het watervormingsproces beheersen. Vanuit een chemisch perspectief bekeken is het echter heel aannemelijk dat de reactie niet tot nauwelijks plaatsvindt. Aan de hand van een gecombineerd experimenteel en theoretisch project is dit inderdaad bevestigd.

VERDELING VAN H EN D IN POLAIR IJS

Zoals hierboven beschreven is het onderzoek naar HDO van belang om te kunnen begrijpen waar het water op aarde vandaan komt. Net zoals water het meest voorkomende molecuul in ijs is, is zwaarder water het meest voorkomende gedeutereerde molecuul. Dit betekent dat wanneer de waterstof- en deuteriumatomen die gebonden zijn aan het zuurstofatoom kunnen uitwisselen met andere atomen in de directe omgeving, dit van invloed kan zijn op de verhouding HDO/H_2O en vergelijkbare verhoudingen voor andere moleculen zoals methanol (CH_3OD/CH_3OH) of ammoniak (NH_2D/NH_3). Dankzij verbeterde meettechnieken is het mogelijk geweest om deze processen te kwantificeren in amorf (niet-kristallijn) ijs. Zowel H_2O als D_2O zijn daartoe tegelijkertijd uitgevroren op het substraat en afhankelijk van de toename in substraattemperatuur is te zien dat de H- en D-atomen zich herverdelen en zo ook HDO vormen.

LAGETEMPERATUURSTUDIE NAAR HDO-VORMING

Wanneer het reactienetwerk zoals weergegeven in figuur 2 wordt verdubbeld zodat ook reacties tussen zuurstof- en deuteriumatomen kunnen plaatsvinden, is al snel duidelijk dat dit ook betekent dat de twee netwerken met elkaar verbonden moeten worden. Twee reacties die deze verbinding tot stand brengen zijn $H_2O + OD \longrightarrow OH + HDO$ en $D_2O + OH \longrightarrow OD + HDO$. Een studie bij lage temperatuur, -258 °C, laat zien dat de eerste reactie snel verloopt en de tweede heeft een veel lagere efficiëntie.

Het werk in dit proefschrift beschreven karakteriseert de vorming van water op ijzige stofdeeltjes in de ruimte vanuit een fysisch-chemisch perspectief. De conclusies die hieruit voortkomen zijn van belang om de aanwezigheid van water in de ruimte – en daarmee uiteindelijk ook de aanwezigheid van water op aarde – te verklaren.

LIST OF PUBLICATIONS

SCIENTIFIC PUBLICATIONS

Low-temperature chemistry between water and hydroxyl radicals; H/D isotopic effects
T. Lamberts, G. Fedoseev, F. Puletti, S. Ioppolo, H. M. Cuppen, and H. Linnartz,
Mon. Not. R. Astron. Soc. (2015) submitted

Thermal H/D exchange in polar ice - deuteron scrambling in space
T. Lamberts, S. Ioppolo, H. M. Cuppen, G. Fedoseev, and H. Linnartz,
Mon. Not. R. Astron. Soc. 448 (2015) 3820

Experimental evidence for glycolaldehyde and ethylene glycol formation by surface hydrogenation of CO molecules under dense molecular cloud conditions
G. Fedoseev, H. M. Cuppen, S. Ioppolo, **T. Lamberts**, and H. Linnartz,
Mon. Not. R. Astron. Soc. 448 (2015) 1288

Low-temperature surface formation of NH_3 and HNCO: hydrogenation of nitrogen atoms in CO-rich interstellar ice analogues
G. Fedoseev, S. Ioppolo, D. Zhao, **T. Lamberts** and H. Linnartz,
Mon. Not. R. Astron. Soc. 446 (2014) 449

On the relevance of the H_2 + O reaction pathway for the surface formation of interstellar water
T. Lamberts, H. M. Cuppen, G. Fedoseev, S. Ioppolo, K.-J. Chuang, and H. Linnartz,
Astron. Astrophys. 570 (2014) A57

The formation of ice mantles on interstellar grains revisited - the effect of exothermicity
T. Lamberts, X. de Vries, and H.M. Cuppen,
Far. Disc. 168 (2014) 327

The Kinetic Monte Carlo Method as a Way To Solve the Master Equation for Interstellar Grain Chemistry
H. M. Cuppen, L. J. Karssemeijer, and **T. Lamberts**,
Chem. Rev., 113 (2013) 8840

SURFRESIDE^2: An Ultrahigh Vacuum System for the Investigation of Surface Reaction Routes of Interstellar Interest
S. Ioppolo, G. Fedoseev, **T. Lamberts**, C. Romanzin, and H. Linnartz,
Rev. Sci. Instrum., 84 (2013) 073112

Water formation at low temperatures by surface O_2 hydrogenation III: Monte Carlo simulation
T. Lamberts H. M. Cuppen, S. Ioppolo, and H. Linnartz ,
Phys. Chem. Chem. Phys., 15 (2013) 8287

Efficient surface formation route of interstellar hydroxylamine through NO hydrogenation. II. The multilayer regime in interstellar relevant ices
G. Fedoseev S. Ioppolo, **T. Lamberts**, J. Zhen, H.M. Cuppen, and H. Linnartz,
J. Chem. Phys., 137 (2012) 054714

NO ice hydrogenation - a solid pathway to NH_2OH formation in space
E. Congiu, G. Fedoseev, S. Ioppolo, F. Dulieu, H. Chaabouni, S. Baouche, J. L. Lemaire, C. Laffron, P. Parent, **T. Lamberts**, H. M. Cuppen, and H. Linnartz,
Astrophys. J. Lett., 750 (2012) L12

CONFERENCE PROCEEDINGS

Solid State Pathways towards Molecular Complexity in Space
H. Linnartz, J. B. Bossa, J. Bouwman, H. M. Cuppen, S. H. Cuylle, E. F. van Dishoeck, E. C. Fayolle, G. Fedoseev, G. W. Fuchs, S. Ioppolo, K. Isokoski, **T. Lamberts**, K. I. Öberg, C. Romanzin, E. Tenenbaum, J. Zhen,
The Molecular Universe, Proceedings of the IAU, IAU Symposium, Volume 280, p. 390-404 (2011)

CURRICULUM VITAE

On 12 September 1987 I was born in the Regent Quarter in Den Haag. Shortly thereafter, my parents decided to move to Zoetermeer, to a district with many other young families. My interest in math and science was nurtured there, both at home as well as by the technical lego of the neighbors and soon I would recite π to many decimal places. I started a classical education, including Greek and Latin, at secondary school. After our move to a small town, Renswoude, in the beautiful center of The Netherlands, I changed school and attended the Ichthus College in the nearby town Veenendaal. There, I faced the difficult choice between studying French language or chemistry.

I chose to study chemistry at the Radboud University Nijmegen, where I was welcomed by a warm atmosphere. I joined the Curriculum committee, which aims to improve and control of the educational quality of the chemistry Bachelor curriculum, and the Parents Day committee, which organizes a day for parents to experience life at the university by attending a special class and practical courses. The flexibility given to students in Nijmegen allowed me to replace chemistry courses by those from the mathematics and physics curriculum. Moreover, I was granted permission to perform three different research projects during my Master program; hydrodynamics of plankton (Denmark), photophysics of inorganic compounds (Ireland), and using phosphorescence in turbulence. During these final two thesis projects I already aimed at combining both experimental and modeled or theoretical results.

It was exactly the combination between experiments and theory, at the Sackler Laboratory in Leiden and at the Department of Theoretical Chemistry in Nijmegen, that made me choose the PhD position that resulted in the publication of this thesis. The membership of the Dutch Astrochemistry Network (DAN) and my close relationship to the Laboratory Astrochemical Surface Science In Europe (LASSIE) network have allowed me to gain acces to a large variety of research topics. I have studied the formation of solid-state regular and singly deuterated water from a physical-chemical perspective against the background of astrochemistry. The experimental work has been performed in an Ultra-High Vacuum system, while the different surface processes are disentangled with a Kinetic Monte Carlo model. Simultaneously, the many Italian collegues at the Observatory inspired and helped me pursue my interest in languages.

During my PhD I have presented my work at various colloquiua and scientific meetings, not only in The Netherlands, but also in Denmark, Germany, the United Kingdom, and the United States. Furthermore, I have given public lectures at amateur astronomers clubs and for school children following an extra-curricular program. Finally I have been involved in the coordination of a PhD/postdoc networking day aiming to enhance the mutual contact between the junior scientists in the field of astrochemistry in The Netherlands.

In the near future I will start as a postdoc in the group of Herma Cuppen at the Radboud University for a few months after which I will move to Stuttgart in Germany and join the group of Johannes Kästner. There, I will be able to transfer my knowledge about astrochemistry, while learning more about quantum chemistry within the framework of the importance of tunneling in chemistry.

DANKWOORD

Writing a thesis may seem to be a lonely task at times, but I feel lucky with the people that have surrounded me, in the various places in The Netherlands and elsewhere around the globe, that have all contributed in their own respective ways. It is thanks to them that this manuscript has been completed and it is thanks to them that I have learned so many things, not only concerning science, but also about life, culture, music, food, and about myself.

First of all, I owe a big thank you to my three supervisors. Harold, dank voor de vrijheid die mij hebt gegund in het vinden van mijn weg. Herma, ik heb me altijd thuis gevoeld in jouw groep, ondanks de kortere tijd die ik daar heb doorgebracht. Dankjewel voor de koffiegesprekken over van-alles-en-dan-nog-wat en voor je chemische blik op ons werk. Sergio, grazie for your instructions first in the laboratory and later from all the various parts of the world that you have traveled.

Leiden Observatory is a very specific place to be employed; not only does it bring together observers, modelers, and experimentalists, it also combines many different nationalities and work styles, and therefore many points-of-view. Allereerst een heel hartelijk dankjewel aan de secretaresses en de computer groep, in het bijzonder Anita, David, Erik, Jeanne en Liesbeth. My office mates, Isa, Umut ('evet'), Joe, Ricardo (we love the 90's!), Merel, and Christian have made the office a better place. My fellow Sackler laboratory members, Anton, Dongfeng, Edith, Euan, Gustavo, Hector, JB, Jo G., Kirsten, Ko-Ju, Pablo, Steven, and Vincent, thanks for the many papercakes that you have caused! Junfeng, I have really appreciated your company. Niels, let's go to a party again! Gleb, without you in the lab and in the Kaiser Lounge, my PhD life would not have been the same, a big big thank you. Iemand die collectief gemist wordt als hij op vakantie is, is Martijn; dankjewel voor jouw bijgedragen steentje. En ook onze nieuwste aanwinst, Aart, dankjewel voor al die flauwe grappen! The Astrochem corridor has been a wonderful place to pick up the necessary astronomical knowledge, thank you for your willingness to teach me, in particular Catherine, Ewine, Daniel H., Kenji, Lars, Maria, Mihkel, and Xander (bedankt voor de koekjes!). Magnus, you also belong in that category, but you and Mihaela are also wonderful BBQ-in-the-rain companions. Caroline, ik had niet gedacht dat het geven van een vak waar ik niets vanaf wist, ook nog een vriendin zou opleveren! Thanks also to Carl, Clément, Cristóbal, Carina, Emanuele, Francisco, Gaby, Heather, Marissa, Mattia, Mher, Monica, Olmo, Tiffany, and Vachail. E poi, gli 'Italiani'! Grazie mille for allowing me to be part of such a wonderful group of friends, for the dinners, birra crucis, flower field cycling trips, Koninginnenach, and all our other activities together. Most of all, thank you for being around during the highs and lows, and for the conversations about the more important things in life. But also... Marco, thank you for your passion of food. Berenice (and Jesús), thank you for introducing the cake game, whichever day the cake finally arrived, it was always a pleasure. I hope to continue to enjoy the parties at Alessandra and Fabio, pulcino pio in particular is engraved in my memory for ever. I am happy to have copied large parts of your music collection, Nicola, otherwise I would have really missed out. Thank you for the two bottles you left us, the production is ongoing! Silvia, thank you for accompanying me to the gym, for the dinners at your house, the girls night out, and the shopping trips we undertook. Singing and playing music live in a bar, or downstairs in the kantine, has been an incredible pleasure with you, Matteo, but never again Broadway! Irene, chica, I will never forget our

Sicilian experience (cannoliiii) nor your crazy energy when you drink a coffee, you are really an amazing person!

Ed anche Gaetano, grazie mille per il tuo aiuto con questa bellisima copertina!

Maar ik heb ook consequent, vier jaar lang, ongeveer een dag in de week in Nijmegen gewerkt, in het Bourgondische Havanna aan de Waal. Met enige regelmaat heb ik daar het gezelschap mogen genieten van twee speciale jongemannen. Onze eerste gezamenlijke avondmaaltijd vond plaats halverwege mijn promotie, toen ik, zacht uitgedrukt, niet de meest enthousiaste promovenda was. Leendertjan, het was goed om met een fysicus te kunnen praten over gecondenseerd water in de ruimte, en in de bergen, net zoals het goed was om samen te koken en een wadloopexcursie op touw te zetten. Joost, jouw passie voor een goede sfeer, het theater, lekkere wijn, mooie kaasjes, je eindeloos-lijkende geheugen en bijzonder goed getimede mailtjes waren een keer op keer een cadeautje. Jolijn, dankjewel voor de gezelligheid tijdens het delen van de kamer op menig conferentie. Adrien, merci de m'avoir aidé à rétablir mon français un peu rouillé! Furthermore, thanks to the office mates, master students and fellow PhD students for their company during the frequent cake meetings: Boy, Daniel, Eduardo, Koos, Lei, Liesbeth, Peter, Sasha, Simone, Tijs en Xander. Ook Gerrit en Ad voor hun aanwezigheid tijdens de dagelijkse groepslunch die het gespreksniveau wisten op te krikken tot schijnbaar onbereikbare hoogten, maar ook voor hun waardevolle wetenschappelijke adviezen.

Being part of the Dutch Astrochemistry Network (DAN) and being related to the Laboratory Astrochemical Surface Science In Europe (LASSIE) meant being lucky enough to meet many interesting people, whichever way you wish to interpret the word 'interesting'. In particular discussions, language exchange and drinks with Ewelina, Fabrizio, Geert, Leon, and Tobias are gratefully acknowledged!

En dan zijn er nog al die mensen die veel minder te maken hebben gehad met mijn dagelijkse bezigheden.

Ook al klaag ik er wel eens over het kneuterige Veenendaal, maar het is heel tof dat we elkaar ieder jaar één keer met z'n allen weten te treffen aldaar om een heerlijk avondmaal te verorberen. Wat zijn we veel veranderd ten opzichte van de vouwwagen kampeertochten die we vroeger maakten, op naar de volgende 10 jaar. Lieve Andrea, Arwin, Cornelie, Jan-Willem, Eline, Michiel, Julia, Arjan, Leendert en Sanne: bedankt!

Het is uiteindelijk dankzij de studie scheikunde, dat ik in Leiden beland ben. Jasper, dankjewel voor je steun, ik weet dat je je best hebt gedaan om elke vrijdag om te toveren in iets positiefs. Jurn, dank voor het logeeradres boven aan de 'berg'. Jan en Cynthia, veel geluk bij de aankomende miljoenenjacht, met de iBood box en tot snel! Bram, dank voor het delen van de promotieperikelen en gezelligheid samen met Michelle. Yvette, het is altijd fijn om even te kunnen bijpraten, ik vind het bijzonder hoe we elkaar toch niet uit het oog verloren zijn. Bijpraten, al dan niet op gchat of aan de telefoon, doe ik ook bijzonder graag met Carlijn. Jij hebt alle ups en downs meegemaakt en hebt mij meer dan eens kritisch en realistisch naar mezelf doen kijken. Ontzettend bedankt, ik kijk uit naar de volgende citytriptreinreis samen!

Nico, pinguinpakje of niet, zonder jou was ik hier wellicht nooit aan begonnen. Dank voor je wetenschappelijke opvoeding en die daarbuiten; ik zie de paddestoelen tegenwoordig zelfs staan als ik op een conferentie langs de bermen loop.

Het heeft even geduurd voordat ik in Leiden mijn plekje had gevonden, maar twee belangrijke factoren die me daarbij geholpen hebben zijn het huis waarin het heb gewoond en het oude fabriekspand waarin ik heb gekookt.

Elles, je bent een beetje gek, ik ook, en dat vind ik leuk, net zoals het dragen van twee verschillende sokken, dat is ook leuk. En Thalassa, hoe had ik ooit #YOLO 2013 kunnen doorkomen zonder jou. Wat hebben we bizar veel mensen ontmoet, chocola gegeten, rare films gezien,

plan A en B geweest, en … gewoon veel meegemaakt. Ik ben benieuwd hoeveel appjes we blijven sturen per dag!
Koken en eten zijn twee terugkerende belangrijke zaken in mijn leven, en die worden uitstekend gecombineerd met interessante mensen en grote idealen bij de Vrijplaats. Tony, Petra, Coen, Maria, Katie en al die anderen, dankjewel voor de bijzondere sfeer die er heerst. Rest mij alleen nog te zeggen dat er niets beters bestaat om je hoofd leeg te maken, dan het snijden van 5 kilo ui.

En natuurlijk niet te vergeten de wat meer recente aanwinst: teh_CRW! Daniel, niet alleen als kritische collega en gids in New York heb ik je gewaardeerd, maar je gezelligheid en uitstapjes naar verschillende muziekaangelegenheden worden ook buiten het lab op prijs gesteld. Dan mijn mede-vega-eerste-keer-wintersporter Jelle, wanneer verhuis je nou naar Leiden? Gezond eten is wel een dingetje in de groep, maar lekker eten nog veel meer: Gerdien wat een geluk dat ik met jou mijn passie voor koken kan delen en wat fijn dat Ashgard daar ook nog eens helemaal in meegaat.

Onderdeel zijn van een familie is iets dat lang ongrijpbaar is geweest, maar gelukkig baart oefening kunst! Tineke, jou valt de eer toe mijn eerste 'leermeester' te zijn geweest in dat opzicht, dank daarvoor. Lieve Stremmelaar-Nolten-Busch ooms, tantes, neven, nichten, aangetrouwde sterrenkundig geinteresseerden of juist helemaal niet; dankjewel voor de bezoekjes aan Duitsland en Frankrijk, voor de gezelligheid bij het Kerstival, voor de slechte grappen en voor jullie lieve (?) (klein-)kinderen! De afgelopen twee-en-een-half jaar koester ik. En Renate, jij in het bijzonder bedankt, zonder jou had ik veel niet gedurfd. Wat betreft familiebijeenkomsten: lieve heren Boltje en dames Vogt en Al-mafraji, dank voor de gezelligheid!

Aan de allerliefste, Daan, ik had nooit durven hopen op zo'n bijzonder afgelopen jaar. Jij hebt mij telkens weer opgevangen en door de moeilijke eindfase heengesleept. Onze levens zijn in elkaar overgevloeid zoals zacht water door je handen kan stromen terwijl je de tijd verliest ;-) Ik heb heel veel zin in een toekomst met jou, in onze eindeloos-energieke-maar-voor-anderen-vermoeiende interactie en de avonturen die ons te wachten staan. Ik vind je tof!

Voordat dit proefschrift op zijn einde loopt, wil ik nog terug naar het allereerste begin. Hoe anders had het kunnen lopen zonder het speelgoed dat zo zorgvuldig werd uitgekozen door mijn vader, zonder de dagelijkse toewijding van mijn moeder en bovenal zonder hun bijzondere, soms uitvoerige, uiteenzettingen over wat echt belangrijk is in dit leven. Het voelt alsof een eenvoudig woord of kleine daad niet genoeg is, maar lieve Herman en Marijke: dankjewel.

On ne voit bien qu'avec le cœur. L'essentiel est invisible pour les yeux.
Antoine de Saint-Exupéry